

Journal of
Green Energy
Research and Innovation

Volume 2, Issue 4, Autumn 2025



PUBLISHER
Arak University

Journal of **G**reen **E**nergy **R**esearch and **I**nnovation **(JGERI)**

Publisher: **Arak University**

Director-in-Charge: **Dr. Ali Asghar Ghadimi**

Editor-in-Chief: **Prof. Gevork B. Gharehpetian**

Deputy Editor: **Dr. Abolghasem Daeichian**

Managing and Executive Editor: **Dr. Mahyar Abasi**

Coverage area: **International**

Journal Type: **Scientific and technical**

Scientific Rank (Iran MSRT): **B**

Language: **English**

Frequency: **Quarterly**

Review Time: **4-8 Weeks**

Publication Type: **Electronic**

Open Access: **Yes**

Licensed by: **CC BY-NC 4.0**

Policy: **Peer-Reviewed**

DOI: **10.61186/jgeri**

E-mails: **jgeri@araku.ac.ir**

Website: **<https://jgeri.araku.ac.ir/>**

Address: **Department of Electrical Engineering, Faculty of Engineering, Arak University, Arak, Iran.**

P.O. Box: **38156-8-8349**

Tel: **086-32625099**

Editorial Board



Director-in-Charge:
Dr. Ali Asghar Ghadimi



Editor-in-Chief:
Prof. Gevork B. Gharehpetian



Deputy Editor:
Dr. Abolghasem Daeichian



Managing and Executive Editor:
Dr. Mahyar Abasi



Assistant Editor:
Dr. Mazdak Ebadi



Assistant Editor:
Dr. Mohammad Reza Miveh



Assistant Editor:
Dr. Mohammad Monfared



Assistant Editor:
Dr. Mahdiah S. Sadabadi



Assistant Editor:
Prof. Keyhan Sheshyekani



Editorial Board:
Dr. Ali Jabbari



Editorial Board:
**Prof. Seyed Ghodratollah
Seyfossadat**



Editorial Board:
Prof. Mohammad Mohammadi



Editorial Board:
Prof. Abdolnabi Kosarian



Editorial Board:
Prof. Sajad Najafi Ravadanegh



Editorial Board:
Prof. Reza Shariatinasab



Editorial Board:
Prof. Soheil Ganjefar



Editorial Board:
Dr. Khosro Khandani



Editorial Board:
Dr. Mohsen Hamzeh



Editorial Board:
Dr. Amin Mirzaei



Editorial Board:
Dr. Amir Hossein Abolmasoumi



Editorial Board:
Dr. Majid Mahdieh



Editorial Board:
Prof. Mohammad Hassan Moradi



Editorial Board:
Prof. Hasan Rastegar



International Editorial Board:
Prof. Akhtar Kalam



International Editorial Board:
Prof. Slobodan Vukosavic



International Editorial Board:
Prof. Francisco Jurado



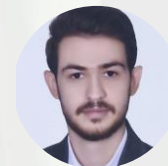
International Editorial Board:
Prof. Pierluigi Siano



International Editorial Board:
Prof. José Manuel Aller Castro



Page Designer:
M-Eng. Mohammad Amin Bahramian



Page Designer:
M-Eng. Morteza Azizi



Graphist:
Dr. Javad Ebrahimi



Language Editor:
MSc. Majid Sadeghzadeh Hemayati

About Journal

JGERI is an international, open-access, and free-of-charge journal in the field of green and renewable energies, published quarterly, only electronically, in cooperation with the Renewable Energy Research Institute (**RERI**) of Arak University and Iranian Association of Electrical and Electronics Engineers (**IAEEE**). Articles accepted and published by **JGERI** are in three formats: research articles, review articles, and applied articles. **JGERI** accepts manuscripts that provide results of scientific achievements in a very wide scope of fundamental, engineering, and industrial research focusing on green energy.

The following articles are acceptable:

- **Research articles** are expected to present innovative solutions, new concepts, or creative ideas that can help solve existing or emerging technical challenges in the field of green and renewable energy.
- **Review articles** are expected to provide enlightening and specialized reviews, trainings, or case studies on an important topic, timely and widely in the field of green and renewable energies.
- **Applied articles** are expected to share the results of the industry's valuable experiences in dealing with challenging technical issues, developing/adopting new standards, applying new technologies or solving complex problems in the field of green and renewable energies. These articles can have a significant impact on the strategic plans of the industry in the coming years.

Aims and Scope

JGERI is interested on the qualified international multidisciplinary research results related to all aspects of green energy. The scope of **JGERI** is very broad, and welcomes original, novel fundamental and engineering research. We also publish reviews and industrial reports of green energy and its impact on the eco-environment.

We welcome research papers that focus on, but are not limited to, the following areas:

- Policies and Strategies for Green Energy Systems
- Fundamental And Industrial Applications for Green Energy Systems
- Energy Conversion, Control Techniques, and Grid Interactive Systems for Green Energy Systems
- Environmental Impacts of Energy Technologies and Pollution Control
- Materials And Catalysis for Green Energy Systems
- Green Energy Consumption
- Artificial Intelligence, Machine Learning, and Computational Methods in Green Energy Systems
- Public Awareness and Education for Green Energy Systems
- Solar Energy and Photovoltaic
- Wind Energy
- Hydrogen Energy and Energy Storage
- Biofuel and Bioenergy
- Utilization of Green Energies in the Structure of Power Systems
- Development of Manufacturing Technology for Green Energy Production Tools
- Electricity Market in the Presence of Green Energies
- The Effects of Green Energy Production on Power Quality of the Power System
- Impact of Expansion Planning of Power Systems on the Development of Green Energy Generation
- Operation of Green Energy-Based Microgrids
- Control and Protection of Power Systems in Networks Equipped with Green and Renewable Generation
- Energy Management in Networks Consisting of Green Energies
- Studies on the Technology of Hybrid Vehicles Based on Green Energy Fuels
- The Future Perspective of the Electricity Industry in the Presence of Production-Based Technologies and Green Energy-Based Consumers
- Green Energy Storage Technologies
- Communication Infrastructures and Protocols and Internet in Green Energy-Based Power Systems
- Cyber Security and Defense Activities in the Field of Green Energy Management

Each manuscript will go through a rigorous peer-review process. you can visit our Guide for Authors page for information on preparing your manuscript.

Guide for Authors

1. Important points and rules for manuscript submission and publication

- Submitting a manuscript to a journal means that the manuscript is not under review or has not been published anywhere in any other language before.
- The submission of the manuscript for publication by the author, implicitly or explicitly, implies the approval of the organization or body where the author works and has used its affiliation.
- By submitting the manuscript, all authors officially declare their agreement to grant the copyright of the manuscript in case of acceptance to Arak University and **JGERI**. However, the authors are responsible for all the contents published in the manuscript, and the journal is only a reviewer and publisher.
- All authors are required to declare any actual or potential conflicts of interest, including financial, personal, or relationships with individuals or organizations that could affect their work.
- Each of the authors must declare their contribution and role in the manuscript on the Title Page to the journal. The statement of approval of all authors and their role in the manuscript is the responsibility of the corresponding author.
- Authors should note that all manuscripts sent to **JGERI** are checked with Authenticate's CrossCheck software to analyze the authenticity of the content. In this analysis, the overlap and similar texts presented in the submitted manuscripts will be determined.
- **JGERI** makes its manuscripts open to access after publication and there is no charge (APC) for reviewing and publication of manuscripts, and readers can download and use the articles for free.
- All authors, if they had financial support in conducting research related to this manuscript, should briefly state their role. If financial source(s) have no role in the results of the research published by the article, this should also be mentioned by the authors.
- Acknowledgments to individuals and institutions can be mentioned in a separate section at the end of the manuscript before References, and they must not be included as footnotes or in any other form. In this section, it is recommended to mention the names of those who have collaborated during the research (such as those helping in the language correctness aspect of the manuscript, assisting in writing the manuscript or proofreading it, and other cases).
- Non-commercial use of the manuscript will be governed by the Creative Commons Attribution-NonCommercial 4.0 International License, which is currently available at the link (<https://creativecommons.org/licenses/by-nc/4.0/>). This certificate allows others to use the authors' work in a non-commercial way and utilize it in their research work, although in the new work, they need to acknowledge the authors and mention its non-commercial nature.

2. Initial submission of the manuscript

Submission to this journal is online and you will be accompanied in all the steps of creating a user account and uploading files. All correspondence, including notification of the editor's decision and request for revision, will be made via email. To submit your manuscript, just click on the **Submit Manuscript** option on the journal page. Then, click on **Register** to create an author account. A message will be sent to your email containing your username and password. Then, log in to the manuscript submission system on the Users login page, where you need to enter the username and password and submit your new manuscript. Once you are logged in, you can change your password by clicking on My Home in the top menu. For the next time, just log in to your account. Please include the names, addresses, and email addresses of at least three potential academic reviewers with the paper. Please include reviewers' names and their academic rank, affiliation, and contact information (mail address is mandatory). However, only the editor has the right to decide on the use of suggested reviewers. All the submitted manuscripts undergo the process of plagiarism check with IThenticate software and the review process begins. According to the journal policy, there is a difference between the requirements for initial and revised submission files. Required files for initial submission include three files: **JGERI_Main_Manuscript**, **JGERI_Form_for_Copyright_Transfer_Statement_and_Conflict_of_Interest_Disclosure** and **JGERI_Cover_Letter**, all three of which must be sent to the journal in PDF format. You can use the links below to download the requirements and suggestions files of these three files.

- [JGERI_Guideline_for_Main_Manuscript](#)
- [JGERI_Guideline_for_Cover_Letter](#)
- [JGERI_Form_for_Copyright_Transfer_Statement_and_Conflict_of_Interest_Disclosure](#)

3. Submission of the revised manuscript

If the submitted manuscript, after going through the initial review process, is evaluated by the officials and reviewers of the journal and a decision is made to make corrections and revisions in the form of minor or major, the authors are obliged to make the corrections and prepare the response letter to the reviewers within the time specified by the journal. Three files must be sent to the journal at this stage: WORD and PDF files of the revised manuscript (changes should be highlighted), PDF file of the response to the reviewers (including the comments and responses of each of the reviewers separately), Title Page and Authorship file in WORD format (containing two main forms: Title Page and Authorship). The link to download the necessary files along with their requirements and instructions is given below. Points raised in the file **JGERI_Revised_Manuscript** must be followed for compiling the revised manuscript. The authors are obliged to submit the revised file in PDF and WORD format to the

journal. Also, different parts of the file [JGERI_Form_for_Title_Page_and_Authorship](#) needs to be completed and signed by the corresponding author, but [JGERI_Response_to_the_Reviewers_Comments](#) is suggested by the journal and it is not necessary to follow all the points of that file. It should be noted that all the stages of page layout and editing in the form of final publication are the responsibility of the journal. In the completion stages of this process, the cooperation of the authors is needed, and we will inform you at each stage. Thus, the minimum requirements for file compilation are provided in the template file.

- [JGERI_Guideline_for_Revised_Manuscript](#)
- [JGERI_Form_for_Title_Page_and_Authorship](#)
- [JGERI_Guideline_for_Response_to_the_Reviewers_Comments](#)

4. **After the final acceptance of the manuscript**

After announcing the final acceptance of the manuscript (reviews may happen several times), the files [JGERI_Revised_Manuscript](#) and [JGERI_Form_for_Title_Page_and_Authorship](#) will be sent to the paging unit for page layout and final editing. After the final acceptance announcement, the authors will be asked to send a graphic abstract included in a single file. Then, the process of compilation of the manuscript will be completed by the journal and finally, the proof version of the manuscript will be sent to the authors. The authors are obliged to check the proof file completely and report to the journal if they find any ambiguity or error in the final file. In some cases, along with the final proof file of the manuscript, there may be a series of errors and ambiguities in the manuscript, which are sent to the author in the form of comments along with the proof version of the manuscript. The corresponding author is obliged to clarify and resolve these problems and ambiguities in the specified time.

5. **After publication on the journal's website**

After announcing the initial acceptance, the information of the article without its content will be indexed in the Articles in the Press section of the website. After including the article in the issue selected by the journal, the desired article will be indexed in the Current Issue unit along with Vol., No., and pp. Also, the electronic file of the article can be introduced in all scientific references through the DOI link. The important point is that, after acceptance and indexing, the names of the authors cannot be changed, that is, it will not be possible to add, delete, or change the order of the names of the authors and their organizational affiliations.

Cooperative Publication Organization



Renewable Energy Research Institute of Arak University
<http://araku.ac.ir/web/riren>



Iranian Association of Electrical and Electronics Engineers
<https://iaeee.ir/>



Iranian Wind Energy Association
<https://www.irwea.org/fa/>

Indexing Databases and Social Networks



Iran MSRT: <https://journals.msrt.ir/home/detail/21538/>



Magiran: <https://www.magiran.com/magazine/8484>



Google Scholar: <https://scholar.google.com/citations?user=47bsJFoAAAAJ&hl=en>



LinkedIn: <https://www.linkedin.com/in/jgeri-arak-university-0818872b9>



Academia: <https://independent.academia.edu/JournalofGreenEnergyResearchandInnovationJGERI>



MyScienceWork: <https://www.mysciencework.com/profile/j.green.energy.res.innov.jgeri>

Contents

| Article Title and Authors | Page No. |
|--|-----------|
| Regional Planning for Green Energy Synergy: A Foresight Analysis of Policies and Infrastructure in Yazd Province Ali Naderi, Reza Naderi | 1 |
| Enhancing Renewable Energy Forecasting: A Hybrid Machine Learning Approach for Solar and Wind Energy Potential in Ahvaz City Mehdi Mohammadian Mehr, Hossein Farzin | 14 |
| Introducing New Control Methods to Apply in Flexible Photovoltaic Systems at the 3-Phase 4-Wire Grids Saeid Khani, Leila Mohammadian | 27 |
| Optimal Configuration of Solar Combined Hydrogen, Heat, and Power (S-CHHP) by Considering Reliability Model Mojtaba Pirmohammad Talatape, Sajad Bagheri, Reza Ghanizadeh, Mohammad Reza Miveh | 45 |
| Flexible Energy Scheduling in the Electrical, Thermal, and Gas Networks, including Energy Hubs with Renewables and Flexible Units Naghi Moaddabi Pirkolachahi, Mehrdad Mallaki, Najmeh Charaghi Shirazi, Mousa Hamrahi | 58 |
| Detection and Determination of Short-Circuit Faulty Phases in Transmission Lines Compensated with a PV-Connected Series Static Synchronous Compensator Mahyar Abasi, Ebrahim Khanfari | 67 |

Regional Planning for Green Energy Synergy: A Foresight Analysis of Policies and Infrastructure in Yazd Province

Ali Naderi, Reza Naderi

Highlights

- ❖ Introduces "green energy synergy" via multi-method foresight to balance Yazd's energy.
- ❖ Highlights disparities: Yazd's surplus shrinks by 2035, while Ashkezar and Bafgh face deepening deficits.
- ❖ Proposes four scenarios from "Synergistic Development" to "Energy Isolation."
- ❖ Recommends county-specific solar strategies, smart grids, and investment funds.
- ❖ Converts regional inequalities into scalable green growth opportunities.

Graphical Abstract

YAZD GREEN ENERGY SYNERGY: FORESIGHT PLAN

THE CHALLENGE



IMBALANCE: 2022 SURPLUS/DEFIT.
2035 DEFICITS WORSEN.

↑↓ QUANTITATIVE TREND ANALYSIS
DELPHI SCENARIOS



KEY INNOVATION: GREEN ENERGY SYNERGY. SCALABLE MODEL

Use your device to scan
and read the article
online



Citation

A. Naderi and R. Naderi, "Regional Planning for Green Energy Synergy: A Foresight Analysis of Policies and Infrastructure in Yazd Province," *Journal of Green Energy Research and Innovation*, vol. 2, no. 4, pp. 1-13, 2025.



<https://doi.org/10.61882/jgeri.2.4.1>





Online ISSN: 3041-9018

Journal of Green Energy Research and Innovation

Journal Homepage: www.jgeri.araku.ac.ir

Regional Planning for Green Energy Synergy: A Foresight Analysis of Policies and Infrastructure in Yazd Province

Ali Naderi ^{1,*}, Reza Naderi ²

¹ Department of Urban planning, Yazd University, Yazd, Iran.

² Department of Engineering, Yazd University, Yazd, Iran.

ARTICLE INFO

Keywords:

Regional planning,
Green Energy Synergy,
Sustainability,
Imbalance,
Renewable Energy.

Article History:

Received: 01 April 2025;
Revised: 14 May 2025;
Accepted: 03 June 2025.

Article type:

Research Article

* Corresponding authors

E-mail address

alinaderi@stu.yazd.ac.ir (A. Naderi)

ABSTRACT

This study aims to enhance regional planning for green energy synergy in Yazd Province by addressing energy imbalances and promoting sustainable development. Significant disparities in production and consumption persist, with Yazd County exhibiting an 8.4-million-kWh surplus in 2022, while counties such as Ashkezar and Bafgh show deficits of approximately 1 million kWh. The analysis indicates that, without intervention, surpluses will decrease and deficits will increase by 2035. Using quantitative trend analysis in MATLAB and participatory Delphi-based scenario development, the study constructs four scenarios: synergistic development, which maximizes renewable energy use; foreign dependency, which sustains disparities; local self-sufficiency, which supports localized solutions; and energy isolation, which exacerbates imbalances. Proposed strategies include decentralized solar power plants, smart grid systems, and a green investment fund. The concept of “green energy synergy” offers a novel framework for transforming regional disparities into opportunities for renewable energy development. This research provides a scalable model for sustainable planning in Yazd and comparable regions, contributing to more effective energy policy formulation.

1. Introduction

Rising global energy demand, reliance on fossil fuels, and inadequate infrastructure have intensified regional energy disparities, threatening economic efficiency, environmental sustainability, and social stability [1,2]. Regional planning for green energy development, as a systemic approach to coordinating resources, infrastructure, and policies, is critical for achieving sustainability and mitigating these disparities [3]. Energy imbalance—defined as the disparity between energy production and consumption—reduces economic efficiency, increases environmental pollution, and amplifies spatial inequalities [4,5]. This imbalance often stems from differences in production and consumption across counties, driven by centralized planning and limited integration of local resources. Yazd Province, located in Iran’s central plateau, exemplifies this challenge. While Yazd County benefits from a significant surplus due to its solar energy potential and industrial base, counties such as Ashkezar, Bafgh, and Taft face persistent deficits, exacerbated by rapid industrial and residential demand growth as well as infrastructural limitations [6]. Existing studies in Iran [7], [8-11] have primarily focused on national-level energy strategies or technical assessments of renewable potential, overlooking the importance of spatial coordination in regional planning. This gap underscores the need for an approach that integrates spatial planning with energy management to transform disparities into opportunities for green development. This study aims to develop a framework for green energy synergy in Yazd Province, emphasizing coordinated regional planning that aligns policies, infrastructure, and renewable energy resources.

Using a multi-method foresight approach—combining quantitative trend analysis with participatory scenario development through the Delphi method—the research forecasts energy trends and evaluates alternative pathways under uncertainty. By addressing the root causes of energy imbalance and proposing decentralized, context-specific strategies, the study contributes both theoretically and practically to regional energy planning. It provides not only a model for Yazd but also a scalable approach for other regions facing similar challenges related to energy justice and sustainability.

2. Literature review

2.1. Theoretical Foundations and Key Concepts

The origins of modern regional planning principles can be traced back to responses to the harsh and unjust conditions created by the Industrial Revolution in 19th-century England and France [12]. Since 1933, regional planning theories have undergone significant transformation. Walter Christaller's Central Place Theory (1933), and August Lösch's expansion of it in 1954 [13], provided a foundational framework for analyzing urban spatial patterns. Earlier, in 1929, Alfred Weber introduced Industrial Location Theory [14], which Walter Isard later expanded in 1956 by focusing on optimizing industrial locations on the basis of transportation costs [15]. In 1957, Gunnar Myrdal introduced the concept of cumulative causation, demonstrating how developed regions benefit from economies of scale [16-18]. This perspective was complemented by François Perroux's Growth Pole Theory in 1950 [19,20] and further refined by Jacques-René Boudeville in 1966, emphasizing the role of large corporations in strengthening regional growth [21,22]. In 1965, Jeffrey Williamson argued that regions initially diverge during early development stages but tend to converge over time.

In the 1980s, influenced by globalization and economic recessions, regional planning shifted toward entrepreneurial and market-driven approaches, highlighting regional competitiveness [23]. The 1990s marked the rise of regional networks and economic clusters, as proposed by Michael Porter and Annalee Saxenian [24,25], while the Rio Summit in 1992 introduced sustainable development as an effort to balance economic, environmental, and social objectives. Since 2000, Richard Florida's Creative Class Theory (2002) has emphasized attracting creative individuals as a driver of regional development [26], although it has faced criticism for reinforcing inequalities. From 2010 to 2025, challenges such as climate change, smart-city expansion, and energy shortages have reinforced the need for sustainable planning, digital development, and green growth.

Energy imbalance, referring to the disparity between energy production and consumption, is a structural challenge that intensifies in regions with weak infrastructure or uncoordinated policies [27]. It describes a condition in which the equilibrium between energy supply and demand is disrupted, resulting in insufficient production to meet existing demand [28]. This imbalance creates multi-dimensional challenges, including reduced industrial efficiency, increased production costs, and environmental degradation [4,5]. In Iran, due to heavy dependence on fossil fuels and unequal resource distribution, energy imbalance has become a serious threat to regional stability [29].

In contrast, the concept of synergy—rooted in systems science—refers to coordination and value creation through the interaction of system components. More specifically, synergy represents functional interactions that generate complex outcomes, playing a critical role in the evolution of complex systems [30]. In the energy sector, synergy involves achieving balance and efficiency through collaboration among resources, infrastructure, and policies. Unlike resilience, which focuses on adapting to shocks, or energy security, which emphasizes maintaining a continuous supply, synergy highlights sustainable value creation [31,32].

This study applies the synergy concept to propose an innovative framework for regional planning, aiming to transform regional inequalities into opportunities for green development. Table 1 compares the current study with previous research.

Table 1. Classification of past scientific research.

| Study | Focus | Key Findings | Difference with Current Study |
|---------------|--------------------------------------|---|--|
| [33] | Energy justice in planning | Emphasized procedural justice in energy projects | Focused on social dimensions; the current study integrates technical foresight. |
| [34] | Rural electrification via renewables | Advocated renewable systems for rural energy access and carbon reduction | The current study addresses spatial imbalance at the county level. |
| [35] | P2P microgrids | Reduced imbalance and improved prosumer benefits | This study uses forecasting combined with policy-based foresight. |
| [36] | Regional strategic energy planning | Developed renewable energy models through local government-university collaboration | Similar participatory elements, but different modeling tools. |
| [37] | Citizen-driven energy transition | Introduced renewable energy communities, highlighting legal and incentive barriers in France | Focused on social participation; the current study emphasizes quantitative forecasting and regional synergy. |
| [38] | Decentralized renewable planning | Advocated bottom-up planning to align renewable resources with local needs in Greece | Focused on resource mapping; the current study integrates multi-method foresight and green synergy. |
| [39] | Infrastructure and inequality | Identified interprovincial disparities | Did not address energy balance or green synergy. |
| [40] | Biomass energy potential | Identified significant biomass resources (agricultural, animal, and municipal) for reducing fossil-fuel reliance | Focused on a single renewable type; the current study addresses broader energy imbalances with a solar emphasis. |
| [41] | Infrastructure and inequality | Identified interprovincial disparities in Iran's infrastructure, with high transport inequality | Did not address energy balance; the current study focuses on energy synergy and county-level solutions. |
| [42] | Energy consumption inequality | Found rising inequality in oil and gas consumption, and stability in electricity use, driven by efficiency patterns | Focused on consumption trends; the current study forecasts energy imbalances and proposes green solutions. |
| [43] | Energy justice | Highlighted energy colonialism and inequality | The current study is quantitative and future-oriented. |
| Current Study | Regional energy imbalance + synergy | Forecasts imbalances and proposes spatial solutions | Introduces "green energy synergy" and a multi-method foresight framework. |

2.2. Research Background on Energy and Regional Planning

Global studies on regional planning and energy have primarily focused on resource allocation and reducing inequalities. For example, study [33] examines inequality in energy access between rural and urban communities and emphasizes the need for regional planning based on energy justice. It proposes integrating the social dimension into technical–economic planning and establishing a social contract that involves all stakeholders in energy decision-making. Article [34] shows that renewable energy systems should be adopted to address the lack of electricity access in rural communities while simultaneously reducing carbon emissions, rather than increasing production from existing power plants. This conclusion is supported through a two-level optimization model designed to balance policymakers (leaders) and industry operators (followers), tested in two case studies in Malaysia.

Study [35] proposes a new peer-to-peer (P2P) energy-trading method for interconnected microgrids, which enhances prosumer economic benefits and reduces supply–demand imbalances at the regional scale. Article [36] explains how strategic planning in Spain’s Jaén Province has been used for regional development and redesign of the energy system, with a focus on solar and biomass resources. This process involved collaboration between the provincial government and the University of Jaén, using SWOT analysis and business-management tools to design a sustainable energy model. Study [37] investigates the role of citizens in regional energy policies and the energy transition in France, introducing models such as “renewable energy communities” that enable citizens to produce, consume, and sell renewable energy. It also analyzes key implementation challenges—including legal constraints and insufficient incentives—contributing to the broader debate on energy decentralization.

In study [38], researchers argue that a shift from centralized planning to regional planning is essential for renewable energy development. They employ a bottom-up approach to align regional renewable resources with the specific energy needs of each region, demonstrated through a case study involving two regions in Greece.

In Iran, studies such as [39,40] have examined infrastructural inequalities across regions but have paid less attention to energy as a central focus of planning. For example, study [41] evaluated the infrastructural development of Iran’s 31 provinces using 20 indicators and ranked them through principal component analysis and TOPSIS. The results showed that inequality in transportation infrastructure was the highest, while rural infrastructure inequality was the lowest, with Tehran and Sistan–Baluchestan ranking first and last, respectively. Study [42] analyzed inequality in CO₂ emissions and energy consumption (oil, gas, electricity) in the household sector across provinces from 2000 to 2017 using the Theil index and the Kaya identity. The findings indicated rising inequality in oil and gas consumption, stability in electricity consumption, and declining CO₂ emissions inequality, with energy efficiency identified as the primary driver and energy consumption as a potential future determinant.

Additionally, study [43], using an energy justice framework, examined conditions in Khuzestan—the first oil-producing region in the Middle East and a cornerstone of Iran’s energy sector. It assessed increasing inequalities, poverty, and unemployment, alongside a history of energy colonialism and extractivism. The study also evaluated community-based efforts toward energy justice and democracy, emphasizing the need for justice-oriented analysis and international alliances.

Regarding green energy development in Iran, several studies have explored renewable potential. Study [44] assessed the country’s renewable energy resources, highlighting challenges arising from pollution and the depletion of non-renewable reserves due to reliance on cheap fossil fuels. It introduced Iran’s diverse renewable options—biofuels, hydropower, wind, solar, and geothermal—as complementary strategies to reduce fossil-fuel dependence and support sustainability. Study [45] focused on biomass energy, categorizing biomass into agricultural residues, animal waste, and municipal waste. It identified 8.78 million tons of agricultural residues, 7.7 million tons of animal waste, and 3 million tons of municipal waste annually as potential resources capable of reducing fossil-fuel reliance and promoting green fuel use. Study [46] examined the necessity of renewable energy adoption due to heavy fossil-fuel dependence and its associated environmental and regional inequalities. Focusing on sustainable rural development, it identified infrastructural, managerial, socio-cultural, and economic barriers and highlighted the need for innovative policymaking.

Global and domestic research demonstrates that regional planning grounded in green energy and energy justice can reduce inequalities and enhance sustainability; however, this approach has been applied only to a limited extent in Iran. Case studies of provinces such as Khuzestan and Yazd indicate both significant infrastructural disparities and substantial renewable potential, yet policy fragmentation and weak infrastructure remain major obstacles. This research addresses these gaps by applying a forward-looking analysis in Yazd Province and proposing strategies to promote synergy between green energy development and sustainable regional planning.

2.3. Key Factors and Uncertainties

Key factors and future uncertainties in regional planning for green energy synergy play a crucial role in shaping policies, decision-making, and the overall development trajectory of this sector. Key factors include supportive government policies, investment levels, technological progress, distribution network capacity, social acceptance, and market competition, which together form the main foundations of this transition. In contrast, future uncertainties—such as sudden policy shifts, economic fluctuations, emerging technologies, climate change, and the level of international cooperation—can alter the development path and create unpredictable outcomes. These elements are derived from findings in the existing research literature and are categorized in [Table 2](#) to present a clear overview of the opportunities and challenges associated with green energy development.

Identifying and analyzing key factors and future uncertainties in regional green energy planning helps policymakers and decision-makers formulate more effective strategies for sustainable development. This classification enables the anticipation of various scenarios and preparation for potential changes, thereby preventing unexpected obstacles. In foresight studies, these factors serve as a foundation for designing development scenarios, assessing risks, and formulating flexible and sustainable policies.

Table 2. Classification of Key Factors and Future Uncertainties.

| Category | Key Factors | Future Uncertainties |
|-------------------------------|--|--|
| Policy and Law | Government policies | Policy and legal changes; sanctions |
| Economy and Investment | Investment and financing | Economic fluctuations, energy price volatility |
| Technology and Infrastructure | Technology and innovation, infrastructure, and distribution networks | Technological advancements |
| Social | Social acceptance | Public acceptance |
| Environmental | Climate change | Impacts of climate change |
| Market and Competition | Green energy competitiveness | International cooperation and sanctions |

2.4. Scientific Contribution and Innovation of the Research

This research introduces the concept of "green energy synergy" as a novel framework for "regional planning, advancing the literature on energy and sustainable development. Unlike previous studies that often focus solely on technical aspects of energy management, this study emphasizes coordination among green energy resources, infrastructure, and policies to create sustainable added value at the regional level. The primary innovation lies in integrating regional planning with green energy strategies, reframing regional inequalities not merely as technical problems but as opportunities for developing decentralized green infrastructure, such as local solar power plants.

The study employs a multi-method foresight approach, combining quantitative trend analysis using MATLAB with participatory scenario development based on local stakeholder input. This approach enables precise prediction of energy imbalances and the formulation of practical, locally tailored strategies in Yazd Province, while offering a framework adaptable to other regions with similar conditions. Emphasizing decentralized infrastructure to reduce regional inequalities—particularly in Iran, with challenges such as sanctions and reliance on fossil fuels—adds a practical and original contribution to energy planning knowledge.

From a scientific perspective, this research fills a gap in Iran’s energy studies, which have largely been limited to macro-level or technical analyses and have paid less attention to regional coordination emphasizing green energy. Consequently, the study not only provides solutions for Yazd’s sustainable development but also offers a model for policymaking in regions with high renewable energy potential and spatial inequalities.

3. Research Methodology

This study, focused on regional planning for green energy synergy in Yazd Province, employs a multi-method foresight approach that integrates quantitative trend analysis with participatory scenarios, providing both accurate predictions and consideration of stakeholders’ qualitative perspectives. This approach enhances the comprehensiveness and reliability of the analysis by combining numerical data with expert input, making it well-suited for examining regional inequalities and informing policymaking under conditions of uncertainty. Figure 1 presents a flowchart of the research process, offering an overview of the study.

3.1. Case Study

Yazd Province, located on Iran’s central plateau (Figure 2), covers 6.3% of the nation’s total land area [47]. Renowned for its abundant mineral resources and major industries, including steel and ceramics, Yazd is a key industrial hub and a frontrunner in adopting renewable energy, particularly solar power. This study selected Yazd as a case study for several reasons. With exceptional geographic and climatic conditions, it ranks among Iran’s hottest and driest regions, facing significant challenges in ensuring a stable energy supply. A major concern is its high energy consumption, especially in the industrial and household sectors [48,49], which amplifies regional energy imbalances. Additionally, as a densely populated industrial center, Yazd’s diverse economic activities strongly influence energy demand and overall efficiency.

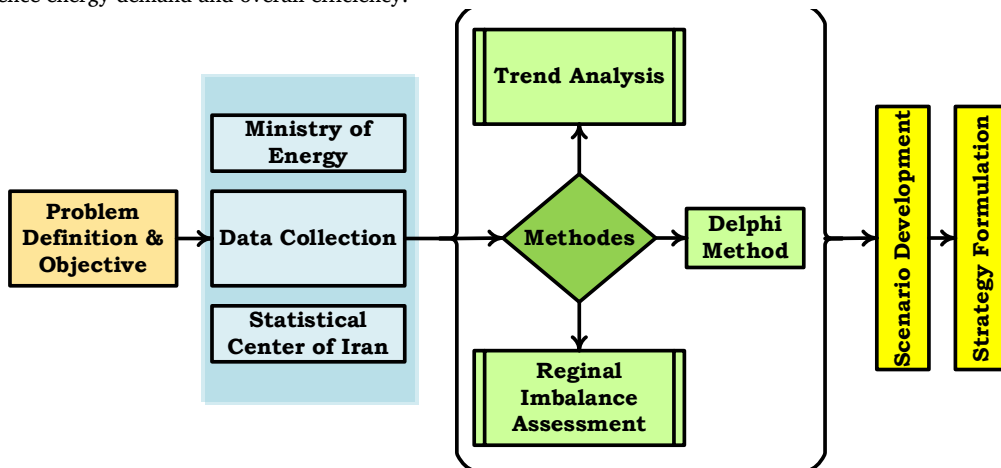


Figure 1. Research process flowchart.

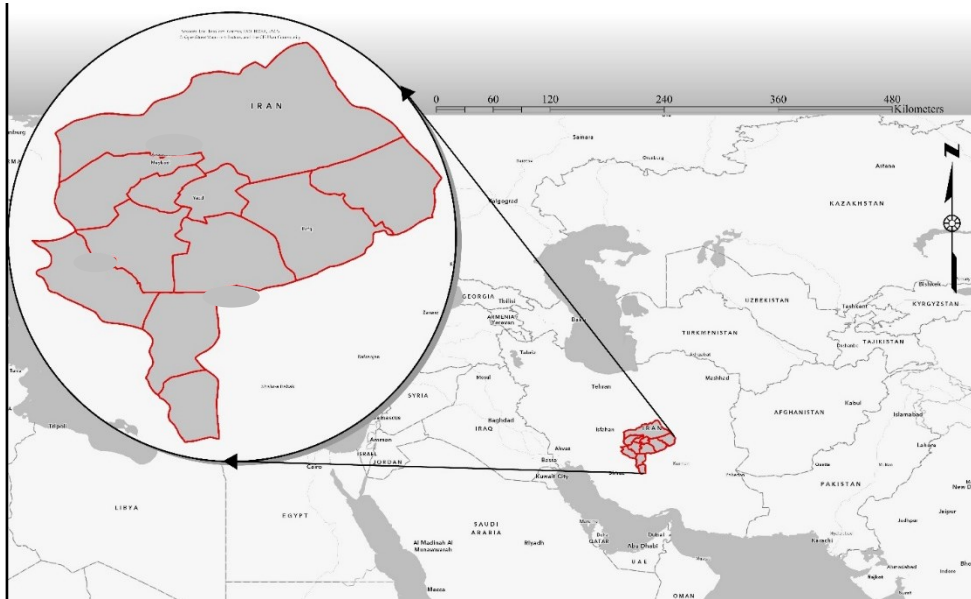


Figure 2. Yazd province's location in Iran.

3.2. Quantitative Trend Analysis

To examine historical patterns and forecast future trends in energy production and consumption in Yazd Province, quantitative trend analysis was conducted using MATLAB. Historical electricity production and consumption data, disaggregated by county, were collected for the period 1394–1401 (Iranian calendar years, equivalent to 2015–2022) from the annual reports of the Ministry of Energy and the Statistical Center of Iran. These sources are considered reliable for regional energy statistics; however, potential limitations include inconsistencies in data reporting across counties and occasional gaps due to incomplete records.

To address missing data, linear interpolation was applied, recognizing that this method assumes linear trends and may oversimplify the nonlinear dynamics of energy systems, particularly in industrially volatile regions such as Yazd. To mitigate this limitation, data were cross-verified with provincial energy audits where available, and only gaps affecting less than 10% of the dataset were interpolated. Using linear regression in MATLAB, trends in production and consumption were projected up to 1414 (2035). To account for uncertainties in long-term forecasting, a sensitivity analysis was performed by varying key inputs (e.g., annual growth rates of consumption and production) by $\pm 10\%$. Error margins for projections were estimated at approximately $\pm 8\%$, based on historical data variability.

Additionally, MATLAB simulations were conducted to model interactions among key variables and identify points of regional imbalance, with a particular focus on counties exhibiting significant inequalities.

3.3. Scenario Development

To formulate future scenarios for green energy synergy in Yazd Province, considering key factors and uncertainties, the Delphi method was employed. This method was chosen for its ability to systematically and anonymously gather expert opinions and build consensus under conditions of uncertainty. A panel of 15 experts was assembled, including professors from the University of Yazd, managers from the Yazd Regional Electricity Company, provincial planners, and industry representatives, each with at least five years of experience in energy or regional planning.

The Delphi process was conducted over three rounds. In the first round, an open-ended questionnaire was distributed to collect expert insights on key drivers, uncertainties, and potential scenarios for green energy development in Yazd Province. Questions addressed topics such as renewable energy adoption, technological advancements, policy frameworks, and socio-economic factors. Responses were analyzed qualitatively to identify common themes and divergent views, which informed the design of a structured questionnaire for the second round.

The second-round questionnaire included Likert-scale and ranking questions to prioritize drivers and uncertainties (e.g., "To what extent will solar energy adoption impact energy synergy by 1414?"). Feedback from this round was summarized and shared anonymously with the panel, highlighting areas of agreement and disagreement. In the third round, experts reviewed the aggregated results and refined their responses to converge on three plausible scenarios. Consensus was measured using a threshold of 70% agreement on Likert-scale items and a reduction in the interquartile range for ranked items between rounds. Divergent opinions were addressed by allowing experts to provide written justifications, which were shared anonymously in subsequent rounds to encourage constructive dialogue.

The final scenarios were developed based on the prioritized drivers and uncertainties, ensuring a robust and reproducible process.

4. Results

4.1. Analysis of the Current Situation and Future Trends of Energy Production, Consumption, and Imbalance in Yazd Province

Figure 3 illustrates the energy imbalance across the ten counties of Yazd Province from 1394 to 1401 (2015–2022), providing a foundation for regional planning aimed at green energy synergy. These charts analyze energy supply and demand in each county, revealing clear patterns of regional inequality. Energy imbalance during this period fluctuated significantly due to factors such as weak transmission infrastructure, rising industrial and domestic consumption, and differences in local production capacities.

Yazd County, with a surplus of 8.4 million kWh in 1401, serves as the province’s primary energy supplier and, given its geographical location and high solar radiation, has the potential to generate 12 MW of solar energy. In contrast, counties such as Ashkezar (-1.65 million kWh), Meibod (-1.03 million kWh), and Bafgh (-0.55 million kWh) face severe deficits, largely due to high industrial consumption (Ashkezar and Meibod) and insufficient local production (Bafgh). Ardakan has seen its imbalance decline from a surplus of 0.78 million kWh in 1394 to a deficit of 0.35 million kWh in 1401, driven by population growth and industrial concentration.

Linear regression analysis predicts that Yazd’s surplus will decrease to 7 million kWh by 1414 (2035) (Figure 4), indicating a higher growth rate in consumption compared to production. Sensitivity analysis suggests that these projections are robust within a ±8% error margin, with Yazd’s surplus potentially ranging from 6.5 to 7.5 million kWh and deficits in counties such as Ashkezar varying between -2.5 and -2.9 million kWh, depending on consumption growth and infrastructure investments. Deficits in other areas are projected to worsen at an annual growth rate of 5–10% due to urban population growth and industrial consumption, unless investments in decentralized solar power plants and distribution network optimization are prioritized. Based on quantitative trend analysis of historical energy production and consumption data from 1394 to 1401, with projections up to 1414, the energy situation in Yazd Province reveals pronounced regional inequalities and structural imbalances that, if unaddressed, threaten the region’s sustainability. Figure 4 illustrates trends in energy production and consumption across the ten counties during this period.

Currently, energy production is concentrated in counties such as Ardakan and Yazd due to industrial infrastructure and large power plants. For instance, Ardakan recorded an average annual production of approximately 3 million kWh in 1401, while Yazd reached around 10 million kWh. In contrast, counties such as Behabad and Bafgh have negligible local production, remaining near zero through 1401.

Energy consumption, however, exhibits an upward trend across all counties, particularly in urban areas such as Yazd (around 2.9 million kWh) and Ashkezar (1.7 million kWh in 1401), driven by population growth and industrial development. This widening gap between production and consumption has made energy imbalance a critical challenge for the province.

Figure 5 illustrates the projected changes in energy imbalances by county. Projections up to 1414 indicate that counties such as Abarkouh, Bafgh, and Ashkezar—characterized by high consumption and minimal local production—will experience sharply negative imbalances, reaching approximately -0.4 million, -1 million, and -2.84 million kWh, respectively. This trend is intensified in Abarkouh and Bafgh due to complete reliance on energy transmission from other areas, and in Ashkezar due to heavy industrial consumption.

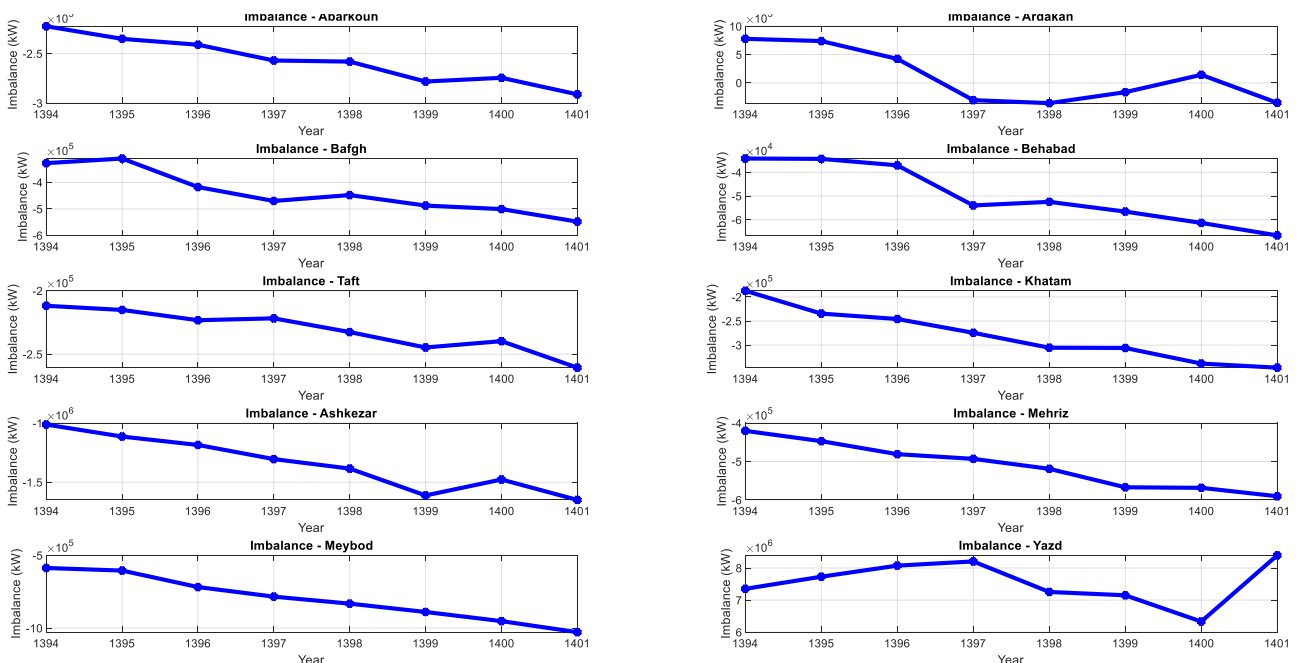


Figure 3. Energy Balance Changes from 1394 to 1401.

In contrast, Yazd maintains a relative production surplus of around 7 million kWh in 1414; however, this surplus is insufficient to fully offset deficits in other counties. Taft and Behabad are projected to experience moderate negative imbalances, reaching approximately -0.3 million and -0.1 million kWh by 1414.

The production trend during the forecast period indicates relative stability in energy-producing regions such as Ardakan and Yazd, while in other counties, particularly Behabad and Bafgh, local production remains negligible. Energy consumption across all regions is projected to increase at an annual rate of approximately 3–6%, with growth more pronounced in industrial and urban areas such as Ashkezar and Yazd.

This pattern underscores a heavy dependence on energy transmission from producing to consuming regions. Given weak infrastructure, transmission constraints, and existing spatial inequalities, this dependence further exacerbates energy imbalances. For example, Mehriz and Meibod, with annual consumption of 0.611 million and 1.054 million kWh in 1401 and minimal production of 21,000 and 26,000 kWh, respectively, exhibit significant negative imbalances, projected to reach approximately -1 million and -2 million kWh by 1414.

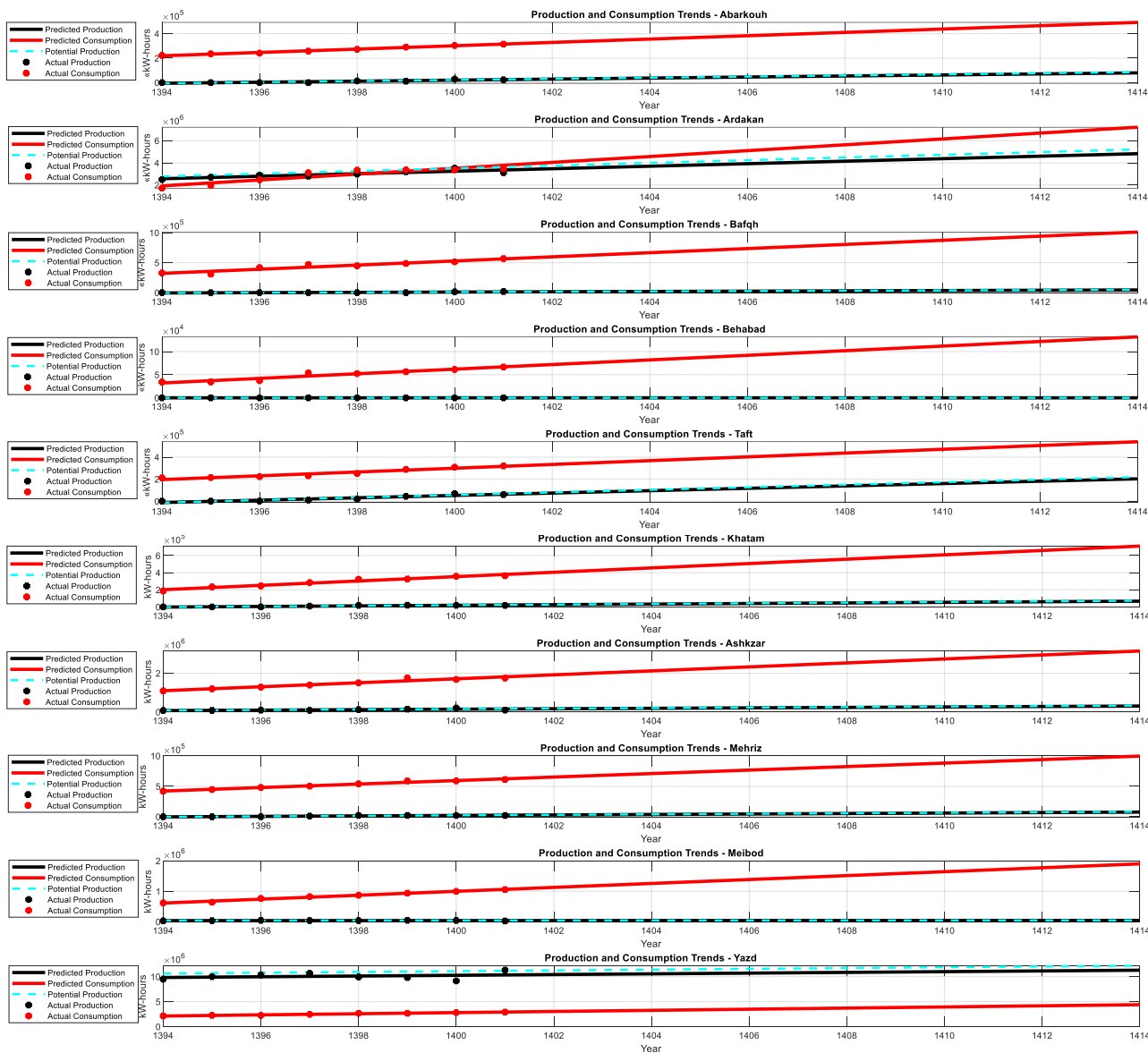


Figure 4. Trends in Energy Production and Consumption from 1394 to 1414.

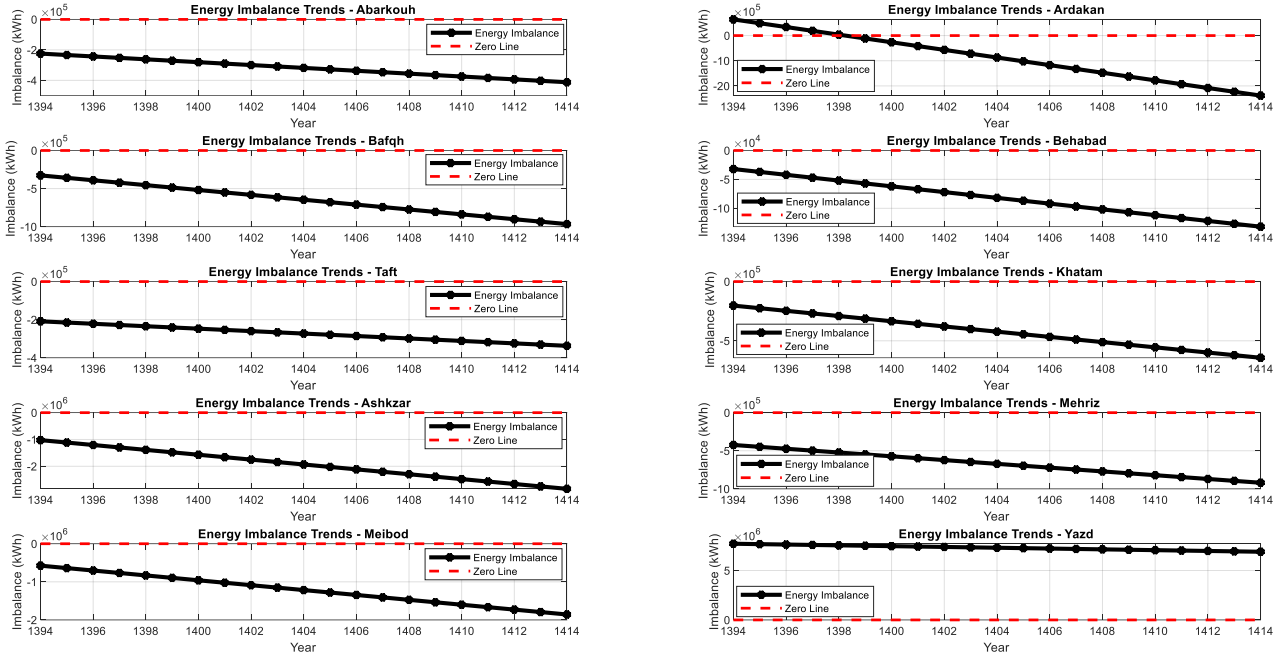


Figure 5. Trends and Forecast of Energy Imbalance Changes by County (1394–1414).

These findings reveal a structural pattern of regional inequality in Yazd Province, where regions with high production potential (e.g., Ardakan and Yazd) contrast sharply with areas lacking infrastructure (e.g., Behabad and Bafgh). The observed imbalances not only threaten energy stability but also highlight opportunities to harness local potential, particularly solar energy in desert regions. Without targeted infrastructure and policy reforms, the production-consumption gap is likely to widen, jeopardizing the region’s long-term sustainability.

These spatial variations can be categorized into three regional types:

- **Energy Surplus Areas** (e.g., Yazd and Ardakan), where industrial infrastructure and high solar capacity enable self-sufficiency and potential energy export.
- **Transitional Zones** (e.g., Taft and Mehriz), which have moderate deficits and potential for solar expansion but currently lack sufficient infrastructure investment.
- **Critical Deficit Areas** (e.g., Ashkezar, Meibod, and Bafgh), where industrial activity exceeds local generation, leading to growing dependence on external energy supply.

This classification supports the prioritization of investment strategies and the targeting of counties based on both urgency and capacity for renewable energy integration.

4.2. Future Scenarios

This study developed four future scenarios for green energy synergy in Yazd Province by 1414 (2035), using the Delphi method and responses from 15 experts. The scenarios were constructed around two key uncertainties: the intensity of sanctions (horizontal axis: reduced to severe) and the level of international cooperation (vertical axis: high to low). These uncertainties were identified during the Delphi rounds as the most influential and unpredictable factors.

The findings integrate quantitative forecast data (energy production and consumption from 1394 to 1414) with qualitative expert consensus. Key factors—including government policies, investment, technology, infrastructure, social acceptance, climate change, and market competitiveness—were incorporated into each scenario to comprehensively reflect regional dynamics. To enhance scenario robustness, MATLAB simulations were performed, combining quantitative forecasts from Section 3.2 with scenario-specific assumptions. For each scenario, key variables (e.g., solar energy adoption rates, infrastructure investment levels, and consumption growth) were adjusted to reflect conditions of reduced or severe sanctions and high or low cooperation. For example, in the Synergistic Development scenario, solar capacity was assumed to grow by 15% annually with high investment, whereas in the Energy Isolation scenario, growth was limited to 2% due to resource constraints.

Table 3. 2 × 2 Matrix of Future Scenarios for Green Energy Synergy in Yazd Province.

| | Reduced Sanctions | Severe Sanctions |
|--------------------------------|-------------------------------------|------------------------------------|
| High International Cooperation | Scenario 1: Synergistic Development | Scenario 3: Local Self-Sufficiency |
| Low International Cooperation | Scenario 2: External Dependency | Scenario 4: Energy Isolation |

Table 4 summarizes the quantitative results of these scenarios for 1414, including sensitivity analysis, stress testing, and system dynamics modeling. In the Synergistic Development scenario, Yazd shows a substantial surplus of 156.58 million kWh, while Ashkezar's deficit decreases to -1.96 million kWh, representing approximately a 30% improvement over the baseline value of -2.84 million kWh.

Conversely, the Energy Isolation scenario exacerbates deficits, with Ashkezar reaching -3.04 million kWh and Ardakan -3.39 million kWh. Stress testing, assuming a 50% reduction in production growth and a 20% increase in consumption growth, highlights system vulnerability: Yazd shifts to a deficit of -76.45 million kWh, and Ashkezar's deficit worsens to -40.11 million kWh. Sensitivity analysis confirms a wide range of outcomes (e.g., Yazd: -19.37 to 33.16 million kWh), emphasizing the need to account for uncertainties.

The system dynamics model, which incorporates consumption feedback on production, produces results close to the baseline (Yazd: 6.88 million kWh; Ashkezar: -2.86 million kWh), partially mitigating the limitations of the linear model. Additional stress tests indicate that the Synergistic Development scenario remains viable even under reduced investment, whereas the Energy Isolation scenario collapses under increased consumption. Sensitivity analysis of strategic interventions—such as decentralized solar plants and smart grids—demonstrates their effectiveness when at least 70% of the proposed capacity is deployed. These findings are summarized in the 2×2 matrix of Table 3 and detailed numerically in Table 4.

5. Discussion

The quantitative findings indicate that energy imbalance in Yazd Province arises from the uneven distribution of production and consumption capacities. Yazd County, with a surplus of 8.4 million kWh in 1401 and a projected 7 million by 1414, serves as the primary production hub, while regions such as Ashkezar (-1.65 million in 1401 and -2.84 million in 1414) and Bafgh (-0.55 million in 1401 and -1 million in 1414) experience severe deficits due to limited local production and dependence on energy transmission. This pattern is consistent with previous studies in Iran, such as [41], and reflects a widespread structural challenge in the country.

What distinguishes this research is its focus on transforming these inequalities into opportunities through decentralized green infrastructure. The identified potential of 12 MW of solar energy in Yazd and 10 MW in Bafgh aligns with global examples, such as strategic energy planning in Jaén, Spain, demonstrating that local renewable resources can help offset deficits. Nevertheless, the projected intensification of imbalances—5–10% annual deficit growth under current conditions—serves as a warning for regional sustainability. This trend aligns with findings from [41] regarding increasing inequality in oil and gas consumption in Iran. However, unlike [42], which emphasized energy efficiency as the primary factor, this study identifies industrial demand growth and weaknesses in the distribution network as key drivers. This perspective underscores the need to reconsider centralized energy transmission policies and promote local production, transforming green energy synergy from a theoretical concept into a practical strategy.

The future scenarios, developed based on the intensity of sanctions and the level of international cooperation, illustrate a broad spectrum of possibilities for green energy development in Yazd. Scenario 1 (Synergistic Development) represents the optimal pathway, reducing imbalances and expanding solar capacity. This outcome aligns with global studies, including peer-to-peer microgrid models that improved supply-demand balance and renewable energy communities in France that emphasized decentralization, highlighting the importance of international cooperation in accessing technology and capital.

In contrast, Scenario 4 (Energy Isolation) predicts the worst-case outcome, with exacerbated deficits and continued dependence on fossil fuels, consistent with Iran's historical experience under severe sanctions and infrastructural constraints.

Table 4. Integrated Results Table for 1414 (kWh).

| | Base Imbalance | Sens-Low | Sens-High | Stress Test | Synergistic Dev. |
|----------|----------------|------------------|------------------|-----------------|------------------|
| Abarkouh | -412325.21 | -2940412.44 | 2115762.01 | -7266299.68 | -575200.35 |
| Ardakan | -2385165.03 | -55689823.93 | 50919493.86 | -156843232.83 | 34852164.22 |
| Bafgh | -966002.64 | -6191348.74 | 4259343.45 | -12477194.84 | -1085152.06 |
| Behabad | -131811.92 | -836818.86 | 573195 | -1541825.79 | -131811.92 |
| Taft | -337266.39 | -4296530.35 | 3621997.57 | -12831094.32 | -745062.39 |
| Khatam | -643194.99 | -4731850.06 | 3445460.06 | -10282480.13 | -735173.37 |
| Ashkzar | -2841614.46 | -18996505.54 | 13313276.61 | -40111506.63 | -1966775.93 |
| Mehriz | -919905.53 | -5533228.66 | 3693417.59 | -11808001.8 | -1022569.21 |
| Meibod | -1857191.96 | -10999230.53 | 7284846.6 | -20257419.09 | -1283861.91 |
| Yazd | 6892622.21 | -19375981.30 | 33161225.73 | -76452109.81 | 156589225.64 |
| | External Dep. | Local Self-Suff. | Energy Isolation | System Dynamics | |
| Abarkouh | -526201.91 | -505491.38 | -499557.35 | -427176.54 | |
| Ardakan | 10079034.74 | -392004.53 | -3392192.11 | -2411795.21 | |
| Bafgh | -1041776.39 | -1023442.48 | -1018189.40 | -984322.61 | |
| Behabad | -131811.92 | -131811.92 | -131811.92 | -131811.92 | |
| Taft | -624574.42 | -573646.89 | -559055.02 | -359328.13 | |
| Khatam | -720714.82 | -714603.51 | -712852.49 | -657282.69 | |
| Ashkzar | -2662232.48 | -2956186.17 | -3040410.5 | -2869121.85 | |
| Mehriz | -1007307.41 | -1000856.59 | -999008.28 | -940212.02 | |
| Meibod | -1646932.32 | -1800393.94 | -1844364.13 | -1858839.71 | |
| Yazd | 61777243.59 | 21702371.76 | 10220022.28 | 6888224.34 | |

The intermediate scenarios (2 and 3) illustrate more fragile balances. Scenario 2 (External Dependency) forecasts concentrated growth in Yazd and Ardakan while maintaining regional inequalities, reflecting Myrdal's Cumulative Causation theory, in which developed regions benefit from accumulated advantages. Scenario 3 (Local Self-Sufficiency) demonstrates the potential of domestic resources by moderately reducing imbalances and expanding solar capacity, though its scale is insufficient to fully meet growing demand.

These findings not only reflect regional disparities identified in previous Iranian studies—such as [41] and [42] on infrastructure and energy consumption inequality—but also provide a new perspective by quantifying future imbalances at the county level. While [42] emphasized energy efficiency as the primary driver of inequality, our results identify industrial demand and infrastructural limitations as the key factors, particularly in counties such as Ashkezar and Meibod. This supports the arguments for decentralized planning made by Shahrom et al. [34], who advocated the use of renewable energy to reduce rural energy gaps, and aligns with Terrados et al. [36], who highlighted the importance of local collaboration in regional energy transitions. Furthermore, the emphasis on “green energy synergy” extends the conceptual frameworks of energy justice discussed by Khayat and Teron [43], offering a quantitative model to operationalize their justice-oriented recommendations.

The findings of this study carry significant implications for multiple stakeholders. For grid operators, identifying high-deficit counties—such as Ashkezar and Meibod—enables targeted infrastructure upgrades, prioritizing smart grid deployment and decentralized generation to stabilize supply-demand dynamics. Policymakers can leverage the foresight scenarios to design adaptive strategies that account for geopolitical and economic uncertainties. For example, under severe sanctions, emphasis on local self-sufficiency and rural solar investments becomes critical, whereas in cooperative conditions, foreign investment and technology transfer can accelerate green energy transitions.

Provincial planners and municipalities can use the model's spatial detail to allocate resources efficiently across the ten counties. The study directly supports its initial objective of creating a regional planning framework to enhance green energy synergy. By combining quantitative forecasting with scenario planning, the results demonstrate that spatial inequalities can be mitigated through tailored strategies, validating the hypothesis that decentralization and synergy improve energy balance. Moreover, the “green energy synergy” model introduced here provides a scalable approach for other regions with similar characteristics—high renewable potential, regional energy imbalance, and centralized policy systems. Provinces in Iran (e.g., Kerman, Khuzestan) or other semi-arid regions in the Global South facing infrastructure gaps can adapt this methodology. Future research could further expand the model by integrating economic cost-benefit analysis, carbon reduction impacts, and social equity indicators.

6. Conclusion

This study advances the concept of “green energy synergy” as an innovative framework for regional planning, reframing energy inequalities in Yazd Province as opportunities for developing decentralized green infrastructure rather than as impediments. By integrating quantitative trend analysis with participatory scenario development, the research leverages the province's substantial solar potential—12 MW in Yazd and 10 MW in Bafgh—to demonstrate its capacity for mitigating energy imbalances and fostering sustainable development.

This approach departs from prior investigations, which predominantly focused on technical or macro-level dimensions, and fills a critical gap in Iran's energy literature by employing a multi-method foresight framework tailored to regional dynamics. The findings reveal pronounced disparities across Yazd's ten counties, with Yazd exhibiting a surplus of 8.4 million kWh in 2022 (projected to decline to 6.89 million kWh by 2035), while counties such as Ashkezar (-1.65 million kWh in 2022, projected to -2.84 million kWh by 2035) and Bafgh (-0.55 million kWh in 2022, projected to -0.96 million kWh by 2035) face escalating deficits, as detailed in [Table 4](#). To address these imbalances, county-specific strategies, carefully delineated in [Figure 6](#), were formulated.

In Ardakan, shared industrial solar plants leverage existing industrial infrastructure to enhance clean energy output, helping to mitigate its 2022 deficit of -0.35 million kWh. Abarkouh employs agricultural solar canopies to integrate electricity generation with temperate farming, offsetting its projected -0.4 million kWh deficit by 2035. Bafgh's mining solar units, utilizing a 10 MW capacity, bolster energy supply for extraction activities, reducing its -0.55 million kWh shortfall. Yazd's urban solar distribution network optimizes its surplus through rooftop installations, facilitating regional energy balance.

Behabad's household solar panels, supported by subsidies, promote local generation to address its modest -0.1 million kWh deficit by 2035, while Ashkezar's factory solar plants target industrial demand to alleviate its substantial -1.65 million kWh shortfall. Taft utilizes hillside solar plants to counter its projected -0.3 million kWh deficit, and Khatam adopts rural biomass units that convert agricultural waste into energy to enhance self-sufficiency. Meibod equips pottery workshops with solar panels to mitigate its -1.03 million kWh deficit, and Mehriz integrates solar lighting along historic tourism routes to support its -0.611 million kWh shortfall.

As illustrated in [Figure 6](#), these strategies are embedded within a cohesive regional framework that employs smart distribution networks to optimize supply-demand dynamics, leveraging Yazd's surplus to support deficit areas. A proposed green investment fund mobilizes resources from governmental, private, and potentially international sources, prioritizing underserved regions. Furthermore, adaptive policymaking—responsive to sanctions and cooperation scenarios—ensures resilience by incentivizing solar adoption or emphasizing local solutions as needed. Collectively, these measures integrate technical innovation, community engagement, and policy adaptability to not only rectify energy disparities in Yazd but also establish a robust, scalable blueprint for green regional planning in Iran and beyond. Realizing this vision requires concerted efforts from policymakers, industry stakeholders, and local communities to position Yazd as a leader in sustainable green development in the region.

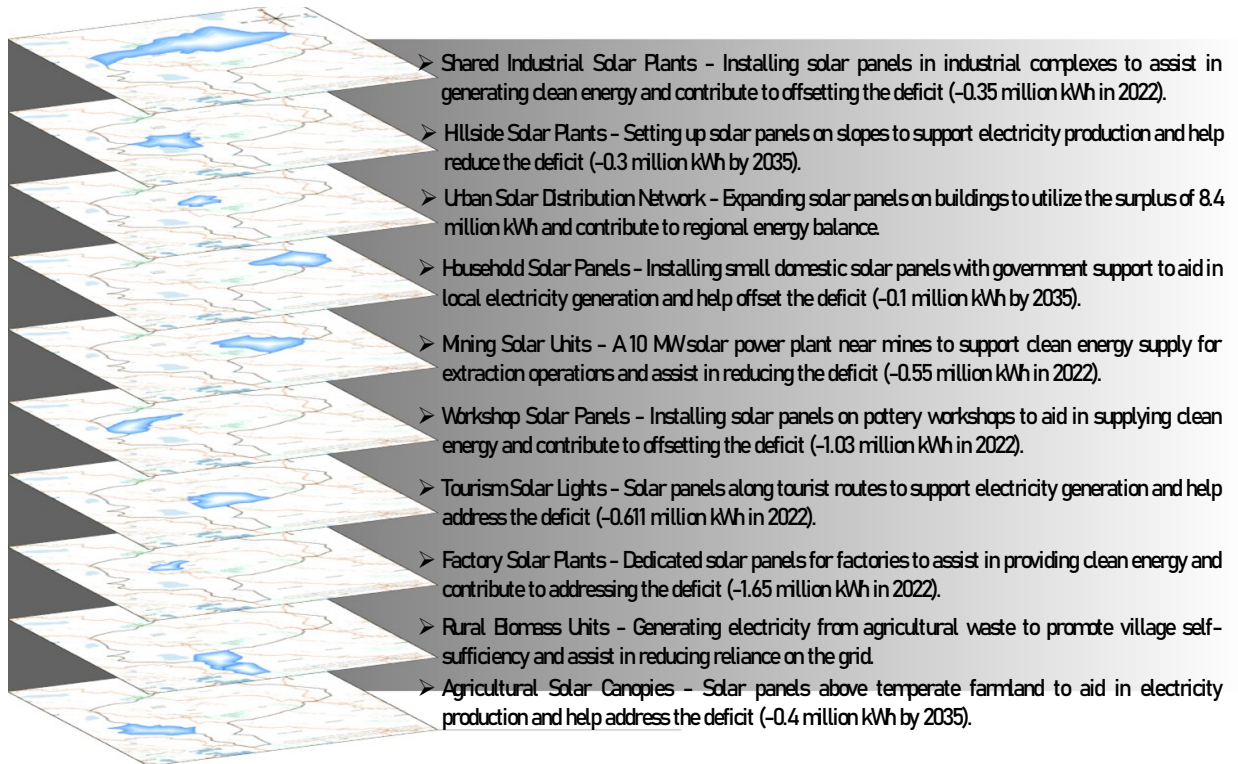


Figure 6. Specific strategies for each county.

This study, while comprehensive in its regional analysis and foresight modeling, has several limitations. First, the energy data were limited to electricity production and consumption, excluding other forms such as gas or heating, which may also influence regional energy balance. Second, although expert opinions were gathered through the Delphi method, the relatively small panel of 15 participants may not fully capture perspectives across all relevant sectors. Third, the financial feasibility and implementation costs of the proposed strategies were not quantitatively assessed.

Future research could address these limitations by incorporating multiple energy sources, conducting cost-benefit analyses of proposed strategies, and employing agent-based models to simulate stakeholder behavior. Additionally, replicating this framework in regions with different climatic, economic, or policy contexts would help evaluate its applicability and generalizability.

References

- [1] C. Bhowmik, S. Bhowmik, and A. Ray, "Green Energy Sources Selection for Sustainable Planning: A Case Study," *IEEE Transactions on Engineering Management*, vol. 69, no. 4, pp. 1322–1334, 2022.
- [2] C. Bhowmik, S. Bhowmik, A. Ray, and K. M. Pandey, "Optimal Green Energy Planning for Sustainable Development: A Review," *Renewable and Sustainable Energy Reviews*, vol. 71, pp. 796–813, 2017.
- [3] K. Wang, H. Li, S. Maharjan, Y. Zhang, and S. Guo, "Green Energy Scheduling for Demand Side Management in the Smart Grid," *IEEE Transactions on Green Communications and Networking*, vol. 2, no. 2, pp. 596–611, 2018.
- [4] "Commodity and Energy Balances," *Studies in Methods (Ser. F)*, pp. 81–119, 2022.
- [5] "Concepts and Definitions," *Energy Balances and Electricity Profiles (Ser. W)*, pp. viii–xxiii, 2023.
- [6] Ministry of Energy, "Energy Imbalance in Yazd province,"
- [7] A. Soltani, and M. A. Imani, "Overcoming Implementation Barriers to Renewable Energy in Developing Nations: A Case Study of Iran Using MCDM Techniques and Monte Carlo Simulation," *Results in Engineering*, vol. 24, 103213, 2024.
- [8] J. Nematian, and I. Rahimi, "Feasibility Study of Using Renewable Energies in Iranian Seas: A Comparative Study," *Renewable Energy*, vol. 189, pp. 383–391, 2022.
- [9] M. Ghouchani, M. Taji, A. S. Chehelatani, and M. S. Chehr, "Developing a Perspective on the Use of Renewable Energy in Iran," *Technological Forecasting and Social Change*, vol. 172, 121049, 2021.
- [10] M. Maleki Tehrani, M. Akhtari, et al., "Techno-Economic Investigation of a Hybrid Biomass Renewable Energy System to Achieve the Goals of SDG-17 in Deprived Areas of Iran," *Energy Conversion and Management*, vol. 291, 117319, 2023.
- [11] M. Pourmoosavi, and T. Amraee, "Stochastic Approaches to Sustainable Energy in Iran: Enhancing Power System Flexibility and Renewable Integration," *Sustainable Energy Technologies and Assessments*, vol. 74, 104145, 2025.
- [12] D. A. Johnson, "Regional Planning, History of," *International Encyclopedia of the Social & Behavioral Sciences*, pp. 141–145, 2015.
- [13] R. Bustin, "Christaller's Central Place Theory Theory," *Teaching Geography*, vol. 45, no. 1, pp. 12–14, 2020.
- [14] R. L. Church, "Alfred Weber (1868–1958): The Father of Industrial Location Theory and Supply-Chain Design," *Footprints of Regional Science*, pp. 89–107, 2023.
- [15] D. Boyce, "Walter Isard (1919–2010): Founding Father of Regional Science," *Footprints of Regional Science*, pp. 15–24, 2020.
- [16] N. Fujita, "Myrdal's Theory of Cumulative Causation," *Evolutionary and Institutional Economics Review*, vol. 3, no. 2, pp. 275–284, 2007.
- [17] N. Fujita, "Myrdal's Theory of Cumulative Causation," *Evolutionary and Institutional Economics Review*, vol. 3, no. 2, pp. 275–284, 2007.
- [18] H. Westlund, "Gunnar Myrdal (1898–1987): Cumulative Causation Theory Applied to Regions," *Footprints of Regional Science*, pp. 121–134, 2020.
- [19] M. Monsted, "Francois Perroux's Theory of 'Growth Pole' and 'Development' Pole: A Critique," *Antipode*, vol. 6, no. 2, pp. 106–113, 1974.
- [20] E. M. Dobrescu, and E. M. Dobre, "Theories Regarding the Role of the Growth Poles in the Economic Integration," *Procedia Economics and Finance*, vol. 8, pp. 262–267, 2014.
- [21] D. C. Lambert, and J. R. Boudeville, "Aménagement Du Territoire Et Polarisation," *Revue économique*, vol. 25, no. 2, 321, 1974.

- [22] J. Boudeville, "Un Modèle De Croissance Polarisée Fondé Sur Le Complexe Agricole Du Rio Grande Do Sul," *Caravelle*, vol. 5, no. 1, pp. 71–91, 1965.
- [23] E. W. Soja, "Regional Planning and Development Theories," *International Encyclopedia of Human Geography*, pp. 331–341, 2009.
- [24] M. E. Porter, "Clusters and the New Economics of Competition," *Harvard Business Review*, vol. 76, no. 6, 1998.
- [25] A. Saxenian, *Culture and Competition in Silicon Valley and Route 128, With a New Preface by the Author*, Harvard University Press, 1996.
- [26] J. Merkel, "Richard Florida: The Rise of the Creative Class," *Schlüsselwerke der Stadtforschung*, pp. 69–90, 2016.
- [27] "World Energy Balances (Edition 2021)," *IEA World Energy Statistics and Balances*, 2021.
- [28] Y. He, Y. Zhou, J. Liu, Z. Liu, and G. Zhang, "An Inter-City Energy Migration Framework for Regional Energy Balance Through Daily Commuting Fuel-Cell Vehicles," *Applied Energy*, vol. 324, 119714, 2022.
- [29] Z. Dehghan Shabani, and R. Shahnazi, "Energy Intensity Convergence in Iranian Provinces: Evidence from Energy Carriers' Consumption Intensity," *Environmental Science and Pollution Research*, vol. 28, no. 21, pp. 26697–26716, 2021.
- [30] P. A. Corning, "Synergy and Self-organization in the Evolution of Complex Systems," *Systems Research*, vol. 12, no. 2, pp. 89–121, 1995.
- [31] P. Li, Q. He, J. Zhang, and Q. Xia, "Analyzing the Impact of Energy Synergy and Renewable Energy Generation on Energy Security: Empirical Evidence from China's Yangtze River Delta Region," *Energy*, vol. 302, 131868, 2024.
- [32] B. Li, H. Xu, et al., "Optimized Field Synergy Analysis Strategy for Heat Transfer Mechanism in Latent Heat Storage: Based on the Front-Tracking Algorithm and the Segmentation Thinking," *Energy*, vol. 315, 134281, 2025.
- [33] N. E. L. Anku, "The Power of Procedural Justice in the Planning of Energy Projects," *Just Transitions*, pp. 63–68, 2023.
- [34] S. F. Shahrom, K. B. Aviso, et al., "Regional Planning and Optimization of Renewable Energy Sources for Improved Rural Electrification," *Process Integration and Optimization for Sustainability*, vol. 7, no. 4, pp. 785–804, 2023.
- [35] J. Sim, D. Lee, and K. Yoon, "Trustful Double Auction Design for Peer-To-Peer Energy Trading Between Interconnected Micro-Grids with Supply-Demand Imbalance," *International Journal of Electrical Power & Energy Systems*, vol. 160, 110117, 2024.
- [36] J. Terrados, G. Almonacid, and L. Hontoria, "Regional Energy Planning Through SWOT Analysis and Strategic Planning Tools," *Renewable and Sustainable Energy Reviews*, vol. 11, no. 6, pp. 1275–1287, 2007.
- [37] M. Aras, "The Concept of Energy Communities as Per the Clean Energy for All Europeans Package: Contribution to the Energy Transition in France," *Palgrave Studies in Energy Transitions*, pp. 543–565, 2024.
- [38] Y. Sarafidis, D. Diakoulaki, L. Papayannakis, and A. Zervos, "A Regional Planning Approach for the Promotion of Renewable Energies," *Renewable Energy*, vol. 18, no. 3, pp. 317–330, 1999.
- [39] M. Zolfaghari, M. Kabiri, and H. Saadatmanesh, "Impact of Socio-Economic Infrastructure Investments on Income Inequality in Iran," *Journal of Policy Modeling*, vol. 42, no. 5, pp. 1146–1168, 2020.
- [40] B. Badakhshan, A. Sharifi, and T. Karami, "Is Life Green on the Other Half? Linking Urban Green Infrastructure to Socio-Economic Inequality and Spatial Segregation in Tehran, Iran," *Applied Geography*, vol. 177, 103562, 2025.
- [41] N. Fallah Haghighi, G. Ramezanzpour Nargesi, G. Abdollahzadeh, and Z. Sharifi, "Development Assessment of Provinces of Iran Based on Infrastructural Indicators," *Journal of Geography and Planning*, vol. 27, no. 83, pp. 103–116, 2023.
- [42] B. Ata, P. Pakrooh, A. Barkat, R. Benhizia, and J. Péntzes, "Inequalities in Regional Level Domestic CO₂ Emissions and Energy Use: A Case Study of Iran," *Energies*, vol. 15, no. 11, 3902, 2022.
- [43] F. Khayat, and L. Teron, "Energy Justice in Southwest Iran: Mitigating the Socio-Economic and Environmental Impacts of the Fossil Fuel Sector and Building the Principles of Equity-Guided Development," *Handbook on Energy Justice*, pp. 269–289, 2023.
- [44] S. E. Hosseini, A. M. Andwari, M. A. Wahid, and G. Bagheri, "A Review on Green Energy Potentials in Iran," *Renewable and Sustainable Energy Reviews*, vol. 27, pp. 533–545, 2013.
- [45] Y. Hamzeh, A. Ashori, B. Mirzaei, A. Abdulkhani, and M. Molaei, "Current and Potential Capabilities of Biomass for Green Energy in Iran," *Renewable and Sustainable Energy Reviews*, vol. 15, no. 9, pp. 4934–4938, 2011.
- [46] N. Afsharzade, A. Papzan, et al., "Renewable Energy Development in Rural Areas of Iran," *Renewable and Sustainable Energy Reviews*, vol. 65, pp. 743–755, 2016.
- [47] A. Mostafaeipour, "Feasibility Study of Harnessing Wind Energy for Turbine Installation in Province of Yazd in Iran," *Renewable and Sustainable Energy Reviews*, vol. 14, no. 1, pp. 93–111, 2010.
- [48] A. Sadeghi, T. Larimian, and A. Molabashi, "Evaluation of Renewable Energy Sources for Generating Electricity in Province of Yazd: A Fuzzy MCDM Approach," *Procedia - Social and Behavioral Sciences*, vol. 62, pp. 1095–1099, 2012.
- [49] A. Dehghan, "Status and Potentials of Renewable Energies in Yazd Province-Iran," *Renewable and Sustainable Energy Reviews*, vol. 15, no. 3, pp. 1491–1496, 2011.

Declaration of competing interest

The authors declare that they have no known competing financial interests or personal relationships that could have appeared to influence the work reported in this paper. The ethical issues, including plagiarism, informed consent, misconduct, data fabrication and/or falsification, double publication and/or submission, redundancy, have been completely observed by the authors.

Bibliography



Ali Naderi was born in Isfahan, Iran and is originally of Qashqai Turkic descent. He earned his Bachelor's degree in Urban Engineering from Ashrafi-e-Isfahani University of Isfahan and completed his Master's degree in Regional Planning at the University of Yazd. His current research focuses on urban and regional resilience as well as regional energy management, with a particular interest in systems-based approaches to sustainability and adaptive planning.

Email: alinaderi@stu.yazd.ac.ir

ORCID: [0009-0007-7915-8159](https://orcid.org/0009-0007-7915-8159)

Contribution Statement: Conceptualization, Investigation, Methodology, Project administration, Roles/Writing - original draft, Writing-review & editing.



Reza Naderi was born in Isfahan, Iran and is originally of Qashqai Turkic descent. He earned his Bachelor's degree in Mechanical Engineering (HVAC Systems) from Shahid Mohsen Mohajer National University of Skills and is currently pursuing a Master's degree in Mechanical Engineering with a specialization in Energy Conversion at the University of Yazd. His current research is focused on the optimization of peristaltic pump design and renewable energy systems.

Email: rezanaderi8106@gmail.com

ORCID: [0009-0005-9632-0635](https://orcid.org/0009-0005-9632-0635)

Contribution Statement: Data curation, Software, Roles/Writing-original draft, Writing-review & editing.

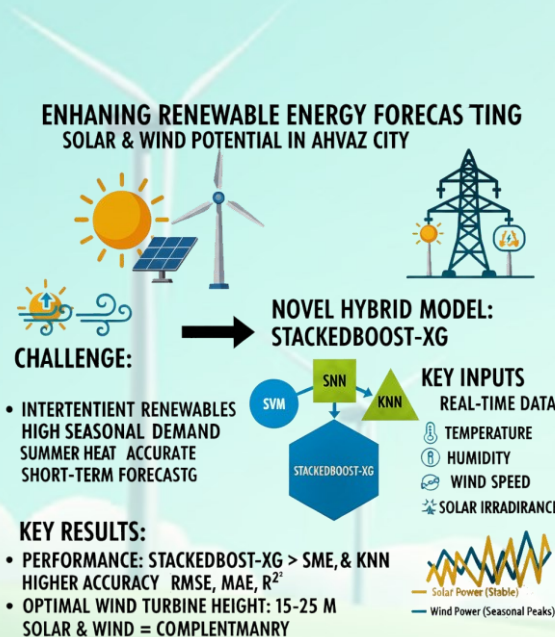
Enhancing Renewable Energy Forecasting: A Hybrid Machine Learning Approach for Solar and Wind Energy Potential in Ahvaz City

Mehdi Mohammadian Mehr, Hossein Farzin

Highlights

- ❖ StackedBoost-XG model combines SVM, KNN & XGBoost for better energy forecasting.
- ❖ Optimizes prediction accuracy, outperforming individual models in dynamic conditions.
- ❖ Application in Ahvaz City, tackling extreme climate & high summer energy demand.
- ❖ Compares SVM, KNN & StackedBoost-XG, proving superior performance in forecasting.

Graphical Abstract



Use your device to scan
and read the article
online



Citation

M. Mohammadian Mehr, and H. Farzin, "Enhancing Renewable Energy Forecasting: A Hybrid Machine Learning Approach for Evaluating Solar and Wind Energy Potential in Ahvaz City," *Journal of Green Energy Research and Innovation*, vol. 2, no. 4, pp. 14-26, 2025.



<https://doi.org/10.61882/jgeri.2.4.14>





Online ISSN: 3041-9018

Journal of Green Energy Research and Innovation

Journal Homepage: www.jgeri.araku.ac.ir

Enhancing Renewable Energy Forecasting: A Hybrid Machine Learning Approach for Solar and Wind Energy Potential in Ahvaz City

Mehdi Mohammadian Mehr, Hossein Farzin *

Department of Electrical Engineering, Faculty of Engineering, Shahid Chamran University of Ahvaz, Ahvaz 61357-43337, Iran.

ARTICLE INFO

Keywords:

Short-term forecasting,
XGBoost,
SVM,
KNN,
StackedBoost-XG,
Energy Grid Optimization,
Renewable Energy Integration.

Article History:

Received: 02 May 2025;
Revised: 15 June 2025;
Accepted: 01 July 2025.

Article type:

Research Article

* Corresponding author

E-mail address

farzin@scu.ac.ir (H. Farzin)

ABSTRACT

This paper introduces a new approach for short-term forecasting of solar and wind energy potential in Ahvaz City. The method is based on the StackedBoost-XG model, a hybrid ensemble that combines Support Vector Machine (SVM) and K-Nearest Neighbors (KNN) with XGBoost as the final estimator. The study focuses on accurately predicting energy generation using real-time meteorological data. Key inputs include temperature, humidity, wind speed, and solar irradiance factors that are crucial for reliable energy forecasting. These variables are integrated into energy production formulas to estimate outputs for both solar and wind sources. This improves prediction accuracy. The model's performance is assessed using standard evaluation metrics: RMSE, MAE, and R^2 . Results indicate that StackedBoost-XG significantly outperforms the individual SVM and KNN models. It shows higher accuracy in forecasting both solar and wind energy. The research also explores the effect of wind turbine height. It finds that optimal energy output occurs at heights between 15 and 25 meters. In addition, the study highlights the importance of managing thermal losses in solar panels, especially during warmer months, to maintain system efficiency. Finally, it emphasizes the complementary nature of solar and wind energy. Solar power offers relatively stable output throughout the year, while wind energy provides higher peaks in specific seasons. By integrating both energy sources, the study proposes a promising solution to address energy demand imbalances in Ahvaz. This study introduces a hybrid forecasting method that uses advanced machine learning and weather data. Its goal is to optimize renewable energy systems and enhance the management of the energy grid.

1. Introduction

1.1. Motivation

In the face of rapidly growing global energy demand, the transition from traditional fossil fuel-based power generation to renewable energy sources has become a critical challenge [1,2]. Among the most promising sources of renewable energy, solar and wind power stand out due to their abundance and environmental sustainability [3-5]. However, despite their potential, the intermittent and unpredictable nature of these energy sources presents significant obstacles for integrating them into power grids [6,7]. The city of Ahvaz is located in the southwestern Iran, where summers are characterized by intense heat waves, leading to sharp increases in electricity consumption, primarily for cooling and air conditioning. This seasonal demand fluctuation further exacerbates the energy supply-demand imbalance, creating a pressing need for more efficient energy management strategies. Notably, the reliance on solar and wind energy in Ahvaz offers a sustainable alternative, but the challenge remains in reliably predicting their performance to match energy supply with peak demand [8,9]. The fluctuating nature of solar and wind energy generation, influenced by factors such as weather patterns, seasonal variations, and geographic conditions, introduces substantial uncertainty in energy forecasting [10,11]. In Ahvaz, the unpredictability of these renewable sources poses a significant challenge in planning for electricity consumption during the summer months.

Accurate forecasting of solar and wind energy output is essential for effective energy planning and improved load balancing, especially during periods of peak demand. This highlights the urgent need for reliable prediction models capable of accurately estimating the performance of solar and wind energy systems. These models help improve the integration of renewable energy sources into the power grid. They reduce the gap between energy supply and demand. In this study, advanced machine learning (ML) techniques are used to improve the accuracy of energy production forecasts from solar and wind sources in Ahvaz. Accurate forecasting of energy generation improves the sustainability of energy systems. It also enables smarter energy management. This reduces dependence on non-renewable backup power, especially during peak demand periods.

1.2. Literature Review

Global electricity demand is steadily increasing, especially during hot summer months. In Ahvaz, this leads to a critical imbalance between energy supply and demand. This issue primarily arises due to the reliance on non-renewable energy sources during peak periods. The increasing demand for sustainable energy solutions necessitates a thorough examination of the renewable energy potential of solar and wind power in Ahvaz. Accurately forecasting the energy output of these sources is crucial for effective energy management. This study aims to address these challenges by developing a mathematical model that converts meteorological parameters into energy outputs for solar panels and wind turbines. A major challenge is the intermittent and fluctuating nature of solar and wind energy. This variability makes accurate energy prediction difficult. Therefore, this study focuses on short-term forecasting using machine learning models. The goal is to improve grid management and optimize the integration of renewable energy in Ahvaz.

Hybrid solar-wind energy systems are gaining attention as an effective solution to reduce grid pressure and support sustainable energy production. For example, one study used transformer models to forecast hybrid photovoltaic-wind systems in urban areas. The results showed a high accuracy of 90.7% for solar energy and 90.4% for wind speed. This highlights the significant role of AI-based models in improving forecasting performance for hybrid energy systems [12]. Several studies have emphasized the critical importance of forecasting for grid stability. One review highlighted the necessity of integrating forecasting methods for wind, solar, and electrical load management. It pointed out that the growing uncertainty in energy production calls for more sophisticated and integrated forecasting models to manage renewable energy sources effectively and reduce fluctuations in energy production [13]. The application of ML techniques has become a central focus in enhancing energy forecasting. A study demonstrated that combining Random Forest, Exponential Smoothing, and Long Short-Term Memory (LSTM) networks for solar power forecasting significantly improved accuracy compared to traditional methods. This underscores the effectiveness of hybrid models in optimizing the prediction of renewable energy generation [14]. Further studies also highlight the value of Earth System Models (ESMs) in long-term energy forecasting. While ESMs are valuable tools, their optimization and integration with advanced forecasting techniques are essential for accurate energy production predictions [15]. Artificial Neural Networks (ANNs) have been applied to predict the energy output of wind and solar systems based on local meteorological data. These models have been shown to be critical in determining the necessary reserve capacities in energy systems, particularly during high-demand periods, emphasizing the importance of accurate forecasting for grid planning and management [16]. The unpredictability of renewable energy sources has driven the development of advanced forecasting methods. For instance, the use of ARIMA and F-Prophet models demonstrated prediction accuracies exceeding 90%, making these models highly reliable for short-term energy forecasting and contributing significantly to renewable energy applications [17]. A comprehensive review of forecasting models has identified the need for precision in energy generation predictions. It emphasized that while physical, statistical, and hybrid models exist, ML-based approaches offer substantial improvements in accuracy. The review also stressed the importance of further research to refine forecasting models and enhance the integration of renewable energy into evolving energy markets [18].

Ensemble methods, particularly those that combine ANNs with other learning techniques, have outperformed individual models in predicting wind and solar power production. These hybrid approaches underline the importance of integrating multiple techniques to improve forecasting accuracy and ensure more reliable energy predictions [19]. The role of artificial intelligence (AI) in renewable energy forecasting is expanding. A study highlighted the potential of explainable AI (XAI) and quantum AI (QAI) to enhance the transparency and reliability of energy predictions. These technologies offer new opportunities for optimizing variable renewable energy systems in the future [20]. Moreover, a comparative study on photovoltaic power generation forecasting using various ML models, such as Support Vector Machines (SVM), Gaussian Process Regression (GPR), and Decision Trees, showed that while computational times varied, these models were effective in predicting solar power, providing valuable insights for the selection of forecasting models [21].

In conclusion, this study addresses the challenges of renewable energy forecasting in regions with high seasonal demand, like Ahvaz. The intermittent nature of solar and wind energy presents a significant challenge to grid stability, which can be mitigated by using machine learning models for short-term forecasting. By improving forecast accuracy, these models can optimize energy generation, enhance grid integration, and aid in the transition to a more sustainable energy future. The study focuses on improving solar and wind energy predictability through advanced ML techniques tailored to Ahvaz's specific needs, ensuring more efficient and sustainable energy systems

1.3. Contributions

This study makes several key contributions to renewable energy forecasting, particularly for predicting solar and wind energy in regions with significant climatic variations, such as Ahvaz:

1. The primary contribution is the introduction of the StackedBoost-XG model. This hybrid ensemble method combines SVM,

K-Nearest Neighbors (KNN), and XGBoost to optimize solar and wind energy forecasting accuracy. By leveraging the strengths of multiple machine learning techniques, this model improves prediction reliability, particularly in dynamic environments, outperforming individual models like SVM and KNN.

2. The study addresses the specific challenges of energy forecasting in Ahvaz, known for its high seasonal temperature fluctuations and significant summer energy demand. The performance of various models in this unique environment provides valuable insights into optimizing renewable energy systems in regions with complex climates and energy needs.
3. A comparative analysis of SVM, KNN, and the StackedBoost-XG model is presented. This analysis highlights the strengths and limitations of each model for forecasting solar and wind energy in Ahvaz. It demonstrates that the StackedBoost-XG model performs superiorly, offering a reliable and accurate energy prediction solution.

The paper is structured as follows: Introduction, Problem Description, Methodology, Data and Preprocessing, Results and Discussion, and Conclusion. Each section addresses key aspects of energy forecasting challenges, model development, and findings.

2. Problem Description

Accurate forecasting of solar and wind energy generation is a significant challenge, particularly in regions like Ahvaz. The city experiences extreme seasonal temperature variations and intense heat during the summer months. These harsh conditions increase energy demand, especially for cooling systems, and place considerable pressure on the energy grid. One of the main difficulties lies in the intermittent and unpredictable nature of renewable energy sources. Weather-related factors such as temperature, humidity, wind speed, and solar irradiance fluctuate continuously, making energy output hard to predict. This variability complicates energy planning and load management during peak demand periods. Due to the lack of reliable forecasting models, Ahvaz often relies on fossil fuel-based power plants. This dependency leads to higher costs and greater environmental harm, undermining efforts to reduce carbon emissions and shift toward sustainable energy systems. As global energy trends move toward renewables, the need for accurate and reliable forecasting becomes more urgent. Existing models often struggle to capture the complexity and non-linearity of energy production under dynamic weather conditions. These limitations reduce the effectiveness of integrating renewable sources into the power grid. To address these challenges, this study introduces the StackedBoost-XG model—a novel hybrid approach that combines SVM, KNN, and XGBoost algorithms. By leveraging the strengths of each method, the model significantly improves forecasting accuracy, even in complex and fluctuating environments. This approach enhances short-term energy predictions, optimizes energy planning, reduces reliance on conventional power sources, and supports the stable integration of renewables into the grid. It is especially valuable for regions like Ahvaz, where climate conditions are highly variable.

3. Methodology

This study employs a hybrid approach that combines meteorological data and ML models to predict the energy output from solar and wind sources. The methodology integrates key environmental parameters, such as temperature, humidity, and wind speed, to estimate the energy production of solar panels and wind turbines. These outputs are used to train forecasting models that can predict future energy production and optimize energy management in the region.

3.1. Solar Energy Production

To estimate the energy produced by a solar panel, Equation (1) calculates the energy output based on solar irradiance [22]:

$$E = G_t \times A \times \eta_t \quad (1)$$

E = Energy produced (Wh)

G_t = Solar irradiance on the panel at a given time (Wh/m²)

A = Area of the solar panel (m²)

η_t = Efficiency of the solar panel

The solar irradiance (G_t) is estimated using a time-dependent model, as Equation (2) [23]:

$$G_t = G_{max} \times \sin\left(\frac{\pi(t - t_{sunrise})}{t_{sunset} - t_{sunrise}}\right) \times (1 - (RH \times K)) \quad (2)$$

G_t = Solar irradiance at time t (Wh/m²)

G_{max} = Daily average solar irradiance (Wh/m²)

RH = Relative humidity

K = Humidity correction factor (typically 0.6)

$t_{sunrise}, t_{sunset}$ = Times of sunrise and sunset

t = Current time of the day

The efficiency η_t of the solar panel is temperature-dependent, meaning it decreases as the temperature increases. This relationship is modeled as Equation (3) [23]:

$$\eta_t = \eta_{ref} \times (1 - \beta(T_{panel} - T_{ref})) \quad (3)$$

η_t = Efficiency of the panel at temperature

η_{ref} = Reference efficiency at 25°C

β = Temperature coefficient

T_{panel} = Actual temperature of the panel (°C)

T_{ref} = Reference temperature (25°C)

Solar panels generally operate at temperatures higher than the ambient environment due to the absorption of solar radiation, which is partly converted into heat. As a result, the panel's temperature can exceed the ambient temperature by 15 to 20°C, especially under direct sunlight. The temperature of the panel, T_{panel} , is influenced by solar radiation and ambient temperature. It is estimated using Equation (4) [23]:

$$T_{panel} = T_{ambient} + \left(\frac{G_t \times (1 - \eta_{thermal})}{H_{thermal}} \right) \quad (4)$$

T_{panel} = Solar panel temperature

$T_{ambient}$ = Ambient temperature

G_t = Solar irradiance on the panel surface (Wh/m²)

$\eta_{thermal}$ = Thermal coefficient of the panel (typically ranging from 0.8)

$H_{thermal}$: The thermal conductivity coefficient (we will assume it to be fixed at 15 W/m²·K)

3.2. Wind Energy Production

For wind energy estimation, the mechanical power output of the wind turbine is calculated using the standard formula derived from Equation (5) [24]:

$$P = \frac{1}{2} \times \rho_h \times C_p \times v^3 \times A \quad (5)$$

P = Mechanical power output of the wind turbine (W)

ρ_h = Air density at height h

A = Swept area of the turbine blades ($A = \pi R^2$, where R is the radius of the turbine blades)

v = Wind speed (m/s)

C_p = Power coefficient of the wind turbine

The air density ρ is calculated based on Equation (6), which accounts for the presence of water vapor in humid air [25]:

$$\rho_h = \frac{P_{air}}{P_{dry} \times T} \times \left(1 - \frac{P_{vapor}}{P_{air}} \right) \quad (6)$$

P_{air} : Total air pressure (Pa)

P_{vapor} : Vapor pressure of water in humid air (Pa). This is calculated using temperature and relative humidity.

P_{dry} : Gas constant for dry air (287.05 J/(kg·K))

T : Absolute temperature (K)

To compute P_{vapor} , the saturation vapor pressure of water (P_{set}) is estimated using the Antoine equation for temperatures below 100°C (as given in Equation (7)) [26]:

$$\log_{10} P_{set} = A' - \frac{B'}{T + C'} \quad (7)$$

P_{set} : Saturation vapor pressure of water (in mmHg)

T : Temperature (in °C)

A' , B' , and C' : Antoine constants for water.

The specific values of the constants for the Antoine equation for water in the temperature range of 0°C to 100°C are as follows: $A' = 8.07131A$, $B' = 1730.63B$, $C' = 233.426C$. The vapor pressure of water P_{Pvapo} can then be determined using the relative humidity (RH) as Equation (8) [25, 26]:

$$P_{Pvapo} = P_{set} \times 133.322 \times \frac{RH}{100} \quad (8)$$

RH is the relative humidity (%), and 133.322 is the conversion factor from mmHg to Pa. Air density also varies with altitude, and this relationship is modeled as Equation (9) [27]:

$$\rho_h = \rho_0 \times e^{\frac{h}{H}} \quad (9)$$

ρ_h is the air density at height h

ρ_0 is the air density at sea level

h is the height above sea level in meters.

H is the scale height (typically around 8500 meters)

Wind speed at various heights is calculated using the Power Law, which converts the wind speed from a reference height h_0 to a desired height h , given in Equation (10) [24]:

$$V_h = V_0 \times \left(\frac{h}{h_0} \right)^\alpha \quad (10)$$

V_h is the wind speed at height $h = 10, 15, 25, 50$ m

V_0 is the wind speed at the reference height $h_0 = 10$ m

h is the desired height.

h_0 is the reference height

α is the power coefficient

The energy produced by the wind turbine is influenced by the wind speed (v) and the air density (ρ), and it can be calculated over time by integrating the power output.

4. Data and Preprocessing

Meteorological data, such as temperature, humidity, and wind speed, are collected as the primary inputs for the energy production models. These data are used to model the output of both solar panels and wind turbines, converting the raw meteorological data into energy predictions.

The following steps outline the process:

1. **Data Collection:** Meteorological data, including hourly temperature, humidity, wind speed, and solar irradiance, are collected from reliable sources.
2. **Modeling Energy Production:** The collected data are used to calculate solar energy output using the solar irradiance formula and wind energy output using the wind turbine formula.
3. **Preprocessing:** Data are cleaned and normalized to ensure accuracy and consistency.
4. **Model Training:** The energy production data, generated from the meteorological inputs, serve as the ground truth for training ML models. These models learn the relationships between weather parameters and energy outputs.
5. **Forecasting:** The trained models are then used to predict energy generation based on future meteorological forecasts.

These steps result in accurate, data-driven models capable of predicting energy production from solar and wind sources under varying climatic conditions.

4.1. Selection of Solar Panel and Wind Turbine

For this study, a solar panel and a wind turbine have been selected to represent the typical renewable energy systems in the region of Ahvaz. These systems will be used to evaluate the potential energy generation from solar and wind resources in the city.

The selected solar panel is the MEP600-T144-GG model from Mana Energy, an Iranian manufacturer, with a rated capacity of 575-600 watts. The panel has an area of $2278 \times 1134 \text{ cm}^2$ and operates at an efficiency of 23.2% at a standard temperature of 25°C [28]. Additionally, the temperature coefficient of the panel is 0.046 %per degree Celsius, which implies that the efficiency will decrease slightly with increases in temperature, a crucial factor in regions with hot climates like Ahvaz. A sample of the Mana Energy panel in a solar power plant is shown in Figure 1.

The wind turbine chosen for this study is the Max600 model from NewSkyPower, with a rated capacity of 600 watts. Manufactured in China, it has a starting wind speed of 1.5 m/s and a blade diameter of 1.7 meters [29]. The power coefficient (C_p) for this model is typically between 0.25 and 0.35, making it suitable for areas with lower wind speeds. This turbine will offer useful insights into the wind energy potential in Ahvaz, which experiences lower wind speeds, especially during certain seasons of the year. The structure of the selected turbine is shown in Figure 2.



Figure 1. 140 MW Solar Power Plant in Mahallat City - Markazi Province – Iran [28].

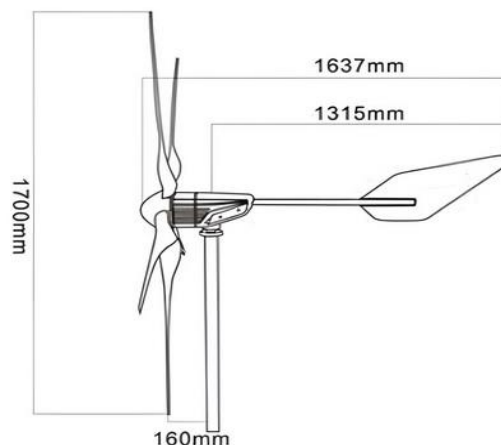


Figure 2. The wind turbine, the Max600 model from NewSkyPower [29].

These components have been selected to evaluate the potential of solar and wind energy generation under comparable capacities, allowing for an analysis of their performance in meeting the city’s energy demand. By considering both solar and wind resources, this study aims to explore the optimal energy mix for Ahvaz to address its energy demand, especially during peak consumption periods.

4.2. ML and DL Models for Energy Prediction

In the context of predicting solar and wind energy production, the problem at hand is a regression task, where the goal is to predict continuous energy output values based on input features such as weather conditions and the physical attributes of energy systems. To address this issue, various ML models can be employed, each offering unique advantages. The ML techniques, such as SVM, KNN, and StackedBoost-XG, are capable of capturing the relationships between the input variables and the energy production. The models and their applications for energy prediction will be introduced in detail in the following.

4.2.1. SVM

The SVMs are powerful supervised learning algorithms used for classification and regression problems. The model works by identifying an optimal hyperplane that separates data into different classes. The key feature of SVM is the maximization of the margin between classes, ensuring the best separation between data points. The method for selecting the hyperplane is discussed in Figure 3. This hyperplane can be linear or non-linear, depending on the problem’s complexity. In high-dimensional spaces, SVM can handle both linear and non-linear problems effectively. SVM’s ability to work with large datasets and find complex decision boundaries makes it a suitable choice for various real-world applications.

4.2.2. K-NN

The K-NN algorithm is a non-parametric method used for classification and regression. This process, illustrated in Figure 4, works by identifying the "K" closest training samples to a new data point and assigning a label based on majority voting (for classification) or averaging the labels (for regression) of those neighbors. The distance between data points is calculated using various distance metrics, such as Euclidean distance, Manhattan distance, or cosine similarity. The choice of "K" is crucial as it affects the model’s performance. A small "K" may lead to overfitting, while a large "K" may cause underfitting. K-NN is simple, interpretable, and often effective in problems where the relationships between data points are important.

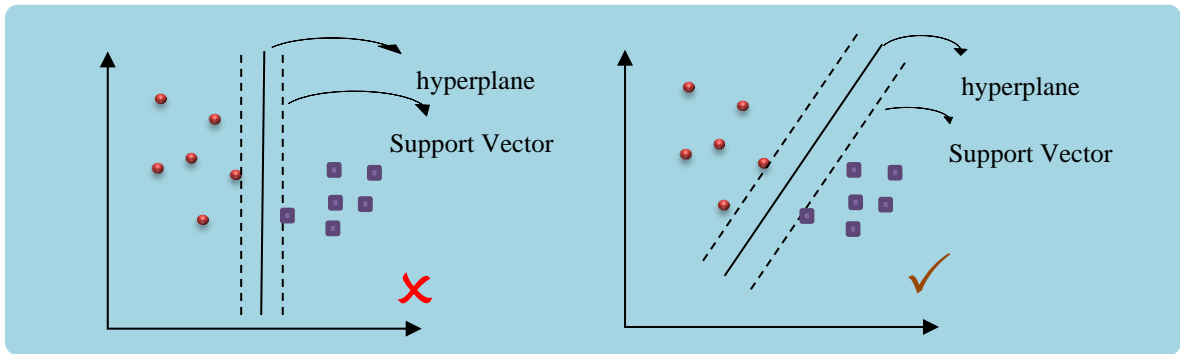


Figure 3. The method for selecting the hyperplane.

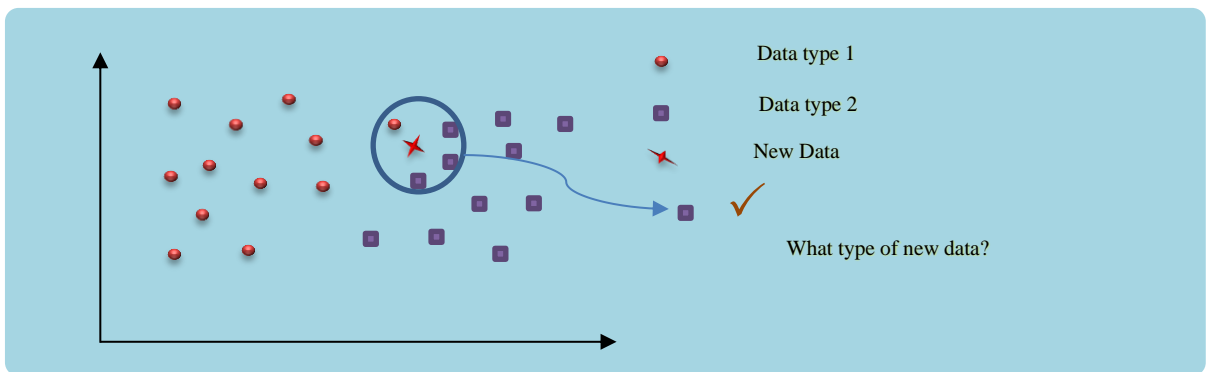


Figure 4. K-NN Algorithm Process.

4.2.3. StackedBoost-XG: Solar and Wind Energy Prediction

The StackedBoost-XG model is a hybrid and advanced approach for predicting solar and wind energy, leveraging a combination of various base models along with a more advanced final model to improve performance. Below is a more detailed and technical explanation of this model and its methods:

4.2.3.1 Base Models (SVM, KNN)

The SVM performs well on datasets that are linearly separable or clearly defined. SVM is particularly suitable for high-dimensional data (such as energy data) and when class boundaries are clearly distinct. It may not perform well with more complex or non-linear data. The KNN model excels in simulating complex, non-linear relationships between data points, relying on similar data for predictions. In noisy datasets or with additional irrelevant features, KNN may struggle. It is highly sensitive to the scaling of data and can perform poorly in noisy environments.

4.2.3.2 Final Model: XGBoost

XGBoost is an advanced algorithm designed to enhance other models through the boosting process. This algorithm excels in predictive tasks involving complex and non-linear data and incorporates features that help prevent overfitting and improve prediction accuracy [30]. Role in Model Combination: After each of the base models (SVM and KNN) generates predictions, XGBoost takes these predictions as inputs and delivers the final result based on the best possible combination of them. This final step acts as the "combiner," improving the strengths of each base model while reducing their limitations.

4.2.3.3 Model Combination (Stacking)

Stacking is a learning method where multiple base models are used simultaneously to make initial predictions, followed by another model (in this case, XGBoost) to combine these predictions and provide the final output [31]. This method typically enhances prediction accuracy by leveraging models with different characteristics. As a result, the base models compensate for each other's weaknesses, and the final model (XGBoost) intelligently combines the predictions.

4.2.3.4 Advantages of StackedBoost-XG

Leveraging the Strengths of Each Model: Each base model brings unique strengths to the table and excels at specific types of predictions. However, each also has its weaknesses. By combining these models with XGBoost, the overall prediction accuracy improves. Mitigating Model Weaknesses: The weaknesses of each base model are compensated for by other models, and the final model (XGBoost) effectively utilizes the strengths of these combinations. The combined model is shown in Figure 5, where the structure of the StackedBoost-XG framework is illustrated.

4.3. Short-Term Forecasting of Solar and Wind Energy Potential

For short-term forecasting of solar and wind energy potential, the accuracy and reliability of input data are paramount. In this study, hourly energy potential is predicted using a dataset that includes both historical and real-time meteorological data. The dataset is divided into training, validation, and test sets, as summarized in Table 1. The model uses real-time weather variables collected over time, referred to as past real-time meteorological data, to reflect actual atmospheric conditions relevant to each hourly prediction. These include temperature, humidity, solar irradiance, wind speed, and other factors detailed in Table 2. While the data is historical in terms of collection period, it retains its real-time characteristics for each recorded instance, making it suitable for developing a practical short-term forecasting model.

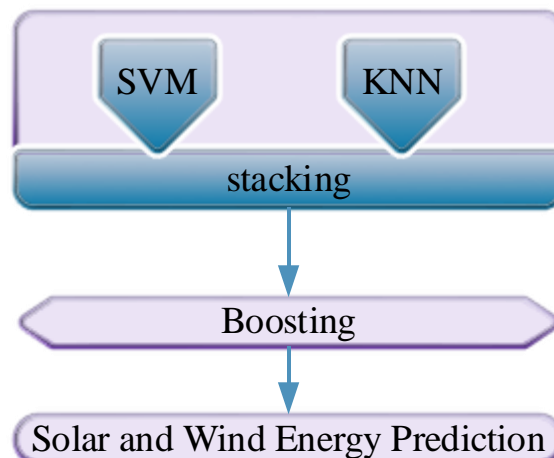


Figure 5. StackedBoost-XG: An Ensemble Model Leveraging Multiple Base.

The forecasting horizon is set to one hour ahead, classifying the model as a short-term prediction framework. Therefore, this approach integrates both past real-time meteorological observations and historical energy production values to improve the precision of hourly predictions. Ultimately, this methodology supports improved energy grid management and enhances the reliability of the renewable energy supply in Ahvaz.

4.4. Evaluation Metrics for Model Comparison

To assess and compare the performance of different predictive models for solar and wind energy forecasting, key metrics such as Mean Absolute Error (MAE), Root Mean Squared Error (RMSE), and R-squared (R^2) are employed. MAE measures the average magnitude of prediction errors, giving insight into how close predicted values are to actual outcomes. RMSE emphasizes larger errors, making it useful for identifying models sensitive to significant deviations. R^2 indicates the proportion of variance explained by the model, with values closer to 1 suggesting better model fit. These metrics collectively help determine the most accurate and reliable model for forecasting energy production. In addition, feature importance was evaluated using XGBoost, which provides insights into the most influential features affecting energy forecasting for both solar and wind energy [32]. To achieve this, the importance of features was computed using XGBoost's built-in feature importance method, and the results were normalized to a scale of 0 to 100 for better interpretability.

5. Results, Discussion, and Insights

Ahvaz is situated at an altitude of only 18 meters above sea level. The climate in Ahvaz is generally warm, with an average annual temperature of 26.9°C and clear skies [33]. The area enjoys a high level of solar exposure, with an average daily solar radiation of 5012 Wh/m² [33]. Solar energy is most effective between 7 AM and 5 PM, allowing for an extended period of sunlight that can be harnessed for renewable energy production [33]. As shown in Table 3, wind speed at different heights was estimated using the power law relationship with the coefficient α [33]. The α value was first determined based on the mean wind speed at the reference height of 10 meters and the mean wind speed at the unknown height, according to Equation (10). This coefficient was then used to convert the wind speed from the reference height to the desired height. This relatively moderate wind speed, combined with the high levels of solar radiation, positions Ahvaz as an ideal location for harnessing both solar and wind energy. The SVR model utilizes the Radial Basis Function (RBF) kernel, effective for modeling complex, non-linear relationships in the data. The KNN model is configured with 6 neighbors, optimizing a balance between flexibility and generalization. The Stacking Model combines the predictions of SVR and KNN, using XGBoost as the final estimator, thereby enhancing predictive performance by leveraging the strengths of both base models and the boosting algorithm. The optimal parameters for these models were determined through a combination of trial and error and systematic tuning methods. These models were implemented using the scikit-learn library in Python.

The potential energy of solar panels has been calculated under two scenarios: one accounting for thermal losses and the other excluding them. The results for these scenarios are presented in Figure 6. The potential energy of the solar panels shows a slight reduction when thermal losses are considered, with the gap being more noticeable in warmer months. The impact of thermal losses is minimal during winter, with differences under 0.2 kWh. However, during summer, especially in May (0.5 kWh difference), thermal losses have a more significant effect. The percentage loss due to thermal effects can be estimated at around 0.7% to 1.5% of the total energy output, depending on the month and environmental conditions. This suggests that managing panel temperature through cooling or improved materials could reduce losses during warmer months. For the wind turbine, potential energy has been calculated across four distinct scenarios, based on different installation heights: 10 meters, 15 meters, 25 meters, and 50 meters. Each scenario reflects the energy output at varying heights, providing insight into how turbine performance changes with altitude. The results are shown in Figure 7. The data for wind turbine energy show that increasing height leads to a higher energy output.

Table 1. Dataset Splitting for Energy Forecasting.

| Dataset Type | Date Range | Percentage of Data | Time Interval |
|----------------|--------------------------------------|--------------------|---------------|
| Training Set | October 1, 2020 – September 30, 2021 | 90% | Hourly |
| Validation Set | October 1, 2020 – September 30, 2021 | 10% | Hourly |
| Test Set | October 2, 2021 – October 12, 2021 | 100% | Hourly |

Table 2. Input Variables for Energy Forecasting.

| Input Variables | Description |
|---------------------|--|
| Energy Data | Hourly solar and wind energy output (Wh) |
| Calendar Data | Time, day, month, year, and season |
| Meteorological Data | Wind speed (m/s), air pressure (Pa), air density(kg/m ³), temperature (°C), Humidity (%) |

Table 3. Wind speed information.

| Height (m) | Average Annual Wind Speed (m/s) | Estimated α Coefficient from 10 m |
|------------|---------------------------------|--|
| 10 | 2.69 | 0 |
| 15 | 2.80 | 0.0988 |
| 25 | 3.02 | 0.1669 |
| 50 | 3.59 | 0.1793 |

5.1. Data-Driven Estimation of Solar and Wind Energy Potential with Thermal Losses and Optimal Heights

However, the difference between 25 meters and 50 meters is minimal, suggesting that beyond 25 meters, the increase in energy production is limited relative to the rising installation costs. The most substantial change in energy output occurs between 15 meters and 25 meters, where energy production increases significantly, making this the optimal height range for installation.

5.2. Short-Term Forecasting of Solar and Wind Energy Potential

The StackedBoost-XG model, a combination of SVM and KNN, outperforms the individual SVM and KNN models in terms of prediction accuracy for both solar energy and wind energy forecasting. This improvement can be attributed to the complementary strengths of both models within the ensemble approach. The performance of these models has been evaluated using a set of key metrics: RMSE, MAE, and R^2 , across both the validation and test datasets, as presented in Table 4. All simulations were carried out on a laptop equipped with an Intel Pentium® CPU N4200 (1.1 GHz) and 8 GB of RAM. The maximum training time for the StackedBoost-XG model was approximately 19 seconds, demonstrating the model’s computational efficiency and suitability for real-time or near-real-time forecasting applications.

5.2.1. Analysis of Solar Energy Forecasting

The forecasting of solar energy potential, as shown in Figure 8, demonstrates the impact of thermal losses and the accuracy of the various models in predicting solar energy output. In the case, as shown in Table 4, the StackedBoost-XG model demonstrates a significant improvement in accuracy compared to the individual models. Specifically, the RMSE of the combined model is 3.78, which is lower than both SVM (RMSE = 4.12) and KNN (RMSE = 4.08). The reduced RMSE indicates that the StackedBoost-XG model better handles both thermal losses and non-linear relationships between variables such as temperature, radiation, and historical energy production. The ability of SVM to capture global patterns and of KNN to address local variations is what allows this combined model to offer superior predictions, particularly in complex scenarios like solar energy forecasting, where both global and local factors influence the output. The SVM and KNN models show RMSE and MAE values that are higher than StackedBoost-XG, which indicates they are more sensitive to the variance in energy production and less effective at minimizing large errors during peak thermal loss months (e.g., summer).

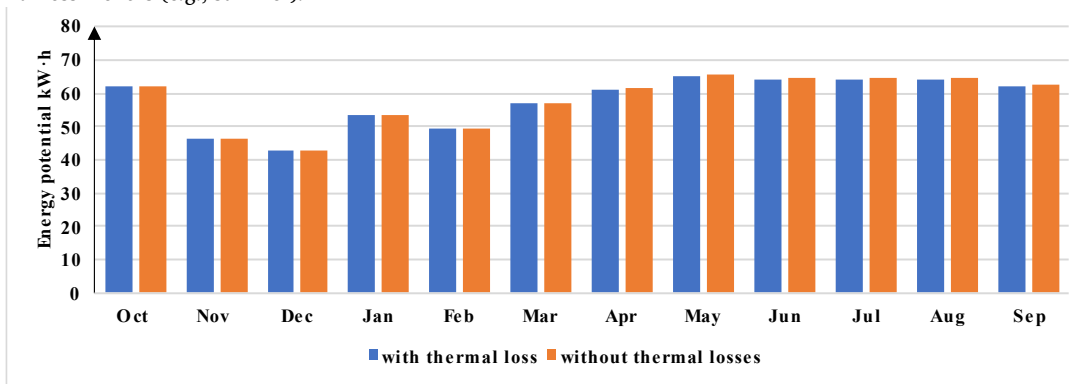


Figure 6. Potential energy of the solar panel in one year.

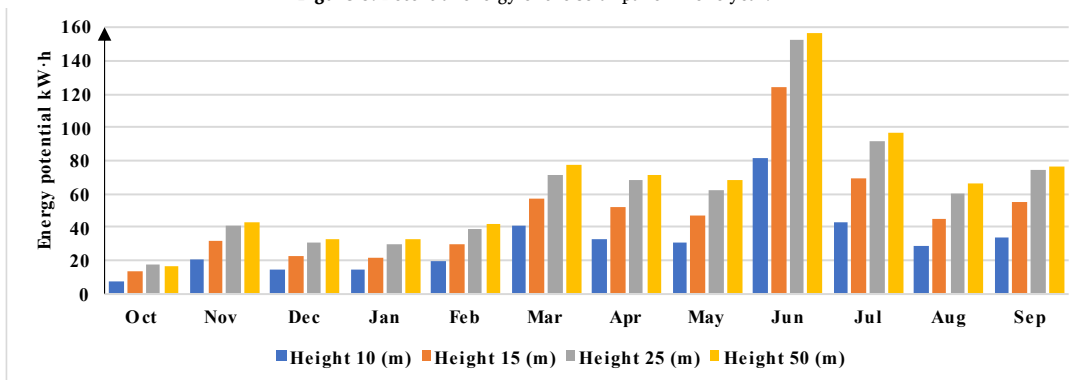


Figure 7. Potential energy of the wind turbine in one year at different heights.

5.2.2. Analysis of Wind Energy Forecasting

For wind energy forecasting, the models' performance is evaluated at different installation heights: 15 meters and 25 meters, as shown in Figures 9 and 10. The results reveal that wind energy predictions improve as the installation height increases. Similarly, in wind energy forecasting, as demonstrated in Table 4, the StackedBoost-XG model provides the lowest RMSE values and highest R² scores. At a 15-meter installation height, the model achieves an RMSE of 2.87, and at 25 meters, it achieves 3.09. In contrast, the individual models SVM and KNN perform less effectively, with RMSE values of 3.45 and 3.56, respectively. These results highlight the model's ability to more accurately capture the underlying dynamics of wind energy production, which can be influenced by factors such as installation height and local wind patterns. By combining SVM's global pattern recognition and KNN's sensitivity to local fluctuations, the ensemble model offers a more robust and accurate forecasting approach.

5.2.3. Performance Improvement of StackedBoost-XG in Energy Forecasting

The StackedBoost-XG model demonstrates a notable enhancement in forecasting both solar and wind energy compared to the individual models (SVM and KNN). For solar energy, the combined model shows a ~5% improvement in accuracy over the SVM model and a ~7% improvement over KNN. In wind energy forecasting, the improvements are even more pronounced. At a 15-meter installation height, the StackedBoost-XG model achieves a ~34% increase in accuracy over SVM and a ~21% improvement over KNN. At a 25-meter height, the model delivers a ~50% improvement compared to SVM and a ~48% increase compared to KNN. Overall, the StackedBoost-XG model results in a significant boost in forecasting accuracy, with an average increase of ~5-48% across both solar and wind energy predictions, making it a more reliable and efficient tool for energy forecasting.

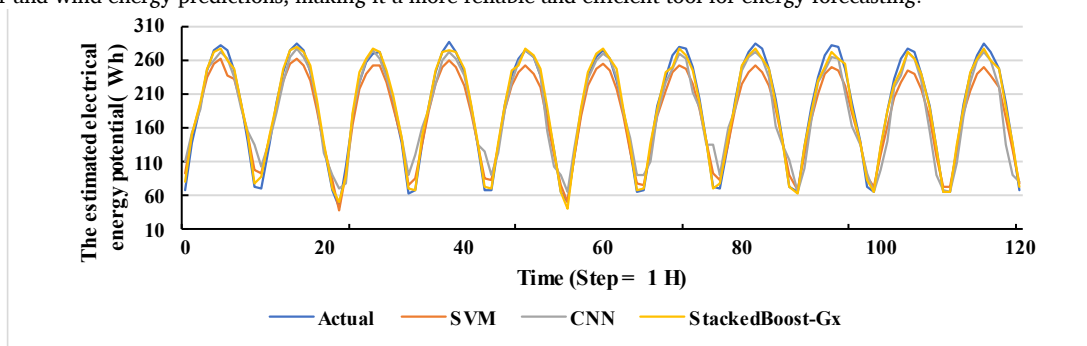


Figure 8. Forecasting the solar energy potential.

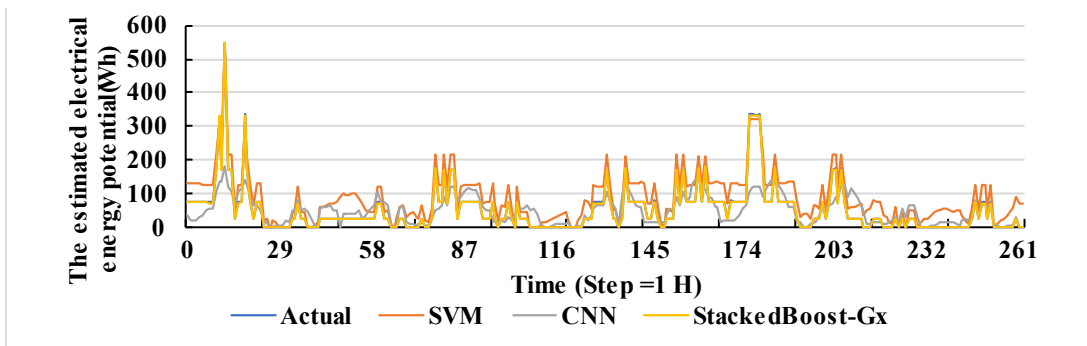


Figure 9. Forecasting the wind energy potential at a height of 15 meters.

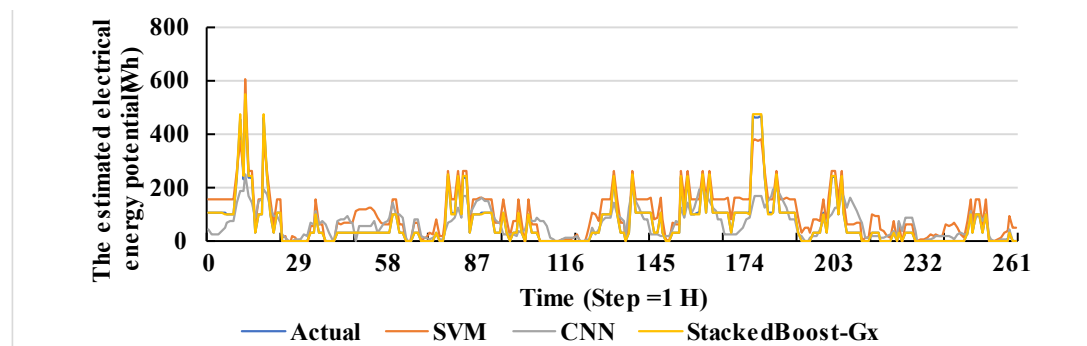


Figure 10. Forecasting the wind energy potential at a height of 25 meters.

Table 4. Comparison of Predictive Model Performance for Solar and Wind Energy Forecasting.

| Model | Energy Type | Validation Set | | | | Test Set | | | Limitations |
|-----------------|--------------|----------------|--------|----------------|----------|----------|--------|----------------|---------------------------|
| | | RMSE Wh | MAE Wh | R ² | Time (s) | RMSE Wh | MAE Wh | R ² | |
| SVM | Solar Energy | 11.83 | 9.8 | 0.97 | 0.14 | 18.43 | 15.80 | 0.94 | Thermal losses considered |
| | Wind Energy | 39.84 | 32.68 | 0.87 | 1.06 | 41.69 | 37.94 | 0.65 | Performance at 15 meters |
| | Wind Energy | 40.51 | 34.34 | 0.90 | 1.72 | 43.49 | 38.10 | 0.78 | Performance at 25 meters |
| KNN | Solar Energy | 12.51 | 9.24 | 0.97 | 0.02 | 21.41 | 16.21 | 0.92 | Thermal losses considered |
| | Wind Energy | 29.99 | 14.26 | 0.92 | 0.05 | 50.86 | 29.81 | 0.49 | Performance at 15 meters |
| | Wind Energy | 34.09 | 17.77 | 0.93 | 0.05 | 65.81 | 40.61 | 0.51 | Performance at 25 meters |
| StackedBoost-XG | Solar Energy | 11.04 | 8.76 | 0.99 | 1.06 | 7.35 | 5.65 | 0.99 | Thermal losses considered |
| | Wind Energy | 2.87 | 1.02 | 0.99 | 14.76 | 0.91 | 0.63 | 0.99 | Performance at 15 meters |
| | Wind Energy | 5.18 | 2.30 | 0.99 | 18.36 | 3.09 | 1.79 | 0.99 | Performance at 25 meters |

5.3. Sensitivity Analysis of Key Factors Affecting Solar and Wind Energy Forecasting

The sensitivity analysis, presented in Figure 11, highlights the varying importance of features in predicting solar and wind energy potential across three scenarios:

For the solar panel scenario, time (100) is the most influential feature, indicating that solar energy generation is predominantly driven by the daily sunlight cycle. Temperature (1) and humidity (72) are also important, with humidity being particularly noteworthy. High humidity or fog can obstruct sunlight, reducing the amount of solar radiation that reaches the panels. Therefore, the higher importance of humidity reflects its impact on solar panel output. Season and day contribute minimally (0 and 0.25, respectively), suggesting that solar energy is less influenced by seasonal variations or specific days. In the wind turbine scenarios, wind speed and air density emerge as the dominant factors. For the wind turbine at 15 m height, wind speed (59.49) and air density (100) are highly influential, and the trend is similar for the wind turbine at 25 m height (58.63 and 100). This underscores the reliance of wind energy on real-time environmental conditions such as wind speed and air density, which directly affect turbine efficiency. Time and humidity have a lower impact, further confirming that wind energy is primarily driven by atmospheric conditions.

6. Conclusions

This study evaluated the solar and wind energy potential in Ahvaz using a combination of machine learning techniques and energy system simulations. The region’s high solar irradiance and moderate wind speeds make it a promising site for hybrid renewable energy systems. Results showed that the 600W wind turbine produces approximately 340.56 kWh/year at 10 meters, increasing to 523.59 kWh at 15 meters, 681.48 kWh at 25 meters, and 719.03 kWh at 50 meters. However, the marginal gain from 25 to 50 meters is relatively small, suggesting that 25 meters represents an optimal trade-off between energy yield and installation cost. For solar energy, the 600W solar panel generates 691.04 kWh/year under optimal conditions. The panel’s output showed consistent energy production across the year, with slight reductions during warmer months due to thermal losses. Wind energy, in contrast, showed greater seasonal variability but significantly higher output when installed at appropriate heights. Therefore, combining both sources could ensure balanced, year-round energy availability, particularly valuable during peak demand periods. From a forecasting perspective, the StackedBoost-XG model, which integrates SVM and KNN with XGBoost as a meta-learner, consistently outperformed individual models. It achieved accuracy improvements of 5–7% for solar energy, and 21–50% for wind energy, depending on height. These improvements demonstrate the advantage of ensemble learning for capturing both global and local data patterns in non-linear, multivariate systems. Additionally, feature sensitivity analysis indicated that time and humidity are critical for solar energy, while wind speed and air density dominate wind energy predictions. These insights are crucial for informed site selection, system design, and adaptive energy management strategies. Overall, the study underscores the value of machine learning in optimizing renewable energy systems and recommends a hybrid solar-wind configuration with wind turbines installed between 15–25 meters, coupled with predictive ML tools, as the most effective strategy for sustainable energy planning in Ahvaz. Future research could validate the model in diverse climatic regions, integrate it with smart grid systems for real-time energy management, and assess the hybrid system’s cost-effectiveness and environmental impact.

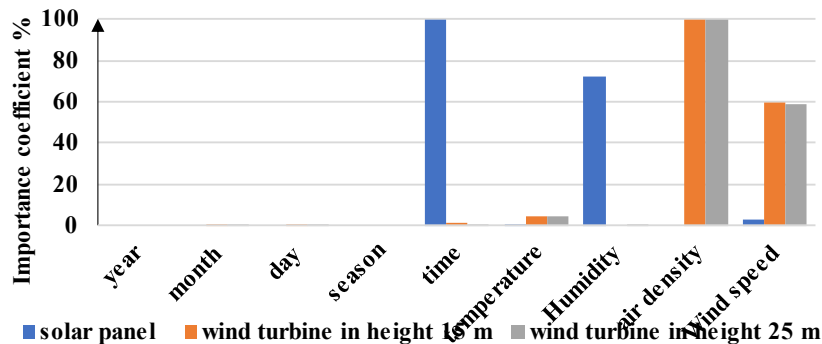


Figure 11. The importance coefficient of features in predicting solar and wind potential energy.

Nomenclature

| Symbol | Description |
|------------------|--|
| E | Energy output from solar panel or wind turbine (Wh) |
| G_t | Solar irradiance on the panel at time t (Wh/m ²) |
| A | Area of solar panel (m ²) or swept area of wind turbine blades (m ²) |
| η_t | Efficiency of solar panel at time t (dimensionless) |
| G_{max} | Daily average solar irradiance (Wh/m ²) |
| RH | Relative humidity (dimensionless) |
| K | Humidity correction factor (dimensionless) |
| $t_{sunrise}$ | Time of sunrise (hours) |
| t_{sunset} | Time of sunset (hours) |
| t | Current time of the day |
| η_{ref} | Reference efficiency at 25 °C (dimensionless) |
| β | Temperature coefficient (°C) |
| T_{panel} | Temperature of solar panel (°C) |
| $T_{ambient}$ | Ambient temperature (°C) |
| T_{ref} | Reference temperature (25 °C) |
| $H_{thermal}$ | Thermal conductivity coefficient (W/m ² K) |
| $\eta_{thermal}$ | Thermal coefficient of panel (dimensionless) |
| P | Mechanical power output of wind turbine (W) |
| ρ | Air density (kg/m ³) |
| C_p | Power coefficient of wind turbine (dimensionless) |
| v | Wind speed (m/s) |
| R | Radius of wind turbine blades (m) |
| A', B', C' | Antoine constants for water |
| P_{air} | Total air pressure (Pa) |
| P_{vapor} | Vapor pressure of water in humid air (Pa) |
| P_{dry} | Gas constant for dry air (287.05 J/(kg·K)) |
| T | Absolute temperature (K) |
| P_{set} | Saturation vapor pressure of water (mmHg) |
| h | Height above sea level (m) |
| H | Scale height (m) |
| V_h | Wind speed at height h (m/s) |
| V_0 | Wind speed at reference height h_0 (m/s) |
| h_0 | Reference height (m) |
| α | Power coefficient for wind speed conversion (dimensionless) |

| Symbol | Description |
|-----------------|--|
| ML | Machine Learning |
| SVM | Support Vector Machine |
| KNN | K-Nearest Neighbors |
| XGBoost | Extreme Gradient Boosting |
| StackedBoost-XG | An Ensemble Model Leveraging Multiple Base |
| ANN | Artificial Neural Network |
| ESM | Earth System Model |
| XAI | Explainable Artificial Intelligence |
| QAI | Quantum Artificial Intelligence |

References

- [1] M. J. B. Kabeyi, and O. A. Olanrewaju, "Sustainable Energy Transition for Renewable and Low Carbon Grid Electricity Generation and Supply," *Frontiers in Energy Research*, vol. 9, 2022.
- [2] J. L. Holechek, H. M. E. Geli, M. N. Sawalhah, and R. Valdez, "A Global Assessment: Can Renewable Energy Replace Fossil Fuels by 2050?," *Sustainability*, vol. 14, no. 8, 4792, 2022.
- [3] L. Amjith, and B. Bavanish, "A Review on Biomass and Wind as Renewable Energy for Sustainable Environment," *Chemosphere*, vol. 293, 133579, 2022.
- [4] A. Rahman, O. Farok, and M. M. Haque, "Environmental Impact of Renewable Energy Source Based Electrical Power Plants: Solar, Wind, Hydroelectric, Biomass, Geothermal, Tidal, Ocean, and Osmotic," *Renewable and Sustainable Energy Reviews*, vol. 161, 112279, 2022.
- [5] Y. Ebazadeh, R. Alayi, E. Jamali, and A. Behvandi, "Modeling and Optimization of The Photovoltaic System Connected to the Grid," *Journal of Green Energy Research and Innovation*, vol. 2, no. 1, pp. 32–43, 2025.
- [6] A. Q. Al-Shetwi, "Sustainable Development of Renewable Energy Integrated Power Sector: Trends, Environmental Impacts, and Recent Challenges," *Science of The Total Environment*, vol. 822, 153645, 2022.
- [7] F. Masteri Farahani, A. Kazemi, and A. Hedayati Aghmashadi, "Optimal Site Selection of Solar Power Plant Stations Using GIS-ANP and Genetic Optimization Algorithm in Markazi Province, Iran," *Journal of Green Energy Research and Innovation*, vol. 1, no. 4, pp. 47–63, 2024.
- [8] C. Sweeney, R. J. Bessa, J. Browell, and P. Pinson, "The Future of Forecasting for Renewable Energy," *WIREs Energy and Environment*, vol. 9, no. 2, 2019.
- [9] A. H. Karamali, A. Daeichian, S. Rezaei, and A. Reihanian, "Assessing Wind Energy Potential in Markazi Province, Iran: A Data-Driven Approach with AI Algorithms,"

- Journal of Green Energy Research and Innovation*, vol. 2, no. 2, pp. 26–35, 2025.
- [10] R. Meenal, D. Binu, et al., "Weather Forecasting for Renewable Energy System: A Review," *Archives of Computational Methods in Engineering*, vol. 29, no. 5, pp. 2875–2891, 2022.
- [11] M. H. Shakoor, "A Survey on Renewable and New Sources of Energies for Electricity Power Production and Its Challenges," *Journal of Green Energy Research and Innovation*, vol. 1, no. 4, pp. 64–85, 2024.
- [12] A. Javaid, M. Sajid, E. Uddin, A. Waqas, and Y. Ayaz, "Sustainable Urban Energy Solutions: Forecasting Energy Production for Hybrid Solar-Wind Systems," *Energy Conversion and Management*, vol. 302, 118120, 2024.
- [13] H. Wang, N. Zhang, et al., "A Comprehensive Review for Wind, Solar, and Electrical Load Forecasting Methods," *Global Energy Interconnection*, vol. 5, no. 1, pp. 9–30, 2022.
- [14] G. Chen, and Z. Ji, "A Review of Solar and Wind Energy Resource Projection Based on the Earth System Model," *Sustainability*, vol. 16, no. 8, 3339, 2024.
- [15] V. Z. Manusov, S. K. Khaldarov, and B. V. Palagushkin, "Short-Term Forecasting of Wind and Solar Power Generation," *Journal of Physics: Conference Series*, vol. 2131, no. 5, 052050, 2021.
- [16] A. Vennila, S. Balambigai, et al., "Predicting Solar and Wind Power Production with the Weather Map Data Approach," *2024 International Conference on Signal Processing, Computation, Electronics, Power and Telecommunication (IconSCEPT)*, pp. 1–6, 2024.
- [17] V. P. Singh, A. Kumar, C. S. Meena, and N. Dutt, "Understanding Forecasting Models for Renewable Energy Generation and Market Operation," *Forecasting Methods for Renewable Power Generation*, pp. 95–130, 2025.
- [18] M. Abdul Baseer, A. Almunif, I. Alsaduni, and N. Tazeen, "Electrical Power Generation Forecasting from Renewable Energy Systems Using Artificial Intelligence Techniques," *Energies*, vol. 16, no. 18, 6414, 2023.
- [19] N. E. Benti, M. D. Chaka, and A. G. Semie, "Forecasting Renewable Energy Generation with Machine Learning and Deep Learning: Current Advances and Future Prospects," *Sustainability*, vol. 15, no. 9, 7087, 2023.
- [20] B. N. Rao, M. Praveen, and D. R. Babu, "A Review on the Role of AI in Optimizing Renewable Energy Grid Management," *International Journal of Scientific Research in Engineering and Management*, vol. 8, no. 11, pp. 1–13, 2024.
- [21] L. A. Yousef, H. Yousef, and L. Rocha-Meneses, "Artificial Intelligence for Management of Variable Renewable Energy Systems: A Review of Current Status and Future Directions," *Energies*, vol. 16, no. 24, 8057, 2023.
- [22] D. Y. Goswami, *Principles of Solar Engineering*, CRC Press, 2022.
- [23] J. A. Duffie, W. A. Beckman, and N. Blair, *Solar Engineering of Thermal Processes, Photovoltaics and Wind*, John Wiley & Sons, 2020.
- [24] J. F. Manwell, J. G. McGowan, and A. L. Rogers, *Wind Energy Explained: Theory, Design and Application*, John Wiley & Sons, 2010.
- [25] R. D. Zucker and O. Biblarz, *Fundamentals of Gas Dynamics*, John Wiley & Sons, 2019.
- [26] J. M. Wallace and P. V. Hobbs, *Atmospheric Science: An Introductory Survey*, Elsevier, 2006.
- [27] C. David Cooper, and F. Chris Alley, "Air Pollution," *Electrical Engineering Handbook*, 2004.
- [28] manaenergypak, "Solar Power Plant Projects,".
- [29] newskypower, "Products,".
- [30] P. P. Deka and J. Weiner, *XGBoost for Regression Predictive Modeling and Time Series Analysis: Learn How to Build, Evaluate, and Deploy Predictive Models with Expert Guidance*, Packt Publishing Ltd, 2024.
- [31] J. Brownlee, *Ensemble Learning Algorithms with Python: Make Better Predictions with Bagging, Boosting, and Stacking*, Machine Learning Mastery, 2021.
- [32] B. Zhang, Y. Zhang, and X. Jiang, "Feature Selection for Global Tropospheric Ozone Prediction Based on the BO-XGBoost-RFE Algorithm," *Scientific Reports*, vol. 12, no. 1, 2022.
- [33] globalsolaratlas, "Map,".

Declaration of competing interest

The authors declare that they have no known competing financial interests or personal relationships that could have appeared to influence the work reported in this paper. The ethical issues, including plagiarism, informed consent, misconduct, data fabrication and/or falsification, double publication and/or submission, redundancy, have been completely observed by the authors.

Bibliography



Mehdi Mohammadian Mehr received a Bachelor's degree in Electrical Engineering, specializing in Power Systems, from Shahid Chamran University of Ahvaz, from 2018 to 2022. He then pursued a Master's degree in Electrical Engineering with a concentration in Power Systems at the same university, from 2022 to 2024. His academic background emphasizes energy systems, particularly in the areas of renewable energy integration, smart grids, and advanced forecasting techniques. His research interests include the application of artificial intelligence in power system optimization, distribution network design and enhancement, electric load forecasting and control, power system reliability and resilience, and the integration of energy storage and renewable energy resources into power grids.

Email: Eng.mohammadianmehr@gmail.com

ORCID: [0009-0003-7270-7849](https://orcid.org/0009-0003-7270-7849)

Contribution Statement: Investigation, Methodology, Software, Roles/Writing - original draft.



Hossein Farzin received the BSc and PhD degrees in Electrical Engineering from Sharif University of Technology, Tehran, Iran, in 2011 and 2016, respectively. He was a postdoctoral researcher at Sharif University of Technology, from 2016 to 2017. He is currently an Associate Professor in the Electrical Engineering Department, Shahid Chamran University of Ahvaz, Ahvaz, Iran. His research interests include microgrids design and optimization, integration of distributed energy resources and electric vehicles in smart grid, and power system reliability and resilience. Dr. Farzin ranked 2nd in Iran's nationwide universities entrance exam in 2007, and is ranked among the world's top 2% most cited researchers in 2021 and 2023. He has authored more than 60 journal and conference papers, and serves as an editor of the *Scientia Iranica* journal.

Email: Farzin@scu.ac.ir

ORCID: [0000-0002-4433-1982](https://orcid.org/0000-0002-4433-1982)

Contribution Statement: Supervision, Validation, Writing-review & editing.

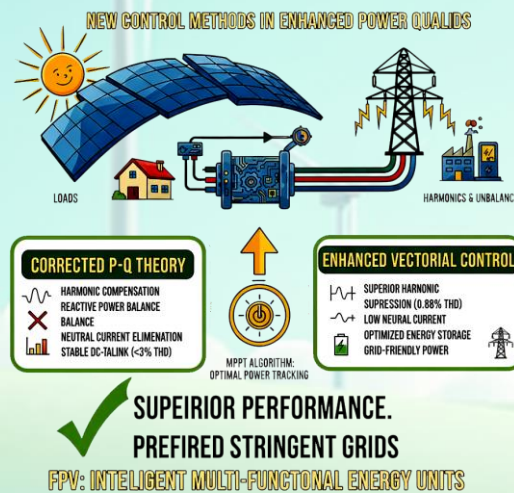
Introducing New Control Methods to Apply in Flexible Photovoltaic Systems at the 3-Phase 4-Wire Grids

Saeid Khani, Leila Mohammadian

Highlights

- ❖ Presents a corrected p-q control strategy for PV systems in unbalanced, distorted 3-phase 4-wire grids.
- ❖ Combines PV with active power filtering to function as a flexible photovoltaic (FPV) system.
- ❖ Proposes enhanced vectorial control to mitigate harmonics, voltage unbalance, and reactive power.
- ❖ Ensures dynamic adaptability to disturbances while maintaining optimal MPPT power extraction.
- ❖ Integrates flexible distributed generation (FDG) models for multi-purpose grid stabilization.

Graphical Abstract



Use your device to scan
and read the article
online



Citation

S. Khani, and L. Mohammadian, "Introducing New Control Methods to Apply in Flexible Photovoltaic Systems at the 3-Phase 4-Wire Grids," *Journal of Green Energy Research and Innovation*, vol. 2, no. 4, pp. 27-44, 2025.



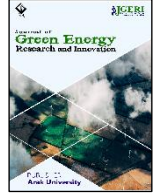
<https://doi.org/10.61882/jgeri.2.4.27>





Online ISSN: 3041-9018

Journal of Green Energy Research and Innovation

Journal Homepage: www.jgeri.araku.ac.ir

Introducing New Control Methods to Apply in Flexible Photovoltaic Systems at the 3-Phase 4-Wire Grids

Saeid Khani¹, Leila Mohammadian^{2,*}

¹ East Azarbaijan Electric Power Distribution Company, Tabriz, Iran.

² Department of Electrical Engineering, Shab.C., Islamic Azad University, Shabestar, Iran.

ARTICLE INFO

Keywords:

Active Filter,
Corrected P-Q Theory,
Enhanced Vectorial Theory,
Flexible Photovoltaic System.

Article History:

Received: 15 April 2025;

Revised: 25 May 2025;

Accepted: 30 June 2025.

Article type:

Research Article

* Corresponding authors

E-mail address

Le.mohammadian@iau.ac.ir (L. Mohammadian)

ABSTRACT

Integrating photovoltaic (PV) generation with active filtering (AF) in three-phase four-wire distribution networks enhances power quality while maximizing renewable energy utilization. This study presents two advanced control strategies—the corrected p-q theory and the enhanced vectorial control method—to optimize system performance under unbalanced and distorted grid conditions. The corrected p-q strategy ensures harmonic compensation, reactive power balance, and neutral current elimination, stabilizing DC-link voltage with THD levels below 3%. Meanwhile, the enhanced vectorial control approach provides superior harmonic suppression, reducing THD to 0.88% and neutral current RMS to 0.035, while maintaining DC-link voltage at a stable level, optimizing energy storage and power conversion. Both strategies are validated through PSCAD/EMTDC simulations, demonstrating their adaptability in dynamically adjusting PV power injection in response to irradiance and temperature variations. The MPPT algorithm effectively tracks optimal power points, ensuring efficient grid interaction and power stabilization. A comparative analysis confirms the enhanced vectorial control method's advantages in harmonic reduction and reactive power compensation, making it preferable for stringent grid applications while reinforcing the role of PV systems as intelligent multi-functional energy units.

1. Introduction

The global energy demand has increased significantly in recent years, requiring advanced power management strategies to ensure grid stability and efficiency. As of today, approximately 75% of global energy consumption relies on fossil fuels, leading to environmental pollution, climate change, and diminishing natural resources [1]. Given these challenges, renewable energy sources, particularly PV systems, have emerged as sustainable alternatives for electricity generation [2].

However, integrating PV systems into modern power grids presents significant challenges due to power quality issues introduced by nonlinear loads such as industrial converters, rectifiers, and EV chargers, leading to harmonic distortions, excessive reactive power demand, and voltage instability [3]. To address these challenges, Active Power Filters (APFs) have been widely adopted to mitigate harmonic contamination, ensuring IEEE-519 standard compliance [4]. Nonetheless, standalone APFs require additional infrastructure investment, limiting their implementation in large-scale power networks [5].

Flexible Photovoltaic (FPV) systems provide an innovative solution by merging PV generation with active filtering capabilities, thereby improving power quality while maintaining energy efficiency. Several studies have explored methods for optimizing FPV systems: Reference [6] investigated the impact of harmonic pollution in distributed networks, proposing optimal capacitor placement to enhance voltage stability and reactive power compensation. Reference [7] explored hybrid AC/DC microgrid architectures, introducing collaborative control mechanisms for harmonic suppression and improved voltage regulation. Authors of [8] proposed a multi-functional PV inverter designed to enhance grid resilience by compensating reactive power and balancing harmonic distortions.

Literature [9] applied machine learning-based controllers to optimize harmonic mitigation and voltage stability, reinforcing the adaptability of PV systems in smart grids. Reference [10] developed fuzzy logic controllers to improve active harmonic filtering, ensuring PV systems remain efficient in dynamically changing grid environments. Paper [11] designed a universal PV-integrated active filter, demonstrating its capability to enhance energy management and grid stability under various operational conditions. Paper [12] investigated smart inverter control methods, emphasizing the need for coordinated reactive power control to prevent voltage violations. Reference [13] studied fault detection and diagnosis techniques for grid-connected PV systems, particularly under irradiance variations, providing insights into stabilizing PV performance under diverse environmental conditions. Paper [14] examined the integration of distributed PV sources into smart grids, offering a comprehensive analysis of the challenges associated with network reliability and operational efficiency. Authors of [15] reviewed vectorial control applications for PV-AF systems, highlighting their advantages in load compensation and harmonic suppression under unbalanced and distorted supply voltages. Reference [16] conducted a broad literature review of control techniques in PV systems, reinforcing the importance of adaptive algorithms for MPPT optimization and power regulation. Literature [17] explored advanced flexible control technologies, showcasing their role in improving PV energy storage integration and network stabilization. Reference [18] investigated emerging trends in grid-connected PV systems, particularly for ancillary services and real-time voltage control strategies. Literature [19] compared harmonic analysis methods for high-voltage vs. medium-voltage PV integration, highlighting their effects on overall system efficiency and stability. Paper [20] introduced a meta-heuristic algorithm-based hybrid power filter, optimizing power flow regulation for improved harmonic compensation in smart grids. Paper [21] discussed grid-friendly power control mechanisms, presenting an adaptive approach for smart PV system operation and voltage control in distributed networks. Despite these technological advancements, FPV systems still face two major challenges that must be addressed:

Maximum Power Point Tracking (MPPT): Maintaining optimal energy extraction under fluctuating irradiance and dynamic load variations.

Reference Current Calculation in Three-Phase Four-Wire Systems: Ensuring accurate harmonic suppression and neutral current elimination, especially under non-sinusoidal and unbalanced supply conditions.

To address these challenges, this study presents two advanced control strategies tailored for FPV systems operating as both an active filter and a power source:

Corrected p-q Theory: An improved formulation of instantaneous power theory, allowing harmonic compensation, reactive power regulation, and DC-link voltage stabilization while ensuring adaptability in PV power injection.

Enhanced Vectorial Control: A grid-compatible compensation technique that ensures balanced sinusoidal source currents, null reactive power, and neutral current suppression, while maintaining high power quality and stable DC-link voltage.

The remainder of this paper is structured as follows:

Section 2 provides a detailed FPV system architecture description, introducing the corrected p-q control strategy.

Section 3 presents the enhanced vectorial control methodology, discussing its theoretical foundation, and reports PSCAD/EMTDC simulation results, assessing system performance under diverse operational scenarios.

Section 4 compares the two control strategies, focusing on harmonic suppression, MPPT efficiency, power regulation, and neutral current elimination, and finally, a comparison between the proposed control methods with other methods in the referenced literature is confirmed.

Section 5 concludes the study, discussing key findings, practical implications, and future research directions.

A graphical abstract summarizing the research workflow, key objectives, and contributions is provided in [Figure 1](#).

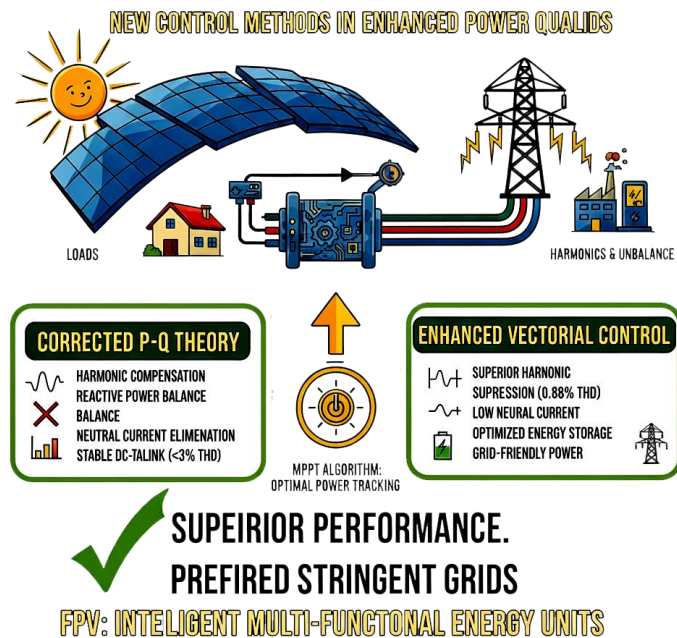


Figure 1. Graphical abstract.

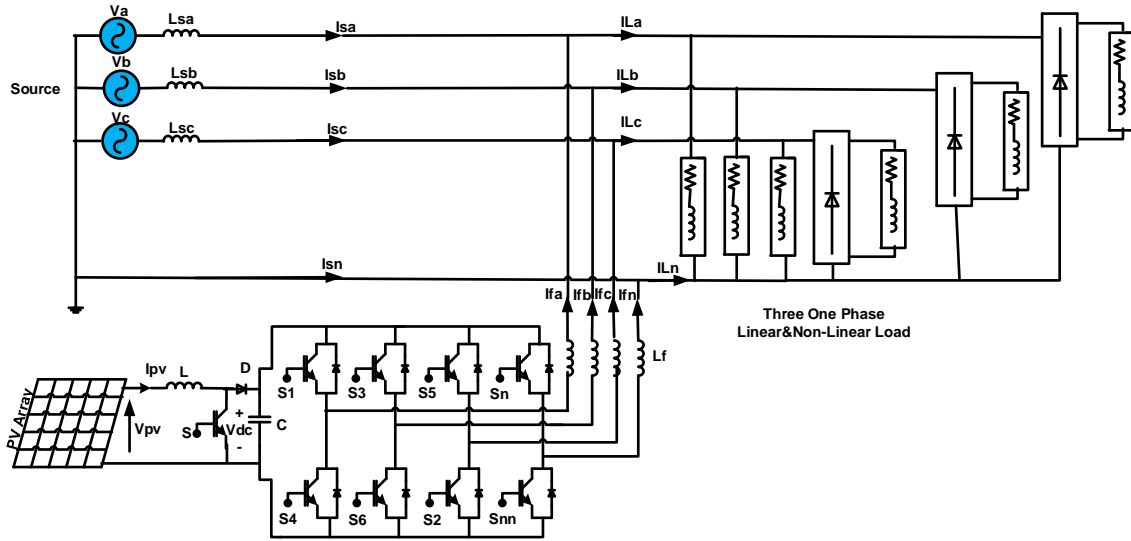


Figure 2. Structure of the FPV system.

2. System Description and the Proposed Corrected p-q Control Strategy

As shown in Figure 2, the FPV system comprises a PV array, a boost converter, and a three-phase four-leg inverter connected to an unbalanced and distorted utility grid. This grid supplies three single-phase linear and nonlinear unbalanced loads. The FPV system employs a corrected p-q control strategy and a simplified MPPT method to inject the maximum available power from the PV array into the grid while compensating for imbalances.

The FPV system uses a three-phase, four-leg inverter to deal with issues such as phase imbalance, harmonic distortion in the load current, reactive power demand, and neutral-line current. An additional DC-DC boost stage performs MPPT. When solar production is low and the PV array cannot deliver the required active power, the AC grid supplies the load directly, while the PV unit contributes only the compensating current needed to cancel the unwanted components created by the nonlinear three-phase load. Under normal conditions, the PV subsystem provides the bulk of the active power for both the load and the grid, allowing the system to operate similarly to a UPS.

A modified p-q approach is used to design the control scheme. This framework regulates the switching pulses for both the boost converter and the inverter based on measurements of the line currents (I_{La} , I_{Lb} , I_{Lc}), phase voltages (u_a , u_b , u_c), dc link voltage (V_{dc}), current and voltage of PV system (I_{pv} , V_{pv}).

2.1. The Proposed Corrected p-q Control Theory

The instantaneous reactive power theory was introduced in the early 1980s as an effective control strategy for mitigating the impact of three-phase nonlinear loads using an APF. The initial p-q theory was developed for three-phase three-wire systems, assuming balanced and sinusoidal supply voltages. The fundamental principle of this theory is based on coordinate transformation, converting the phase reference system into the 0- α - β reference frame, thereby facilitating the separation of active and reactive power components for precise control and compensation [13,14].

Throughout this paper, the following notational conventions are adopted:

- Lowercase variables represent instantaneous values.
- Uppercase variables denote average values (steady-state components).
- Lowercase variables with a tilde (\sim) indicate oscillatory components.
- Subscript 'L' refers to load requirements.
- Subscript 'C' corresponds to compensator supply (APF output).
- Subscript 'S' designates source supply (grid-side power).

$$\vec{u} = [u_a \quad u_b \quad u_c]^t \tag{1}$$

$$\vec{i}_L = [i_{La} \quad i_{Lb} \quad i_{Lc}]^t \tag{2}$$

The Clarke transformation (also known as the α - β transformation) is used to convert three-phase system voltages and currents from the a-b-c reference frame (given in Equations (1) and (2)) to the 0- α - β reference frame, facilitating analysis and control in instantaneous power theory and harmonic compensation applications. The transformation equations are defined as Equations (3) and (4).

$$\begin{bmatrix} e_0 \\ e_\alpha \\ e_\beta \end{bmatrix} = \sqrt{\frac{2}{3}} \begin{bmatrix} \frac{1}{\sqrt{2}} & \frac{1}{\sqrt{2}} & \frac{1}{\sqrt{2}} \\ 1 & -\frac{1}{2} & -\frac{1}{2} \\ 0 & \frac{\sqrt{3}}{2} & -\frac{\sqrt{3}}{2} \end{bmatrix} \begin{bmatrix} u_a \\ u_b \\ u_c \end{bmatrix} \tag{3}$$

$$\begin{bmatrix} i_{L0} \\ i_{L\alpha} \\ i_{L\beta} \end{bmatrix} = \sqrt{\frac{2}{3}} \begin{bmatrix} \frac{1}{\sqrt{2}} & \frac{1}{\sqrt{2}} & \frac{1}{\sqrt{2}} \\ 1 & -\frac{1}{2} & -\frac{1}{2} \\ 0 & \frac{\sqrt{3}}{2} & -\frac{\sqrt{3}}{2} \end{bmatrix} \begin{bmatrix} i_{La} \\ i_{Lb} \\ i_{Lc} \end{bmatrix} \tag{4}$$

In the transformed 0- α - β coordinate system, the various power terms associated with the load can be defined based on the instantaneous p-q theory. These terms distinguish between active, reactive, and oscillatory power components, enabling precise control and compensation in three-phase four-wire systems (refer to Equation (5)).

$$p_{L0}(t) = e_0 i_{L0} = p_{L0} + \bar{P}_{L0}$$

$$p_{L\alpha\beta}(t) = \begin{bmatrix} e_\alpha & e_\beta \end{bmatrix} \begin{bmatrix} i_{L\alpha} \\ i_{L\beta} \end{bmatrix} = p_{L\alpha\beta} + \bar{P}_{L\alpha\beta} \tag{5}$$

$$\bar{q}_{L\alpha\beta}(t) = \begin{bmatrix} e_\alpha & e_\beta \end{bmatrix}^T \times \begin{bmatrix} i_{L\alpha} & i_{L\beta} \end{bmatrix}^T$$

In the vectorial representation of the instantaneous p-q theory, the voltage space vectors can be defined to enhance power control analysis. The three voltage space vectors are given by Equation (6) and are shown in Figure 3.

$$\bar{e}_0 = \begin{bmatrix} e_0 \\ 0 \\ 0 \end{bmatrix}, \bar{e}_{\alpha\beta} = \begin{bmatrix} 0 \\ e_\alpha \\ e_\beta \end{bmatrix}, \bar{e}_{-\beta\alpha} = \begin{bmatrix} 0 \\ -e_\beta \\ e_\alpha \end{bmatrix} \tag{6}$$

In the 0- α - β reference frame, the load current vector can be expressed using Clarke transformation principles. This formulation facilitates instantaneous power analysis and harmonic compensation in three-phase systems. The vector representation is given by Equation (7):

$$\bar{i}_L = \frac{p_{L\alpha\beta}(t)}{e_{\alpha\beta}^2} \bar{e}_{\alpha\beta} + \frac{p_{L0}(t)}{e_0^2} \bar{e}_0 + \frac{q_{L\alpha\beta}(t)}{e_{\alpha\beta}^2} \bar{e}_{-\beta\alpha} \tag{7}$$

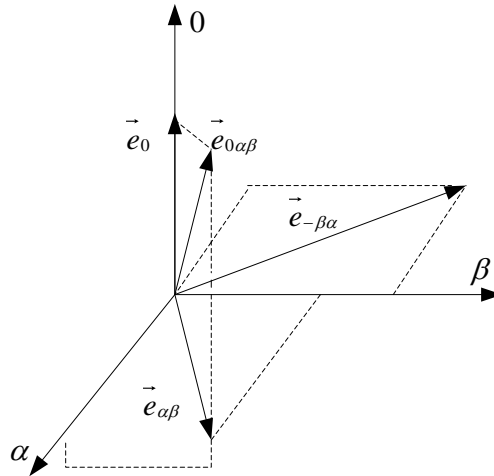


Figure 3. New voltage vectors in 0- α - β coordinates system.

In the sinusoidal source current compensation objective of p-q theory, the goal is to achieve a sinusoidal and balanced source current, ensuring it remains in phase with the supply voltage under ideal conditions. When the voltage is sinusoidal and balanced, the source current aligns precisely with it. However, in cases where the voltage exhibits distortions or unbalanced components, the source current must still align with the positive-sequence fundamental element of the voltage to maintain grid stability. This condition must be satisfied regardless of supply voltage variations and load characteristics, ensuring adequate compensation across different operating scenarios. Consequently, after implementing harmonic mitigation and reactive power compensation, the source current can be mathematically represented as Equation (8):

$$\vec{i}_S = G_e \vec{e}_{\alpha\beta 1}^{++} \quad (8)$$

The instantaneous power balance in a system involving a source, load, and compensator can be expressed as Equation (9):

$$p_C(t) = p_L(t) - p_S(t) \quad (9)$$

Then, substituting Equation (8) in Equation (9), Equation (10) is given:

$$p_C(t) = p_L(t) - \vec{e}_{\alpha\beta} \vec{G}_e \vec{e}_{\alpha\beta 1}^{++} \quad (10)$$

In the conventional p-q theory, the compensator's average power is considered zero. However, in the corrected p-q theory, a nonzero compensator power, $P_{PV} - P_{cap}$, is introduced to ensure DC-link voltage stability at its reference value while simultaneously enabling PV power injection into the grid. Consequently, the proportionality constant is derived as Equation (11).

$$\frac{1}{T} \int_T p_C(t) dt = \frac{1}{T} \int_T p_L(t) dt - \frac{1}{T} \int_T \vec{e}_{\alpha\beta} \vec{G}_e \vec{e}_{\alpha\beta 1}^{++} dt = P_{PV} - P_{cap} \quad (11)$$

$$\frac{1}{T} \int_T p_L(t) dt - P_{PV} + P_{cap} = \frac{1}{T} \int_T \vec{e}_{\alpha\beta} \vec{G}_e \vec{e}_{\alpha\beta 1}^{++} dt$$

$$G_e = \frac{\overline{P_{La\beta}} - P_{PV} + P_{cap}}{E_1^{+2}}$$

Where E_1^{+2} represents the square of the RMS value of the positive-sequence fundamental component of the voltage. This term is crucial in determining the proportionality constant required for ensuring DC-link voltage regulation and simultaneous PV power injection into the grid, as established in the corrected p-q theory formulation (refer to Equation (12)).

$$E_1^{+2} = \frac{1}{T} \int (e_{\alpha 1}^{+2} + e_{\beta 1}^{+2}) dt \quad (12)$$

Hence, after compensation, the source's current expression will be as Equation (13):

$$\vec{i}_S = \frac{\overline{P_{La\beta}} - P_{PV} + P_{cap}}{E_1^{+2}} \vec{e}_{\alpha\beta 1}^{++} \quad (13)$$

Thus, from Equations (7) and (13), the compensation current is calculated as Equation (14).

$$\begin{aligned} \vec{i}_C = \vec{i}_L - \vec{i}_S &= \frac{p_{La\beta}(t)}{e_{\alpha\beta}^2} \vec{e}_{\alpha\beta} + \frac{p_{L0}(t)}{e_0^2} \vec{e}_0 + \frac{q_{La\beta}(t)}{e_{\alpha\beta}^2} \vec{e}_{-\beta\alpha} \\ &- \frac{\overline{P_{La\beta}} - P_{PV} + P_{cap}}{E_1^{+2}} \vec{e}_{\alpha\beta 1}^{++} \end{aligned} \quad (14)$$

Therefore, different power terms of the compensator are defined in Equation (15).

$$\begin{aligned} p_{C0}(t) &= \vec{e}_0 \cdot \vec{i}_C = p_{L0}(t) \\ p_{Ca\beta}(t) &= \vec{e}_{\alpha\beta} \cdot \vec{i}_C = p_{La\beta}(t) - \frac{\overline{P_{La\beta}} - P_{PV} + P_{cap}}{E_1^{+2}} (e_{\alpha} e_{\alpha 1}^{+} + e_{\beta} e_{\beta 1}^{+}) \\ q_{Ca\beta}(t) &= \vec{e}_{-\beta\alpha} \cdot \vec{i}_C = q_{La\beta}(t) - \frac{\overline{P_{La\beta}} - P_{PV} + P_{cap}}{E_1^{+2}} (e_{\alpha} e_{\beta 1}^{+} - e_{\beta} e_{\alpha 1}^{+}) \end{aligned} \quad (15)$$

In the mapping matrices format, the control strategy may be expressed as Equation (16).

$$\begin{bmatrix} i_{0,ref} \\ i_{\alpha,ref} \\ i_{\beta,ref} \end{bmatrix} = \frac{1}{e_0 e_{\alpha\beta}^2} \begin{bmatrix} e_{\alpha\beta}^2 & 0 & 0 \\ 0 & e_0 e_{\alpha} & -e_0 e_{\beta} \\ 0 & e_0 e_{\beta} & e_0 e_{\alpha} \end{bmatrix} \times \begin{bmatrix} p_{L0}(t) \\ p_{L\alpha\beta}(t) - \frac{\bar{P}_{L\alpha\beta} - P_{PV} + P_{cap}}{E_1^{+2}} (e_{\alpha} e_{\alpha 1}^+ + e_{\beta} e_{\beta 1}^+) \\ q_{L\alpha\beta}(t) - \frac{\bar{P}_{L\alpha\beta} - P_{PV} + P_{cap}}{E_1^{+2}} (e_{\alpha} e_{\beta 1}^+ - e_{\beta} e_{\alpha 1}^+) \end{bmatrix} \quad (16)$$

Eventually, Equation (17) provides the reference currents in *abcn* reference frame.

$$\begin{bmatrix} i_{a,ref} \\ i_{b,ref} \\ i_{c,ref} \end{bmatrix} = \frac{\sqrt{2}}{3} \begin{bmatrix} \frac{1}{2\sqrt{2}} & 1 & 0 \\ \frac{1}{2\sqrt{2}} & -\frac{1}{2} & \frac{\sqrt{3}}{2} \\ \frac{1}{2\sqrt{2}} & -\frac{1}{2} & -\frac{\sqrt{3}}{2} \end{bmatrix} \begin{bmatrix} i_{0,ref} \\ i_{\alpha,ref} \\ i_{\beta,ref} \end{bmatrix} \quad (17)$$

$$i_{n,ref} = i_{a,ref} + i_{b,ref} + i_{c,ref}$$

These reference currents enable the PV array to deliver its maximum extractable power to the grid while simultaneously correcting current imbalance, suppressing load-current harmonics, supplying the load’s reactive power requirement, and canceling the neutral-line current.

2.2. MPPT Control Theory

The PV array power curve exhibits a zero slope at the MPP, a positive slope on the side before the MPP, and a negative slope beyond the MPP, as indicated in Equation (18).

$$\begin{cases} \frac{dP}{dV} = 0 & \text{at MPP} \\ \frac{dP}{dV} > 0 & \text{left of MPP} \\ \frac{dP}{dV} < 0 & \text{right of MPP} \end{cases} \quad (18)$$

A straightforward proportional-integral (PI) controller can be used to maintain $dP/dV = 0$. The PI controller’s output determines the duty cycle (*D*) of the boost converter. The block diagram illustrating this approach is presented in Figure 4. Using Equations (17) and (18) as a basis, the proposed control scheme is developed and depicted in Figure 5.

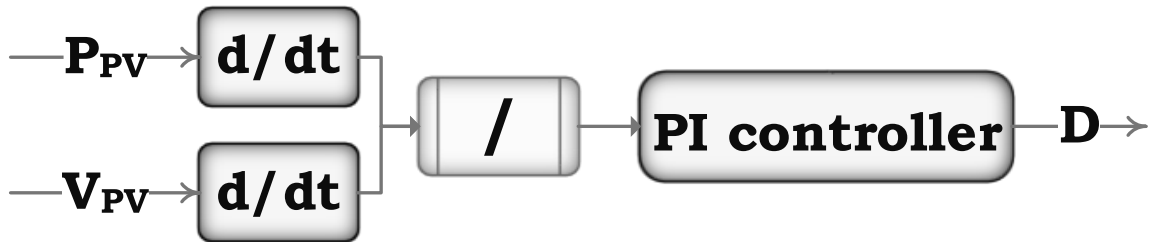


Figure 4. A simple MPPT algorithm.

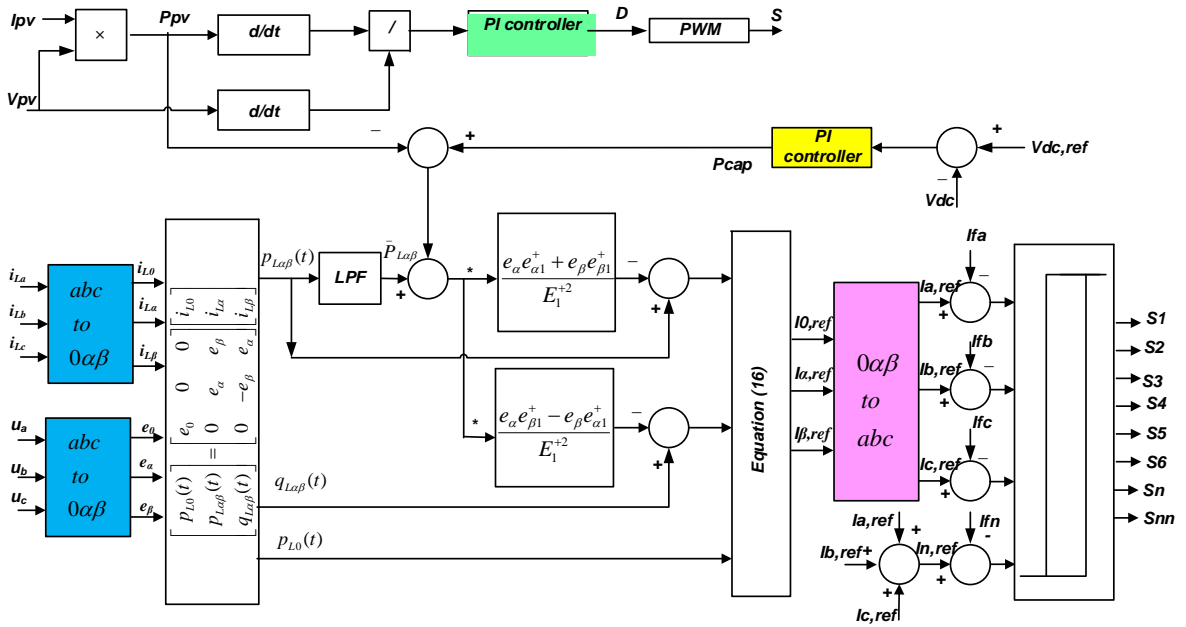


Figure 5. Block diagram of the system controller.

2.3. Simulation Report of the Suggested Corrected p-q Control Strategy

To validate the proposed corrected p-q control strategy for the FPV system connected to a three-phase four-wire network, a detailed simulation study was performed using PSCAD/EMTDC software. To assess the system’s response to variations in PV power, three operational scenarios were considered, reflecting changes in irradiance and temperature. Figure 6 illustrates these three stages. In the first stage (0–0.1 s), the irradiance is approximately 800 W/m² and the temperature is 40°C. The second stage begins when the temperature drops to 15°C while irradiance remains constant, lasting until 0.175 s. The third stage, from 0.175 s to 0.25 s, assumes irradiance falls to 0 W/m², temperature remains steady, and the FPV real power output is zero.

Figure 7(a) shows the supply voltages in all scenarios, given by:

- $U_a = 254.55\sin(2\pi \cdot 60t) + 25.45\sin(2\pi \cdot 300t) + 17.67\sin(2\pi \cdot 420t)$
- $U_b = 311.5\sin(2\pi \cdot 60t - 120^\circ) + 31.1\sin(2\pi \cdot 300t + 120^\circ) + 21.21\sin(2\pi \cdot 420t - 120^\circ)$
- $U_c = 353.55\sin(2\pi \cdot 60t + 120^\circ) + 35.35\sin(2\pi \cdot 300t - 120^\circ) + 24\sin(2\pi \cdot 420t + 120^\circ)$

The neutral line current and load currents are depicted in Figure 7(b). Table 1 lists the power system parameters applied in the simulations.

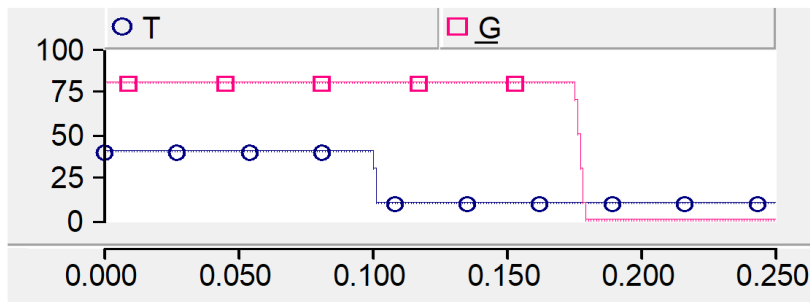


Figure 6. Diagram of variation in light intensity and temperature.

Table 1. Simulation Parameters.

| | |
|------------------------|--------------------------------|
| $L_f = 10$ mH | $V_{LL,rms} = 380$ v |
| $L_{dc} = 26$ mH | $f_s = 60$ Hz |
| $C_{dc} = 650$ μ F | $V_{dc,ref} = 800$ v |
| $f_{boost} = 3500$ Hz | Linear balanced and unbalanced |
| | load = 1.5 kW, 2 kVAR |

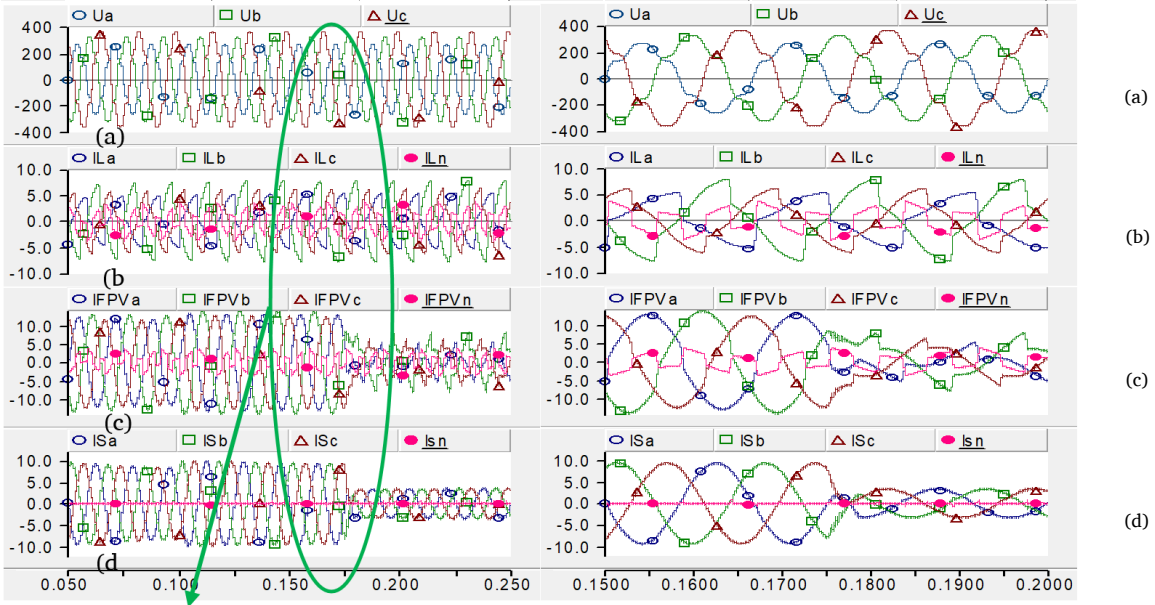


Figure 7. Simulation results: (a) Grid Voltage, (b) unbalanced load currents, (c) FPV currents, (d) Grid Currents.

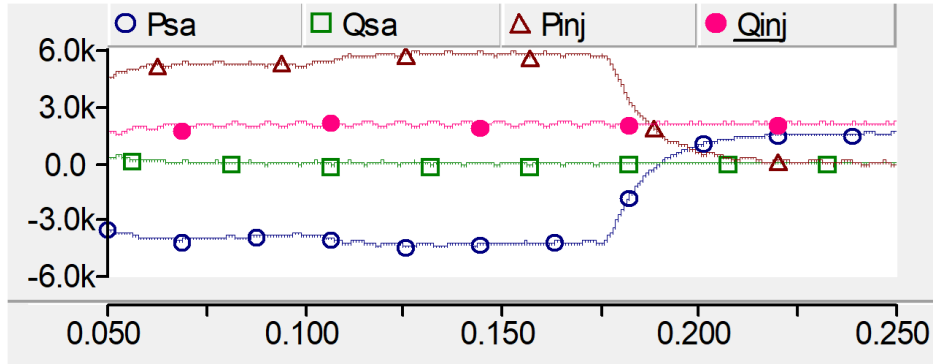


Figure 8. The Source and FPV active and reactive injected power.

Table 2. THD Values.

| THD(%) | i_{sa} | i_{sb} | i_{sc} |
|--|----------|----------|----------|
| Before compensation | 30.3 | 20.52 | 16.73 |
| After compensation ($P_{inj} = 0 \text{ kw}$) | 3 | 2.45 | 2.81 |
| After compensation ($P_{inj} = 5 \text{ kw}$) | 1.16 | 1.26 | 1.3 |
| After compensation ($P_{inj} = 5.8 \text{ kw}$) | 1.1 | 1.21 | 1 |

Figure 7 presents the simulation outcomes for the three operational stages, demonstrating the FPV system’s capability to operate simultaneously as an active power filter (APF) and a power supplier, or solely as an APF, under unbalanced and non-sinusoidal voltage conditions. The green circle highlights the moment when grid disturbances occur, with a zoomed-in view on the right side of the figure to clearly depict these disturbances. As shown in Figure 7(d), the FPV system effectively compensates for current unbalance, load current harmonics, load reactive power, and neutral line current. Across all stages, the total harmonic distortion (THD) remains below 3%, and the RMS value of the neutral current is 0.09 A. Detailed THD values for source currents under all scenarios are provided in Table 2. Figure 8 displays the active and reactive power injected by both the source and the FPV system, indicating that the PV array supplies the entire reactive power demanded by the load.

Moreover, Figure 9 illustrates the DC-link voltage of the capacitor for these three stages. As illustrated, the capacitor voltage is stabilized at 800V, which is approximately twice the magnitude of the line voltage (380V), ensuring efficient energy management and system performance.

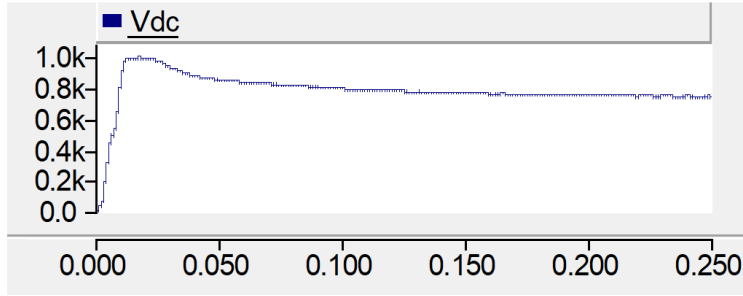


Figure 9. The DC-Link Voltage.

2.4. Results Analysis of the Proposed Corrected p-q Control Theory

In the previous section, the corrected p-q control theory was applied to a Flexible Photovoltaic (FPV) system integrated into a three-phase four-wire distribution grid, accounting for both unbalanced linear and nonlinear loads, as well as a distorted and unbalanced voltage supply. Applying this control strategy compensates for current unbalance, suppression of load current harmonics, fulfillment of reactive power demand, and neutral current mitigation. Consequently, the source current became balanced and sinusoidal, with a unity power factor achieved under all operational conditions. Simulation results illustrate the performance of the FPV system across various PV operational conditions. During the first two stages, the FPV system injects real power generated from the PV array into the grid and functions as an APF, ensuring enhanced power quality. In the third stage, the FPV system operates solely as an APF, with no power injection from the PV source. Across all three operating scenarios, PV power injection is different, and the THD is calculated for each condition.

The results demonstrate that the proposed control strategy effectively compensates for current unbalance, suppresses load current harmonics, meets reactive power demand, and eliminates neutral current fluctuations, reinforcing its applicability for power quality enhancement in renewable energy-integrated distribution networks.

3. System Description and the Proposed Enhanced Vectorial Control Strategy

3.1. System Description

The circuit block diagram of the grid-connected PV system is shown in Figure 10. As shown in the figure, the whole 4-wire system is composed of a PV array, a Boost converter, a three-phase inverter, a three-phase balanced, linear, and non-linear load, and the unbalanced and harmonic utility grid. The proposed scheme employs a vectorial theory-controlled three-phase 4-leg inverter to perform reactive power compensation, harmonic elimination, and to inject the maximum power of the PV array into the grid. A DC/DC voltage boost converter is used to address the MPPT. Under poor generation conditions of the PV system, the AC source supplies the active power to the load directly, and the PV system only injects the compensating current to eliminate the undesired current components generated by a three-phase nonlinear load. In the normal mode, the PV system mainly provides active power to the load and utility; in other words, it acts as an uninterruptible power supply. The vectorial theory is applied to design the control system, which provides pulse gates of the Boost switches and inverter switches by measuring the line currents (I_{La} , I_{Lb} , I_{Lc}), phase voltages (V_a , V_b , V_c), dc link voltage (V_{dc}), current and voltage of the PV system (I_{pv} , V_{pv}).

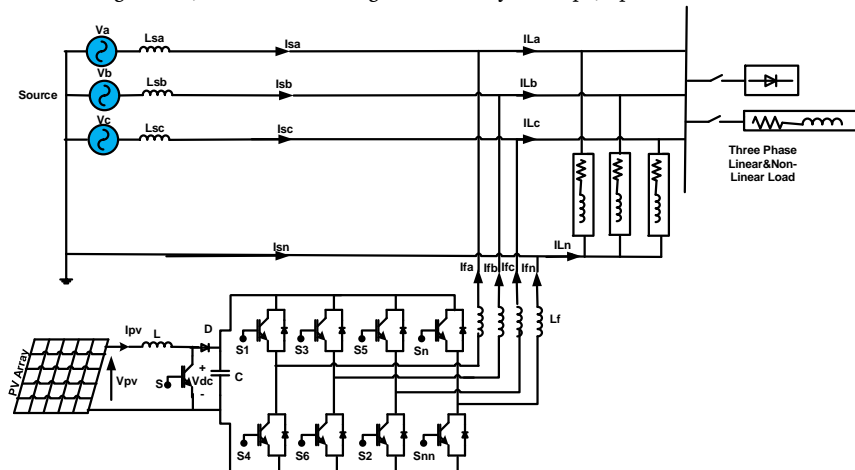


Figure 10. The whole structure of the three-phase 4-wire grid-connected PV power system.

3.2. The Proposed Enhanced Vectorial Control Strategy

In the early 1980s, the instantaneous reactive power theory was developed to provide an effective control approach for compensating three-phase nonlinear loads via APFs [11]. Its original form, the p-q theory, was intended for three-phase, three-wire nonlinear systems under balanced conditions with sinusoidal voltage sources. This strategy successfully ensured that, after compensation, the source currents remained sinusoidal and closely followed the supply voltage waveform. Over the years, various modifications and alternative formulations have been proposed, enhancing and refining the original p-q theory. These include:

- The Park transformation (d-q coordinates),
- The corrected or cross-product theory,
- The p-q-r theory, a novel extension of the original approach,
- The vectorial theory offers an advanced perspective on power compensation.

In the following section, an enhanced vectorial theory, applied to achieve the stated control objectives, is explored in detail.

Voltage and current phase vectors are represented by Equations (19) and (20).

$$\vec{u} = \begin{bmatrix} u_a & u_b & u_c \end{bmatrix}^t \quad (19)$$

$$\vec{i} = \begin{bmatrix} i_a & i_b & i_c \end{bmatrix}^t \quad (20)$$

The zero-sequence phase voltage vector is defined as Equation (21).

$$\vec{v}_0 = \begin{bmatrix} v_0 & v_0 & v_0 \end{bmatrix}^t$$

$$v_0 = \frac{u_a + u_b + u_c}{3} \quad (21)$$

Thus, the voltage vector \vec{v} is provided as Equation (22).

$$\vec{v} = \vec{u} - \vec{v}_0 \quad (22)$$

Unlike the other formulations discussed, the vectorial theory does not require any coordinate transformations. It retains the original power variables to define instantaneous active power without the zero-sequence component $p(t)$, instantaneous zero-sequence power $p_0(t)$, and instantaneous imaginary power $q(t)$ directly in the phase coordinates, as expressed in Equations (23)–(25).

$$p(t) = \vec{v} \cdot \vec{i} = v_a i_a + v_b i_b + v_c i_c \quad (23)$$

$$p_0(t) = \vec{v}_0 \cdot \vec{i} = v_0 i_a + v_0 i_b + v_0 i_c \quad (24)$$

$$\vec{q}(t) = \vec{v} \times \vec{i} = \begin{bmatrix} v_a \\ v_b \\ v_c \end{bmatrix} \times \begin{bmatrix} i_a \\ i_b \\ i_c \end{bmatrix} = \begin{bmatrix} v_a i_c - v_c i_b \\ v_c i_a - v_a i_c \\ v_a i_b - v_b i_a \end{bmatrix} \quad (25)$$

Equation (26) determines the currents concerning the three power variables.

$$\begin{bmatrix} i_a \\ i_b \\ i_c \end{bmatrix} = \frac{P}{v^2} \begin{bmatrix} v_a \\ v_b \\ v_c \end{bmatrix} + \frac{P_0}{v_0^2} \begin{bmatrix} v_0 \\ v_0 \\ v_0 \end{bmatrix} + \frac{1}{\sqrt{3}} \frac{|\vec{q}(t)|}{v^2} \begin{bmatrix} v_b - v_c \\ v_c - v_a \\ v_a - v_b \end{bmatrix} \quad (26)$$

Considering the constant source power as a compensation objective and unbalanced and non-sinusoidal supply voltage, the compensation current in vectorial theory is achieved as Equation (27).

$$\begin{bmatrix} i_{ca} \\ i_{cb} \\ i_{cc} \end{bmatrix} = \begin{bmatrix} i_{La} \\ i_{Lb} \\ i_{Lc} \end{bmatrix} - \frac{P_{Lu}}{U_1^{+2}} \begin{bmatrix} u_{a1}^+ \\ u_{b1}^+ \\ u_{c1}^+ \end{bmatrix} \quad (27)$$

u_{a1}^+ , u_{b1}^+ and u_{c1}^+ are the voltage-positive sequence fundamental components of each phase, and U_1^{+2} show the RMS value of the voltage's positive sequence fundamental component as given by Equation (28).

$$U_1^{+2} = \frac{1}{T} \int_T (u_{a1}^{+2} + u_{b1}^{+2} + u_{c1}^{+2}) dt \tag{28}$$

Moreover, P_{Lu} is time average value of the load's instantaneous real power as defined by Equation (29).

$$p_{Lu}(t) = \vec{u} \cdot \vec{i} = u_a i_a + u_b i_b + u_c i_c = p_{Lu} + P_{Lu} \tag{29}$$

To enable injection of instantaneous PV power, a DC term P_{pv} is incorporated into Equation (9). Similarly, an additional term P_{cap} is included to control the capacitor voltage [10]. Consequently, the overall reference currents are determined as shown in Equation (30).

$$\begin{bmatrix} i_{a,ref} \\ i_{b,ref} \\ i_{c,ref} \end{bmatrix} = \frac{P_L}{v} \begin{bmatrix} v_a \\ v_b \\ v_c \end{bmatrix} - \frac{P}{U_1^{+2}} \begin{bmatrix} u_{a1}^+ \\ u_{b1}^+ \\ u_{c1}^+ \end{bmatrix} + \frac{P_{L0}}{v} \begin{bmatrix} v_0 \\ v_0 \\ v_0 \end{bmatrix} + \frac{1}{\sqrt{3}} \frac{|q_L|}{v} \begin{bmatrix} v_b - v_c \\ v_c - v_a \\ v_a - v_b \end{bmatrix} \tag{30}$$

$$P = P_{Lu} + P_{cap} - P_{pv}$$

Based on Equation (30), the control system is designed as in Figure 11.

3.3. Simulation Results for the Proposed Enhanced Vectorial Control Strategy

In this section, the simulations for this study were conducted using PSCAD/EMTDC. The FPV model was designed to operate under three distinct environmental conditions:

1. Standard PV operation (800 W/m², 40°C) – tracking optimal MPPT while providing active filtering.
2. Reduced temperature condition (15°C, constant irradiance) – testing adaptability to dynamic conditions.
3. Zero irradiance scenario (0 W/m², constant temperature) – evaluating system performance when PV generation ceases, operating solely as an APF.
4. Key system parameters included:
 - DC-link voltage: 1200V (maintaining stability under load fluctuations).
 - Total Harmonic Distortion (THD): Below 1%, demonstrating compliance with IEEE standards.
 - Compensation Efficiency: Neutral current reduced to 0.035 RMS, proving effective load balancing.

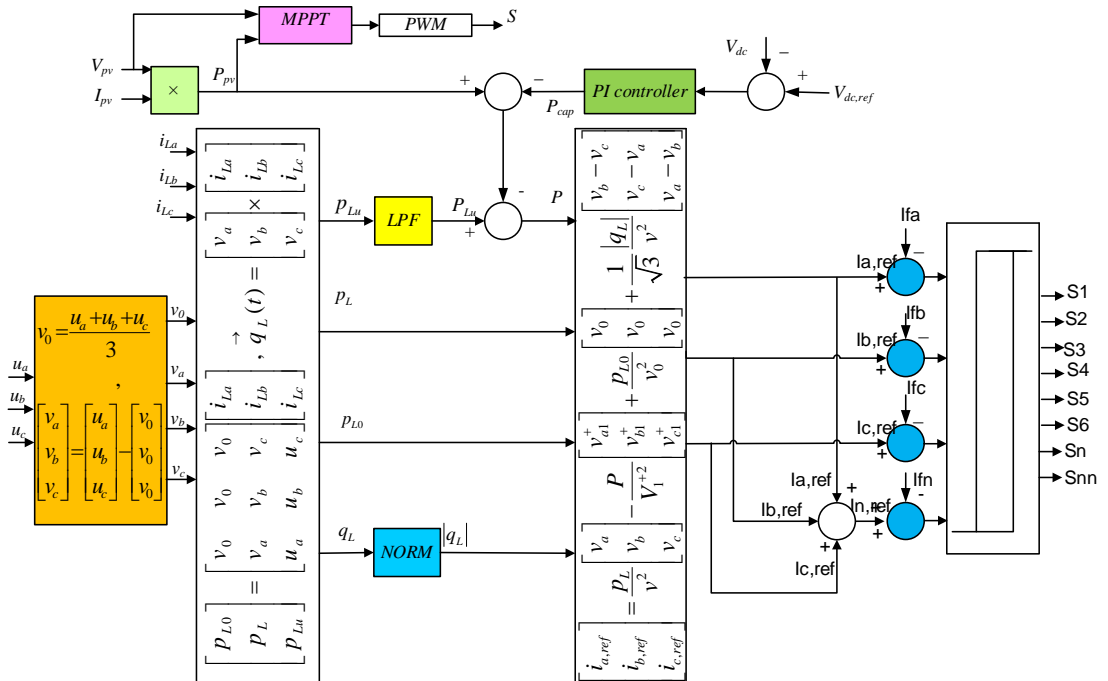


Figure 11. The system controller block diagram based on vectorial theory.

The system was analyzed under four different PV power injection conditions. In the first simulation, the PV system’s injection was neglected, evaluating its operation solely as an active filter under unbalanced and non-sinusoidal voltage supply. In the subsequent simulations, the performance of the proposed system in tracking the PV array’s maximum power point (MPP) while compensating for nonlinear and unbalanced load currents across varying PV conditions was examined. The supply voltages and load currents are as follows (Figures 12 and 13):

- **Ua:** $254.55 \sin(2\pi \times 60t) + 25.45 \sin(2\pi \times 300t) + 17.67 \sin(2\pi \times 420t)$
- **Ub:** $311 \sin(2\pi \times 60t - 120) + 31.1 \sin(2\pi \times 300t + 120) + 21.21 \sin(2\pi \times 420t - 120)$
- **Uc:** $353.55 \sin(2\pi \times 60t + 120) + 35.35 \sin(2\pi \times 300t - 120) + 24 \sin(2\pi \times 420t + 120)$

The resulting neutral line current is illustrated in Figure 13(b). Power system parameters used for the simulations are summarized in Table 3.

Table 3. Parameters of the simulated power system.

| | |
|------------------------------------|---|
| $L_f = 10 \text{ mH}$ | $V_{LL,rms} = 380 \text{ v}$ |
| $C_f = 1 \text{ }\mu\text{F}$ | $f_s = 60 \text{ Hz}$ |
| $L_{dc} = 300 \text{ mH}$ | $V_{dc,ref} = 1200 \text{ v}$ |
| $C_{dc} = 600 \text{ }\mu\text{F}$ | Linear balanced and unbalanced load = 1.7 kW, 1.7 kVAR |
| $f_{boost} = 3500 \text{ Hz}$ | Non-linear load = 14.6 kW, 6 kVAR |

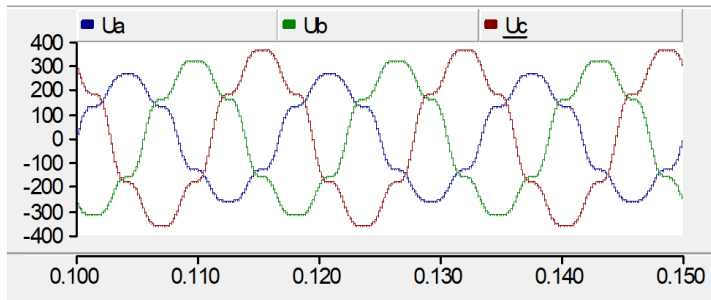
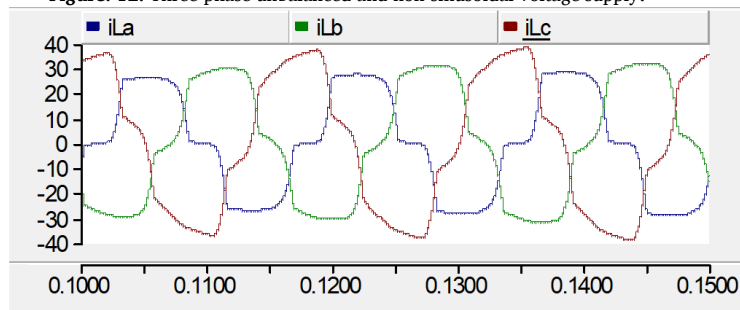
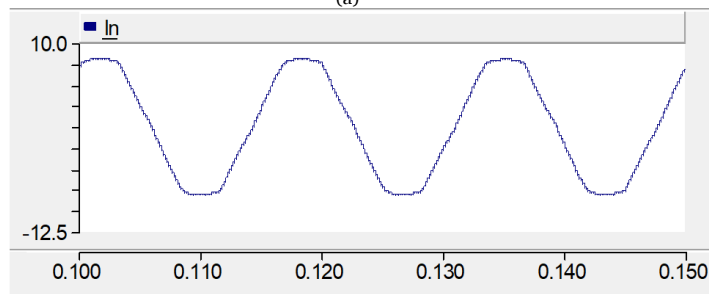


Figure. 12. Three-phase unbalanced and non-sinusoidal voltage supply.



(a)



(b)

Figure 13. (a) Three-phase non-linear and unbalanced load current, (b) neutral current.

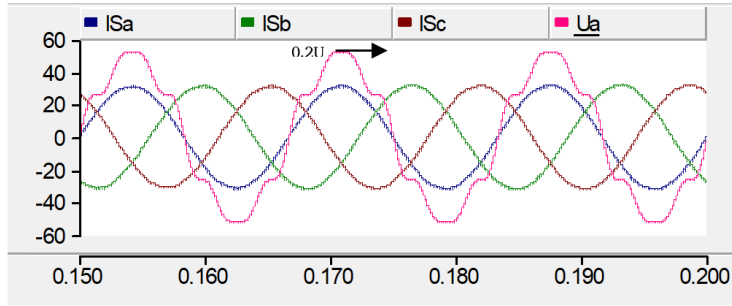


Figure 14. Compensated line currents and voltage of phase a.

3.3.1. PV Compensating Operational Mode without Power Generation

The performance of PV as just AF is described in this section to demonstrate the capability of the proposed system to compensate load current harmonics, eliminate the 4th wire current, and correct the power factor. In this part, no power is injected into the grid. As shown in Figure 14, the line currents drawn from the utility are sinusoidal and balanced. They are in phase with their related voltage. This shows the efficient usage of utility power. The line currents exhibit only high-frequency, low-amplitude harmonic components, ensuring that total harmonic distortion (THD) remains at approximately 0.88%. This indicates that the applied control strategy effectively minimizes harmonic distortions and improves power quality and grid compliance with IEEE standards.

3.3.2. System Performance as both AF and Power Supply

This section of the simulation assesses the system’s response to variations in PV power due to changes in light intensity and temperature. Figure 14 illustrates three distinct stages caused by these variations:

- Stage 1 (0–0.2 sec): Light intensity is approximately 800 W/m², and temperature is around 35 °C.
- Stage 2 (0.2–0.5 sec): Light intensity jumps to 1100 W/m² while temperature remains constant.
- Stage 3 (0.5–0.6 sec): Temperature drops sharply to 10 °C, with light intensity unchanged.

As depicted in Figure 15, the PV array’s P–V curves shift according to these stages, shown in Figure 16(a). The Boost converter’s duty cycle adjusts dynamically to track the maximum power point (MPP) under each condition (Figure 16(b)). Additionally, Figure 16(c) presents the corresponding PV array voltage and current variations throughout the simulation.

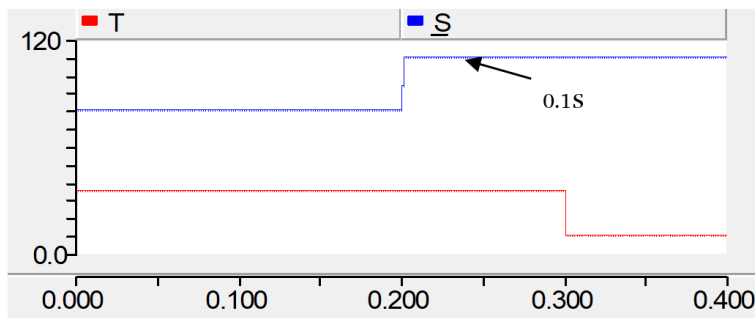
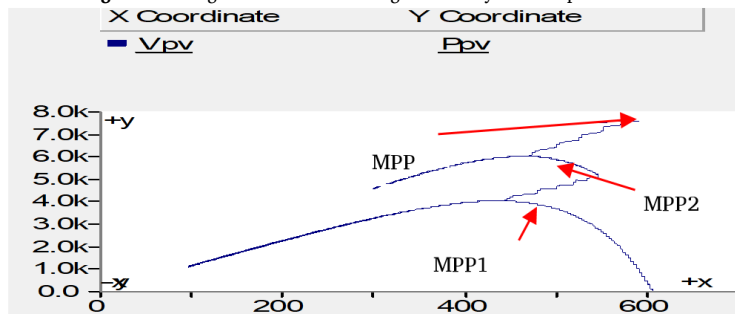


Figure 15. Diagram of variation in light intensity and temperature.



(a)

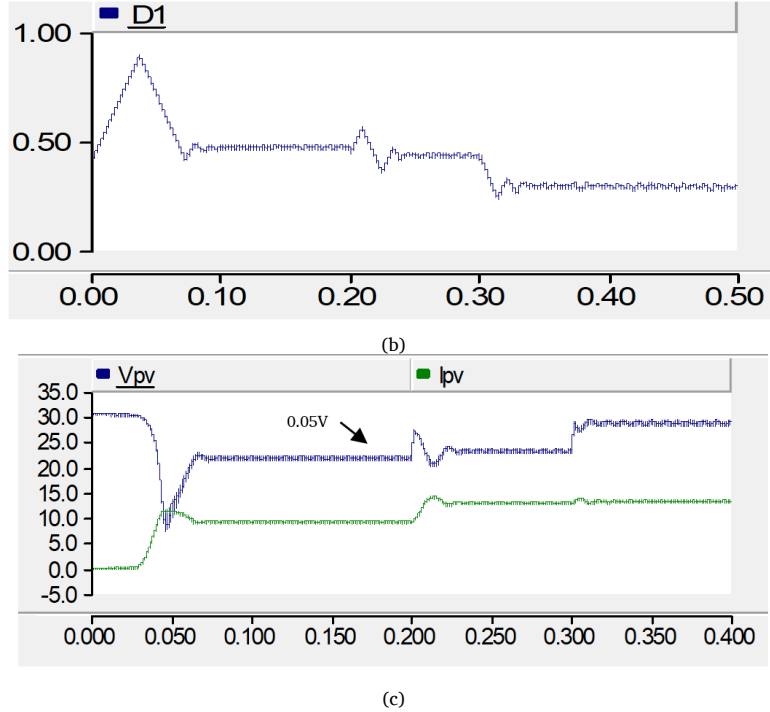


Figure 16. Variations of three stages (a) P-V curves of PV array, (b) duty cycle, (c) Voltage and current PV array.

The simulation outcomes for the three stages, presented in Figure 15, demonstrate that the PV system can operate simultaneously as an AF and a power source under unbalanced and non-sinusoidal voltage conditions. Figure 17 illustrates the active and reactive power injected by both the source and the PV array. The PV array provides the reactive power required by the load and also performs a peak-shaving function: as PV real power injection rises, the power supplied by the main source correspondingly decreases.

As shown in Figure 18, the PV system effectively compensates for load current harmonics across all stages, maintaining THD below 1%. Moreover, it eliminates neutral current, with the RMS value of the neutral line current recorded at 0.035 A (Figure 19). Detailed THD values of the source currents for all cases are summarized in Table 4.

The DC link voltage of the capacitor is shown in Figure 20 for the three stages. The capacitor voltage is precisely maintained at 1200V, corresponding to approximately three times the line voltage (380V). This regulation ensures stable energy storage and effective power conversion, optimizing system performance and operational efficiency.

Table 4. THD values.

| | THD (i_{sa})% | THD (i_{sb})% | THD (i_{sc})% |
|--|-------------------|-------------------|-------------------|
| Before compensation | 21.24 | 15.63 | 14.52 |
| After compensation ($P_{inj} = 0$ kw) | 0.57 | 0.65 | 0.88 |
| After compensation ($P_{inj} = 4$ kw) | 0.76 | 0.66 | 0.7 |
| After compensation ($P_{inj} = 6$ kw) | 0.82 | 0.75 | 0.77 |
| After compensation ($P_{inj} = 7.5$ kw) | 1 | 0.9 | 0.93 |

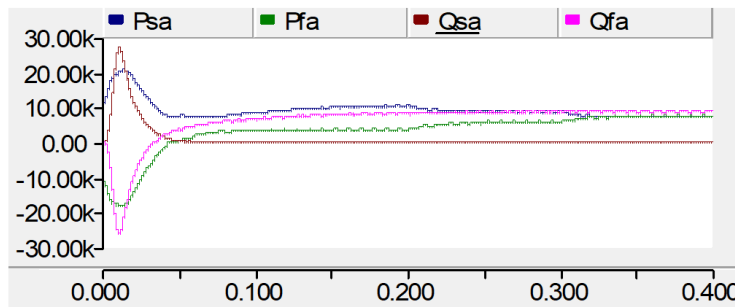
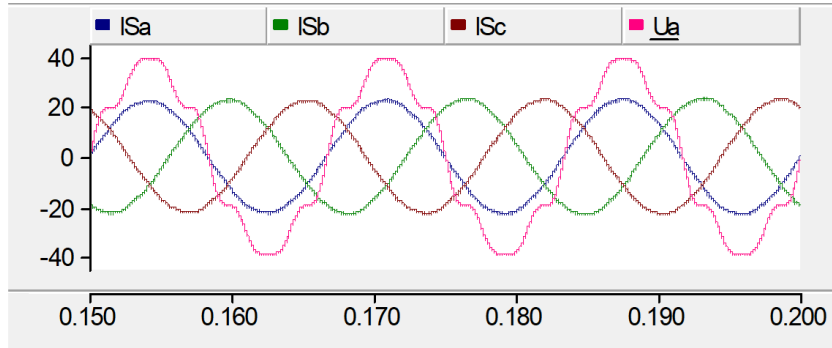
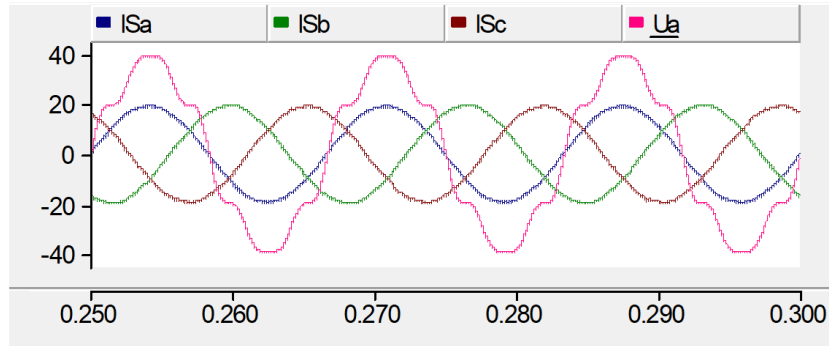


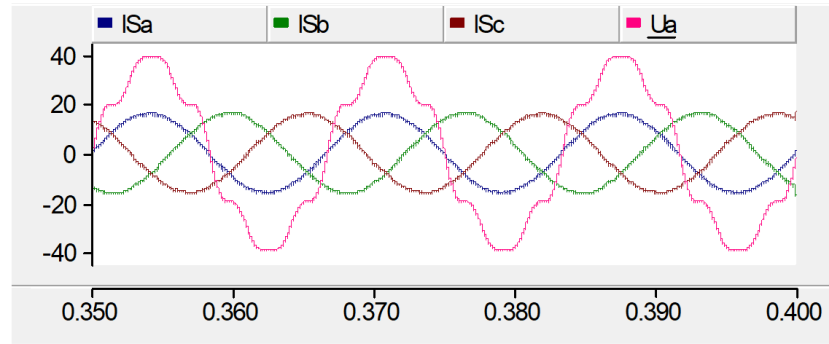
Figure 17. The source and PV active and reactive injected power.



(a)



(b)



(c)

Figure 18. Compensated currents and utility voltage with balanced and non-sinusoidal voltage supply (a) stage one, (b) stage two, (c) stage three.

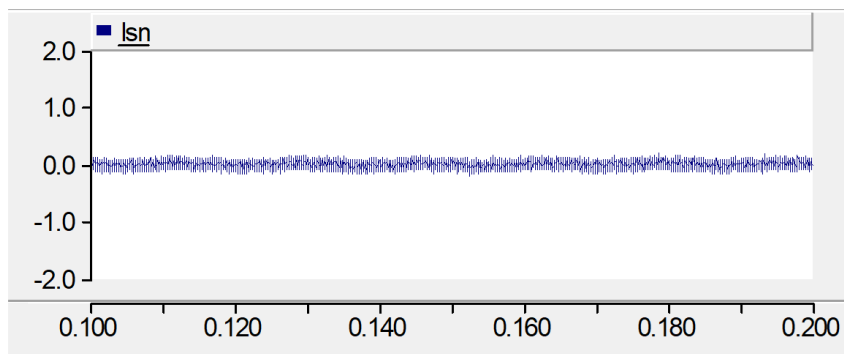


Figure 19. Neutral current after compensation.

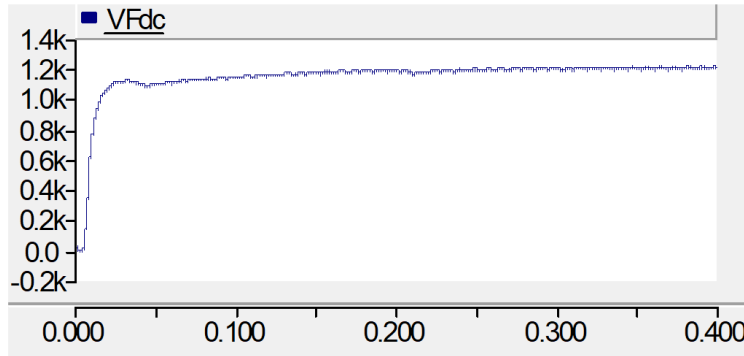


Figure 20. The DC link voltage.

3.4. Analysis of the results for the Proposed Enhanced Vectorial Theory Control System

The simulation results demonstrate the effectiveness of the enhanced vectorial control strategy in managing a grid-connected 4-wire PV-AF system under various operational conditions. The following key observations highlight the system's performance:

Harmonic Suppression and Power Factor Correction: The proposed PV-AF system effectively mitigates harmonic distortions, ensuring that THD remains below 1% across different PV power injection levels. The system maintains a unity power factor, indicating optimized active power utilization and minimal reactive power demand.

Neutral Current Compensation: Under unbalanced load conditions, the neutral current was significantly suppressed, reducing its RMS value to approximately 0.035. This confirms the APF functionality in addressing issues related to neutral current fluctuation in three-phase four-wire systems.

Adaptive PV Power Injection: The MPPT algorithm effectively tracks the MPP across varying solar irradiance and temperature levels, ensuring efficient energy conversion. The system dynamically adjusts real power injection, thus optimizing grid interaction and reducing the source's burden.

DC-Link Voltage Stability: The DC-link capacitor voltage was consistently regulated at 1200V, which is approximately three times the line voltage (380V), providing stable energy buffering for effective power compensation and injection.

Overall, the results validate the proposed enhanced vectorial control strategy, confirming its capability to enhance grid stability, harmonic suppression, neutral current elimination, and PV power utilization.

4. Comparative Results Analysis for the Two Proposed Control Strategies

Harmonic Suppression and Power Quality Improvement: The corrected p-q control strategy effectively maintains THD below 3%, ensuring harmonic suppression while compensating for current unbalance, reactive power demand, and neutral current fluctuations. The enhanced vectorial control theory, however, achieves a lower THD (approximately 0.88%), demonstrating superior harmonic mitigation under various operational conditions.

Neutral Current Compensation: The corrected p-q theory maintains the RMS neutral line current at 0.09, providing satisfactory neutral current suppression. The enhanced vectorial control-based system achieves a lower RMS neutral line current (0.035), indicating stronger compensation performance for neutral current elimination.

Adaptive PV Power Injection and MPPT Efficiency: The corrected p-q theory implementation operates under three PV power injection stages, efficiently tracking environmental variations. The system successfully injects real power alongside reactive power compensation to stabilize grid operations. The enhanced vectorial control theory-based system operates across four PV injection stages, offering enhanced adaptability in tracking the MPP across a wider range of irradiance and temperature variations.

DC-Link Voltage Stability: The corrected p-q theory system stabilizes DC-link voltage at 800V, ensuring sufficient energy buffering for compensation and PV power injection. The enhanced vectorial control system, however, maintains DC-link voltage at 1200V, approximately three times the line voltage (380V), indicating a more robust energy management strategy.

Source Current Regulation and Reactive Power Compensation: The corrected p-q theory system ensures balanced and sinusoidal source currents, providing compensation for unbalanced, nonlinear, and reactive load currents while achieving grid compliance. The enhanced vectorial control approach delivers enhanced performance, maintaining balanced and sinusoidal source currents while demonstrating optimized reactive power compensation, ensuring utility power factor correction, and efficient energy utilization. Table 5 shows a comparison between the two proposed control methods.

Results indicate that the proposed enhanced vectorial control offers superior power quality, making it more suitable for grid applications with strict harmonic constraints. Below is a comparative analysis in Table 6 comparing the corrected p-q control strategy and enhanced vectorial control from the present paper with other methods discussed in the referenced literature. This table considers key parameters such as harmonic suppression, power factor correction, neutral current elimination, MPPT efficiency, and DC-link stability. Based on Table 6, the Enhanced Vectorial Control strategy proposed in the present paper proves to be one of the most effective methods for harmonic suppression and grid stabilization, competing closely with Neural Network-Based and Meta-Heuristic approaches. However, its complexity and cost are higher compared to simpler Instantaneous p-q Theory or Fuzzy Logic-Based Controllers.

Table 5. Comparison between the two proposed control methods.

| Control Strategy | Harmonic Suppression (THD) | Power Factor Correction | Neutral Current Reduction | DC-Link Stability |
|----------------------------|----------------------------|-------------------------|---------------------------|-------------------|
| Corrected p-q Theory | Below 3% | Moderate | RMS = 0.09 | stable |
| Enhanced Vectorial Control | Below 1% | Excellent | RMS = 0.035 | stable |

Table 6. Comparison between the proposed control methods with other methods in the referenced literature.

| Control Method | Harmonic Suppression (THD) | Power Factor Correction | Neutral Current Reduction | MPPT Efficiency | DC-Link Stability | Complexity and Cost |
|---|----------------------------|-------------------------|---------------------------|-------------------|-------------------|---------------------|
| Corrected p-q Theory (This Paper) | Below 3% | Moderate | RMS = 0.09 | Efficient | 800V | Medium |
| Enhanced Vectorial Control (This Paper) | Below 1% | Excellent | RMS = 0.035 | Highly Efficient | 1200V | High |
| Instantaneous p-q Theory [6] | Moderate (5-8%) | Good | Limited | Moderate | Variable | Low |
| Fuzzy Logic-Based APF [10] | Below 5% | Moderate | Moderate | Adaptive | Stable | Medium |
| Neural Network-Based Control [9] | Below 2% | Excellent | Strong | Self-Optimizing | Highly Stable | High |
| Hybrid AC/DC Microgrid Control [7] | Below 4% | Adaptive | Moderate | Good | Variable | Medium |
| Meta-Heuristic Algorithm-Based Filtering [20] | Below 1.5% | Excellent | Strong | High Adaptability | Highly Stable | High |
| Grid-Friendly Smart Inverter Control [21] | Below 3% | High | Moderate | Advanced MPPT | Stable | High |

5. Conclusion

This paper proposes two control strategies: the corrected p-q control strategy and the enhanced vectorial control theory. The comparative analysis highlights the strengths and trade-offs between these two methods when applied to grid-connected FPV systems in three-phase four-wire distribution grids:

- The corrected p-q theory approach is effective in harmonic suppression, reactive power compensation, and adaptive PV power injection, ensuring stable power quality under dynamic environmental conditions.
- The enhanced vectorial control theory approach, however, offers superior harmonic suppression, improved neutral current elimination, and robust DC-link voltage stabilization, making it a more efficient solution for power management and grid stability enhancement.

Simulation results confirm that both methods significantly improve power quality, but vectorial control outperforms traditional techniques by reducing THD to 0.88% and enhancing neutral current mitigation. Future research should focus on real-world implementation, cost analysis, and experimental validation using hardware prototypes.

References

- [1] J. Ebrahimi, and M. Abasi, "Design of a Power Management Strategy in Smart Distribution Networks with Wind Turbines and EV Charging Stations to Reduce Loss, Improve Voltage Profile, and Increase Hosting Capacity of the Network," *Journal of Green Energy Research and Innovation*, vol. 1, no. 1, pp. 1–15, 2024.
- [2] N. Bagheri, M. A. Bahramian, and A. A. Ghadimi, "Optimal Capacitor Placement in Distributed Networks Polluted with Harmonics in the Presence of Wind Energy-Based Distributed Generation Sources," *Journal of Green Energy Research and Innovation*, vol. 1, no. 4, pp. 1–16, 2024.
- [3] M. Shiravand, and A. Nahavandi, "Control and Improvement of Power Quality in Hybrid Three-Terminal AC/DC Microgrids," *Journal of Green Energy Research and Innovation*, vol. 1, no. 2, pp. 31–45, 2024.
- [4] S. Khani, L. Mohammadian, and S. H. Hosseini, "Controlling a 4-Wire PV-AF System in Existence of Unbalanced and Distorted Supply Voltages," *20th Iranian Conference on Electrical Engineering (ICEE2012)*, pp. 473–478, 2012.
- [5] M. E. Ali, S. Mahmud, M. O. Ali, and M. F. Ahmed, "PV-Based Active Harmonic Power Filter for Power Quality Analysis," *IOSR Journal of Electrical and Electronics Engineering*, vol. 18, no. 1, pp. 57–66, 2023.
- [6] A. Khandelwal, and N. Joshi, "Implementation of Fuzzy Controller Based Active Filter for Harmonic Mitigation of Grid-Connected PV-System," *International Journal of Applied Power Engineering (IJAPE)*, vol. 13, no. 3, 539, 2024.
- [7] M. Golla, K. Chandrasekaran, and S. P. Simon, "PV Integrated Universal Active Power Filter for Power Quality Enhancement and Effective Power Management," *Energy for Sustainable Development*, vol. 61, pp. 104–117, 2021.
- [8] T. Green, and J. Marks, "Control Techniques for Active Power Filters," *IEE Proceedings - Electric Power Applications*, vol. 152, no. 2, pp. 369–381, 2005.
- [9] F. Osorio, M. A. Mantilla, J. M. Rey, and J. F. Petit, "A Flexible Control Strategy for Multi-Functional PV Inverters with Load Compensation Capabilities Considering Current Limitations and Unbalanced Load Conditions," *Energies*, vol. 17, no. 17, 4218, 2024.
- [10] J. Fu, T. Li, et al., "Three-Phase Four-Wire OPF-Based Collaborative Control of PV Inverter and ESS for Low-Voltage Distribution Networks with High Proportion PVs," *Frontiers in Energy Research*, vol. 8, 2021.
- [11] R. Wagle, P. Sharma, C. Sharma, and M. Amin, "Optimal Power Flow Based Coordinated Reactive and Active Power Control to Mitigate Voltage Violations in Smart Inverter Enriched Distribution Network," *International Journal of Green Energy*, vol. 21, no. 2, pp. 359–375, 2023.
- [12] M. Hajji, Z. Yahyaoui, M. Mansouri, H. Nounou, and M. Nounou, "Fault Detection and Diagnosis in Grid-Connected PV Systems Under Irradiance Variations," *Energy Reports*, vol. 9, pp. 4005–4017, 2023.
- [13] S. Chen, and G. Heilscher, "Integration of Distributed PV into Smart Grids: A Comprehensive Analysis for Germany," *Energy Strategy Reviews*, vol. 55, 101525, 2024.
- [14] S. Khani, S. H. Hosseini, and L. Mohammadian, "Application of the Vectorial Theory in PV-AF System for Load Supply and Harmonic Compensation with Unbalanced and Distorted Supply Voltages," *19th Iranian Conference on Electrical Engineering (ICEE2011)*, pp. 1–6, 2011.
- [15] D. Murillo-Yarce, J. Alarcón-Alarcón, M. Rivera, C. Restrepo, J. Muñoz, C. Baier, and P. Wheeler, "A Review of Control Techniques in Photovoltaic Systems," *Sustainability*, vol. 12, no. 24, p. 10598, 2020.
- [16] J. Hu, and K. Zhang, "Research on Flexible Control Technology of Photovoltaic and Energy Storage System," *2022 12th International Conference on Power and Energy Systems (ICPES)*, pp. 876–879, 2022.

- [17] J. M. R. Dominguez, J. Riquelme, and S. Martinez, "New Trends in the Control of Grid-Connected Photovoltaic Systems for the Provision of Ancillary Services," *Energies*, vol. 15, p. 7934, 2022.
- [18] K. Reham, A. Wael, and N. Mohamed, "Harmonic Analysis Comparison between PV Integration in High Voltage and Medium Voltage Networks," *American Journal of Engineering Research*, vol. 10, pp. 263–276, 2021.
- [19] P. Rahmati Kahkha, A. HossienPour, and A. Khajeh, "Four-Switch Inverter Based Hybrid Power Filter Optimized by Meta-Heuristic Algorithm of SPEA," *International Journal of Industrial Electronics Control and Optimization*, vol. 6, no. 2, pp. 133–141, 2023.
- [20] D. Murillo-Yarce, J. Alarcón-Alarcón, et al., "A Review of Control Techniques in Photovoltaic Systems," *Sustainability*, vol. 12, no. 24, 10598, 2020.
- [21] Q. Peng, A. Sangwongwanich, Y. Yang, and F. Blaabjerg, "Grid-Friendly Power Control for Smart Photovoltaic Systems," *Solar Energy*, vol. 210, pp. 115–127, 2020.

Declaration of competing interest

The authors declare that they have no known competing financial interests or personal relationships that could have appeared to influence the work reported in this paper. The ethical issues, including plagiarism, informed consent, misconduct, data fabrication and/or falsification, double publication and/or submission, redundancy, have been completely observed by the authors.

Bibliography



Saeid Khani was born in Tabriz, Iran, 1984. He received his B.Sc. degree in electrical engineering from the University of Zanjan, Iran and M.Sc. and Ph.D. degrees in electrical engineering from the University of Tabriz, Iran in 2007, 2011 and 2023 respectively. His research interests include power electronic converters and power electronic application in renewable energy systems, power quality enhancement and facts.

Email: Saeid_khani82@yahoo.com

ORCID: [0009-0009-0956-2097](https://orcid.org/0009-0009-0956-2097)

Contribution Statement: Formal analysis, Methodology, Software, Roles/Writing-original draft, Writing-review & editing.



Leila Mohammadian was born in Tabriz, Iran, in 1984. She received her B.S., M.S., and Ph.D. degrees in Electrical Engineering from the Department of Electrical and Computer Engineering, University of Tabriz, Tabriz, Iran, in 2007, 2011, and 2015, respectively. She has been with the Department of Electrical Engineering, Shab.C., Islamic Azad University, Shabestar, Iran, since 2011. She has been an Assistant Professor since 2015. She is the author of more than 60 journal and conference papers. Her current research interests include the analysis and control of power electronic converters and their applications, power quality enhancement and FACTS devices, application of control systems and theory in power engineering, and power system dynamics, renewable energy sources, and energy storage systems.

Email: le.mohammadian@iau.ac.ir

ORCID: [0000-0001-5202-1397](https://orcid.org/0000-0001-5202-1397)

Contribution Statement: Conceptualization, Investigation, Methodology, Supervision, Writing-review & editing.

Optimal Configuration of Solar Combined Hydrogen, Heat, and Power (S-CHHP) by Considering Reliability Model

Mojtaba Pirmohammad Talatape, Sajad Bagheri, Reza Ghanizadeh, Mohammad Reza Miveh

Highlights

- ❖ Presenting reliability model of solar-based-CHHP (S-CHHP).
- ❖ Utilizing LSTM-CNN to predict system uncertainties.
- ❖ Utilizing K-means clustering as a scenario reduction method.
- ❖ Combined hydrogen, heat and power (CHHP) to generate three kinds of energy demands.

Graphical Abstract



Use your device to scan and read the article online



Citation

M. Pirmohammad, S. Bagheri, R. Ghanizadeh, and M. R. Miveh, "Optimal Configuration of Solar Combined Hydrogen, Heat and Power (S-CHHP) by Considering Reliability Model," *Journal of Green Energy Research and Innovation*, vol. 2, no. 4, pp. 45-57, 2025.

 <https://doi.org/10.61882/jgeri.2.4.45>





Online ISSN: 3041-9018

Journal of Green Energy Research and Innovation

Journal Homepage: www.jgeri.araku.ac.ir

Optimal Configuration of Solar Combined Hydrogen, Heat, and Power (S-CHHP) by Considering Reliability Model

Mojtaba Pirmohammad Talatape¹, Sajad Bagheri^{1*}, Reza Ghanizadeh², Mohammad Reza Miveh³

¹ Department of Electrical Engineering, Ar.C., Islamic Azad University, Arak, Iran.

² Department of Electrical Engineering, Ur.C, Islamic Azad University, Urmia, Iran.

³ Department of Electrical Engineering, Tafresh University, Tafresh, Iran.

ARTICLE INFO

Keywords:

S-CHHP,
Markov chain,
Shark Smell Optimizer.

Article History:

Received: 01 July 2025;
Revised: 29 August 2025;
Accepted: 01 December 2025.

Article type:

Research Article

* Corresponding author

E-mail address
Sajad.bagheri@iaua.ac.ir (S. Bagheri)

ABSTRACT

Environmental and economic concerns of utilizing fossil fuels reveal the need to use alternative sources. Due to various kinds of energy demands, choosing the proper generation units is the main aim of energy administrators. Simultaneous generation units are the proper choice to meet several kinds of demands. Combined hydrogen, heat, and power (CHHP) is a cogeneration system that generates three kinds of energy demands. Presenting the comprehensive reliability model of CHHP is the main part of this study. State-space and continuous Markov models with hydrogen, heat, and power generation systems are considered in the reliability model of CHHP. Loss of load expectation (LOLE) and expected energy not supplied (EENS) are considered as reliability indices to verify the efficiency of the proposed reliability model of the CHHP. Due to the important role of communication and data gathering, sending and receiving, the necessity to have a system to minimize the errors in data gathering and processing, and sending is unavoidable. Natural language program (NLP) is the best tool for managing data received, processing, and sending within the system with high accuracy.

1. Introduction

Rising energy demand and inefficiencies in production may soon outstrip supply, forcing the countries to import energy and causing major economic and social problems [1]. Reference [2] examines water-energy systems as a vital component of modern energy policies, analyzing hydraulic efficiency (EH) and annual water output. Findings show that multi-pump stations achieve 97% EH, surpassing mono-pump systems. The research also tackles power management challenges in PV-powered water stations using a Mixed Integer Linear Programming (MILP) model to optimize both solar power use and water production. Additionally, it highlights cogeneration—simultaneous production of multiple energy types—as a solution to boost efficiency, cut primary energy use, and reduce emissions. A key example is Combined Hydrogen, Heat, and Power (CHHP), integrating electrolyzers, fuel cells, and storage for cleaner, more efficient energy systems. In [3], the author presents a smarter way to manage renewable energy and storage, making electricity distribution more cost-effective, reliable, and eco-friendly. Tests and case studies show that this approach works well. By optimizing the solar-hydrogen storage system, the study improves the network's performance, saves money, and reduces environmental impact compared to traditional energy management methods. It also discusses a CHHP system by emphasizing reliability modeling (using state-space and Markov models) and the need for efficient data handling via Natural Language Programming (NLP). Paper [4] presents a reinforcement learning (RL)-based energy management system (EMS) for multi-energy microgrids (MEMGs), optimizing both economic efficiency and system durability. Literature [5] presents a scalable approach to microgrid planning by incorporating dynamic degradation cost models for both solar PV systems and battery storage, addressing the shortcomings of conventional fixed or computationally intensive methods. Choosing and using simultaneous production systems depends a lot on the desired site, rules, and how to use them. Some of the effective factors are as follows:

- Cogeneration system design depends heavily on fuel and electricity prices, as well as thermal energy requirements (temperature/pressure). For instance, high-cycle systems suit a sugar plant (120°C), while cement plants (1450°C) need low-cycle systems, with demand patterns dictating type and size [6-9].
- The hydrogen/heat-to-power ratio, fuel availability, and demand reliability critically influence cogeneration system selection. Matching consumer needs with unit specifications—while balancing cost, redundancy, and grid connectivity—determines whether the system meets partial/full demand or sells excess output [10-14].
- Environmental laws may prohibit the use of some fuels due to high pollution, which may limit the choice of the type of cogeneration system [15].

Optimal sizing and siting of the CHHP in the distribution power system with considering technical and economic functions as provided in [16]. In [17], a new approach to empirical electrical modelling of a fuel cell, an electrolyzer, or a regenerative fuel cell was discussed. Modelling system uncertainties in the planning problem helped to give comprehensive results. In [18], the authors used the Monte Carlo method (MCM) to predict system uncertainties. Improving reliability indices in the planning problem is the main aim of several works of literature. In [19], the authors used a reliability-constrained optimization approach to model participation of private investors and distribution network operators. To enhance the reliability features of the multi-microgrid, the authors suggested a fair electricity market strategy [20]. To improve patterns of energy consumption of the consumers, some programs are introduced as demand responses. These programs are in two cases: time (or price) based and incentive-based programs. Reference [21] presented the impacts of employing a demand response program in the optimal sizing of a CHP unit. Reference [22] introduced a three-stage hybrid robust-stochastic framework for modeling the coordinated operation of CHP units and compressed-heat energy storage, formulated as a MILP problem.

In this paper, solar-based CHHP is proposed to be used as a generation unit. The reliability model of S-CHHP will be introduced and used to meet the residential-based load. Loss of load expectation (LOLE) and expected energy not supplied (EENS) are used as reliability indices. MILP is adopted and modelled in the general algebraic model system (GAMS) software.

The main contribution of this paper is classified as follows:

- Presenting a reliability model of solar-based CHHP (S-CHHP)
- Utilizing long short-term memory (LSTM)-convolutional neural network (CNN) to predict system uncertainties
- Utilizing K-means clustering as a scenario reduction method

The rest of the paper is organized as follows. Section 2 provides the CHHP model. Section 3 presents the main objective function. All of the simulation results are evaluated in Section 4. Section 5 concludes the work.

2. Problem definition

- Definition of S-CHHP features

The CHHP system, comprising an electrolyzer, fuel cell, and thermal/hydrogen storage, effectively meets residential energy demands. Since electrolyzers have low efficiency, photovoltaic (PV) systems directly power them, as illustrated in Figure 1 [23].

- Reliability modelling of the S-CHHP

In this study, the input power of the electrolyzer is fed by a PV system. For the reliability modelling of the S-CHHP, the series of PV, thermal, hydrogen, power, and CHHP are considered as the Figure 2. In the S-CHHP, the reliability of the system is calculated by multiplying the probability of the series subsystem. The number of failures in the year and the frequency of repairs in that year are known as two important reliability parameters: failure time and repair time.

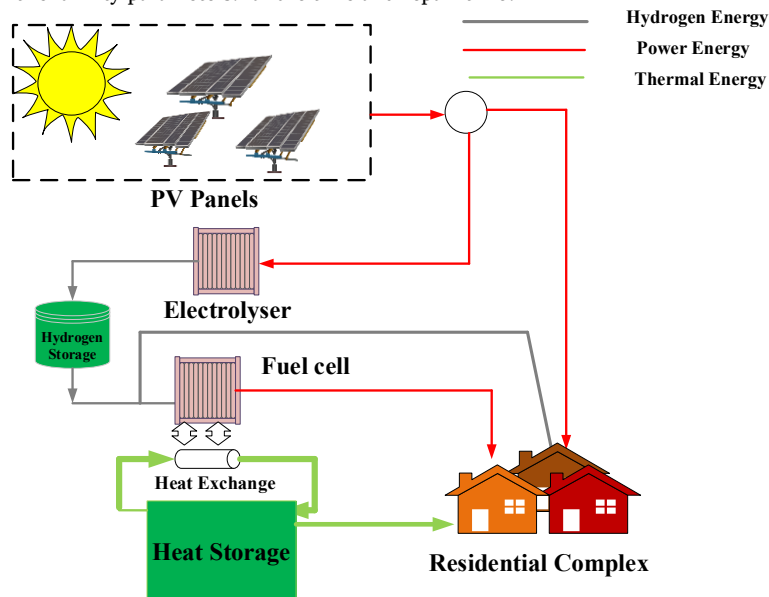


Figure 1. The proposed S-CHHP.

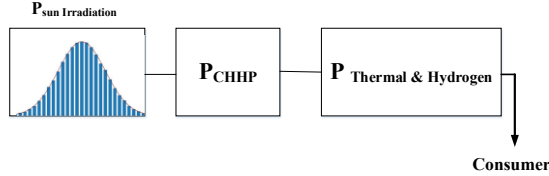


Figure 2. Reliability representation of S-CHHP.

The reliability of S-CHHP is defined as Equation (1).

$$R_{S-CHHP} = R_{PV} \times R_{Th} \times R_{Power} \times R_{Hyd} \tag{1}$$

Figure 3 shows 11 states that can happen in the operational condition of S-CHHP.

- Markov Model

Markov modeling provides an effective reliability analysis for memoryless systems with constant failure/repair rates, where availability becomes more critical than reliability in multistate systems due to computational complexity [24]. Figure 3 shows 11 states that can happen in the operational condition of S-CHHP.

Availability of subsystems is defined as follows:

$$Availability_{Thermal} = P1 + P2 \qquad Availability_{Power} = P1 + P5 \qquad Availability_{Hydrogen} = P1 + P3$$

- Problem Formulation

The main function of this paper is to increase the reliability level of the proposed CHHP-based energy system by reducing total annualized costs and considering system constraints. The proposed planning problem formulation is defined as Equation (2).

$$OF = \min (IC^{CHHP} + \sum_{s=1}^{N_s} \sum_{t=1}^{8760} \pi_s \times (IRL_{s,t} + OC_{s,t})) \tag{2}$$

IC and OC are the investment cost and operational cost, respectively. IRL is the reliability-based cost and is defined as Equation (3).

$$IRL = EENS \times C_{Loss} \quad (\$/ \text{ year}) \tag{3}$$

The proposed planning problem has been applied to the large residential load with thermal, hydrogen, and power demands.

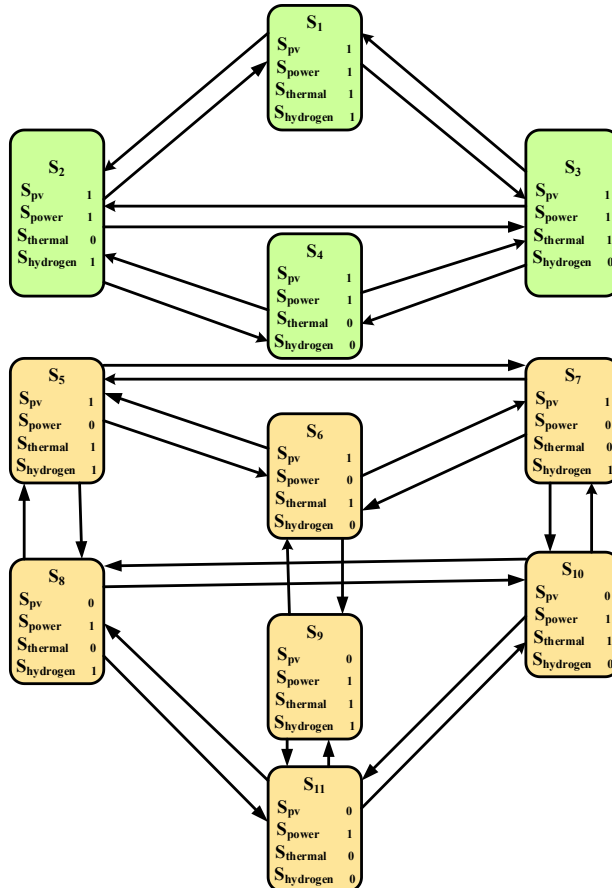


Figure 3. Markov block diagram of S-CHHP.

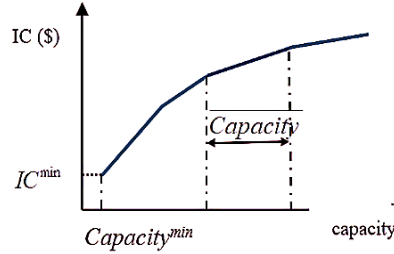


Figure 4. The linear model of investment cost.

2.1. Investment

The increasing size of the generation unit has an inverse relation with the price of its components (\$/kW). Figure 4 shows the relation between size and investment cost of components.

The linear form of the (IC-Capacity) curve is defined in Equation (4) [25].

$$IC = IC^{\min} \times \delta_1 + \sum_{k=1} slope_k \times capacity_k \tag{4}$$

$$\delta_k \leq 1 + \frac{capacity_{k-1} - capacity_{k-1}}{capacity_{k-1}} \tag{5}$$

δ_k is the binary variable, and $slope_k$ is the slope of the k th segment.

2.2. Operational constraints of S-CHHP

This section defines the operational constraints of S-CHHP.

• PV

The electrical output of a photovoltaic installation is primarily influenced by ambient temperature, the intrinsic efficiency of the PV modules, and the intensity of the solar irradiance they absorb. These parameters jointly determine the system’s real power production, which is formally expressed through Equation (6) [26]. In practical operation, variations in any of these factors—such as temperature-induced efficiency losses or fluctuations in incident sunlight—directly translate into measurable changes in PV performance. This relationship forms the basis for accurate modeling, forecasting, and optimization of PV energy generation under diverse environmental conditions.

$$P_{out,t}^{PV} = \eta^{PV} \times A \times (25 - T_{amb}) \times I_r \tag{6}$$

• Electrolyzer

Hydrogen and oxygen are separated from water using an electrolyzer, which drives an electric current through two physically isolated electrodes to initiate the decomposition process. The electrolyzer’s power output follows the relationship defined in Equation (7) [27]. In operational settings, the electrical input, electrode characteristics, and system efficiency all influence the rate and quality of gas production, making the governing equation essential for performance assessment and system design.

$$P_t^{Out_EL} = P_t^{Out_SPL} \times \eta^{EL} \tag{7}$$

• Fuel cell

A fuel cell converts the chemical energy stored in hydrogen and oxygen directly into electrical power through an electrochemical reaction rather than combustion. Its electrical output is quantified using the relationship expressed in Equation (8) [28]. In practice, this output depends on factors such as reactant flow rates, cell temperature, and internal losses, making the governing equation a key reference for evaluating performance and integrating the device into broader energy systems.

$$P_t^{FuelCell} = P_t^{HSS_Fuelcell} \times \eta^{fuelcell} \tag{8}$$

• Hydrogen storage

Hydrogen storage serves as a buffering component that stabilizes the operation of intermittent electrolyzers and fuel cells, ensuring a continuous supply of hydrogen regardless of production or consumption fluctuations. The corresponding hydrogen flow rate associated with the storage unit is characterized by the relation given in Equation (9) [29], which governs how hydrogen is charged into or discharged from the storage system under varying operating conditions.

$$HSS_t = HSS_{t-1} + \eta^{PH} \times P_t^{PH} - \frac{P_t^{HP}}{\eta^{HP}} \tag{9}$$

• Heat storage

Heat transfer within the thermal storage system is governed by the relation expressed in Equation (10) [30]. This formulation specifies the rate at which heat is accumulated or released by the storage unit, reflecting its dynamic response to charging and discharging conditions in the broader energy system.

$$Heat_t^{HS} = \eta^{HS} \times Heat_{t-1}^{HS} + Heat_{t-1}^{HS-in} - Heat_{t-1}^{HS-out} \tag{10}$$

2.3. Power, heat, and hydrogen balance equation

The governing constraints for maintaining power, heat, and hydrogen balance within the system are specified in Equations (11) through (13). These expressions ensure that all inflows and outflows of energy and mass remain consistent with the operational and physical limits of the integrated system.

$$P_t^{S-CHHP} + P_t^{Grid-Sell} - P_t^{Grid-buy} = P_t^{Load} \tag{11}$$

$$Heat_t^{S-CHHP} = Heat_t^{Storage} + Heat_t^{Load} \tag{12}$$

$$Hyd_t^{S-CHHP} = Hyd_t^{Storage} + Hyd_t^{Load} \tag{13}$$

2.4. Reliability indices

This study employs Loss of Load Expectation (LOLE) and Expected Energy Not Supplied (EENS) as the primary reliability metrics for the system. These indices quantify the likelihood and magnitude of insufficient power supply and are mathematically expressed in Equations (14) and (15), respectively [31]. LOLE measures the expected number of hours in which the system cannot meet the load, while EENS represents the expected energy deficit during these periods, providing a comprehensive assessment of system reliability.

$$LOLE = \sum \pi_s \times \sum_{t=1}^{n \times 8760} LSIX_t \leq \overline{LOLE} \tag{14}$$

$LSIX$ is the binary variable equal to 1 when load shading occurs [32].

$$EENS = \sum \sum \pi_s \times \sum_{t=1}^{n \times 8760} LS_t \leq \overline{EENS} \tag{15}$$

LS is load curtailment.

3. Optimization Algorithm

3.1. Shark smell optimization (SSO)

The Shark Smell Optimization (SSO) algorithm is a novel population-based optimization technique inspired by sharks' natural ability to detect and move toward prey, representing an optimal solution. In this approach, the initial population is generated by assigning potential positions to each shark, which serve as candidate solutions in the search space.

$[X_1^1, X_2^1, \dots, X_{NP}^1]$. NP = Population Size

So, the i th initial location vector, which represents the i th initial option solution for the optimization problem, is given by Equation (16).

$$X_i^1 = [x_{i,1}^1, x_{i,2}^1, \dots, x_{i,ND}^1]. \quad i = 1, 2, \dots, N \tag{16}$$

In this formulation, x_{ij} represents the j th dimension of the i th shark's initial position, corresponding to the j th decision variable of the i th individual X_i , with the total number of decision variables denoted as ND . During the optimization process, the sharks update their positions and velocities as they move toward the prey, with the velocity vector of the i th shark defined by Equation (17).

$$V_i^1 = [v_{i,1}^1, v_{i,2}^1, \dots, v_{i,ND}^1] \tag{17}$$

The movement of the shark towards the prey is based on its "forward smell" motion, and its "rotation" is based on a gradient function, given by Equation (18) [33].

$$V_i^k = \eta_k \cdot R1 \cdot \nabla(OF)|_{x_i^k} \tag{18}$$

For a population size of $i = 1, \dots, NP$ and iteration index $k = 1, \dots, k_{max}$, where k_{max} denotes the maximum number of algorithmic iterations, the objective function (OF) represents the performance metric to be optimized. The gradient of the objective function, $\nabla(OF)$, provides directional information for movement toward optimal solutions. Building upon the previous velocity of the individual shark, the current velocity at iteration k can be expressed as in Equation (19). This formulation enables the algorithm to dynamically adjust the search direction and step size, thereby enhancing convergence efficiency and the ability to explore the solution space effectively in population-based optimization scenarios. Additionally, by incorporating the gradient information, the algorithm achieves a balance between global exploration and local exploitation, which is critical for avoiding premature convergence and ensuring robust optimization performance.

$$|V_{i,j}^k| = Min \left[\left| \eta_k \cdot R1 \cdot \frac{\partial(OF)}{\partial x_j} \right|_{x_{i,j}^k} + \alpha_k \cdot R2 V_{i,j}^{k-1} \right] \cdot |\beta_k V_{i,j}^{k-1}| \tag{19}$$

In this formulation, $j = 1, \dots, ND$, where ND represents the number of decision variables. The parameters $\eta_k \in [0,1]$ and $\alpha_k \in [0,1]$ are user-defined coefficients within the SSO algorithm, governing the relative influence of the newly computed velocity component in comparison to the previous velocity during the k -th iteration. The terms R_1 and R_2 are random variables uniformly sampled from the interval $[0, 1]$, introducing stochasticity to the search process. Additionally, β_k denotes a rate-limiting factor applied in iteration k to control the maximum allowable velocity change, thereby preventing overshooting of the optimum.

Based on these velocity updates, the projected position of each shark, reflecting its forward movement toward the prey, can subsequently be determined as expressed in Equation (20). This step is fundamental in ensuring that the algorithm balances exploration and exploitation, enabling effective navigation through complex, multidimensional solution spaces while maintaining convergence stability.

$$Y_i^{k+1} = X_i^k + V_i^k \Delta t_k \tag{20}$$

So, Δt_k determines the time interval in the k th iteration. Therefore, the rotational movement of the shark can be expressed as Equation (21).

$$Z_i^{k+1,m} = Y_i^{k+1} + R_3 \cdot V_i^{k+1} \tag{21}$$

In this context, $m = 1, \dots, M_a$, where M_a represents the total number of discrete points along the shark’s circular search trajectory during each iteration. The variable R_3 is a random number uniformly sampled from the interval $[-1, +1]$, introducing variability into the search pattern to enhance exploration. M denotes the total number of points evaluated along the circular path in a given iteration. At each of these points, the objective function (OF) value is calculated, and the shark’s updated position is determined according to Equation (22). This mechanism allows the algorithm to exploit local regions effectively while simultaneously exploring the surrounding solution space, improving the likelihood of identifying global optima in complex, multidimensional optimization problems.

$$X_i^{k+1} = \operatorname{argmax} \{OF(Y_i^{k+1}) \cdot OF(Z_i^{k+1,1}) \dots OF(Z_i^{k+1,M})\} \tag{22}$$

In this formulation, the operator $\operatorname{argmax} \{\cdot\}$ identifies the argument that maximizes the objective function $OF(\cdot)$, effectively selecting the optimal candidate from the evaluated positions. Upon completing the iterative process, each individual in the population updates its position according to the described operators, and the overall best-performing individual is reported as the solution at the final iteration of the algorithm. Figure 5 illustrates the modeled behavior of a shark navigating toward an odor source, guided by the gradient of concentration, which serves as an analogy for the algorithm’s directed search towards the global optimum.

The New SSO (NSSO) introduces an additional operator in its first step to enhance the search process by considering the shark’s best position in relation to its neighborhood. This is achieved by evaluating the neighborhood using best-neighbor information. Specifically, the algorithm calculates the Euclidean distance between the position of shark X_i^1 and all other candidate solutions. These individual distances, denoted as $d(i, j)$, are then averaged to obtain the mean distance md_i , which quantifies the spatial distribution of the neighborhood. This metric allows the algorithm to guide the shark more effectively toward promising regions in the search space, leveraging local information for improved convergence.

$$md_i = \frac{\sum_{j=1}^M d(i, j)}{M - 1} \tag{23}$$

In this framework, a candidate solution x_j is considered part of the neighborhood of X_i^1 if its distance $d(i, j)$ is smaller than the mean distance md_i , ensuring that only sufficiently close solutions influence the shark’s movement.

To address premature convergence, the second step incorporates an abandonment mechanism. Here, a parameter $l(i)$ is introduced for each shark ($i = 1, \dots, M$) and initially set to zero. If a shark’s position does not improve during an iteration, the parameter is incremented as $l(i) = l(i) + 1$; otherwise, it is reset to zero. When the stagnation persists beyond a threshold, the parameter reaches a maximum value L , signaling the need for exploration. This mechanism allows the algorithm to adaptively modify the search behavior, encouraging movement toward new regions in the solution space and is formalized in Equation (24).

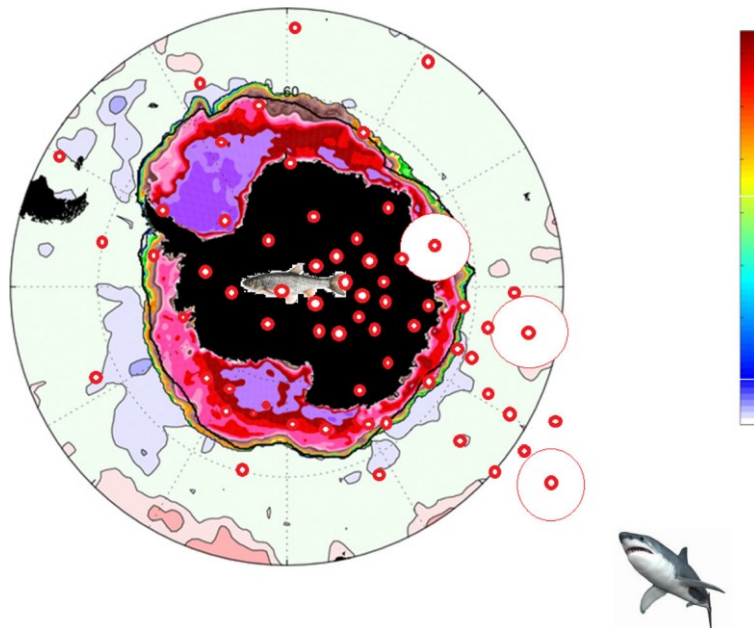


Figure 5. Shark smell behavior.

$$x_{new} = \tau * P_g + \emptyset * (P_g - x_i) \tag{24}$$

In this formulation, \emptyset represents a randomly generated number within the range [-1, 1], while τ acts as a weighting factor that regulates the influence of the global best solution during the current iteration, increasing progressively over time. Using this equation, the new position x_{new} is determined with considerable randomness, allowing the search to explore broadly initially and then focus closely around the global best solution P_g in the final stages. For the final refinement step in the algorithm, three random variables from the SSO framework— R_1 and R_2 associated with forward movement, and R_3 related to rotational movement—are generated according to Equations (25) and (26), enhancing the stochastic exploration and exploitation balance.

$$C_{k+1} = 4C_k(1 - C_k) \text{ for } R1 \text{ and } R2 \tag{25}$$

$$C'_{k+1} = 2C_{k+1} - 1 \text{ for } R3 \tag{26}$$

In this approach, C_k and C_{k+1} are values produced by the chaotic pendulum operator, with $C_k, C_{k+1} \in (0,1)$ and $C'_{k+1} \in (-1,1)$. The operator is initialized by generating C_0 randomly within the interval (0,1), ensuring that $C_0 \notin \{0.25, 0.5, 0.75\}$ to avoid fixed points that could reduce chaotic behavior. Additionally, a random mutation operator is applied to each $G_{i,j}^g$ with a predefined probability p_b . This mutation enhances population diversity, preventing premature convergence and improving the algorithm's exploratory capability, as described in Equations (27) and (28).

$$G_{i,j}^g = rand(L B_j . U B_j) \text{ if } rand(0.1) < p_b \tag{27}$$

$$G_{i,j}^g = G_{i,j}^g \text{ otherwise} \tag{28}$$

A. Long-Short term memory (LSTM)

In recent years, LSTM neural networks have gained significant attention due to their ability to address long-term dependencies in sequential data [34]. LSTM networks are specifically designed to retain information over extended periods, making them highly effective at learning temporally separated patterns. Like all recurrent neural networks (RNNs), LSTMs consist of a chain of interconnected modules; however, unlike simple RNNs with basic recurrent units, LSTM modules have a more sophisticated internal architecture.

A fundamental component of LSTM networks is the cell state C_t , which acts as a memory pathway capable of selectively adding or removing information. This functionality is regulated by specialized structures known as gates, which determine how information flows into, through, and out of the cell. At each time step t , the input X_t is processed by the input gate I_t , which controls the amount of new information stored in the cell state C_t . Simultaneously, the forget gate F_t regulates the retention of the previous cell state C_{t-1} , selectively discarding irrelevant information. Finally, the output gate determines which portion of the updated cell state contributes to the network's output h_t . The dynamics of these gates and the updated cell state are mathematically defined in Equations (29)–(31), capturing the flow and transformation of information within the LSTM unit.

$$C_t = F_t \times C_{t-1} + I_t \times (\tanh(W_c \times [O_{t-1}, X_t] + b_c)) \tag{29}$$

$$I_t = \sigma(W_i \times [O_{t-1}, X_t] + b_i) \tag{30}$$

$$F_t = \sigma(W_f \times [O_{t-1}, X_t] + b_f) \tag{31}$$

In the preceding equations, W_c , W_f , and W_i represent the weight matrices associated with the cell, forget, and input gates, respectively. The term O_{t-1} denotes the output of the LSTM cell from the previous time step, while X_t corresponds to the current input at time t . The vectors b_c , b_i , and b_f are the bias terms applied to the cell, input, and forget gates, facilitating the adjustment of the gate activations during network training. In this case, the output is as Equation (32).

$$O_t = \sigma_t \times \tanh(C_t) \tag{32}$$

3.2. Convolutional Neural Network (CNN)

CNNs utilize multilayer perceptrons with adaptive weights to learn nonlinear input-output relationships through convolutional layers (feature extraction), pooling (dimensionality reduction), and fully connected layers (final feature integration), where 3D filters in the initial layer generate output feature maps. To obtain the mapping relation of the first layer from the one-dimensional input $x = (x_t)_{t=0}^{(N-1)}$ with size N , the filter combinations w_h^1 for $h = 1, \dots, M_1$ are as Equation (33).

$$a^1(i, h) = (w_h^1 * x)(i) = \sum_{j=-\infty}^{\infty} w_h^1(j) x(i - j) \tag{33}$$

In this equation w_h^1 and a^1 belong to the sets $R^{1 \times k \times 1}$ and $R^{1 \times N - k + 1 \times M_1}$, respectively.

Similar to feedforward neural networks, the output is processed through a nonlinear activation function h to yield $f = h(a)$. For each subsequent layer $l = 2, \dots, L$ in the mapping network, the feature map $f^{(l-1)} \in R^{1 \times N_{l-1} \times M_{l-1}}$, with dimensions $1 \times N_{l-1} \times M_{l-1}$, is combined with the output from the preceding convolution filter. This operation produces the mapped feature map $a^l \in R^{1 \times N_l \times M_l}$, as expressed in Equation (34).

$$a^l(i, h) = (w_h^l * f^{l-1})(i) = \sum_{j=-\infty}^{\infty} \sum_{m=1}^{M_{l-1}} w_h^l(j, m) f^{l-1}(i - j, m) \tag{34}$$

3.3. Combinational LSTM and CNN (CNN-LSTM)

This section presents our hybrid model for short-term load forecasting (STLF). The overall architecture of the CNN-LSTM-based deep learning network applied to Urmia city is illustrated in Figure 6. The CNN feature extraction module consists of three one-dimensional convolutional layers, each followed by Max-Pooling (to reduce spatial dimensions) and ReLU activation functions (to maintain gradient stability). Early convolutional layers focus on capturing low-level features, while the pooling layers reduce positional variance and computational load.

K-means clustering

K-Means is an iterative clustering algorithm that partitions unlabeled data into 'k' distinct, non-overlapping groups by minimizing within-cluster variances (using squared Euclidean distances) while maximizing between-cluster separation, following the Expectation-Maximization approach with 'k' requiring predefinition.

Step 1: Determine the number of clusters by selecting the value of K.

Step 2: Initialize K centroids, either randomly or through a specific calculation. The Euclidean distance is used to select the initial centers.

Step 3: Assign each data point to the nearest centroid, forming K initial clusters.

Step 4: Compute the mean of each cluster and update the centroid to this new value.

Step 5: Reassign all data points to the nearest updated centroid, refining the cluster assignments.

Step 6: Repeat the centroid update and reassignment steps until no significant changes occur, indicating convergence.

Step 7: Finalize the clustering model, which is now ready for use.

Equation (35) is the objective function of the k-means clustering algorithm. It measures how “tight” the clusters are. Lower J means better, more compact clusters.

$$J = \sum_{k=1}^k \sum_{p_i \in S_k} (p_i - c_k)^2 \tag{35}$$

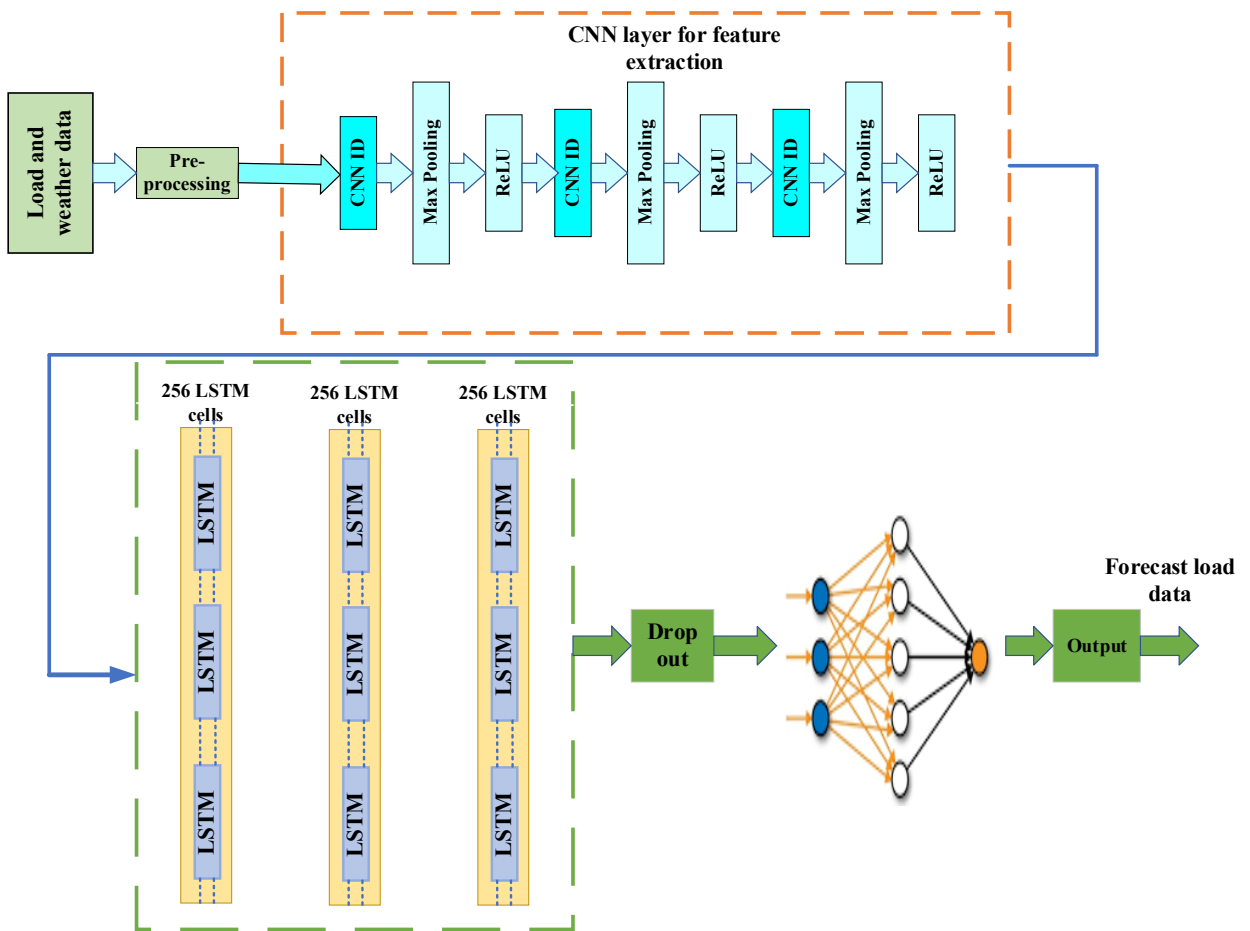


Figure 6. LSTM model.

4. Simulation results

In this section, we will examine the performance of the methods presented in the article and compare them with the proposed methods of past research to identify their strengths and weaknesses. Also, the criteria of good or bad performance of these methods will be introduced, and by using practical simulations with real data, load prediction charts and tables will be presented.

4.1. 4.1. Input data

Figure 6 illustrates the typical demand for electricity, heat, and hydrogen in a day. The electric, heat, and hydrogen base loads are 1800, 3500, and 1000kW, respectively. Table 1 gives the parameters of S-CHHP. Table 2 tabulates the time of use-based demand response and fuel cell parameters.

4.2. The optimal size of CHHP

The rest of the scenarios after employing the k-means clustering algorithm are given in Table 3. Figures 7-11 show the predicted values by LSTM. The lowest MAPE error values can be achieved using the deep learning scheme proposed by CNN-LSTM in this thesis. The closest MAPE value to our proposed method is the GRU network in the reference, which is obtained by a powerful STLF tool. Compared to the reference results, MAPE improvement is achieved at least 0.2%, which can lead to extensive cost savings in electric power generation plants. Root Mean Square Error (RMSE) and Mean Absolute Percentage Error (MAPE) have been used to evaluate the accuracy of the proposed model. RMSE measures the amount of error between two data sets according to Equation (36).

$$RMSE = \sqrt{\frac{1}{n} \sum_{i=1}^n (\hat{Y}_i - Y_i)^2} \tag{36}$$

Here, Y_i represents the observed load at time i , while \hat{Y}_i denotes the forecasted value. The MAPE is used as a metric to evaluate the accuracy of a prediction model. It expresses the forecast error as a percentage and is computed according to Equation (37).

$$MAPE = \frac{1}{n} \sum_{i=1}^n \left| \frac{\hat{Y}_i - Y_i}{Y_i} \right| \tag{37}$$

Table 4 presents a comparative analysis between the proposed STLF model and existing forecasting models reported in the literature.

Table 1. CHHP parameters.

| Unit | CHHP | | PV | | | | | | | |
|-----------|-----------------------|-------------|----------|-------------|-----|-------|----|----|------------------|----------|
| Parameter | $\eta^{Electrolyser}$ | η^{HE} | ω | η^{PV} | S | T_a | If | Ir | (year) τ | α |
| Value | 0.7 | 0.92 | 0.75 | 15.5% | 750 | 25 | 9% | 9% | 15 | 2% |

Table 2. Demand response parameter.

| TOU Program | | | | Fuel Cell |
|--------------|--------------|--------------|--|---------------------|
| Peak | Normal | Low | | |
| 20-23 | 7:00-19:59 | 0:00-6:59 | | $\eta^{Fuel\ cell}$ |
| 0.48(\$/kWh) | 0.35(\$/kWh) | 0.22(\$/kWh) | | 0.75 |

Table 3. Scenarios after employing scenario reduction.

| Scenario | 1 | 2 | 3 | 4 | 5 |
|-------------|-------|-------|-------|-------|-------|
| Probability | 0.012 | 0.043 | 0.387 | 0.023 | 0.068 |
| Scenario | 6 | 7 | 8 | 9 | 10 |
| Probability | 0.033 | 0.017 | 0.117 | 0.2 | 0.1 |

Table 4. Results of different prediction methods.

| Forecasting Method | MAPE |
|-----------------------|------|
| DNN | 1.32 |
| RNN | 1.19 |
| LSTM | 1.01 |
| GRU | 0.84 |
| The Proposed CNN-LSTM | 0.61 |

Obviously, the lowest MAPE error values can be achieved using the CNN-LSTM deep learning scheme proposed in this thesis. The closest MAPE value to our proposed method is the GRU network in the reference, which is obtained by a powerful STLF tool. Compared to the reference results, MAPE improvement is achieved at least 0.2%, which can lead to extensive cost savings in electric power generation plants. The storage efficiency is 90%, its minimum and maximum energy values are 100 and 260 kWh, respectively, and finally, its initial and final energy values are considered to be 180 kilowatt hours. The results of the optimal planning problem are given in Table 5. The value of the lost load is 10 \$/kWh, the cost of providing the reservation is 0.4 cents/kWh, and the duration of the reservation is assumed to be 1 hour. Daily costs of planning problem are illustrated in Figure 12. Loss of load probability (LOLP) in the 24 hours is shown in Figure 13.

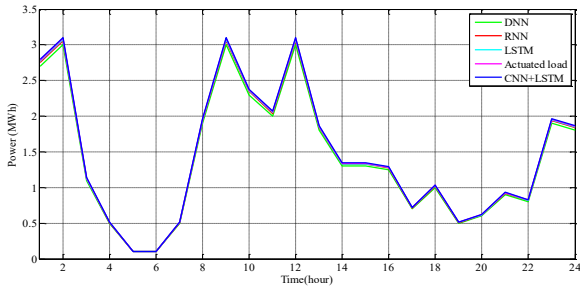


Figure 7. Demand prediction (MW).

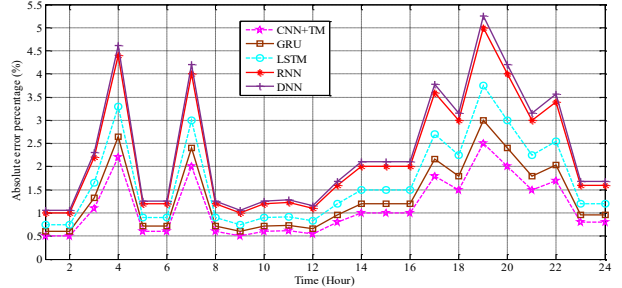


Figure 8. Electrical load.

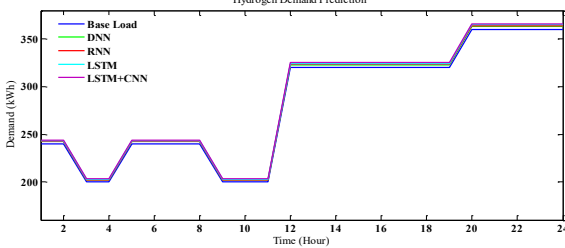


Figure 9. Hydrogen demand.

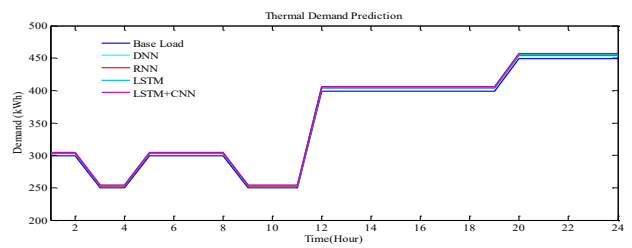


Figure 10. Heat demand.

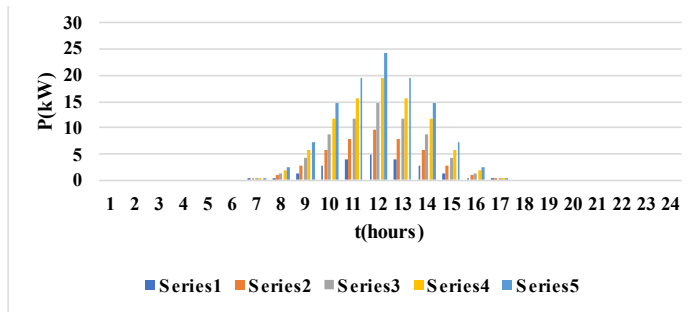


Figure 11. Solar irradiation.

Table 5. Optimal planning solutions.

| | | Without a heat & hydrogen tank | With a heat & hydrogen tank |
|--|------------|--------------------------------|-----------------------------|
| Total net present cost (\$*10 ⁶) | | 8.1564 | 7.8295 |
| Operation cost (\$) | | 3511433 ± 25408 | 3599251 ± 25426 |
| Payback period (year) | | 6.3 | 5.4 |
| IRR (%) | | 28 | 30 |
| CHHP capacity (KW) | Unit 1 | 1100 | 1180 |
| | Unit 2 | 1082 | 1095 |
| PV capacity (kW) | Unit 1 | 400 | 420 |
| | Unit 2 | 280 | 0 |
| LOLE (days/10yrs) | Electrical | 0.92 | 0.94 |
| | Thermal | 0.84 | 0.90 |
| | Hydrogen | 0.80 | 0.82 |
| EENS (kWh/year) | Electrical | 600 | 580 |
| | Thermal | 1320 | 2400 |
| | Hydrogen | 860 | 920 |

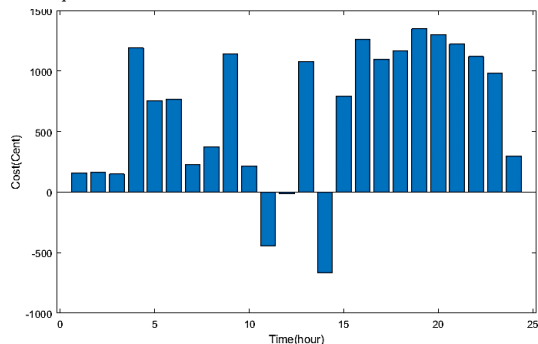


Figure 12. Daily total costs of S-CHHP.

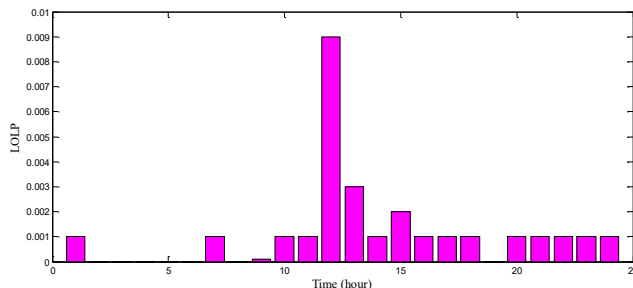


Figure 13. LOLP index.

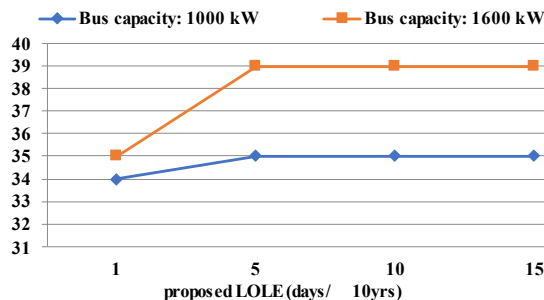


Figure 14. IRR of the proposed problem.

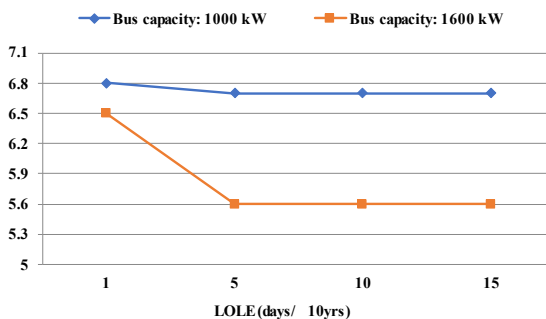


Figure 15. Payback duration in the planning horizon.

4.3. Economic parameter

In this section, the sensitivity of the internal rate of return (IRR) and payback duration in the planning horizon and with the proposed LOLE value are analyzed. Figure 14 shows the IRR values in two allowed exchangeable power with the upstream grid. Figure 15 shows the payback duration changes in the planning horizon. As it is clearly seen from this figure, the payback duration time is reduced by increasing power exchange between the upstream network and the proposed CHHP. Furthermore, considering grid grid-connected bus, the value of IRR for the presented paper is increased. LSTM is used to model system uncertainties.

5. Conclusion

The S-CHHP represents an innovative cogeneration system designed to simultaneously generate hydrogen, thermal energy, and electrical power. This study investigates the optimal configuration of the S-CHHP system by formulating a Markov chain model. Reliability and economic performance are assessed using the LOLP and payback period, respectively, while the accuracy of the proposed model is evaluated via RMSE and MAPE metrics. The optimization problem is addressed using the SSO algorithm. Comparative analysis with alternative prediction approaches demonstrates the effectiveness and superior performance of the proposed method.

References

- [1] A. Jafari, H. G. Ganjehlou, T. Khalili, and A. Bidram, "A Fair Electricity Market Strategy for Energy Management and Reliability Enhancement of Isolated Multi-Microgrids," *Applied Energy*, vol. 270, 115170, 2020.
- [2] M. Abidi, A. B. Rhouma, and J. Belhadj, "Optimal Coordinated Planning of Water-Energy System-Based MILP Algorithm of a Multi-Pump PV Water Station by Deeming Power Commitment," *Electric Power Systems Research*, vol. 220, 109343, 2023.
- [3] E. Akbari, "Stochastic Scheduling of Integrated System of Solar Resources and Hydrogen Storage in the Smart Distribution Network Considering a Multi-Objective Energy Management Model," *Journal of Green Energy Research and Innovation*, vol. 2, no. 3, pp. 44-53, 2025.
- [4] E. Hosseini, P. García-Triviño, et al., "A Novel Reinforcement Learning-Based Multi-Objective Energy Management System for Multi-Energy Microgrids Integrating Electrical, Hydrogen, and Thermal Elements," *Electric Power Systems Research*, vol. 242, 111474, 2025.
- [5] H. Z. Butt, and X. Li, "Enhancing Optimal Microgrid Planning with Adaptive BESS Degradation Costs and PV Asset Management: an Iterative Post-Optimization Correction Framework," *Electric Power Systems Research*, vol. 247, 111785, 2025.
- [6] A. Mansoori, M. Parsa Moghaddam, and H. Delkhosh, "A Hybrid Stochastic-Robust Approach for Power System Security-Constrained Scheduling in the Presence of Flexibility Facilities," *IEEE Transactions on Power Systems*, vol. 39, no. 2, pp. 4064-4076, 2024.
- [7] M. Omri, M. Jooshaki, A. Abbaspour, and M. Fotuhi-Firuzabad, "Modeling Microgrids for Analytical Distribution System Reliability Evaluation," *IEEE Transactions on Power Systems*, vol. 39, no. 5, pp. 6319-6331, 2024.
- [8] Y. Kabiri-Renani, A. Arjomandi-Nezhad, M. Fotuhi-Firuzabad, and M. Shahidehpour, "Transactive-Based Day-Ahead Electric Vehicles Charging Scheduling," *IEEE Transactions on Transportation Electrification*, vol. 10, no. 4, pp. 8235-8245, 2024.
- [9] N. Pourghaderi, M. Fotuhi-Firuzabad, M. Moeini-Aghtaie, M. Kabirifar, and P. Dehghanian, "A Local Flexibility Market Framework for Exploiting DERs' Flexibility Capabilities by a Technical Virtual Power Plant," *IET Renewable Power Generation*, vol. 17, no. 3, pp. 681-695, 2022.
- [10] H. Ghasemi, E. Shahrabi Farahani, et al., "Equipment Failure Rate in Electric Power Distribution Networks: An Overview of Concepts, Estimation, and Modeling Methods," *Engineering Failure Analysis*, vol. 145, 107034, 2023.
- [11] F. K. Alabbas, M. Khalilifar, S. M. Shahrtash, and D. A. Khaburi, "A novel data driven model for voltage stability status prediction and instability mitigation," *International Transactions on Electrical Energy Systems*, vol. 2025, no. 1, p. 6575682, 2025.
- [12] M. Taheri, M. Abedini, and F. Aminifar, "A Novel Centralized Load Shedding Approach to Assess Short-Term Voltage Stability: A Model-Free Using Time Series

- Forecasting," *IEEE Transactions on Power Delivery*, vol. 38, no. 5, pp. 3076–3083, 2023.
- [13] S. Solat, F. Aminifar, A. Safdarian, and H. Shayanfar, "An Expansion Planning Model for Strategic Visioning of Active Distribution Network in the Presence of Local Electricity Market," *IET Generation, Transmission & Distribution*, vol. 17, no. 24, pp. 5410–5429, 2023.
- [14] M. A. A. Al-Ja'afreh, G. Mokryani, and B. Amjad, "An Enhanced CNN-LSTM Based Multi-Stage Framework for PV and Load Short-Term Forecasting: DSO Scenarios," *Energy Reports*, vol. 10, pp. 1387–1408, 2023.
- [15] J. A. Marquez, M. A. A. Al-Ja'afreh, et al., "Optimal Planning and Operation of Distribution Systems Using Network Reconfiguration and Flexibility Services," *Energy Reports*, vol. 9, pp. 3910–3919, 2023.
- [16] M. H. Shariatkhah, M. R. Haghifam, and M. A. Paqaleh, "Simultaneous Placement of DGs and Capacitors in Distribution Networks—Determining the Optimum Configuration," *Energy Engineering and Management*, vol. 1, no. 1, pp. 11–18, 2023.
- [17] R. Khalilzadeh, and M. R. Haghifam, "Planning and Comparing a Pure AC or a Hybrid AC/DC Distribution Network: A Case Study for an Urban Zone and an Industrial Park," *Journal of Iranian Association of Electrical and Electronics Engineers*, vol. 20, no. 2, pp. 77–86, 2023.
- [18] M.-A. Efstratiadis, S. Tsakanikas, P. Papadopoulos, and D. R. Salinas, "A Novel Holistic Energy Management System Incorporating PV Generation and Battery Storage for Commercial Customers," *IEEE Transactions on Sustainable Energy*, vol. 15, no. 3, pp. 1475–1485, 2024.
- [19] A. Ntafalias, S. Tsakanikas, et al., "Design and Implementation of an Interoperable Architecture for Integrating Building Legacy Systems into Scalable Energy Management Systems," *Smart Cities*, vol. 5, no. 4, pp. 1421–1440, 2022.
- [20] Y. Zhou, J. Wu, and W. Gan, "P2P Energy Trading Via Public Power Networks: Practical Challenges, Emerging Solutions, and the Way Forward," *Frontiers in Energy*, vol. 17, no. 2, pp. 189–197, 2023.
- [21] R. Bo, L. Bai, et al., "Special Section on Local and Distributed Electricity Markets," *IEEE Transactions on Smart Grid*, vol. 14, no. 2, pp. 1347–1352, 2023.
- [22] L. Zhang, J. Li, et al., "High Spatial Granularity Residential Heating Load Forecast Based on Dendrite Net Model," *Energy*, vol. 269, 126787, 2023.
- [23] Y. Cai, X. Xu, J. Liu, X. Yu, and H. Jia, "Coordinative Control of Hydropower Plant and Industrial Thermostatically Controlled Loads for Frequency Response," *2023 IEEE Power & Energy Society General Meeting (PESGM)*, pp. 1–5, 2023.
- [24] V. Bafandegan Emroozi, and M. Doostparast, "Markov Chain-Based Model for IoT-Driven Maintenance Planning with Human Error and Spare Part Considerations," *Reliability Engineering & System Safety*, vol. 261, 111052, 2025.
- [25] R. Rostami, and H. Hosseinnia, "Energy Management of Reconfigurable Distribution System in Present of Wind Turbine by Considering Several Kinds of Demands," *7th Iran Wind Energy Conference (IWEC2021)*, pp. 1–4, 2021.
- [26] M. Hemmati, N. Amjadi, and M. Ehsan, "Islanded Micro-Grid Modeling and Optimization of its Operation Considering Cost of Energy not Served by an Enhanced Differential Search Algorithm," *Energy Engineering and Management*, vol. 3, no. 4, pp. 2–13, 2023.
- [27] S. Rezaeian, N. Bayat, A. Rabiee, S. Nikkhal, and A. Soroudi, "Optimal Scheduling of Reconfigurable Microgrids in Both Grid-Connected and Isolated Modes Considering the Uncertainty of DERs," *Energies*, vol. 15, no. 15, 5369, 2022.
- [28] S. Toghraanegar, A. Rabiee, and A. Soroudi, "Enhancing the Unbalanced Distribution Network's Hosting Capacity for DERs Via Optimal Load Re-Phasing," *Sustainable Cities and Society*, vol. 87, 104243, 2022.
- [29] M. Zamudio López, H. Zareipour, and M. Quashie, "Forecasting the Occurrence of Electricity Price Spikes: A Statistical-Economic Investigation Study," *Forecasting*, vol. 6, no. 1, pp. 115–137, 2024.
- [30] N. Daryani, K. Zare, S. Tohidi, J. M. Guerrero, and N. Bazmohammadi, "Optimal Construction of Microgrids in a Radial Distribution System Considering System Reliability Via Proposing Dominated Group Search Optimization Algorithm," *Sustainable Energy Technologies and Assessments*, vol. 63, 103622, 2024.
- [31] Y. Zou, and M. Čepin, "Loss of Load Probability for Power Systems Based on Renewable Sources," *Reliability Engineering & System Safety*, vol. 247, 110136, 2024.
- [32] N. Popli, E. Davoodi, F. Capitanescu, and L. Wehenkel, "Machine Learning Based Binding Contingency Pre-Selection for AC-PSCOPF Calculations," *IEEE Transactions on Power Systems*, vol. 39, no. 2, pp. 4751–4754, 2024.
- [33] Y. Xie, S. Wang, et al., "Optimized Multi-Hidden Layer Long Short-Term Memory Modeling and Suboptimal Fading Extended Kalman Filtering Strategies for the Synthetic State of Charge Estimation of Lithium-Ion Batteries," *Applied Energy*, vol. 336, 120866, 2023.
- [34] D. Pagnani, Ł. Kocewiał, J. Hjerrild, F. Blaabjerg, and C. L. Bak, "Integrating Black Start Capabilities into Offshore Wind Farms by Grid-forming Batteries," *IET Renewable Power Generation*, vol. 17, no. 14, pp. 3523–3535, 2023.

Declaration of competing interest

The authors declare that they have no known competing financial interests or personal relationships that could have appeared to influence the work reported in this paper. The ethical issues, including plagiarism, informed consent, misconduct, data fabrication and/or falsification, double publication and/or submission, redundancy, have been completely observed by the authors.

Bibliography



Mojtaba Pirmohammad Talatape was born in Iran, in 1992. He is currently a PhD student at Islamic Azad University, Arak Branch. He is currently a lecturer at Azad University and manager of the charging department in a private company. He works as the manager of the charging unit in the field of car batteries, UPS and reverse charging, and since 2022, he has been working as a referee for international conferences in the field of electricity distribution and renewable energy. His research interests are power system stability, reactive power control in transmission and distribution systems, power quality studies and electric energy production in renewable systems and related issues.

Email: Pirmomojtaba1372@gmail.com

ORCID: [0000-0002-4587-1403](https://orcid.org/0000-0002-4587-1403)

Contribution Statement: Conceptualization, Data curation, Investigation, Software, Validation, Roles/Writing - original draft, Writing-review & editing.



Sajad Bagheri was born in Arak, Iran, in 1989. He received the Ph.D. degree in electrical engineering from Semnan University, Semnan, Iran, in 2017. He is currently an Assistant Professor with the Electrical Engineering Faculty, Islamic Azad University, Arak Branch, Arak, Iran. Also, he is research Consultant of the Markazi province electric distribution company. His research interests include power system protection, Diagnosis, condition monitoring and detection of winding movement of power transformers and Renewable Resources. Dr. Bagheri is a member of the Young Researchers and Elite Club, the Iranian Wind Energy Association and the Iranian Society of Smart Grid. Also, He was selected as the top Researcher at the universities of Markazi province in the field of electrical engineering and top Researcher of Young researchers and Elite Club of Islamic Azad University, Arak Branch at 2016 & 2019.

Email: Sajad.bagheri@iau.ac.ir

ORCID: [0000-0002-3553-5510](https://orcid.org/0000-0002-3553-5510)

Contribution Statement: Conceptualization, Formal analysis, Investigation, Methodology, Supervision, Validation, Writing-review & editing.



Reza Ghanizadeh was born in Mianeh, Iran, in 1987. He received his B.Sc. degree in Electrical Engineering from University of Mohaghegh Ardabili, Ardabil, Iran, in 2008, and his M.Sc. degree from University of Birjand, Birjand, Iran, in 2012. He is currently working as an assistant professor at Urmia Azad University. His research interests are power system stability, reactive power control in transmission & distribution systems, power quality studies and FACTS devices.

Email: reza.ghanizadeh@iau.ac.ir

ORCID: [0000-0003-2093-0267](https://orcid.org/0000-0003-2093-0267)

Contribution Statement: Visualization, Writing-review & editing.



Mohammad Reza Miveh received his Ph.D. degree in Electrical Engineering from Universiti Teknologi Malaysia (UTM), Malaysia, in 2017. Currently, he is an Assistant Professor with the Department of Electrical Engineering, Tafresh University, Iran. His main research interests include control and protection of large-scale hybrid AC/DC grids, distributed generation and microgrids.

Email: miveh@tafreshu.ac.ir

ORCID: [0000-0002-6130-6703](https://orcid.org/0000-0002-6130-6703)

Contribution Statement: Investigation, Methodology, Resources.

Flexible Energy Scheduling in the Electrical, Thermal, and Gas Networks, including Energy Hubs with Renewables and Flexible Units

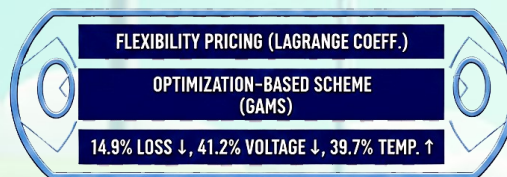
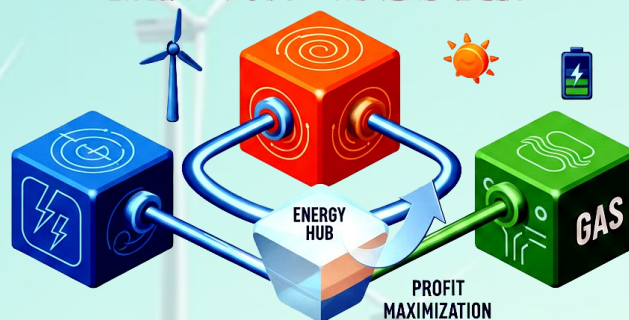
Naghi Moaddabi Pirkolachahi, Mehrdad Mallaki, Najmeh Charaghi Shirazi, Mousa Hamrahi

Highlights

- ❖ Development of a comprehensive flexibility model for energy hubs.
- ❖ Introduction of a methodology for flexibility pricing.
- ❖ Advancement in energy network flexibility management across diverse systems.

Graphical Abstract

FLEXIBLE ENERGY SCHEDULING ELECTRICAL, THERMAL, & GAS NETWORKS ENERGY HUBS + RENEWABLES



KEYWORDS: FLEXIBILITY, ENERGY HUB, OPTIMIZATION

Use your device to scan
and read the article
online



Citation

M. Hamrahi, M. Mallaki, N. Moaddabi Pirkolachahi, and N. Cheraghi Shirazi, "Flexible Energy Scheduling in the Electrical, Thermal and Gas Networks including Energy Hubs with Renewables and Flexible Units," *Journal of Green Energy Research and Innovation*, vol. 2, no. 4, pp. 58-66, 2025.



<https://doi.org/10.61882/jgeri.2.4.58>





Online ISSN: 3041-9018

Journal of Green Energy Research and Innovation

Journal Homepage: www.jgeri.araku.ac.ir

Flexible Energy Scheduling in the Electrical, Thermal, and Gas Networks, including Energy Hubs with Renewables and Flexible Units

Mousa Hamrahi, Mehrdad Mallaki^{*}, Naghi Moaddabi Pirkolachahi, Najmeh Charaghi Shirazi

Department of Electrical Engineering, Bu.C., Islamic Azad University, Bushehr, Iran.

ARTICLE INFO

Keywords:

Flexibility pricing,
Grid-connected energy hub,
Flexible energy management,
Penalty function,
Operation limit.

Article History:

Received: 25 May 2025

Revised: 01 July 2025;

Accepted: 31 July 2025.

Article type:

Research Article

* Corresponding authors

E-mail address

mallaki@aut.ac.ir (M. Mallaki)

ABSTRACT

This paper addresses the issue of flexibility pricing for grid-connected energy hubs (EHs) under the influence of uncertain energy generation resources. An optimization-based scheme is proposed to tackle this challenge. The objective of the problem is to maximize the profitability of these resources within the flexibility market. Key constraints include the flexibility model of energy storage systems, load response mechanisms, and controllable distributed generation units. Additional restrictions involve the optimal load distribution equations across energy networks, the utilization model of EHs incorporating various active resources and loads, as well as the flexibility constraints specific to EHs. The flexibility model hinges on the active power generated by these resources. The flexibility price is determined by the Lagrange coefficients corresponding to the flexibility constraint. To compute this price, a penalty function associated with the flexibility constraint is incorporated into the objective function. The proposed framework is implemented in the GAMS software environment and tested on a 9-bus electric grid, a 4-bus gas system, and a 7-bus thermal network. Ultimately, the scheme's effectiveness in enhancing operational performance, flexibility, and economic outcomes for both energy networks and EHs is thoroughly analyzed. So that based on optimal operation of resources, storage devices, and responsive loads, total energy losses, maximum voltage drop, and temperature improvements of approximately 14.9%, 41.2%, and 39.7%, respectively, when compared to load distribution studies.

1. Introduction

Concerns over environmental pollution stemming from excessive fossil fuel consumption have prompted various organizations to advocate for the adoption of environmentally friendly energy sources. As a result, recent years have seen a notable rise in the integration of renewable energy sources (RES), such as wind and solar systems, into power grids. Additionally, deploying distributed generation (DG) at local consumption points diminishes reliance on centralized power plants, contributing to reduced emissions from these plants. DG technologies, including fuel cells (FC), microturbines (MT), diesel generators (DiG), and combined heat and power (CHP) systems, exhibit significantly lower pollution levels compared to traditional power plants. Moreover, energy storage systems (ESSs) and demand response programs (DRPs) play a crucial role in curbing pollution by minimizing energy losses at the consumption level. Even mobile ESSs, such as electric vehicles (EVs), contribute to reducing emissions typically associated with conventional fossil fuel-powered vehicles. However, achieving meaningful environmental benefits from these advancements relies heavily on integrating a substantial number of resources and active loads (ALs) into the power grid, particularly within distribution networks. This increased volume of data poses significant challenges for distribution system operators (DSOs), complicating network management processes. To address these complexities, smart grid principles advocate for employing resource aggregators and active loads within configurations such as virtual power plants (VPPs) and energy hubs (EHs). Managing multiple energy types simultaneously proves more effective than handling them individually, especially given the interconnected nature of diverse technologies like CHP systems. Considering the interdependence among various energy sources and the need for cohesive coordination, adopting the EH model offers an efficient framework for managing distributed energy resources and active loads comprehensively.

Numerous studies and research endeavors have focused on integrating energy hubs (EHs) into various energy networks. In reference [1], the authors explored the stochastic modeling of grid-connected EH participation in the day-ahead (DA) energy market. This study utilized EHs to coordinate RES, CHP, electric vehicle (EV) parking, battery storage, and DRP. By employing a linear approximation model, the problem in [1] was solved with optimal solutions with reduced computational time. Findings from this study demonstrated that the coordinated management of resources and ALs within the EH framework provided greater financial benefits compared to their independent operation. Additionally, the optimal scheduling of EHs significantly enhanced key performance metrics for electricity, gas, and heat networks. This improvement included reduced energy losses, as shown in power distribution studies, and smoother voltage, pressure, and temperature profiles. In study [2], EHs were employed to coordinate RES, batteries, and CHP systems, focusing on their role in the electricity, gas, and heat sectors. The electricity component of the EH participated in two energy market models: power pool and bilateral contracts. Results from [2] supported the findings of [1], confirming the capability of EHs in improving both the operational performance and economic outcomes of the integrated networks. The stochastic operational model of EHs analyzed in [3] incorporated renewable sources, a combined cooling, heating, and power (CCHP) system, various storage solutions, and DRPs. Leveraging storage significantly reduced operating costs. A comparable model was examined in [4], which extended the implementation to EHs connected to a microgrid. To ensure computational efficiency, [4] also adopted a linear approximation model, achieving an optimal solution with minimal error—approximately 2.5% for active and reactive power across scenarios [1-2,4]. The reliability of EHs under N-1 contingency events (i.e., element failure) was investigated in the study [5]. The results highlighted the capacity of optimally scheduled EH resources and ALs to maintain high reliability. In [6], a scenario-based stochastic operational analysis was conducted for residential EHs while considering RES uncertainties, EVs, and thermal energy storage (TES). This study also incorporated Monte Carlo simulations (MCS) to account for fluctuations in energy prices and active power output by distributed generation resources (RDGs). Findings revealed that EVs and TES played significant roles in reducing operational costs for EHs. Notably, formulating the operational framework for energy networks with EH integration is inherently nonlinear. Studies such as [1-2] and [4] employed linear approximation models (LAM) to simplify these problems for computational efficiency. Other research works, including [7-8], utilized non-linear heuristic evolutionary algorithms (NHEA) to determine optimal solutions. These included methods like modified teaching-learning-based optimization (MTLBO) in [7] and genetic algorithms (GA) in [8]. Robust modeling techniques have also been applied to address uncertainties by focusing on worst-case scenarios to derive optimized solutions. Robust optimization approaches typically exhibit lower computational time compared to stochastic programming while ensuring a favorable performance across other scenarios beyond the worst-case outcome. For instance, study [9] presented robust modeling strategies that ensured robust optimization outcomes were superior to traditional optimal responses in standard scenarios. Meanwhile, reference [10] introduced a bounded uncertainty robust optimization (BURO) method. This approach aligned uncertainty parameters with their upper or lower bounds as they related to their positions within the original problem formulation. In conclusion, extensive research has underscored the versatility of EHs in improving energy network performance and economic outcomes while leveraging advanced modeling techniques such as stochastic programming, linear approximations, heuristic algorithms, and robust optimization methodologies to address operational challenges efficiently.

The text highlights several research gaps, particularly in the domain of system flexibility modeling. Although substantial research has been conducted across diverse fields, notably energy hubs and other systems, the aspect of flexibility modeling remains inadequately explored. Accurately determining the status of a system's indicator requires numerical results that can only be obtained through mathematical modeling. Therefore, to assess the flexibility status of energy networks and EHs, integrating a mathematical model of the targeted flexibility indicator into the operational analysis of these networks is critical. Energy hubs offer multiple flexibility resources such as stationary and mobile ESSs, DRPs, and controllable distributed generation units. These resources are anticipated not only to provide essential flexibility services but also to generate financial gains through their participation. This dual-purpose approach presents an efficient method for involving these resources in flexibility services. However, the academic and practical discourse around this topic has been relatively minimal, leaving significant research gaps unaddressed. To address these gaps, this paper introduces a framework for tackling the flexibility pricing problem in grid-connected energy hubs under conditions of uncertain energy generation. The proposed solution employs an optimization-based approach, aiming to maximize the financial benefits of these resources within the flexibility market. The problem formulation incorporates constraints such as the flexibility models of energy storage systems, responsive loads, and controllable distributed generation. Additional constraints include optimal load distribution equations for energy networks, utilization models for EHs with integrated active resources and loads, and specific flexibility limitations of EHs. The flexibility models for these resources depend on their active power contributions to the system. To quantify flexibility pricing, the Lagrange multipliers associated with the flexibility constraints are utilized. A penalty function corresponding to these constraints is incorporated into the objective function, ensuring accurate pricing. The key contributions of this work are summarized as follows: 1) Development of a comprehensive flexibility model for energy hubs. 2) Introduction of a methodology for flexibility pricing. 3) Advancement in energy network flexibility management across diverse systems.

Section 2 outlines the problem's formulation. Section 3 details the test system. Section 4 provides the numerical results, followed by the conclusion in Section 5.

2. Formulation

Formulation of the problem is as Equation (1).

$$\begin{aligned} \max \quad \text{Profit} = & \sum_s \rho_s \sum_{i,t} \left(\bar{\lambda}_{i,t,s}^{ef} EF_{i,t,s}^U + \underline{\lambda}_{i,t,s}^{ef} EF_{i,t,s}^D \right) + \\ & \sum_s \rho_s \sum_{i,t} \left(\bar{\lambda}_{i,t,s}^{hf} HF_{i,t,s}^U + \underline{\lambda}_{i,t,s}^{hf} HF_{i,t,s}^D \right) \end{aligned} \quad (1)$$

Subject to Equations (2)-(48).

$$EF_{i,t,s}^U = UF_{i,t,s}^{DRPe} + UF_{i,t,s}^{EES} + UF_{i,t,s}^{CHP} \quad \forall i,t,s \tag{2}$$

$$EF_{i,t,s}^D = DF_{i,t,s}^{DRPe} + DF_{i,t,s}^{EES} + DF_{i,t,s}^{CHP} \quad \forall i,t,s \tag{3}$$

$$HF_{i,t,s}^U = UF_{i,t,s}^{DRPh} + UF_{i,t,s}^{TES} \quad \forall i,t,s \tag{4}$$

$$HF_{i,t,s}^D = DF_{i,t,s}^{DRPh} + DF_{i,t,s}^{TES} \quad \forall i,t,s \tag{5}$$

$$UF_{i,t,s}^{DRPe} - DF_{i,t,s}^{DRPe} = P_{i,t,s}^{DRP} - P_{i,t,s=1}^{DRP} \quad \forall i,t,s \tag{6}$$

$$UF_{i,t,s}^{EES} - DF_{i,t,s}^{EES} = (P_{i,t,s}^{DCH} - P_{i,t,s}^{CH}) - (P_{i,t,s=1}^{DCH} - P_{i,t,s=1}^{CH}) \quad \forall i,t,s \tag{7}$$

$$UF_{i,t,s}^{CHP} - DF_{i,t,s}^{CHP} = P_{i,t,s}^{CHP} - P_{i,t,s=1}^{CHP} \quad \forall i,t,s \tag{8}$$

$$UF_{i,t,s}^{DRPh} - DF_{i,t,s}^{DRPh} = H_{i,t,s}^{DRP} - H_{i,t,s=1}^{DRP} \quad \forall i,t,s \tag{9}$$

$$UF_{i,t,s}^{TES} - DF_{i,t,s}^{TES} = (H_{i,t,s}^{DCH} - H_{i,t,s}^{CH}) - (H_{i,t,s=1}^{DCH} - H_{i,t,s=1}^{CH}) \quad \forall i,t,s \tag{10}$$

$$UF, DF \geq 0 \quad \forall i,t,s \tag{11}$$

$$P_{ne,t,s}^S + \sum_i K_{ne,i}^E P_{i,t,s}^{EH} - \sum_l L_{ne,l}^E P_{ne,l,t,s}^L = P_{ne,t,s}^D \quad \forall ne,t,s \tag{12}$$

$$Q_{ne,t,s}^S + \sum_i K_{ne,i}^E Q_{i,t,s}^{EH} - \sum_l L_{ne,l}^E Q_{ne,l,t,s}^L = Q_{ne,t,s}^D \quad \forall ne,t,s \tag{13}$$

$$H_{nh,t,s}^S + \sum_i K_{nh,i}^H H_{i,t,s}^{EH} - \sum_l L_{nh,l}^H H_{nh,l,t,s}^L = H_{nh,t,s}^D \quad \forall nh,t,s \tag{14}$$

$$G_{ng,t,s}^S + \sum_i K_{ng,i}^G G_{i,t,s}^{EH} - \sum_l L_{ng,l}^G G_{ng,l,t,s}^L = G_{ng,t,s}^D \quad \forall ng,t,s \tag{15}$$

$$P_{ne,l,t,s}^L = g_{ne,l}^L (V_{ne,t,s})^2 - V_{ne,t,s} V_{l,t,s} \{ g_{ne,l}^L \cos(\alpha_{ne,t,s} - \alpha_{l,t,s}) + b_{ne,l}^L \sin(\alpha_{ne,t,s} - \alpha_{l,t,s}) \} \quad \forall ne,l,t,s \tag{16}$$

$$Q_{ne,l,t,s}^L = -b_{ne,l}^L (V_{ne,t,s})^2 + V_{ne,t,s} V_{l,t,s} \{ b_{ne,l}^L \cos(\alpha_{ne,t,s} - \alpha_{l,t,s}) - g_{ne,l}^L \sin(\alpha_{ne,t,s} - \alpha_{l,t,s}) \} \quad \forall ne,l,t,s \tag{17}$$

$$H_{nh,l,t,s}^L = \varpi_{nh,l} (T_{nh,t,s} - T_{l,t,s}) \quad \forall nh,l,t,s \tag{18}$$

$$G_{ng,l,t,s}^L = v_{ng,l} \text{sign}(\beta_{ng,t,s}, \beta_{l,t,s}) \sqrt{\text{sign}(\beta_{ng,t,s}, \beta_{l,t,s}) ((\beta_{ng,t,s})^2 - (\beta_{l,t,s})^2)} \quad \forall ng,l,t,s \tag{19}$$

$$V_{ne}^{\min} \leq V_{ne,t,s} \leq V_{ne}^{\max} \quad \forall ne,t,s \tag{20}$$

$$T_{nh}^{\min} \leq T_{nh,t,s} \leq T_{nh}^{\max} \quad \forall nh,t,s \tag{21}$$

$$\beta_{ng}^{\min} \leq \beta_{ng,t,s} \leq \beta_{ng}^{\max} \quad \forall ng,t,s \tag{22}$$

$$\sqrt{(P_{ne,l,t,s}^L)^2 + (Q_{ne,l,t,s}^L)^2} \leq S_{ne,l}^{L \max} \quad \forall ne,l,t,s \tag{23}$$

$$-H_{nh,l,t,s}^{L \max} \leq H_{nh,l,t,s}^L \leq H_{nh,l,t,s}^{L \max} \quad \forall nh,l,t,s \tag{24}$$

$$-G_{ng,l,t,s}^{L \max} \leq G_{ng,l,t,s}^L \leq G_{ng,l,t,s}^{L \max} \quad \forall ng,l,t,s \tag{25}$$

$$\sqrt{(P_{ne,t,s}^S)^2 + (Q_{ne,t,s}^S)^2} \leq S_{ne}^{S \max} \quad \forall ne = o,t,s \tag{26}$$

$$-H_{nh}^{S \max} \leq H_{nh,t,s}^S \leq H_{nh}^{S \max} \quad \forall nh = o,t,s \tag{27}$$

$$-G_{ng}^{S \max} \leq G_{ng,t,s}^S \leq G_{ng}^{S \max} \quad \forall ng = o,t,s \tag{28}$$

$$P_{i,t,s}^{EH} = P_{i,t,s}^{CHP} + P_{i,t,s}^{RES} + P_{i,t,s}^{DRP} + (P_{i,t,s}^{DCH} - P_{i,t,s}^{CH}) - P_{i,t,s}^D \quad \forall i,t,s \tag{29}$$

$$Q_{i,t,s}^{EH} = Q_{i,t,s}^{CHP} - Q_{i,t,s}^D \quad \forall i,t,s \tag{30}$$

$$H_{i,t,s}^{EH} = H_{i,t,s}^{CHP} + H_{i,t,s}^{DRP} + (H_{i,t,s}^{DCH} - H_{i,t,s}^{CH}) - H_{i,t,s}^D \quad \forall i,t,s \tag{31}$$

$$G_{i,t,s}^{EH} = -G_{i,t,s}^{CHP} - G_{i,t,s}^D \quad \forall i,t,s \tag{32}$$

$$H_{i,t,s}^{CHP} = P_{i,t,s}^{CHP} \frac{(1 - \eta^T - \eta^L) \eta^H}{\eta^T} \quad \forall i,t,s \tag{33}$$

$$G_{i,t,s}^{CHP} = P_{i,t,s}^{CHP} \frac{1}{\eta^T} \quad \forall i,t,s \tag{34}$$

$$\sqrt{(P_{i,t,s}^{CHP})^2 + (Q_{i,t,s}^{CHP})^2} \leq S_i^{CHP \max} \quad \forall i,t,s \tag{35}$$

$$-H_i^{CHP \max} \leq H_{i,t,s}^{CHP} \leq H_i^{CHP \max} \quad \forall i,t,s \tag{36}$$

$$-\omega_t P_{i,t,s}^D \leq P_{i,t,s}^{DRP} \leq \omega_t P_{i,t,s}^D \quad \forall i,t,s \quad (37)$$

$$\sum_i P_{i,t,s}^{DRP} = 0 \quad \forall i,s \quad (38)$$

$$-\omega_t H_{i,t,s}^D \leq H_{i,t,s}^{DRP} \leq \omega_t H_{i,t,s}^D \quad \forall i,t,s \quad (39)$$

$$\sum_i H_{i,t,s}^{DRP} = 0 \quad \forall i,s \quad (40)$$

$$0 \leq P_{i,t,s}^{CH} \leq ECR_i \quad \forall i,t,s \quad (41)$$

$$0 \leq P_{i,t,s}^{DCH} \leq EDR_i \quad \forall i,t,s \quad (42)$$

$$E_i^{\min} \leq EI_i + \sum_{h=1}^t \left(\eta_i^{CH} P_{i,h,s}^{CH} - \frac{1}{\eta_i^{DCH}} P_{i,h,s}^{DCH} \right) \leq E_i^{\max} \quad \forall i,t,s \quad (43)$$

$$0 \leq H_{i,t,s}^{CH} \leq HCR_i \quad \forall i,t,s \quad (44)$$

$$0 \leq H_{i,t,s}^{DCH} \leq HDR_i \quad \forall i,t,s \quad (45)$$

$$E_i^{\min} \leq EI_i + \sum_{h=1}^t \left(\eta_i^{CH} H_{i,h,s}^{CH} - \frac{1}{\eta_i^{DCH}} H_{i,h,s}^{DCH} \right) \leq E_i^{\max} \quad \forall i,t,s \quad (46)$$

$$-\Delta F \leq P_{i,t,s}^{EH} - P_{i,t,s=1}^{EH} \leq \Delta F : \underline{\lambda}_{i,t,s}^{ef}, \bar{\lambda}_{i,t,s}^{ef} \quad \forall i,t,s \quad (47)$$

$$-\Delta F \leq H_{i,t,s}^{EH} - H_{i,t,s=1}^{EH} \leq \Delta F : \underline{\lambda}_{i,t,s}^{hf}, \bar{\lambda}_{i,t,s}^{hf} \quad \forall i,t,s \quad (48)$$

This section focuses on the expected profit maximization of flexibility sources (FSs) deriving from offering flexibility services in energy hubs (EHs), as defined by the objective function in Equation (1) [11]. In the context of flexibility management, two operational models are examined: 1. When the real-time (RT) RES power exceeds the DA scheduled power. Here, FSs are required to reduce their power injection into the system during RT operation compared to the DA operation. This is referred to as the downward flexibility operating mode. 2. Conversely, when the RT RES power is less than the DA scheduled power, FSs operate in the inverse manner of the first mode, described as upward flexibility. As such, flexibility pricing in Equation (1) accounts for these two operational modes: downward and upward. The first term of the equation captures the revenue earned by electric FSs from providing flexibility services in the electrical domain of EHs [11]. The second term addresses the benefits gained from providing flexibility services within the thermal domain. In Equations (2) and (3), the total flexible power provided by electric FSs under upward and downward operational modes in EHs is modeled. Correspondingly, Equations (4) and (5) establish a similar representation for the thermal domain within EHs. Equations (6) through (10) detail the flexible power contributions across different components: electric DRP, EES, CHP, thermal DRP, and TES under both operational modes. To enhance flexibility from a modeling standpoint, minimizing system deviations in active (thermal) power under scenarios relative to those in a deterministic scenario (scenario 1, based on predicted uncertainties) is crucial. Within Equations (6)-(10), flexible power for FSs is computed as the difference between the active power of FSs under scenario s and the baseline deterministic scenario. A positive deviation value represents flexible power under the upward operating mode; otherwise, it corresponds to downward operation. Notably, these power values always remain positive as defined in Equation (11). The network Equations for this model are detailed within Equations (12)-(28). Equations (12)-(19) represent the power distribution model across electrical, thermal, and gas networks [12-14]. Specifically, Equations (12) and (13) handle active and reactive power balances across electrical network buses, respectively. Equation (14) ensures thermal power balance at thermal network nodes, while Equation (15) addresses gas power balance within gas network nodes. Similarly, Equations (16)-(19) calculate active and reactive power flow through electric lines, thermal power flow within heat pipes, and gas power flow passing through gas pipelines. Operational restrictions across networks are presented in Equations (20)-(28): Voltage, temperature, and pressure range limitations are incorporated in Equations (20), (21), and (22), respectively. Apparent power limits for electric lines, along with thermal and gas flow limits for pipelines, are included in Equations (23)-(25). Analogous limitations for substations servicing electrical, thermal, and gas networks are outlined in Equations (26)-(28) [15-17].

The performance formulation of EHs is detailed across Equations (29)-(48). Equations (29)-(32) specifically model the balancing of active, reactive, thermal, and gas power within EHs. The operational modeling of CHP systems is described in Equations (33)-(36). Here, Equations (33) and (34) determine the thermal and gas power generated by the CHP, derived from its active power output. Meanwhile, the limitations of CHP's output capacity for electrical and thermal energy are addressed in Equations (35) and (36), respectively [10-11]. The electrical DRP framework appears in Equations (37)-(38) [18]. Equation (37) incorporates the active power control range into the program. Within this program, it is assumed that the energy demands of consumers must be fully met within the operational time horizon, and this requirement is enforced by Equation (38). Similarly, the thermal DRP performance follows a comparable structure to its electrical counterpart, aligning with Equations (39)-(40) while sharing Equations (37),(38). The main distinction lies in replacing variable P with variable H to represent thermal power. In this study, the gas network is treated solely as a source for CHP-generated electricity or heat; hence, no DRP model is considered for gas usage. The functional model for EES is laid out in Equations (41)-(43) [19]. Notably, an aggregation model for EVs shares similarities with these Equations but incorporates time (t) and scenario (s) indices to account for dynamic EV connectivity to EHs. Parameters such as ECR , EDR , EI , $Emin$, and $Emax$ adjust based on these indices. At any given moment or scenario, ECR and EDR represent the cumulative charging and discharging rates of EVs connected to the EH.

Hourly EI reflects the initial energy contributions of newly connected EVs during that time. $Emin$ corresponds to the aggregated

minimum energy levels of all connected EVs, while E_{max} signifies the total future trip energy requirements of these vehicles. In the EV aggregation model's Equations, the equality operator replaces the less-than-or-equal-to operator from Equation (43) [1,10]. The formulation for TES operation is presented in Equations (44)-(46), mimicking the structure of Equations (41)-(43) but substituting variable P with H to reflect thermal energy considerations. Finally, EH flexibility constraints for the electrical and thermal sectors are expressed through Equations (47) and (48). From a mathematical modeling perspective, enhancing flexibility involves minimizing deviations in active or thermal power outputs in a given scenario when compared to those in the baseline deterministic model (scenario $s = 1$) [20]. Equations (47) and (48) impose an upper limit of ΔF on these deviations, where ΔF represents flexibility tolerance. Setting ΔF to zero implies complete (100%) flexibility. The dual variables associated with these constraints correspond to flexibility prices [11]. Flexibility prices are derived by incorporating the penalty functions of Equations (47) and (48) into the objective function as detailed in Equation (49). This enables simultaneous calculation of both primary and dual variables by the solver. For a constraint of the form $a \leq b$, the corresponding penalty function is defined as $\lambda \cdot \max(0, a - b)$, where λ represents the dual variable of the constraint.

$$\begin{aligned} \max \text{ Profit} = & \sum_s \rho_s \sum_{i,t} \left(\bar{\lambda}_{i,t,s}^{ef} EF_{i,t,s}^U + \underline{\lambda}_{i,t,s}^{ef} EF_{i,t,s}^D \right) + \\ & \sum_s \rho_s \sum_{i,t} \left(\bar{\lambda}_{i,t,s}^{hf} HF_{i,t,s}^U + \underline{\lambda}_{i,t,s}^{hf} HF_{i,t,s}^D \right) + \\ & \sum_{i,t,s} \left(\bar{\lambda}_{i,t,s}^{ef} \max(0, P_{i,t,s}^{EH} - P_{i,t,s=1}^{EH} - \Delta F) + \underline{\lambda}_{i,t,s}^{ef} \max(0, -\Delta F - P_{i,t,s}^{EH} + P_{i,t,s=1}^{EH}) \right) + \\ & \sum_{i,t,s} \left(\bar{\lambda}_{i,t,s}^{hf} \max(0, H_{i,t,s}^{EH} - H_{i,t,s=1}^{EH} - \Delta F) + \underline{\lambda}_{i,t,s}^{hf} \max(0, -\Delta F - H_{i,t,s}^{EH} + H_{i,t,s=1}^{EH}) \right) \end{aligned} \tag{49}$$

3. Test system

The proposed scheme has been implemented on three types of ring networks: a 9-bus electric network, a 4-bus gas network, and a 7-bus thermal network, as illustrated in Figure 1. Detailed data for these networks can be found in [1]. The hourly load for each network is determined as the product of the peak load and the daily load factor curve, also provided in [1]. The system includes 7 EHs, whose specific locations across the different networks are depicted in Figure 1. The peak loads of these EHs, along with their components, are outlined in [1]. Two RESs are incorporated into the scheme: wind turbines (WT) and photovoltaic (PV) systems. Each has a maximum capacity of 0.25 MW, and their hourly power output is calculated by multiplying their respective capacities by a daily power generation rate curve, as documented in [1]. The scheme also utilizes two types of EES: batteries and EV aggregations. The battery specifications include a storage capacity ranging from 0.2 MWh to 1.5 MWh, with an initial energy level of 0.2 MWh. It features charging and discharging rates of 0.8 MW and an efficiency of 90% for both operations. Additionally, the system assumes the presence of 60 EVs within the EHs equipped with EV parking facilities. The number of EVs fluctuates hourly based on the product of total EVs and a daily penetration rate curve, as described in [1,11]. Key characteristics of individual EVs, including charging and discharging rates, efficiency, and energy consumption details, are also reported in [11]. Within the EHs, consumer participation in the proposed DRP is set at 40%. Furthermore, CHP units are integrated in EHs 4, 6, and 7. These units have a maximum apparent power of 1 MVA and provide up to 1 MW of thermal power. They operate with turbine efficiency at 40%, loss efficiency at 9%, and thermal efficiency at 40%. For TES within these EHs, the characteristics are similar to those of the battery storage system, except for a slightly lower charging and discharging efficiency of 80%. To enhance operational flexibility, the flexibility tolerance (ΔF) is specified as 0.05 per unit in this scheme, ensuring the desired level of adaptability for energy hubs.

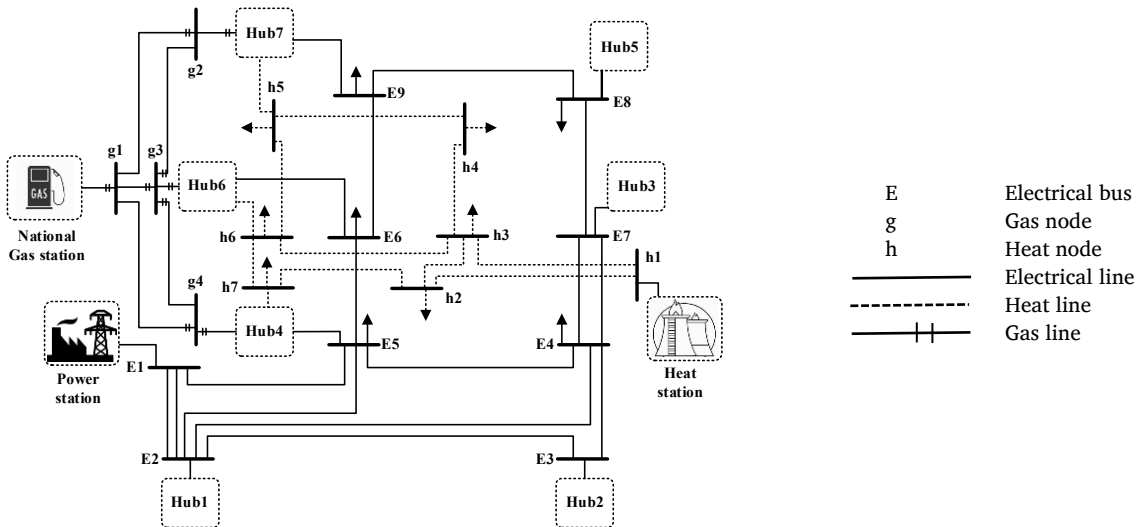


Figure 1. Test system [1].

4. Numerical results

The problem was solved by IPOPT in GAMS software [21]. Table 1 illustrates the variations in the expected value of flexibility power and the average flexibility incentive price (FIP) in the electrical and thermal sectors under ascending and descending modes, corresponding to changes in ΔF. The analysis reveals that as ΔF increases, the flexibility power diminishes. This increase in ΔF, as described by Equations (47) and (48), indicates a reduced emphasis on the flexibility of EHs within electrical and thermal networks. Consequently, a higher ΔF aligns the operations of storage generators, resources, and responsive loads more toward minimizing network operation costs, thereby leading to less contribution toward enhancing EH flexibility. As a result, flexibility power declines with rising ΔF. For instance, at elevated ΔF values, where Equations (47) and (48) are effectively disregarded, minimizing operational costs becomes significantly more critical than improving system flexibility. Under such circumstances, DRPs will typically switch to charging during periods of low demand or cheap energy prices and discharge during high load or expensive energy periods, remaining inactive at other times. On the other hand, at low ΔF values, such as when ΔF equals zero, the DRP remains active throughout, either drawing power from the grid or supplying it back. Additionally, as indicated in Table 1, an increase in ΔF also leads to a reduction in the FIP for both electrical and thermal sectors across ascending and descending modes. This outcome is directly tied to a decline in the flexibility capacity within these sectors and operating conditions. Finally, Figure 2 presents the trend of flexibility service providers' (FSSs) profits within the flexibility market as ΔF varies. The graph demonstrates that rising ΔF results in decreased FSSs' profits due to reductions in both FIP and flexibility power, as outlined in Table 1. This reflects the diminishing role of flexibility under these conditions.

Table 2 presents operational indicators for two study scenarios within electric, gas, and heat networks. Case I involves analyzing load distribution across these networks, while Case II focuses on the proposed design for varying levels of ΔF. The table includes data on energy losses, maximum voltage drops (or pressure/temperature decreases), and maximum overvoltage (or pressure/temperature increases). In Case I, all indicator values for the gas network are zero due to the absence of consumers. However, these indicators show significant levels within the electric and heat networks. Total energy losses are quantified at 7.42 MWh. The maximum voltage drop and temperature drop reach 0.114 and 0.121 per unit, respectively, both exceeding the allowable limit of 0.1 per unit (based on the range of 0.9 to 1). No overvoltage or temperature increase is observed in this scenario. In Case II, for ΔF = 0 (representing 100% flexibility), energy losses are notably reduced in the electric and heat networks by approximately 33.1% and 31.5%, respectively, compared to Case I. Conversely, the gas network experiences an energy loss increase of 1.32 MWh relative to Case I. Overall, total network energy losses decrease by about 14.9% in this scenario compared to Case I. Regarding operational improvements in Case II, the maximum pressure drop rises slightly to 0.042 per unit, while maximum overvoltage and temperature increases reach 0.025 and 0.031 per unit, respectively. However, there is a significant reduction in maximum voltage drop and temperature drop by 41.2% and 39.7%, respectively, compared to Case I. Moreover, all voltage, temperature, and pressure values remain within permissible limits (0.9 to 1.1 per unit) under this scenario. It is important to note that as ΔF increases, the performance improvement of these indicators becomes more pronounced compared to Case I. This is because decreasing the emphasis on flexibility (i.e., increasing ΔF) allows EHs to prioritize optimizing network operations, as reflected in the data presented in Table 2.

Table 1. Value of flexibility power and FIP in ΔF.

| ΔF (p.u.) | 0 | 0.05 | 0.20 |
|---|-------|-------|------|
| $\sum_{i,t,s} \rho_s EF_{i,t,s}^U$ (p.u.) | 14.09 | 11.97 | 8.34 |
| $\sum_{i,t,s} \rho_s EF_{i,t,s}^D$ (p.u.) | 4.5 | 3.99 | 2.78 |
| $\sum_{i,t,s} \rho_s HF_{i,t,s}^U$ (p.u.) | 12.43 | 10.56 | 7.36 |
| $\sum_{i,t,s} \rho_s HF_{i,t,s}^D$ (p.u.) | 4.15 | 3.52 | 2.46 |
| $\frac{1}{24 \times 7} \sum_{i,t,s} \rho_s \bar{\lambda}_{i,t,s}^{ef}$ (\$/MWh) | 5.99 | 4.37 | 2.34 |
| $\frac{1}{24 \times 7} \sum_{i,t,s} \rho_s \underline{\lambda}_{i,t,s}^{ef}$ (\$/MWh) | 2.47 | 1.80 | 0.92 |
| $\frac{1}{24 \times 7} \sum_{i,t,s} \rho_s \bar{\lambda}_{i,t,s}^{hf}$ (\$/MWh) | 5.57 | 4.06 | 2.08 |
| $\frac{1}{24 \times 7} \sum_{i,t,s} \rho_s \underline{\lambda}_{i,t,s}^{hf}$ (\$/MWh) | 2.29 | 1.66 | 0.85 |

Table 2. Operation indices value in ΔF.

| Parameter | Energy loss (MWh) in electrical, heat, and gas networks | | | | Maximum drop (p.u.) of | | | Maximum over (p.u.) - | | |
|--------------------|---|------|------|-------|------------------------|-------------|----------|-----------------------|-------------|----------|
| | Electrical | Heat | Gas | Total | Voltage | Temperature | Pressure | Voltage | Temperature | Pressure |
| Case I | 5.21 | 2.20 | 0 | 7.42 | 0.114 | 0.121 | 0 | 0 | 0 | 0 |
| Case II for ΔF = 0 | 3.48 | 1.51 | 1.32 | 6.32 | 0.067 | 0.073 | 0.042 | 0.025 | 0.031 | 0 |
| ΔF = 0.05 | 3.42 | 1.46 | 1.31 | 6.20 | 0.067 | 0.073 | 0.042 | 0.027 | 0.033 | 0 |
| ΔF = 0.10 | 3.35 | 1.41 | 1.31 | 6.08 | 0.066 | 0.072 | 0.042 | 0.028 | 0.034 | 0 |

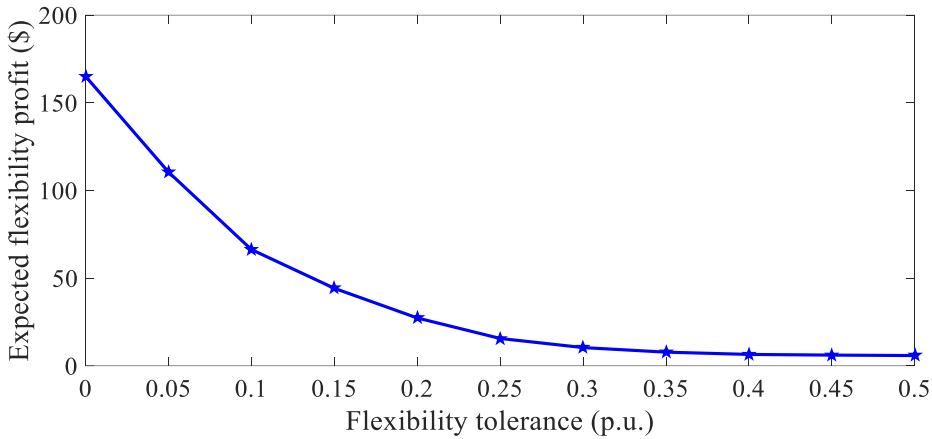


Figure 2. Flexibility profit curve in ΔF.

5. Conclusion

This paper delves into the pricing mechanisms for flexibility within EHs, focusing on electric, gas, and heat networks. The proposed framework aims to optimize the profitability of flexible resources housed within EHs by considering their specific flexibility models. Key constraints include the optimal power flow equations for the energy networks and the operational models of these hubs. From the analyzed data, several insights emerged: 1) A decrease in flexibility tolerance boosts the power of flexible resources, subsequently raising flexibility prices. 2) This adjustment significantly enhances the profits of flexible resources participating in the flexibility market within EHs. 3) Optimal operation of resources, storage devices, and responsive loads in this framework leads to improved network performance, with total energy losses, maximum voltage drop, and temperature improvements when compared to load distribution studies. 4) Maximum pressure drop and overvoltage, as well as temperature and pressure readings, remain within acceptable limits but show an upward trend compared to load distribution studies. 5) Increasing the emphasis on flexibility or reducing flexibility tolerance can elevate network operating costs. 6) The proposed model successfully achieves full flexibility conditions, effectively tolerating zero flexibility. 7) Enhanced flexibility levels correlate with increases in network energy losses, voltage drop, and temperature drop.

EHS are located in consumption areas. Therefore, if a fault occurs in the network, the EH can supply part of the energy consumed by the consumers. Therefore, the EH can be effective in improving the reliability and resilience of the network. This issue is considered as future work in the proposed design.

List of symbols

Variables (in p.u.)

- Flexibility power of electrical DRP, EES, CHP in downward mode
- Flexibility power of thermal DRP, TES in downward mode
- Hub flexibility power in upward and downward modes in the electrical section
- Gas and heat power of EH
- Gas and heat power of the line
- Gas and heat power of the substation
- Thermal power of TES for charging and discharging modes
- Hub flexibility power in upward and downward modes in the heat section
- Hub active and reactive power
- Active power of EES for charging and discharging modes
- Active, reactive, heat, and gas power of CHP
- Active and heat power of DRP
- Active and reactive power of the line
- Active and reactive power of the substation
- Temperature
- Flexibility power of electrical DRP, EES, CHP in upward mode
- Flexibility power of thermal DRP, TES in upward mode
- Range and angle of voltage
- Pressure
- FIP in the electrical section
- FIP in thermal section

- $D_{DRPe}^{FORPc}, D_{EES}^{EES}, D_{CHP}^{CHP}$
- $D_{DRPth}^{FORPth}, D_{TES}^{TES}$
- EP^e, EF^e
- G^{EH}, H^{EH}
- G^l, H^l
- G^s, H^s
- H^{CH}, H^{DCH}
- HP^e, HP^t
- P^{EH}, Q^{EH}
- P^{CH}, P^{DCH}
- $P^{CHP}, Q^{CHP}, H^{CHP}, G^{CHP}$
- P^{DRP}, H^{DRP}
- P^l, Q^l
- P^s, Q^s
- T
- $UF_{DRPe}^{DRPe}, UF_{EES}^{EES}, UF_{CHP}^{CHP}$
- $UF_{DRPth}^{DRPth}, UF_{TES}^{TES}$
- V, α
- β
- $\lambda^{ef}, \bar{\lambda}^{ef}$
- $\underline{\lambda}^{ef}, \bar{\lambda}^{ef}$

Parameters (in p.u.)

- Charge and discharge rates in EES
- Initial energy in EES
- Min and Max of stored energy in EES
- Charge and discharge rates in TES
- Gas and heat load
- Max capacity in electrical, heat, and gas lines
- Max capacity in electrical, heat, and gas stations
- Max of heat and apparent power of CHP
- Active and reactive load
- Min and max values of temperature

- ECR, EDR
- EI
- E^{min}, E^{max}
- HCR, HDR
- G^l, H^l
- $G^{lmax}, H^{lmax}, S^{lmax}$
- $G^{smax}, H^{smax}, S^{smax}$
- H^{CHPmax}, S^{CHPmax}
- P^l, Q^l
- T^{min}, T^{max}

Min and max values of the voltage amplitude
 Min and max value of pressure
 Efficiency of EES in charge and discharge modes
 Efficiency of turbine, loss, and heat in CHP
 Scenario probability
 Heat and gas constant for the pipeline
 Consumers' contribution rate in DRP
 Flexibility tolerance

V^{min}, V^{max}
 β^{min}, β^{max}
 η^{CH}, η^{DCH}
 $\eta^T, \eta^L, \eta^{HT}$
 ρ
 σ, ω
 ΔF

Indices

Bus, heat node, and gas node
 EH
 Bus or node
 Scenario
 Hour

ne, nh, ng
 i
 l
 s
 t

References

- [1] A. Dini, S. Pirouzi, M. Norouzi, and M. Lehtonen, "Grid-Connected Energy Hubs in the Coordinated Multi-Energy Management Based on Day-Ahead Market Framework," *Energy*, vol. 188, 116055, 2019.
- [2] K. Afrashi, B. Bahmani-Firoouzi, and M. Nafar, "Multicarrier Energy System Management as Mixed Integer Linear Programming," *Iranian Journal of Science and Technology, Transactions of Electrical Engineering*, vol. 45, no. 2, pp. 619–631, 2020.
- [3] A. Heidari, S. Mortazavi, and R. Bansal, "Stochastic Effects of Ice Storage on Improvement of an Energy Hub Optimal Operation Including Demand Response and Renewable Energies," *Applied Energy*, vol. 261, 114393, 2020.
- [4] M. Jalili, M. Sedighzadeh, and A. S. Fini, "Stochastic Optimal Operation of a Microgrid Based on Energy Hub Including a Solar-Powered Compressed Air Energy Storage System and an Ice Storage Conditioner," *Journal of Energy Storage*, vol. 33, 102089, 2021.
- [5] J. Faraji, H. Hashemi-Dezaki, and A. Ketabi, "Stochastic Operation and Scheduling of Energy Hub Considering Renewable Energy Sources' Uncertainty and N-1 Contingency," *Sustainable Cities and Society*, vol. 65, 102578, 2021.
- [6] P. Emrani-Rahaghi, and H. Hashemi-Dezaki, "Optimal Scenario-Based Operation and Scheduling of Residential Energy Hubs Including Plug-In Hybrid Electric Vehicle and Heat Storage System Considering the Uncertainties of Electricity Price and Renewable Distributed Generations," *Journal of Energy Storage*, vol. 33, 102038, 2021.
- [7] A. Shabanpour-Haghighi, and A. R. Seifi, "Multi-Objective Operation Management of a Multi-Carrier Energy System," *Energy*, vol. 88, pp. 430–442, 2015.
- [8] M. Moeini-Aghtaie, A. Abbaspour, M. Fotuhi-Firuzabad, and E. Hajipour, "A Decomposed Solution to Multiple-Energy Carriers Optimal Power Flow," *IEEE Transactions on Power Systems*, vol. 29, no. 2, pp. 707–716, 2014.
- [9] A. Dolatabadi, M. Jadidbonab, and B. Mohammadi-ivatloo, "Short-Term Scheduling Strategy for Wind-Based Energy Hub: A Hybrid Stochastic/IGDT Approach," *IEEE Transactions on Sustainable Energy*, vol. 10, no. 1, pp. 438–448, 2019.
- [10] H. Zafarani, S. A. Taher, and M. Shahidehpour, "Robust Operation of a Multicarrier Energy System Considering EVs and CHP Units," *Energy*, vol. 192, 116703, 2020.
- [11] M. Hamrahi, M. Mallaki, N. M. Pirkolachahi, and N. C. Shirazi, "Flexibility Pricing of Grid-Connected Energy Hubs in the Presence of Uncertain Energy Resources," *International Journal of Energy Research*, vol. 2023, pp. 1–21, 2023.
- [12] K. Afrashi, B. Bahmani-Firoouzi, and M. Nafar, "IGDT-Based Robust Optimization for Multicarrier Energy System Management," *Iranian Journal of Science and Technology, Transactions of Electrical Engineering*, vol. 45, no. 1, pp. 155–169, 2020.
- [13] M. Alipour, K. Zare, and M. Abapour, "MINLP Probabilistic Scheduling Model for Demand Response Programs Integrated Energy Hubs," *IEEE Transactions on Industrial Informatics*, vol. 14, no. 1, pp. 79–88, 2018.
- [14] M. Jadidbonab, A. Dolatabadi, B. Mohammadi-ivatloo, M. Abapour, and S. Asadi, "Risk-constrained Energy Management of PV Integrated Smart Energy Hub in the Presence of Demand Response Program and Compressed Air Energy Storage," *IET Renewable Power Generation*, vol. 13, no. 6, pp. 998–1008, 2019.
- [15] J. Liu, A. Wang, Y. Qu, and W. Wang, "Coordinated Operation of Multi-Integrated Energy System Based on Linear Weighted Sum and Grasshopper Optimization Algorithm," *IEEE Access*, vol. 6, pp. 42186–42195, 2018.
- [16] Y. Zhang, X. Wang, J. He, Y. Xu, and W. Pei, "Optimization of Distributed Integrated Multi-Energy System Considering Industrial Process Based on Energy Hub," *Journal of Modern Power Systems and Clean Energy*, vol. 8, no. 5, pp. 863–873, 2020.
- [17] D. Xu, Q. Wu, et al., "Distributed Multi-Energy Operation of Coupled Electricity, Heating, and Natural Gas Networks," *IEEE Transactions on Sustainable Energy*, vol. 11, no. 4, pp. 2457–2469, 2020.
- [18] H. Hamidpour, J. Aghaei, S. Dehghan, S. Pirouzi, and T. Niknam, "Integrated Resource Expansion Planning of Wind Integrated Power Systems Considering Demand Response Programmes," *IET Renewable Power Generation*, vol. 13, no. 4, pp. 519–529, 2019.
- [19] R. Homayoun, B. Bahmani-Firoouzi, and T. Niknam, "Multi-objective Operation of Distributed Generations and Thermal Blocks in Microgrids Based on Energy Management System," *IET Generation, Transmission & Distribution*, vol. 15, no. 9, pp. 1451–1462, 2021.
- [20] A. Jamali, J. Aghaei, et al., "Self-Scheduling Approach to Coordinating Wind Power Producers with Energy Storage and Demand Response," *IEEE Transactions on Sustainable Energy*, vol. 11, no. 3, pp. 1210–1219, 2020.
- [21] Generalized Algebraic Modeling Systems (GAMS).

Declaration of competing interest

The authors declare that they have no known competing financial interests or personal relationships that could have appeared to influence the work reported in this paper. The ethical issues, including plagiarism, informed consent, misconduct, data fabrication and/or falsification, double publication and/or submission, redundancy, have been completely observed by the authors.

Bibliography



Mousa Hamrahi was born in Bushehr, Iran in 1984. He received the B.Sc. (2011), M.Sc. (2017) and Ph.D. (2025) degrees from Islamic Azad University Science and Research branch, Bushehr, Iran, respectively, all in Electrical Engineering. His research interests include Smart Grids, Electricity Markets, Power System Dynamics and Renewable Energy Integration.

Email: Mousa.hamrahi@yahoo.com

ORCID: [0009-0001-5362-9457](https://orcid.org/0009-0001-5362-9457)

Contribution Statement: Formal analysis, Funding acquisition, Investigation, Methodology, Project administration, Resources, Software, Visualization, Roles/Writing-original draft, Writing-review & editing.



Mehrdad Mallaki was born in Bushehr, Iran in 1981. He received the B.Sc. (2004), M.Sc. (2006) and Ph.D. (2020) degrees from IUST, KNTU and AUT, respectively, all in Electrical Engineering. From 2007, he joined Islamic Azad University, Bushehr, Iran, where he is now working as Assistant Professor in electrical engineering department. His research interests include Smart Grids, Electricity Markets, Power System Dynamics and Renewable Energy Integration.

Email: mallaki@aut.ac.ir

ORCID: [0000-0002-2878-9328](https://orcid.org/0000-0002-2878-9328)

Contribution Statement: Investigation, Methodology, Project administration, Resources, Software, Supervision, Validation.



Naghi Moaddabi Pirkolachahi was born in Rasht, Iran, in 1984. He received the B.Sc. and M.Sc. degrees in Electrical Engineering from the Amirkabir University of Technology (Tehran Polytechnic), Tehran, Iran, in 2006 and 2008, respectively, and the Ph.D. degree in Electrical Engineering from the same university in 2014. He joined Islamic Azad University, Bushehr, Iran, as an Assistant Professor in 2015. His research interests include power system protection, transient stability, smart grids, and renewable energies.

Email: nima.moaddabi@gmail.com

ORCID: [0000-0002-4226-3322](https://orcid.org/0000-0002-4226-3322)

Contribution Statement: Conceptualization, Data curation, Formal analysis, Funding acquisition, Investigation, Methodology, Project administration, Resources, Software.



Najmeh Charaghi Shirazi was born in Shiraz, Iran in 1982. She received the B.Sc. and M.Sc. degrees from Islamic Azad University of Bushehr, Iran, in 2005 and 2009, respectively, and the Ph.D. degree from the Islamic Azad University Science and Research branch, Tehran, Iran, in 2018, all in Electrical Engineering. From 2019, she joined Islamic Azad University, Bushehr, Iran, as an Assistant Professor. Her research interests include RFIC, circuit design, energy harvesting, and converters.

Email: Nch_shirazi@yahoo.com

ORCID: [0000-0001-6113-537X](https://orcid.org/0000-0001-6113-537X)

Contribution Statement: Validation, Visualization, Roles/Writing-original draft, Writing-review & editing.

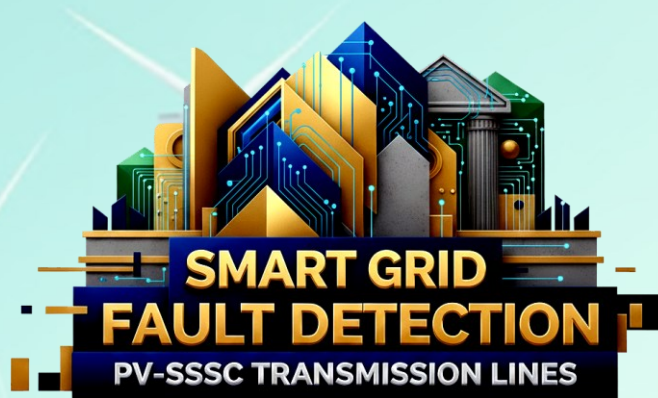
Detection and Determination of Short-Circuit Faulty Phases in Transmission Lines Compensated with a PV-Connected Series Static Synchronous Compensator

Mahyar Abasi, Ebrahim Khanfari

Highlights

- ❖ Design and Implementation of a Fault Phase Detection Algorithm for Transmission Lines Utilizing SSSC with Solar-Powered Energy Sources
- ❖ Formulation of a Fault Phase Detection Algorithm for Transmission Lines Based on Local Terminal Voltage Signal Analysis
- ❖ Development of a Fault Phase Detection Algorithm Leveraging Traveling Wave

Graphical Abstract



SOLAR
INTEGRATION



WAVELET ALGORITHM



98% ACCURACY

RELIABLE, GREEN POWER

Use your device to scan
and read the article
online



Citation

M. Abasi, and E. Khanfari, "Detection and Determination of Short-Circuit Faulty Phases in Transmission Lines Compensated with a PV-Connected Series Static Synchronous Compensator," *Journal of Green Energy Research and Innovation*, vol. 2, no. 4, pp. 67-85, 2025.



<https://doi.org/10.61882/jgeri.2.4.67>





Online ISSN: 3041-9018

Journal of Green Energy Research and Innovation

Journal Homepage: www.jgeri.araku.ac.ir

Detection and Determination of Short-Circuit Faulty Phases in Transmission Lines Compensated with a PV-Connected Series Static Synchronous Compensator

Mahyar Abasi^{1,2,*}, Ebrahim Khanfari³

¹ Department of Electrical Engineering, Faculty of Engineering, Arak University, Arak 38156-8-8349, Iran.

² Research Institute of Renewable Energy, Arak University, Arak 38156-8-8349, Iran.

³ Department of Electrical and ICT, Faculty of Technical Engineering, Institute for Higher Education, ACECR, Khuzestan, Iran.

ARTICLE INFO

Keywords:

Fault Detection and Classification, Series Static Synchronous Compensator (SSSC), Wavelet Transform in Power Systems, Renewable Energy Systems, Photovoltaic (PV) Integration.

Article History:

Received: 02 July 2025;
Revised: 02 August 2025;
Accepted: 05 September 2025.

Article type:

Research Article

* Corresponding author

E-mail address
m-abasi@araku.ac.ir (M.Abbasi)

ABSTRACT

Fault detection and classification in transmission lines equipped with Flexible Alternating Current Transmission System (FACTS) devices is one of the basic challenges in line protection. In the event of a fault on one side of this equipment, relays installed at the other terminal often struggle to detect the fault and determine the faulty phases due to control system interruptions in the line. The Series Static Synchronous Compensator (SSSC) is a series-connected device in transmission lines that addresses reactive power control challenges in the network. This study proposes a highly accurate and fast algorithm to detect and classify various short-circuit faults in transmission lines compensated with an SSSC. Crucially, the SSSC in this study is connected via its DC link to a solar photovoltaic (PV) farm, specifically utilizing Trina Solar Vertex N 210R-N-66 panels, allowing it to act as both a reactive power compensator and a means to seamlessly integrate this significant source of green energy into the grid. This integration highlights the method's relevance to modern renewable energy systems, particularly in enhancing the protection and monitoring of solar-powered infrastructures. The algorithm analyzes voltage signals from one side of the line, employing a discrete wavelet transform and a decision-making algorithm. The proposed method was simulated and implemented for at least 4000 fault scenarios under normal and critical conditions. Based on the extensive fault scenarios and reported results, the algorithm's performance accuracy is estimated to be approximately 98%, demonstrating its potential in improving the reliability and performance of smart and green power systems.

1. Introduction

1.1. Research motivation

One of the challenges that the electricity industry is facing today is the increasing consumption of electrical energy and the inherent lack of capacity in transmission lines. Solving the problem of line congestion and maximizing the capacity of transmission and sub-transmission lines are always the main focus of experts in the electricity sector [1]. Various solutions, such as the construction of new lines, double or multi-circuit lines, transferring power generation closer to demand centers, implementing load management at the distribution level, or the use of reactive power compensators, have been proposed. While each method offers technical advantages, they often come with their own technical or even economic disadvantages. A harmonized approach has consistently been sought to tackle this fundamental challenge. One of the plans that has attracted significant attention globally, especially in widespread countries, is the utilization of Flexible Alternating Current Transmission Systems (FACTS) devices, which are new-generation reactive power compensators. The adoption of this type of compensator in the power system assists in compensating reactive power of the load on a wide level, releasing line capacity, and increasing the active power transmission bandwidth in the lines, which, in addition to this, are very effective in dynamic and stability issues [1-3].

Furthermore, in the contemporary energy landscape, the imperative to transition towards sustainable and green energy sources has become paramount. Solar photovoltaic (PV) energy, with its abundance and environmental benefits, is a key component of this transition. Integrating large-scale solar farms into existing grid infrastructure, however, presents unique challenges, including voltage stability, power quality, and protection coordination. FACTS devices offer a promising solution by providing the necessary control and flexibility to seamlessly integrate such renewable energy sources. This integration is crucial for reducing carbon emissions, enhancing energy independence, and mitigating the impacts of climate change.

However, a significant challenge with these compensation schemes lies in the protection of transmission lines. The presence of these compensators virtually alters line parameters, rendering traditional distance relay designs ineffective in such topologies; therefore, designing protection algorithms for this type of structure is one of the critical study challenges in this field. Amongst the most prominent FACTS devices, considered a primary reactive power compensator in transmission lines, is the Series Static Synchronous Compensator (SSSC). When an SSSC is installed in the transmission line, the exact time of fault occurrence and the type of faulty phases might be misinterpreted in this topology. This is because of the very impactful dynamics of the SSSC at the time of short-circuit fault occurrence [1]. In this study, we specifically consider an SSSC whose DC link is connected to a solar farm, allowing for bi-directional power flow and enhanced grid support from renewable energy sources. This configuration adds another layer of complexity to fault detection and classification, but also offers significant advantages in terms of grid modernization and sustainability. Thus, according to the issues raised, the main challenge considered here is to address the problem of short-circuit fault detection and classification in SSSC-compensated transmission lines, particularly those integrated with solar power.

1.2. A review of the literature and research gaps

In general, the related studies and research conducted can be categorized into three basic groups based on series compensators in transmission lines. The problem considered in these three categories of issues is the discrimination of faults and non-fault conditions, and the identification of faulty phases in the transmission lines with these compensators. There are three basic categories of series compensators installed in the transmission system. Their division in this study is based on their technology. The first category includes the series capacitor compensator, which is fixed in the line and does not use any type of control switch. The second category is related to the thyristor-controlled series capacitor (TCSC) compensator, which belongs to the first generation of FACTS devices. In this type of compensator, control techniques are used to connect the capacitors to the circuit, but it still uses the static element of the capacitor in its structure. The third category of FACTS depends on the type of voltage source converter. The capacitor is not used in their structure, and the control operation is performed through a gate turn-off thyristor (GTO) switch and voltage source converters. The third type category is the most complete type of series compensator in the transmission line, whose degree of freedom and stability margin are much higher than the other two categories.

- In references [4-9], as the first category of studies, fault detection and classification methods in transmission lines compensated with series capacitors are presented, which are reviewed in detail in the following.

In reference [4], a method for detecting, classifying, and locating the faults in series capacitor-compensated transmission lines (SCTLs) is presented. Fault current signal analysis was adopted by using the combination of the discrete wavelet transform in the first level of samples and a machine learning technique. In reference [5], a method for detecting the type of faulty phase(s) in SCTLs is presented by relying on the training and learning method of neural networks based on measuring the current signal of one terminal. In this reference, the convolutional neural network based on least square error and least square regression with forgetting factor has been used. In reference [6], a protection method for fault identification and classification in series compensated transmission lines is introduced by considering the changes in instantaneous active and reactive powers. The measured quantities are drawn in a two-dimensional coordinate system, as a result of which the geometric location of each pair of instantaneous active and reactive power forms a P-Q loci curve. The quadrant of the plane where the curve starts is selected as a reference, and the curve structure is examined to identify the fault according to the displacement of the starting point under different fault conditions. In this study, the polarities of the extracted powers are also used to classify the fault based on a decision tree. In reference [7], a new method for detecting and classifying faulty lines in double-circuit SCTLs is presented by analyzing the current signals of a terminal and using the energy content of the traveling wave arriving at the terminal. The proposed method in this reference has a good performance in detecting and classifying single-circuit and intra-circuit faults in this topology. Reference [8] suggests an approach to classifying the faulty phases in high-voltage SCTLs, where the current signal of one cycle from the terminals of one side of the line is investigated based on multi-resolution wavelet analysis and a support vector machine with different feature vectors. In reference [9], a method for determining faulty phases in SCTLs based on wavelet packet transform is presented. In this method, the db10 wavelet package is used to analyze the waveform of the faulty phase current to obtain the wavelet energy coefficients.

- As the second category of studies, in references [10-18], fault detection and classification methods in TCSC-compensated transmission lines are presented, which are reviewed in detail below.

In reference [10], a method based on the combination of minimal radial basis function neural networks and fuzzy neural networks is presented for classifying and locating the faults in lines compensated with TCSC. This requires the smallest number of neurons, fewer fuzzy rules, and less processing. In reference [11], a new approach based on a decision tree is presented to find the faulty area and categorize the faulty lines in the transmission lines compensated with TCSC and using the current signals of one terminal and zero-sequence voltage. In reference [12], a method for fault location and faulty line identification in transmission lines with a TCSC is discussed. The method uses the current signals of one terminal for the input of a binary and multi-class support vector machine solver. In reference [13], a method is introduced by adopting the support vector machine to recognize the type of fault in TCSC-compensated transmission lines. The approach uses three-phase half-cycle current samples for fault detection. In reference [14], based on the superimposed energy method, a fault identification and categorization in TCSC-compensated transmission lines is

provided. In this reference, energy polarity analysis is used to identify fault occurrence within the zone and outside the zone. In reference [15], mathematical morphology is utilized to detect and classify faults in TCSC-compensated transmission lines. The method adopts the features of simplified mathematical morphology to analyze the current signals of a terminal in the transmission line. In reference [16], a fault detection and classification method for transmission lines with a TCSC linked to a wind farm is presented. The theory uses the distance relay comprehensive protection scheme based on the fuzzy characteristic curve in an adaptive way. The method is robust against fault resistance. In reference [17], a fault classification method in transmission lines with a TCSC is presented using the fault current analysis and support vector machine classifier method. The latter is very resistant to the saturation of current transformers and the presence of noise. In reference [18], a fault detection method during power fluctuation in transmission lines with a TCSC is provided based on three-phase current measurements of one terminal. The solution incorporates a decision tree to solve the mentioned challenge. In the following, in references [19-24], as the third category of studies, fault detection and classification methods in SSSC-compensated transmission lines are presented, which are reviewed in detail below.

In reference [19], a fault classification technique in transmission lines with an SSSC is introduced. It depends on the entropy technique combined with the wavelet in the time-frequency domain to analyze the current and voltage signals during the fault. In reference [20], a comprehensive distance protection scheme using the wavelet packet entropy analysis is used to solve the challenge of correctly detecting the faulty area in SSSC-compensated transmission lines. In this design, the frequency resolution has been improved at high-frequency levels. In reference [21], a fault detection and classification scheme in transmission lines with an SSSC is presented with relying on wavelet transform and regression trees. In this design, both the advantages of the resolution characteristic of the wavelet transform and Shannon entropy are used in the description of the signal characteristics and as the input of the decision tree. In reference [22], a fault detection and location scheme in SSSC-compensated transmission lines is discussed based on traveling wave theory. The method uses the wavelet transform and modal transform to analyze current and voltage signals. The main focus of this plan is to prevent the low-frequency interference created by the system when a fault occurs on the left and right sides of the SSSC. In reference [23], a pilot distance protection method is presented to enhance the distance relay's performance in case of faults in SSSC-compensated transmission lines. The design can be implemented adaptively by digital relaying algorithms. In reference [24], an ultra-fast protection method based on wavelet transform is presented for internal and external fault discrimination in transmission lines with an SSSC by incorporating storage components. The design is resistant to the operation state of the compensator, and there is no need to utilize adaptive designs.

Based on a comprehensive analysis of the existing literature cited in this study ([1]– [20]), we have identified several critical research gaps that directly motivate and justify the contributions of the proposed method. These are summarized below:

1. Dependency on Current Signals and Dual-Terminal Measurements : Many previous works ([1], [3], [6], [12], [14]) rely on both voltage and current measurements, and some even require synchronized dual-terminal data. These approaches are vulnerable to CT saturation, require expensive infrastructure, and are impractical in weakly monitored or rural lines .

❖ Our method uses only single-terminal voltage, thus reducing cost, improving reliability, and simplifying deployment.

2. Lack of Realistic Modeling for FACTS Devices Integrated with Renewables: While FACTS-based protection methods are explored (e.g., [5], [8], [10]), most assume idealized models of SSSC and neglect the complexity introduced by PV integration. The nonlinear dynamics of SSSC operation with a photovoltaic DC source are often not considered.

❖ Our model includes a realistic PV-fed SSSC with dynamic interaction, reflecting real-world control behavior and voltage support characteristics.

3. Generic or Arbitrary Use of Wavelet Transforms : Prior wavelet-based techniques ([2], [11], [13]) often select decomposition levels arbitrarily and fail to justify the use of specific mother wavelets. Some focus on higher levels (e.g., CD4–CD6), ignoring the high-frequency transients essential for fast detection.

❖ We use db6 with 9 levels and focus on CD1, which was empirically validated to be the most responsive to fault-induced disturbances.

4. Limited Fault Scenarios and Lack of Stress Testing: Many methods are validated only under ideal or limited operating conditions, with few works testing under high-resistance faults, noise, load fluctuations, or power oscillations ([4], [9], [15]).

❖ We conducted over 4000 simulations, including 7 critical scenarios involving high-impedance faults, dynamic SSSC modes, zero-crossings, noise, and no-fault disturbances.

5. No Integration with PV Source Behavior in Protection Logic: Very few works consider the impact of PV intermittency and power injection patterns on fault detection performance.

❖ Our method maintains detection accuracy despite transient power variability from the PV-connected SSSC, which is critical for smart grid deployment.

6. Threshold Selection Lacks Statistical Justification: Several studies use static thresholds or heuristics without quantitative calibration ([3], [10], [13]).

❖ We employ a data-driven threshold strategy using a wavelet-energy-based statistical analysis derived from a comprehensive dataset of simulated events.

7. Absence of Real-World Implementation Considerations: Some AI- or ML-based methods ([16], [17], [18]) are difficult to implement in real-time due to black-box behavior or excessive computational cost.

❖ The suggested method is simple, interpretable, and suitable for relay-level implementation without complex hardware dependencies.

These gaps directly shape the foundation of our proposed algorithm. We have designed the method to address real-world protection challenges in PV-integrated SSSC environments using a robust, scalable, and computationally efficient voltage-based wavelet technique. This ensures practical feasibility and scientific innovation aligned with the modern requirements of smart and renewable-rich power systems.

1.3. Novelty and contribution

The present study provides a high-performance approach to fault detection and classification in transmission lines compensated with an SSSC, specifically focusing on scenarios where the SSSC's DC link is connected to a solar photovoltaic (PV) farm utilizing Trina Solar Vertex N 210R-N-66 panels. This configuration is increasingly vital for integrating clean and green energy sources into the grid, but it also introduces complexities in grid protection. The proposed method uniquely utilizes only the three-phase voltages from one terminal on the fault side, enhancing its practicality and cost-effectiveness for such critical infrastructure. The measured voltage signals transform into a set of coefficients, specifically one approximate and nine detail coefficients, using the discrete wavelet transform with the db6 mother wavelet and a decomposition level of 9. The detail coefficient of level 1 from all three phases, combined with a decision tree-based process and predetermined threshold values proportional to the network under study and derived from the Otsu method, is effectively employed for robustly detecting and classifying various short-circuit faults, including Single-Line-to-Ground (SLG), Line-to-Line-to-Ground (LLG), Line-to-Line (LL), and Three-Phase (LLL) faults, on both sides of the SSSC. The technique was meticulously programmed in the MATLAB software environment and rigorously analyzed and evaluated across numerous normal and critical scenarios, including those reflecting the dynamic behavior associated with solar farm integration. The reported results consistently confirm the algorithm's highly acceptable performance, demonstrating its potential to significantly enhance the reliability of modern power grids relying on renewable energy.

The key innovations of this paper are presented below:

1. Design and implementation of a faulty phase detection algorithm for transmission lines utilizing SSSC with solar-powered energy sources.
2. Formulation of a faulty phase detection algorithm for transmission lines based on local terminal voltage signal analysis.
3. Development of a faulty phase detection algorithm leveraging traveling wave characteristics and wavelet transform techniques.
4. Establishment of a faulty phase detection algorithm independent of fault section identification in relation to SSSC.

1.4. Paper organization

The remaining sections of the paper are introduced here. [Section 2](#) provides the methodology, the suggested algorithm, and the complete flowchart of the problem. [Section 3](#) reports the results of implementing the algorithm in the software platform. [Section 4](#) describes the sensitivity analysis reports of the algorithm. The conclusions and a summary of the paper are given in [Section 5](#).

2. The proposed method

2.1. Structure of the network under study

The test network is introduced in a general way. According to [Figure 1](#), the network considered in this paper consists of two Thevenin's equivalent circuits, which are considered main networks and are interconnected via a transmission line between terminals T_1 and T_2 . In this structure, a dynamic load that is a reactive power consumer is connected to terminal T_2 . An SSSC is located in the middle of the line to compensate for reactive power and also to control dynamic load fluctuations. In the current study, three-phase voltages measured at terminal T_1 are sampled by a transducer with a sampling frequency of 10 kHz and are provided to the algorithm for fault detection and classification.

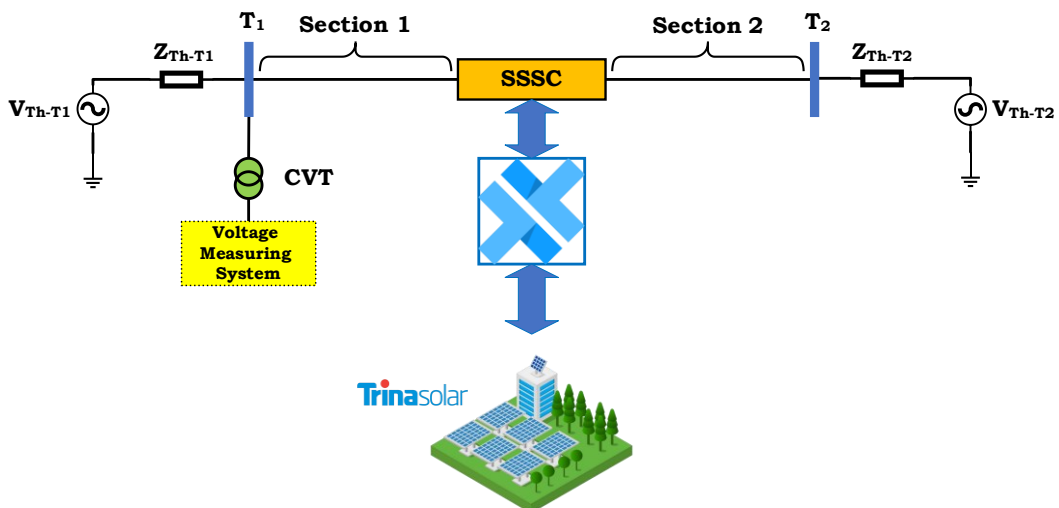


Figure 1. Single-line diagram of the test system.

2.2. Formulation

This subsection presents the formulation of the problem. Discrete Wavelet Transform (DWT) is utilized to establish the proposed algorithm. By analyzing the three-phase voltage signal at different levels, extracting accurate and approximate coefficients from low-pass and high-pass filters, and designing a comparison algorithm based on an innovative decision tree, a method for detecting the faulty phase(s) has been presented. In the following, the theory of DWT is presented first, and then the proposed method to solve the challenge of classifying the faulty phases in a topology compensated with SSSC will be presented.

2.2.1. DWT theory

Wavelet theory was proposed a few decades ago for the analysis of non-stationary signals. Due to its oscillating characteristic, the wavelet provides the conditions to perform a time-frequency analysis of the signal. Similar to the Fourier transform, the wavelet of a signal can be expanded based on the mother and daughter wavelets. Wavelet functions are obtained from a function called the mother wavelet, and these functions are called daughter wavelets. Each daughter wavelet is created by scaling and shifting the mother wavelet. Like the Fourier series, if we consider c_j as wavelet coefficients and $w_j(x)$ as the mother wavelet set, the function $f(x)$ is expanded in the form of Equation (1).

$$f(x) = \sum_{j=0}^m c_j w_j(x) \tag{1}$$

In Equation (1), $m + 1$ is the total number of coefficients and $M = 2^m - 1$ is the number of levels in the wavelet transform. Finally, after applying the wavelet functions at different levels, $f(x)$ can be expanded in the form of Equation (2).

$$f(x) = c_0 \varphi(x) + \sum_{i=0}^{\infty} \sum_{k=0}^{2^i-1} c_{2^i+k} w(2^i x - k) \tag{2}$$

where, $\varphi(x)$ is called the scale function. Theoretically, the wavelet transform of a signal can be continued up to infinity, but the number of wavelet transform levels depends on the type of analysis and the need we have to extract different frequencies from the signal. So, in Equation (2), the upper limit of parameter i is set to the number M , which is the last level required for the wavelet transform. Suppose we expand the function $f(x)$ at the $(j + 1)$ th level using only the scale functions $\varphi_{j+k}(x)$, where j is the number of the level and k is the position of the scale function. The coefficients that express the relationship between the function $f(x)$ and the function $f(x)$ can be represented by a , which is taken from the word "approximation", as given in Equation (3).

$$f(x) = a_1 \varphi(x) + a_2 \varphi(2x) + a_3 \varphi(2x - 1) + \dots \tag{3}$$

which are obtained from Equation (4) by considering the orthogonality condition of the scaling functions of coefficients a .

$$a_{j+1}(k) = 2^{j+1} \int f(x) \varphi(2^{j+1} x - k) dx \tag{4}$$

Finally, having a coefficient, $f(x)$ is written as Equation (5):

$$f(x) = \sum_k a_{j+1}(k) \varphi(2^{j+1} x - k) \tag{5}$$

Now, with a lower level, i.e., up to the j th level, if we expand the function $f(x)$ mentioned in Equation (6) using scale functions and wavelet functions, the coefficients obtained from wavelet functions are shown by the letter d , which is derived from the word "detail".

$$f(x) = \sum_k a_j(k) \varphi(2^j x - k) + \sum_k d_j(k) w(2^j x - k) \tag{6}$$

where, $a_j(k)$ and $d_j(k)$ can be described using Equations (7) and (8).

$$a_j(k) = 2^j \int f(x) \varphi(2^j x - k) dx \tag{7}$$

$$d_j(k) = 2^j \int f(x) w(2^j x - k) dx \tag{8}$$

By inserting the scale function $\varphi(x)$ and the wavelet function $w(x)$, Equations (7) and (8) will become as Equations (9) and (10), respectively [25].

$$a_j(k) = 2^j \int f(x) \langle \sum_n g_0(n) \varphi(2^j x - k - n) \rangle dx \tag{9}$$

$$d_j(k) = 2^j \int f(x) \langle \sum_n g_1(n) \varphi(2^j x - k - n) \rangle dx \tag{10}$$

By swapping integral and sum operators, Equation (9) can be expanded first as Equation (11) and finally as Equation (12).

$$a_j(k) = 2^j \sum_n g_0(n) \int f(x) \varphi(2^j x - k - n) dx \tag{11}$$

And if $2k + n = m$, then we have Equation (12):

$$a_j(k) = \sum g_0(m - 2k) 2^j \int f(x) \varphi(2^j x - m) dx \tag{12}$$

And finally, after equating, Equation (12) can be expanded as Equation (13), where $h_0(n)$ are coefficients of the decomposer high-pass filter.

$$a_j(k) = \frac{1}{2} \sum g_0(m - 2k) a_{j+1}(m) = \sum h_0(2k - m) a_{j+1}(m) \tag{13}$$

And if we write the same equations for Equation (10), finally, we can reach Equation (14) without providing intermediate relations. where $h_1(n)$ are coefficients of the decomposer high-pass filter.

$$d_j(k) = \frac{1}{2} \sum g_1(m - 2k) a_{j+1}(m) = \sum h_1(2k - m) a_{j+1}(m) \tag{14}$$

Equations (13) and (14) are the main relations of the discrete wavelet transform. These two equations state that every discrete data set can be divided into two categories. The first category is the details that are obtained by passing the information through a high-pass filter, and the second category is the estimate that is obtained by passing the information through a low-pass filter.

In Equations (13) and (14), a concept called decimation is used. In the literal sense, decimation means choosing one object from among 10 objects, but in the above equations, it means choosing one among the numbers output from the filters. This action is also called down-sampling. The opposite of decimation is the act of interpolation, that is, placing one number between two other numbers. This concept is used in the reconstruction of signals whose wavelet coefficients are available. According to the concept expressed in the wavelet transform, M in the discrete wavelet transform is 2 [26,27]. In other words, the relationship between input $(x(n))$ and output $(y(n))$ is as follows:

$$y(n) = x(2n) \tag{15}$$

Finally, the basic structure of the discrete wavelet transform can be shown in Figure 2:

In Figure 1, $u_d(k)$ and $u_a(k)$ are obtained from Equations (16) and (17):

$$u_d(k) = \sum h_1(k-n)a_{j+1}(n) \tag{16}$$

$$u_a(k) = \sum h_0(k-n)a_{j+1}(n) \tag{17}$$

With decimation, Equations (16) and (17) can be written as Equations (18) and (19).

$$d_j(k) = \sum h_1(2k-n)a_{j+1}(n) = \sum h_1(n)a_{j+1}(2k-n) \tag{18}$$

$$a_j(k) = \sum h_0(2k-n)a_{j+1}(n) = \sum h_0(n)a_{j+1}(2k-n) \tag{19}$$

If we decompose an arbitrary signal with the coefficients of the decomposing filter ($h_0(n)$ and $h_1(n)$) by using the coefficients of the reconstruction filters ($g_0(n)$ and $g_1(n)$), the original signal will be re-established. If signal $f(k)$ is a discrete function, its wavelet transform can be described in the form of Equations (20) and (21), where $d(k)$ represents the coefficients of the wavelet transform of signal f at the first level, and other numbers obtained from the signal decomposition are an estimate of the signal.

$$d(k) = \sum_{n=0}^{N-1} h_1(2k-n)f(n) = \sum_{n=0}^{N-1} h_1(n)f(2k-n) \tag{20}$$

$$a(k) = \sum_{n=0}^{N-1} h_0(2k-n)f(n) = \sum_{n=0}^{N-1} h_0(n)f(2k-n) \tag{21}$$

In this paper, to analyze the three-phase signal measured from terminal T_1 , level 9 wavelet signal analysis is used. The selection of level 9 for wavelet decomposition was made based on extensive testing under various fault conditions. In over 4000 simulated fault scenarios—including SLG, LLG, LL, and LLL faults—level 9 decomposition using the db6 mother wavelet provided the most consistent and discriminative CD1 coefficients across all three phases. Higher decomposition levels enable better isolation of the high-frequency transients generated by different fault types, especially those masked by the dynamic behavior of the SSSC and the intermittent output of the connected PV system. Lower levels (e.g., 4 to 7) resulted in insufficient frequency resolution, causing overlap between fault and non-fault events, while levels above 9 increased computations without noticeable performance gain. Thus, level 9 offered an optimal trade-off between resolution and efficiency, ensuring precise classification of faulted phases with minimal complexity. This empirical tuning was a key step in maximizing the detection accuracy of the proposed method. After extracting CD₀ from the voltage of all three phases and using a decision tree-based plan depending on the threshold values, it is possible to detect a fault and categorize the faulty phases. Figure 3 shows the decomposition diagram of a signal into estimated and detailed coefficients in level 9. The selection of this level for the analysis of the raised problem was done by trial and error and experimentally in the implementation of different fault scenarios. At this level, the algorithm’s performance is the best performance state with the least error [28].

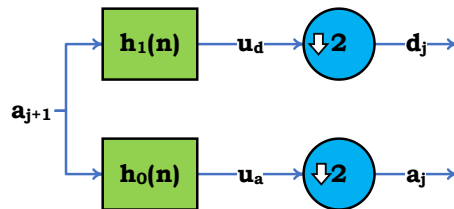


Figure 2. Signal decomposition into two levels.

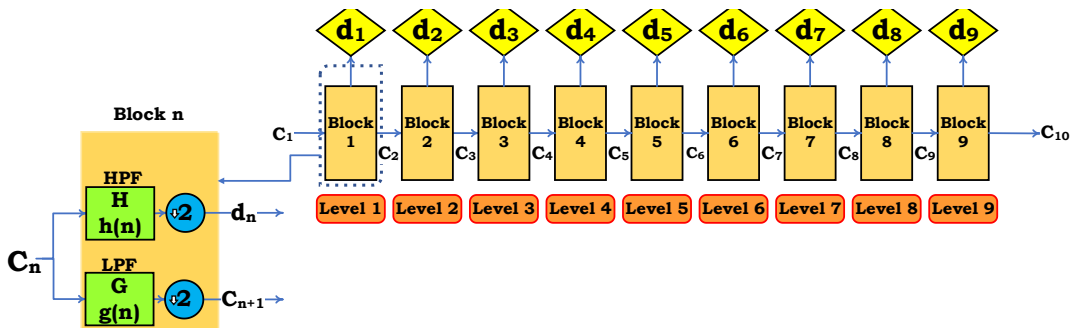


Figure 3. Diagram of decomposing signal into nine levels.

2.2.2. Describing the logic of the proposed algorithm

In this subsection, the aim is to present the logic of the algorithm according to the results of applying the wavelet transform on the three-phase voltage signal. This study exclusively uses three-phase bus voltage signals at terminal T_1 for fault detection and classification. This choice is deliberate and offers practical benefits. Voltage signals are more stable and reliable than current signals, especially under severe fault conditions where current transformers (CTs) may saturate and distort measurements. Voltage transformers (VTs), on the other hand, are less affected by such distortions. Additionally, using only voltage reduces sensor requirements, simplifies implementation, and lowers costs—making the method well-suited for real-world applications, particularly in smart grids with integrated renewable energy. It also ensures robust performance by minimizing the influence of current variations caused by load changes or PV power fluctuations. Overall, this design enhances reliability and is considered one of the key strengths of the proposed method. According to the results of the coefficients extracted from the wavelet transform used for the three-phase voltage signal, the fault detection and classification algorithm is defined as follows in different parts. The theory presented uses three threshold values, namely, Thr0, Thr1, and Thr2, whose values are obtained in a per-unit system based on the implementation of at least 4000 scenarios. In the simulation section, the numerical values of these thresholds are given according to the network under study.

A. Fault detection

At this level, it must first be determined whether a fault has occurred at all or not. To implement this problem, the maximum value of the detail coefficient 1 (MAX_CD1) can be used. If MAX_CD1 exceeds Thr0 for even one of the phases (a, b, c), then a fault must have occurred. The reason is that if at least one phase is involved in a fault, then high-frequency fluctuations of that phase will be higher than the predetermined threshold value, and a fault must have appeared. If there is no fault, CD1 in a pre-unit system is almost zero, but when a fault occurs, the high-frequency fluctuations of the voltage of that phase increase, so in this case, a fault must have happened, but its type is not clear at this stage.

B. Ground fault detection

If the value of MAX_CD1 of two phases is greater than Thr1 (the threshold value), or MAX_CD1 of all three phases is less than Thr2, then no ground fault has occurred; otherwise, if one of the rules is rejected when a non-grounded fault occurs, the high-frequency oscillation behavior of at least two phases relative to the other phase increases from the threshold value of Thr1, which is several times greater than Thr2. If it is a grounded fault, MAX_CD1 will never increase from the Thr3 because some of the fault energy is damped through the ground, which causes high-frequency oscillations in the faulty phases in at least one of the faulty phases smaller than Thr1. Also, if the MAX_CD1 values of all three phases are smaller than Thr2, then it is a non-ground fault that can cover the three-phase state. Otherwise, a ground fault must have occurred.

C. Faulty phase(s) detection

This case itself is divided into two parts, which will be discussed separately in the following.

Case 1: The fault is phase-to-phase. In this case, if the MAX_CD1 of two phases is greater than the threshold value of Thr1, it means that the fault must have occurred in those two phases; otherwise, the fault is a three-phase type.

Case 2: The fault is in the form of phase(s) to ground. In this case, the fault occurs either as LG or LLG. If the fault is LG, the MAX_CD1 of that phase will be higher than the other two phases, and also the MAX_CD1 of the other two phases will be lower than Thr2. However, in the case the fault is LLG, then MAX_CD1 of the faulty two phases will be higher than MAX_CD1 of the non-fault phase, and at the same time, MAX_CD1 of the faulty phases becomes larger than Thr2; otherwise, the fault is a LLLG.

The threshold values Thr0, Thr1, and Thr2 used in the proposed fault classification algorithm were derived through a rigorous multi-stage process involving signal processing, empirical analysis, and classification validation. These thresholds serve as discriminators to identify faulty phases under various fault types by evaluating the behavior of voltage waveforms using wavelet-based energy signatures. The voltage signals at terminal T_1 were processed using the discrete wavelet transform (DWT) with the db6 mother wavelet at decomposition level 9. This setup was chosen to capture transient components localized in the high-frequency range — typically caused by abrupt impedance discontinuities during fault inception. Among all decomposition levels, detail level 1 (CD1) was found to be the most sensitive and consistent in revealing fault-related variations across different phases. To calibrate the thresholds, we simulated over 4000 fault scenarios encompassing:

- All major fault types (SLG, LL, LLG, LLL),
- Wide fault resistance variation (1–100 Ω),
- Different inception angles and times (6.5–9 s),
- Both left-side and right-side positions with respect to the SSSC.

For each scenario, the CD1 energy peak of each phase was recorded, normalized, and categorized. Using statistical methods inspired by Otsu-based clustering, the optimal thresholds were selected such that intra-class variance (between faulty and non-faulty phase energy levels) was minimized. Threshold Thr0 acts as the primary activation level, distinguishing between faulty and healthy phases. Thr1 and Thr2 serve as secondary criteria to refine fault classification in the presence of overlapping waveform energies, particularly under low-resistance or remote faults where waveform energy is less pronounced. The derived thresholds are thus specific to the signal dynamics of the test system, shaped by the SSSC's real-time compensation behavior and the intermittency of the PV source. This tuning strategy enhances faulty phase identification accuracy and reduces misclassification in complex operating environments.

2.3. Pseudo-code of the proposed algorithm

In this part, the general program related to the proposed algorithm is given in several levels in [Figure 4](#).

```

START
Stage 1. Calling the three-phase voltage signal of the terminal
    Vt=Vabc.Signals. values';
Stage 2. Run the wavelet transform
wpt = wpdec(P,9,'db6');
cfs = abs (wpcoef(wpt,[9 0]));
    For Level=1 to 9
wpt = wpdec(P,9,'db6');
cfs = abs (wpcoef(wpt,[ Level 1]));
    End
Stage 3. Fault detection and classification
3.1. Determining threshold values, calculating peak values , and defining error flags
3.2. Fault detection unit
    For all phases
        If peak values are greater than the threshold value
            Fault Flag = 1
        Else
            Fault Flag = 0
    End
3.3. Ground fault detection unit
    If Fault Flag = 1
        For all phases
If PeakVal of two phases is greater than Thr1 OR Three of PeakVal are less than Thr2
Ground Flag = 0
Else
            Ground Flag = 1
        End
    End
Else
        Display "No Fault"
    End
3.4. Phase-to-phase fault detection unit
    If Ground Flag = 1
        For all phases
If PeakVal of two phases is greater than Thr1
Phase-to-phase fault detected in these two phases
Else
            Three-phase faults
        End
    End
End
3.5. phase(s) to the ground fault detection unit
    If Ground Flag = 1
        For all phases
If PeakVal of one phase is greater than PeakVal of two phases
AND
        PeakVal of two phases Less than Thr2
        One phase to ground fault
Else if PeakVal of one phase is less than PeakVal of two phases
AND
        PeakVal of two phases Greater than Thr2
        Two-phase-to-ground fault
    End
    End
End
END

```

Figure 4. Pseudo-code of the proposed algorithm.

3. Software simulation and results analysis

3.1. Normal operation

Now we introduce the network under study in the MATLAB/Simulink software. According to Figure 5, this network includes two main grids with a 500 kV voltage level and 1400 MVA power, which feed a dynamic load with a power of 220 MVA through a 100 km line. The complete information of this network for implementation in the MATLAB/Simulink software is given in Table 1. Since the reactive power demand of the dynamic load is assumed very high in this network, an SSSC based on a power oscillator (POD) has been adopted to provide this reactive power and also to control the desired load. According to the intended goals, the considered SSSC is located in the middle of the 100 km line. Under fault-free conditions, the performance of the network under study in the presence of SSSC has been investigated in terms of compensating for the reactive power demanded by the load. The considered dynamic load consumes 0.8 p.u. amount of reactive power. In this simulation, the moment the SSSC is switched to the network is considered 5 seconds after the start of the simulation. The reference value of v_q is set at 0.05 p.u. After switching on the SSSC, a part of the reactive power demanded by the dynamic load is supplied through the SSSC, and the reactive power output of the connected networks in both terminals is reduced. Figure 6 displays the three-phase voltage and current measured from two terminals on both sides of the fault. Also, according to Figure 7, the reactive power demand of the load, reactive power injected by the SSSC, and reactive power produced by the networks connected to the terminals are measured in this case. Figure 7 shows that when the SSSC switches on the circuit at the moment $t = 5$ s, the SSSC injects reactive power equivalent to 1 p.u. into the transmission line. Concurrently, the power consumption of the load has not changed, but this injected power compensates for a part of the reactive power demand of the load, and for this reason, the production power of networks 1 and 2 decreases. Moreover, to examine the performance of the SSSC control system, the reference and actual values of v_q followed by the POD controller are plotted in Figure 8. As it is observed, at $t = 5$ s that the SSSC is switched on, q-axis voltage follows the reference value with high accuracy and injects part of the reactive power demand of the load into the network. Figure 8 also demonstrates that the SSSC controller can follow the reference value of 0.05 p.u. with high accuracy and thus inject the predicted reactive power into the network. By increasing the power ratio of SSSC, compensation can be done in such a way that all the power demand of the dynamic load is fed by the compensator, and the reactive power produced by the main grids reaches zero.

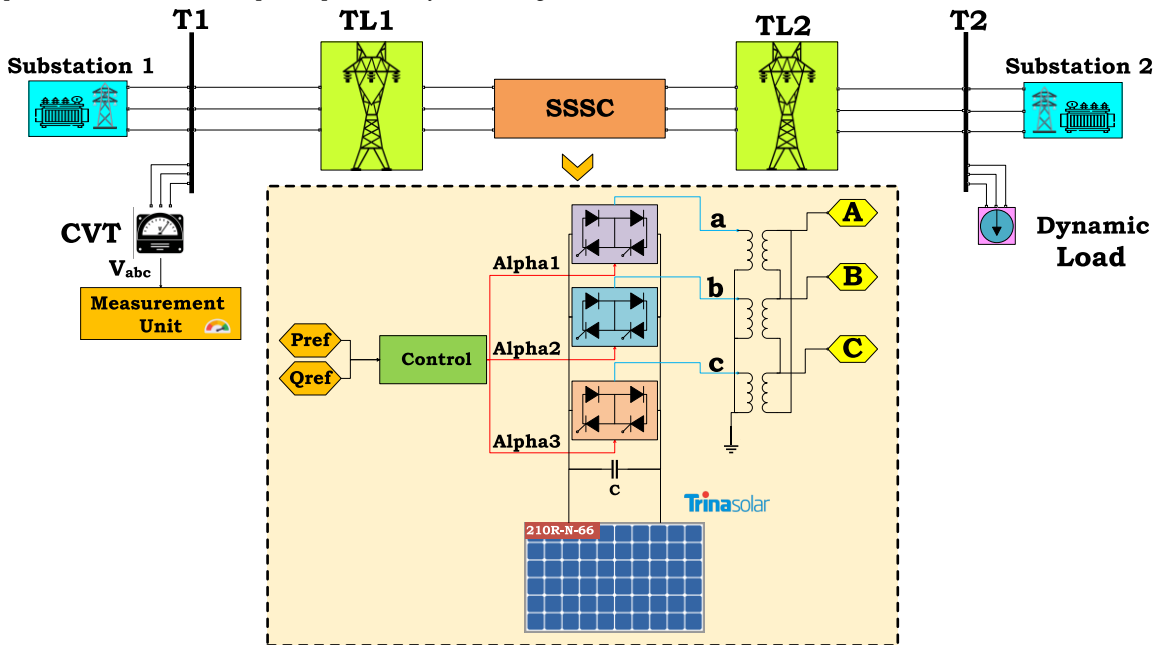


Figure 5. Three-phase diagram of the test network in MATLAB simulation environment.

Table 1. Data of the test network for MATLAB simulation.

| Line parameters | Value |
|---|------------------------|
| Positive-sequence resistance (R1) (Ω /km) | 0.02546 |
| Zero-sequence resistance (R0) (Ω /km) | 0.3864 |
| Positive-sequence inductance (L1) (H/km) | 0.00093 |
| Zero-sequence inductance (L0) (H/km) | 0.0041264 |
| Positive-sequence capacitance (C1) (H/km) | 1.27×10^{-8} |
| Zero-sequence capacitance (C0) (H/km) | 7.751×10^{-9} |
| Length of the line segment (km) | 50 |
| Line frequency (Hz) | 50 |
| Synchronous generator parameters | Value |
| Rated voltage (kV) | 13.8 |
| X_d (p.u.) | 1.305 |
| X_d' (p.u.) | 0.296 |

| | |
|---|-------------------|
| Xd" (p.u.) | 0.252 |
| Xq (p.u.) | 0.474 |
| Xq" (p.u.) | 0.243 |
| Xl (p.u.) | 0.18 |
| Frequency of power sources (Hz) | 50 |
| Td' (s) | 1.01 |
| Td" (s) | 0.053 |
| Tq0" (s) | 0.1 |
| Rs | 0.0028544 |
| H (s) | 3.7 |
| Pair of poles | 32 |
| Initial angle (deg) | -58.9841 |
| Initial current of phases a, b, c (p.u.) | 0.763417 |
| Initial angle of phase a (deg) | 14.3746 |
| Initial angle of phase b (deg) | -105.625 |
| Initial angle of phase c (deg) | 134.375 |
| Excitation voltage (p.u.) | 1.2256 |
| Parameters of generators' three-phase transformers | |
| Rated power (MVA) | 2100 |
| Frequency (Hz) | 50 |
| Primary voltage (kV) | 13.8 |
| Secondary voltage (kV) | 500 |
| R1 (p.u.) | 0.002 |
| L1 (p.u.) | 0 |
| R2 (p.u.) | 0.002 |
| L2 (p.u.) | 0.12 |
| Rm (p.u.) | 500 |
| Lm (p.u.) | 500 |
| Connection type | Star-delta |
| Characteristics of the dynamic load | |
| Rated voltage (kV) | 500 |
| Rated frequency (Hz) | 50 |
| Active power (W) | 2.2×10^9 |
| Reactive power (Var) | 0.8×10^8 |
| Primary positive-sequence voltage (p.u.) | 1.00208 |
| Primary positive-sequence angle (deg) | 20.9514 |
| Characteristics of the SSSC | |
| Rated voltage (kV) | 500 |
| Rated frequency (Hz) | 50 |
| Rated power of the series converter (MVA) | 100 |
| Injected voltage (p.u.) | 0.1 |
| R (p.u.) | 0.00533 |
| L (p.u.) | 0.16 |
| DC-link voltage (V) | 40000 |
| DC-link capacitance (F) | 0.000375 |
| Trina Solar- 210R-N-66 | |
| Module power (W) | 700 |
| Module Efficiency (%) | 22.5 |
| ISC (A) | 17.44 |
| VOC(V) | 49.4 |
| Maximum Power Voltage-VMPP (V) | 43.2 |
| Maximum Power Current-IMPP (A) | 9.96 |
| NOCT (Nominal Operating Cell Temperature) | 43 |
| Max Series Fuse Rating (A) | 25 |

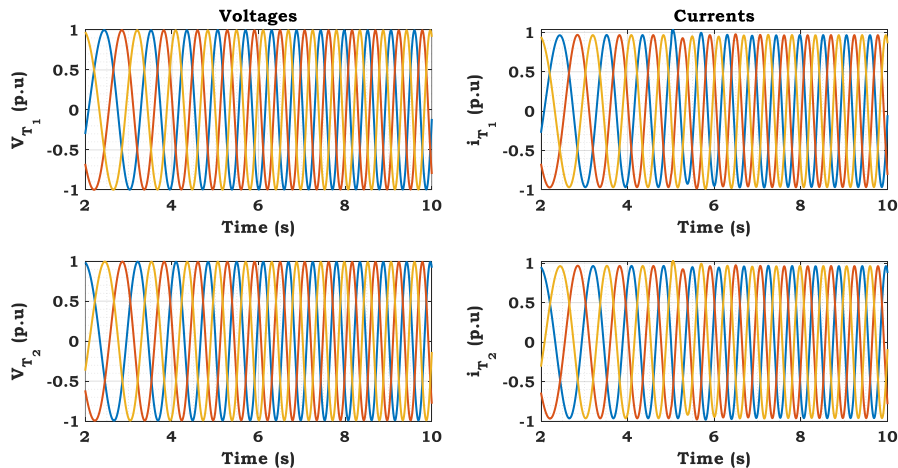


Figure 6. Three-phase voltages measured on terminals T₁ and T₂ of the transmission line.

3.2. Fault scenarios and results analysis

In this part, the goal is to evaluate the algorithm in different fault scenarios in the transmission line compensated with SSSC. According to the network modeled in Figure 5 and also the pseudocode of the algorithm in Figure 4, the threshold values of this network are equal to 0.05, 1.7, and 0.6, respectively. These threshold values have been obtained in a per-unit system based on the implementation of at least 4000 fault scenarios. To evaluate the proposed algorithm, the three-phase voltages of terminal T_1 , as well as the threshold values, are needed. In the following, five scenarios are used to test the proposed algorithm. These scenarios have been implemented for different points of the line on both sides of the SSSC, as well as for different resistance values and different phases. According to the results presented in the implementation of the scenarios, the algorithm's performance is assessed as very favorable.

Scenario 1: In this scenario, an AG fault appears 80 km away from terminal T_1 with $R = 10 \Omega$ at $t = 7$ s. The three-phase voltage diagram of terminal T_1 in the time domain is given in Figure 9. After measuring this voltage and applying DWT and extracting CD1 according to Figure 10 for all three phases and measuring the maximum values of this detail coefficient and comparing them with the threshold values and with each other, according to the flowchart in Figure 4, the implementation result is given in Figure 11, where the performance of the proposed algorithm is evaluated as very favorable.

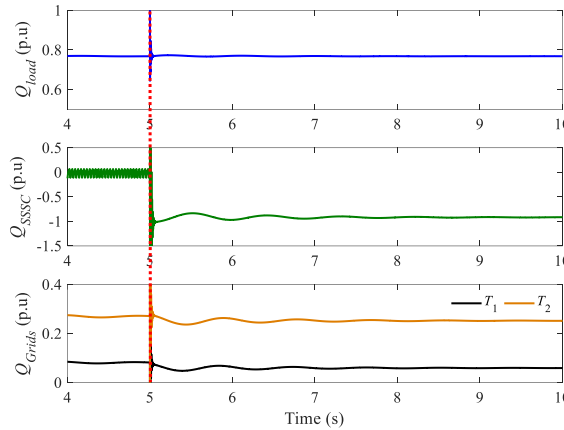


Figure 7. The reactive power demand of the dynamic load, the reactive power injected by SSSC on Terminal 2, and the reactive power generated by the networks connected to Terminals 1 and 2.

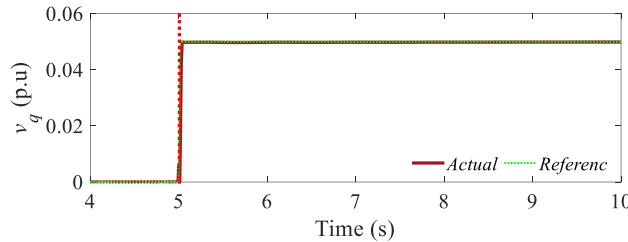


Figure 8. Real and reference v_q values tracked by the POD controller.

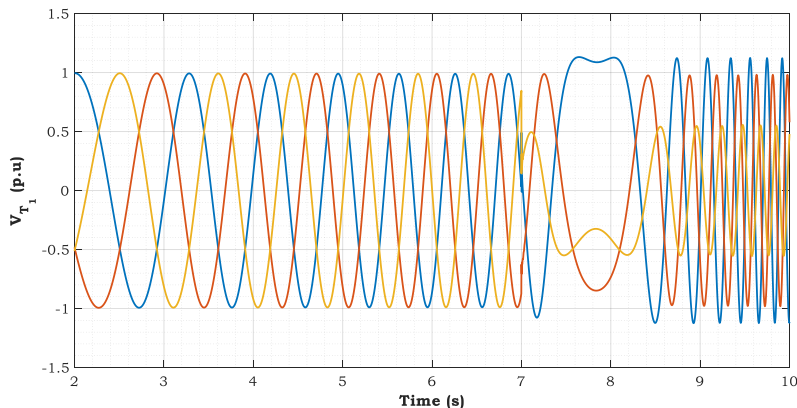


Figure 9. Three-phase voltage of terminal T_1 in accordance with the implementation of Scenario 1.

Scenario 2. In this scenario, an AG fault appears 30 km away from terminal T_1 with $R = 10 \Omega$ at $t = 8$ s. The three-phase voltage diagram of terminal T_1 in the time domain is given in Figure 12. After measuring this voltage and applying DWT and extracting CD1 according to Figure 13 for all three phases and measuring the maximum values of this detail coefficient and comparing them with the threshold values and with each other according to the flowchart in Figure 4, the result of implementation is shown in Figure 14, where the performance of the proposed algorithm is evaluated as very favorable.

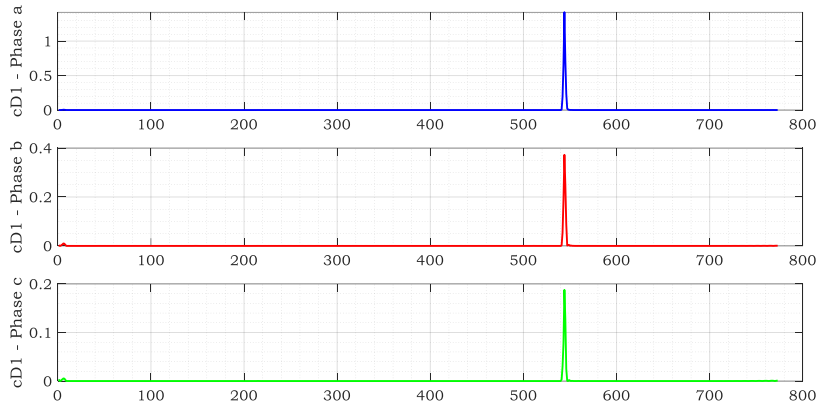


Figure 10. Detail coefficients of level 1 of all three phases a, b, and c, corresponding to the three-phase voltage of Terminal T_1 in Scenario 1.

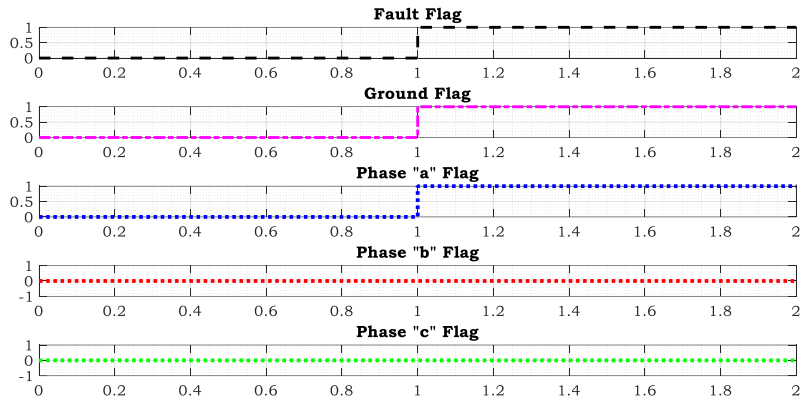


Figure 11. The performance results of the algorithm in detecting a fault, detecting whether the fault is grounded or not, and detecting the faulty phases in Scenario 1.

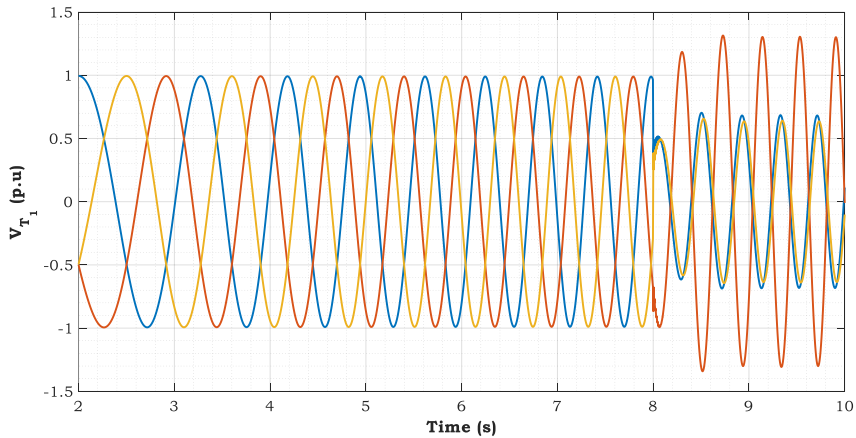


Figure 12. Three-phase voltage of terminal T_1 according to the implementation of scenario 2.

Scenario 3. In this scenario, an ABG fault occurs at 55 km away from terminal T_1 with $R = 50 \Omega$ at $t = 6.5$ s. The three-phase voltage diagram of terminal T_1 in the time domain is given in Figure 15. After measuring this voltage and applying DWT and extracting CD1 according to Figure 16 for all three phases and measuring the maximum values of this detail coefficient and comparing them with the threshold values and with each other according to the pseudocode of Figure 4, the result of the implementation is depicted in Figure 17, where the algorithm’s performance is evaluated as very favorable.

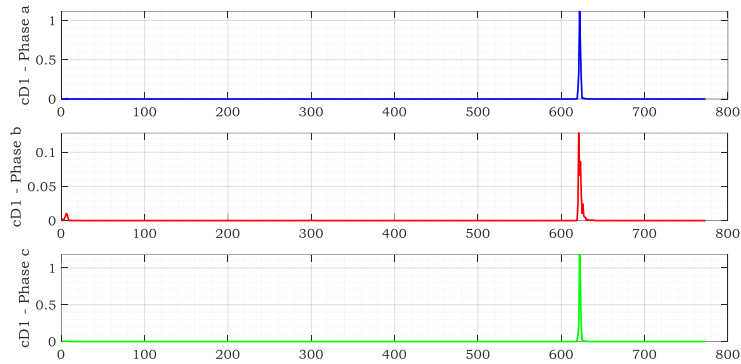


Figure 13. Detail coefficients of level 1 of all three phases a, b, and c, corresponding to the three-phase voltage of terminal T_1 in scenario 2.

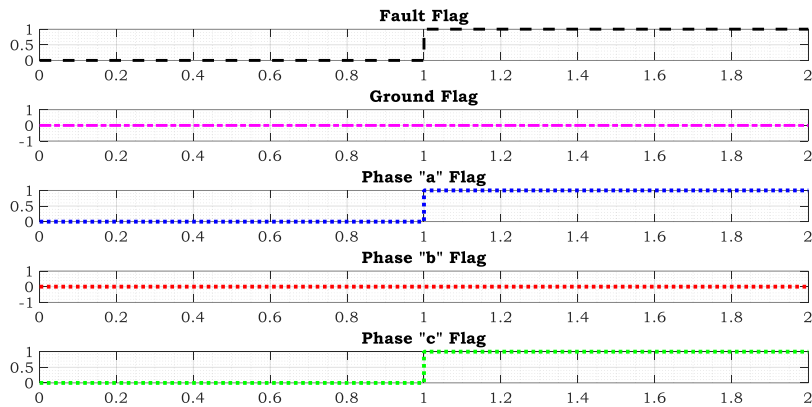


Figure 14. The performance results of the algorithm in detecting a fault, detecting whether the fault is grounded or not, and detecting the faulty phases in scenario 2.

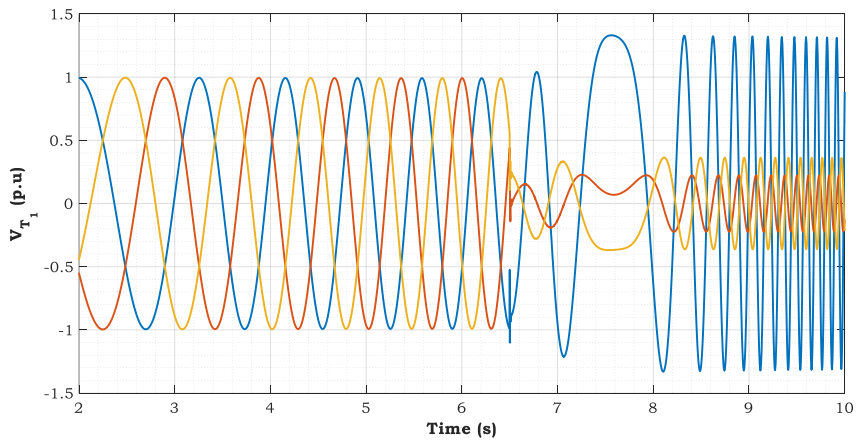


Figure 15. Three-phase voltage of terminal T_1 according to the implementation of scenario 3.

Scenario 4: In this scenario, an ABC fault appears 20 km away from terminal T_1 with $R = 1 \Omega$ at $t = 8$ s. The three-phase voltage diagram of terminal T_1 in the time domain is given in Figure 18. After measuring this voltage and applying DWT and extracting CD1 according to Figure 19 for all three phases and measuring the maximum values of this detail coefficient and comparing them with the threshold values and with each other according to the flowchart in Figure 4, the result of implementation is provided in Figure 20, where the algorithm's performance is evaluated as very favorable.

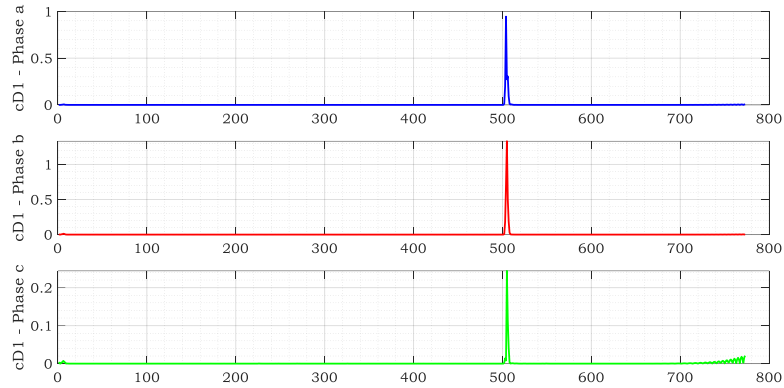


Figure 16. Detail coefficients of level 1 of all three phases a, b, and c, corresponding to the three-phase voltage of terminal T_1 in scenario 3.

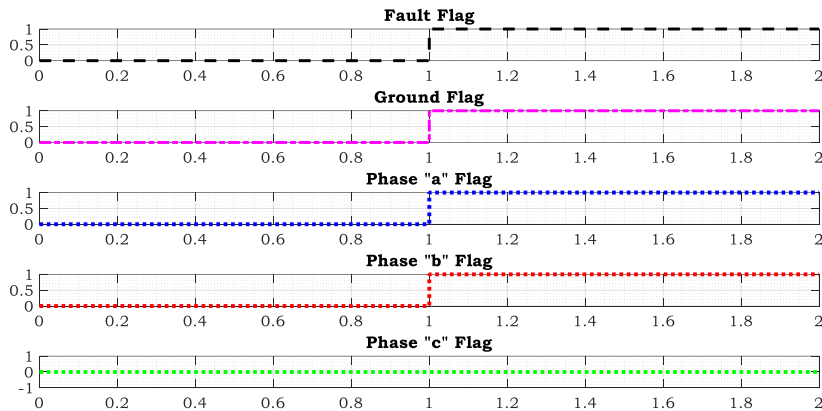


Figure 17. The performance results of the algorithm in detecting a fault, detecting whether the fault is grounded or not, and detecting the faulty phases in scenario 3.

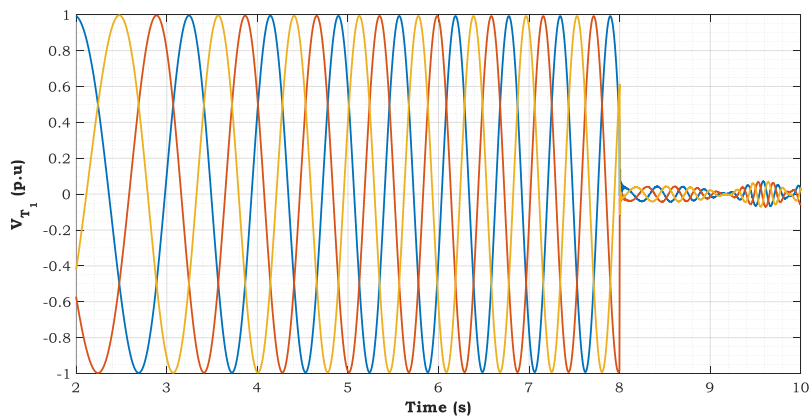


Figure 18. Three-phase voltage of terminal T_1 according to the implementation of scenario 4.

Scenario 5: In this scenario, a CG fault appears 65 km away from terminal T_1 with $R = 100 \Omega$ at $t = 9$ s. The three-phase voltage diagram of terminal T_1 in the time domain is given in Figure 21. After measuring this voltage and applying DWT and extracting CD1 according to Figure 22 for all three phases and measuring the maximum values of this detail coefficient and comparing them with the threshold values and also comparing them with each other according to the pseudocode of Figure 4, the result of the implementation is illustrated in Figure 23, where the algorithm's performance is evaluated as very favorable.

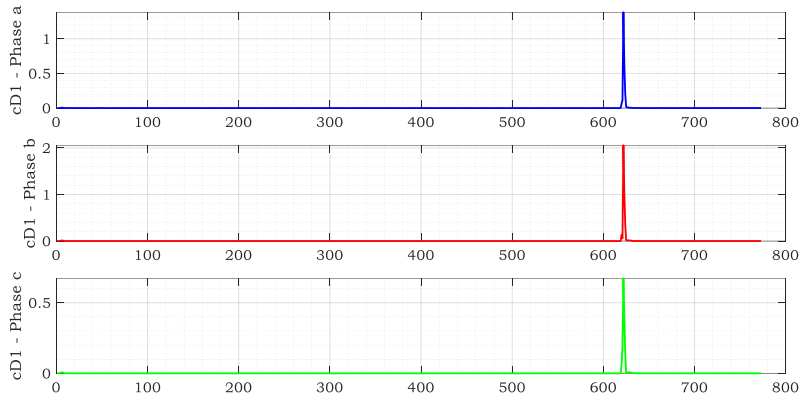


Figure 19. Detail coefficients of level 1 of all three phases a, b, and c, corresponding to the three-phase voltage of terminal T_1 in Scenario 4.

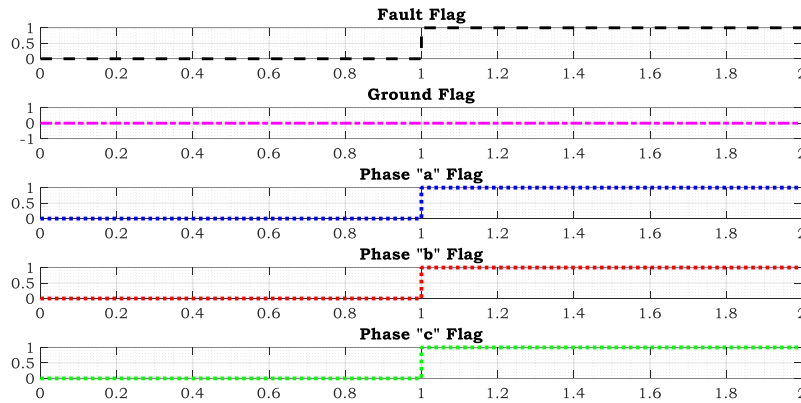


Figure 20. The performance results of the algorithm in detecting a fault, detecting whether the fault is grounded or not, and detecting the faulty phases in Scenario 4.

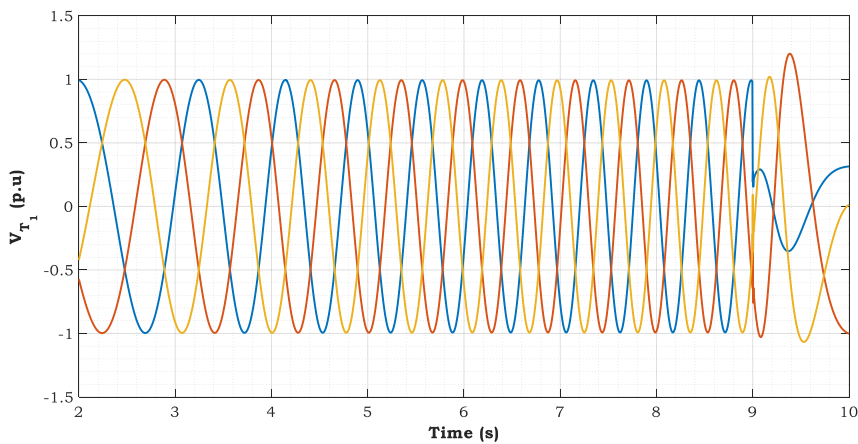


Figure 21. Three-phase voltage of terminal T_1 according to the implementation of Scenario 5.

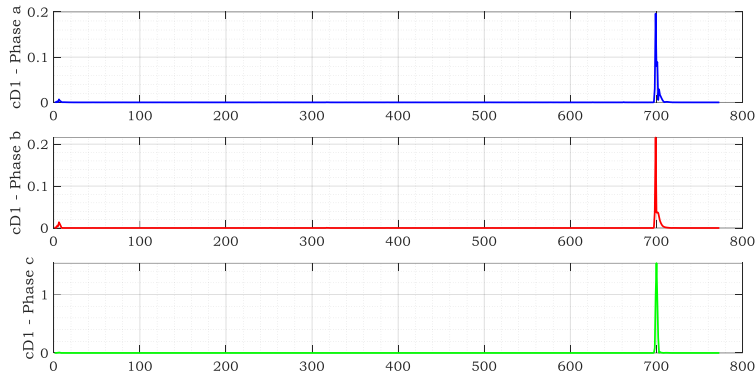


Figure 22. Detail coefficients of level 1 of all three phases a, b, and c corresponding to the three-phase voltage of terminal T₁ in Scenario 5.

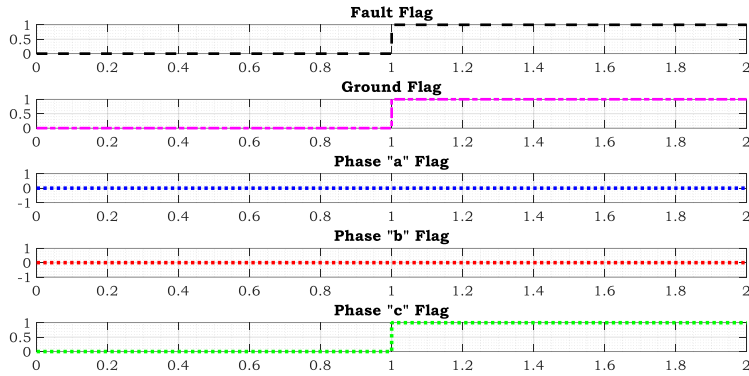


Figure 23. The performance results of the algorithm in detecting a fault, detecting whether the fault is grounded or not, and detecting the faulty phases in Scenario 5.

4. Sensitivity analysis of the proposed algorithm

The goal here is to evaluate the proposed algorithm with respect to seven critical scenarios. According to the results obtained in Section 3, the algorithm’s performance during a fault is very favorable in normal conditions. Nonetheless, now we evaluate the algorithm’s performance for very critical conditions. Here, the resistance of the algorithm to critical conditions has been tested and evaluated.

Scenario 1 sensitivity analysis: In this sensitivity analysis, the SSSC is assumed to be placed 25% closer to terminal T₂. An AB fault occurred 90 km away from terminal T₁ at $t = 6$ s with a resistance of 20 Ω. The implementation results of this scenario are tabulated in Table 2 in the row related to SA1. According to the obtained results, the algorithm is not sensitive to the location of SSSC and works correctly.

Scenario 2 sensitivity analysis: In this sensitivity analysis, a BCG fault is assumed at 60 km away from terminal T₁ with a fault resistance value of 250 Ω at $t = 5.5$ s. The implementation results are provided in Table 2 in the row related to SA2. According to the obtained results, the suggested algorithm is a little sensitive to the high-resistance fault. The final value of this resistance is 317 Ω at and the fault occurs at 95 km away from terminal T₁ and is a single-phase to ground fault.

Scenario 3 sensitivity analysis: In this sensitivity analysis, an AG fault appears at 40 km away from terminal T₁ with a phase-to-phase resistance of 3 Ω when phase A voltage of terminal T₁ crosses the zero point. The implementation results are shown in Table 2 in the row related to SA3. According to the obtained results, it is shown that the proposed algorithm is resistant to crossing the zero-voltage point.

Scenario 4 sensitivity analysis: In this sensitivity analysis, a power oscillation is assumed with a frequency deviation of 1 Hz in the generator connected to terminal T₂ for 3 cycles before a solid AB fault occurrence at 55 km away from terminal T₁ at $t = 6$ s. The fault occurred during power oscillation. The implementation results are presented in Table 2 in the row related to SA4. According to the obtained results, the algorithm is resistant to power oscillations due to the use of POD.

Scenario 5 sensitivity analysis: In this sensitivity analysis, the dynamic fluctuations of the load connected to terminal T₂ will increase by 20% in terms of active power (this process is done by increasing the angle and frequency). In this case, no fault has occurred in the network. The implementation results are presented in Table 2 in row SA5. According to the presented results, the suggested algorithm successfully detects the absence of a fault and has not detected this phenomenon as a fault. As shown, the algorithm is resistant to critical conditions similar to faults.

Scenario 6 sensitivity analysis. In this sensitivity analysis, the operation mode of SSSC is changed. In this case, the reference value has changed from 0.5 to 0.1 p.u. In this situation, a CG fault occurred 75 km away from terminal T₁ at t = 7 s with R = 50 Ω. The implementation results are tabulated in Table 2 in row SA6. According to the results, the algorithm is resistant to changing the learning mode of SSSC, so the proposed design can be implemented in any operation mode.

Scenario 7 sensitivity analysis. In this sensitivity analysis, a white Gaussian noise of 20 dB is injected into the voltage measurement of bus T₂ for 3 cycles before the fault. In this case, an AB fault appears at 80 km away from terminal T₁ with R = 10 Ω. The value of 20 dB considered in this case is the critical limit of injection noise, in which case the algorithm works correctly; otherwise, the performance of the algorithm will be disturbed by increasing the value of this level of noise. The implementation results are provided in Table 2 in row SA7. According to the presented results, the performance of the algorithm in these critical limit conditions is acceptable.

The conducted sensitivity analysis rigorously evaluates the algorithm’s performance under extreme grid conditions that frequently challenge conventional protection schemes. Each of the seven scenarios targets a distinct vulnerability in real-world transmission systems compensated by FACTS devices and exposed to renewable integration. These include:

- High-impedance faults (SA2, SA6): where signal attenuation tests the algorithm’s capacity to distinguish low-energy transients.
- Zero-voltage crossing conditions (SA3): This challenges the time-frequency resolution of CD1 features.
- Pre-fault power oscillations (SA4): This introduces false harmonic content, potentially masking true fault signatures.
- Non-fault dynamic load shifts (SA5): Validating the algorithm’s immunity to operational disturbances.
- Controller setpoint variation in the SSSC (SA6): This alters the voltage regulation regime and affects waveform morphology.
- Gaussian noise in VT measurements (SA7): pushing the threshold margins to their detection limits.

Across all scenarios, the proposed threshold-based decision logic—grounded in energy analysis of level-1 wavelet coefficients (CD1)—demonstrates consistent phase selectivity and fault-type discrimination. The statistical dispersion of CD1 peak values across faulted and non-faulted phases remained within designed bounds (Thr0, Thr1, Thr2), ensuring high robustness even under distorted, delayed, or weakened signal conditions. This sensitivity validation confirms that the threshold values are not only empirically optimized but “electrodynamically grounded”, accounting for the nonlinearities introduced by SSSC control behavior, PV intermittency, and measurement imperfections. The algorithm’s resilience to these multidimensional disturbances substantiates its suitability for deployment in complex modern grids.

5. Conclusion

This paper developed and validated a novel, high-performance algorithm for detecting and classifying short-circuit faults in SSSC-compensated transmission lines, using only single-terminal voltage measurements. The method is rooted in a signal processing approach that exploits the high time-frequency localization properties of the DWT. By employing the db6 wavelet function and decomposing the voltage signals up to level 9, the algorithm captures subtle high-frequency transients associated with fault inception. Among all decomposition levels, the first-level detail coefficients (CD1) consistently exhibited the highest sensitivity to abrupt disturbances, making them ideal for fault signature extraction. A rigorous feature extraction mechanism based on CD1 peak energy across phases was established, followed by a multi-threshold decision algorithm utilizing three empirically calibrated thresholds (Thr0, Thr1, Thr2). These thresholds effectively separated faulty from healthy phases under complex system conditions. To ensure robustness, the method was evaluated across more than 4000 fault scenarios, covering:

- All conventional fault types (SLG, LL, LLG, LLL),
- Fault resistances ranging from 1 to 317 Ω,
- Different locations relative to the SSSC (both left and right sides),
- Variable fault inception times (6.5–9.0 s),
- Phase-dependent zero-crossing conditions.

In addition to normal scenarios, seven critical operating conditions were simulated, such as:

- SSSC control reference variation, altering the line's reactive compensation dynamics,
- Gaussian white noise (20 dB) added to voltage signals,
- Pre-fault power oscillations that distort the voltage waveform spectrum,
- Dynamic load changes, mimicking active disturbances in practical systems.

Table 2. The results of the implementation of different sensitivity analysis scenarios.

| Scenario No. | Maximum values of CD1 for the three phases of terminal T ₁ | | | Implementation results | | | | |
|--------------|---|---------|---------|------------------------|-----------------------|------------------------|---------|---------|
| | Phase c | Phase b | Phase a | Is there a fault? | Is it a ground fault? | Which phase is faulty? | | |
| | | | | | | Phase c | Phase b | Phase a |
| SA1 | 1.1 | 1.09 | 0.15 | Yes | No | | | |
| SA2 | 0.25 | 1.4 | 1.01 | Yes | Yes | | | |
| SA3 | 1.39 | 0.29 | 0.22 | Yes | Yes | | | |
| SA4 | 1.12 | 0.12 | 1.11 | Yes | No | | | |
| SA5 | 0.15 | 0.11 | 0.09 | No | No | | | |
| SA6 | 0.26 | 0.33 | 1.32 | Yes | Yes | | | |
| SA7 | 1.13 | 1.11 | 0.17 | Yes | No | | | |

Despite these challenges, the algorithm maintained a 98% accuracy rate in correctly detecting faulty phases and classifying fault types. The wavelet-based energy signatures proved resilient against noise and signal distortion, and the algorithm's independence from current measurements mitigates CT saturation and reduces implementation complexity. Unlike many prior studies, which either rely on dual-terminal data, assume ideal conditions, or ignore FACTS behavior, the proposed method explicitly accounts for the dynamic behavior of an SSSC connected to a PV source — a non-trivial integration often ignored in literature.

Proposed research directions (deep and technically grounded) include:

1. Adaptive threshold tuning using real-time disturbance metrics: Developing an online adjustment mechanism for Thr0–Thr2 based on instantaneous signal quality or system states (e.g., SSSC modulation depth or PV variability).
2. Hybrid wavelet-ML architectures: Integrating machine learning models (e.g., ensemble classifiers, GBDT, CNN) trained on wavelet-domain features to enhance classification under uncertain topologies.
3. Spatiotemporal coordination with PMU data: Extending the method to wide-area protection schemes using synchronized phasor measurements and GPS-based event correlation.
4. Real-time FPGA/RTDS implementation: Deploying the proposed method on hardware platforms to evaluate latency, resource usage, and feasibility in practical protection relays.
5. multi-objective optimization of wavelet parameters: Using evolutionary algorithms (e.g., NSGA-II) to jointly optimize wavelet type, decomposition depth, and threshold margins under noisy or uncertain environments.
6. Generalization to meshed and looped networks: Validating the method in more complex topologies where multiple FACTS or PV sources introduce nonlinear interactions in the protection zone.

References

- [1] M. Abasi, M. Joorabian, A. Saffarian, and S. Seifossadat, "A Comprehensive Review of Various Fault Location Methods for Transmission Lines Compensated by FACTS Devices and Series Capacitors," *Journal of Operation and Automation in Power Engineering*, vol. 9, no. 3, pp. 213–225, 2021.
- [2] M. Abasi, and O. Sadeghian, "A Ground Fault Location Algorithm in Double-circuit Transmission Lines with T-off Connection to an Industrial Microgrid by Using Current and Voltage Phasors Information of a Single Terminal," *IET Generation, Transmission & Distribution*, vol. 18, no. 8, pp. 1714–1741, 2024.
- [3] M. Abasi, A. Saffarian, M. Joorabian, and S. G. Seifossadat, "Fault Location in Double-Circuit Transmission Lines Compensated by Generalized Unified Power Flow Controller (GUPFC) Based on Synchronous Current and Voltage Phasors," *IEEE Systems Journal*, vol. 15, no. 2, pp. 2190–2200, 2021.
- [4] V. Malathi, N. Marimuthu, S. Baskar, and K. Ramar, "Application of Extreme Learning Machine for Series Compensated Transmission Line Protection," *Engineering Applications of Artificial Intelligence*, vol. 24, no. 5, pp. 880–887, 2011.
- [5] B. Y. Vyas, B. Das, and R. P. Maheshwari, "Improved Fault Classification in Series Compensated Transmission Line: Comparative Evaluation of Chebyshev Neural Network Training Algorithms," *IEEE Transactions on Neural Networks and Learning Systems*, vol. 27, no. 8, pp. 1631–1642, 2016.
- [6] J. R. Moparthi, D. P. Chinta, and S. Nakka, "Two-Dimensional Curve Variation Approach-Based Quick Fault Detection and Classification Scheme for Series Compensated Transmission Line System," *International Transactions on Electrical Energy Systems*, vol. 29, no. 3, e2738, 2018.
- [7] G. Kapoor, "A Protection Technique for Series Capacitor Compensated 400 kV Double Circuit Transmission Line Based on Wavelet Transform Including Inter-Circuit and Cross-Country Faults," *International Journal of Engineering, Science and Technology*, vol. 11, no. 2, pp. 1–20, 2019.
- [8] P. D. Raval, and A. S. Pandya, "A Novel Fault Classification Technique in Series Compensated Transmission Line Using Ensemble Method," *International Journal of Pattern Recognition and Artificial Intelligence*, vol. 34, no. 04, 2050009, 2019.
- [9] A. R. Adly, S. H. Abdel Aleem, M. A. Elsadd, and Z. M. Ali, "Wavelet Packet Transform Applied to a Series-Compensated Line: A Novel Scheme for Fault Identification," *Measurement*, vol. 151, 107156, 2020.
- [10] D. Pradhan, and Panda, "Application of Artificial Intelligence Techniques for Classification and Location of Faults on Thyristor-Controlled Series-Compensated Line," *Electric Power Components and Systems*, vol. 31, no. 3, pp. 241–260, 2003.
- [11] S. Samantaray, "Decision Tree-Based Fault Zone Identification and Fault Classification in Flexible AC Transmissions-Based Transmission Line," *IET Generation, Transmission & Distribution*, vol. 3, no. 5, pp. 425–436, 2009.
- [12] B. Yashvantrao Vyas, R. P. Maheshwari, and B. Das, "Pattern Recognition Application of Support Vector Machine for Fault Classification of Thyristor Controlled Series Compensated Transmission Lines," *Journal of The Institution of Engineers (India): Series B*, vol. 97, pp. 175–183, 2016.
- [13] B. Yashvantrao Vyas, R. P. Maheshwari, and B. Das, "Pattern Recognition Application of Support Vector Machine for Fault Classification of Thyristor Controlled Series Compensated Transmission Lines," *Journal of The Institution of Engineers (India): Series B*, vol. 97, no. 2, pp. 175–183, 2015.
- [14] O. H. Gupta, and M. Tripathy, "Superimposed Energy-Based Fault Detection and Classification Scheme for Series-Compensated Line," *Electric Power Components and Systems*, vol. 44, no. 10, pp. 1095–1110, 2016.
- [15] G. Kapoor, "An SMMBG-Based Relaying Technique for Detection and Categorization of Faults in TCSC-Compensated Transmission Lines," *Journal of Electrical and Electronics Engineering*, vol. 13, no. 1, 2020.
- [16] A. A. R. Mohamed, H. M. Sharaf, and D. K. Ibrahim, "Enhancing Distance Protection of Long Transmission Lines Compensated with TCSC and Connected with Wind Power," *IEEE Access*, vol. 9, pp. 46717–46730, 2021.
- [17] N. H. Kothari, B. R. Bhalja, V. Pandya, and P. Tripathi, "A Rate-Of-Change-Of-Current Based Fault Classification Technique for Thyristor-Controlled Series-Compensated Transmission Lines," *International Journal of Emerging Electric Power Systems*, vol. 23, no. 3, pp. 289–304, 2021.
- [18] S. Kumar Mohanty, A. Swetapadma, P. Kumar Nayak, and O. P. Malik, "Decision Tree Approach for Fault Detection in a TCSC Compensated Line During Power Swing," *International Journal of Electrical Power & Energy Systems*, vol. 146, 108758, 2023.
- [19] A. M. El-Zonkoly, and H. Desouki, "Wavelet Entropy Based Algorithm for Fault Detection and Classification in FACTS Compensated Transmission Line," *Energy and Power Engineering*, vol. 03, no. 01, pp. 34–42, 2011.
- [20] Q. Liu, Y. Y. Chang, and Y. Xu, "Fault Position Identification for Series Compensated Lines with SSSC Based on Improved Wavelet Packet Entropy," *Advanced Materials Research*, vol. 383–390, pp. 5200–5205, 2011.
- [21] M. Geethanjali, M. A. Alias, and T. K. S. Pandya, "Discrete Wavelet Transform Based Fault Detection and Classification in a Static Synchronous Series Compensated Transmission System," *Advances in Intelligent Systems and Computing*, pp. 85–94, 2014.
- [22] E. Reyes-Archundia, J. L. Guardado, E. L. Moreno-Goytia, J. A. Gutierrez-Gnechchi, and F. Martinez-Cardenas, "Fault Detection and Localization in Transmission Lines with a Static Synchronous Series Compensator," *Advances in Electrical and Computer Engineering*, vol. 15, no. 3, pp. 17–22, 2015.
- [23] M. M. Almomani and S. F. Algharaibeh, "Modelling and Testing of a Numerical Pilot Distance Relay for Compensated Transmission Lines," *International Journal of Scientific Research and Engineering Development*, vol. 3, no. 6, 2020.
- [24] H. V. Gururaja Rao, N. Prabhu, and R. C. Mala, "Wavelet Transform-Based Protection of Transmission Line Incorporating SSSC with Energy Storage Device," *Electrical Engineering*, vol. 102, no. 3, pp. 1593–1604, 2020.
- [25] H. Hanif, M. Zand, M. Azimi Nasab, S. M. S. Ghiasi, and S. Padmanaban, "Scenario-Based Planning of Participation of Virtual Power Plants in Storage and Energy Markets in Terms of Load Response and Market Price Uncertainty," *Journal of Green Energy Research and Innovation*, vol. 1, no. 3, pp. 77–95, 2024.
- [26] B. Rostami, J. Ebrahimi, Z. Sabzian Molaei, V. Davatgaran, and S. A. Alavi, "Improving the Technical and Economic Indexes of Distribution Network by Three-Stage Enhanced Imperialist Competitive Algorithm," *Journal of Green Energy Research and Innovation*, vol. 1, no. 3, pp. 1–15, 2024.
- [27] S. Darvish Kermani, M. Fayazi, J. Barati, and M. Joorabian, "Percentage of Islanding and Peninsulating Detection in Large Microgrids with Renewable Energy Resources with Multiple Connection Points to Different Grids," *Journal of Green Energy Research and Innovation*, vol. 1, no. 2, pp. 1–14, 2024.
- [28] H. Makvandi, M. Abasi, et al., "Design of New Intelligent Islanding Detection Scheme in Multi-Machine Power Systems to Prevent Wide-Area Blackouts," *2022 12th Smart Grid Conference (SGC)*, pp. 1–7, 2022.

Declaration of competing interest

The authors declare that they have no known competing financial interests or personal relationships that could have appeared to influence the work reported in this paper. The ethical issues, including plagiarism, informed consent, misconduct, data fabrication and/or falsification, double publication and/or submission, redundancy, have been completely observed by the authors.

Bibliography



Mahyar Abasi was born in Iran, in 1989. He received the Ph.D. degree in electrical power engineering from Shahid Chamran University of Ahvaz, Ahvaz, Iran, in 2021. He is currently an Assistant Professor with the Electrical Engineering Department, Arak University, Arak, Iran. In 2021, he was introduced as the top researcher of Khuzestan Province, Iran. From 2021 to 2023, he successfully received four titles from the membership schemes of the National Elite Foundation in Iran. His research background is more than 60 published journal and conference papers, more than ten authored books, 11 industrial research projects, and a patent in power systems. His specialized interests are fault protection, detection, classification, and location in HVAC and HVDC transmission lines, control of reactive power and FACTS devices, evaluation and improvement of power quality, and power system studies.

Email: m-abasi@araku.ac.ir

ORCID: [0000-0001-5228-6803](https://orcid.org/0000-0001-5228-6803)

Contribution Statement: Conceptualization, Data curation, Formal analysis, Investigation, Methodology, Resources, Software, Supervision, Roles/Writing - original draft, Writing-review & editing.



Ebrahim Khanfari was born in 1989 in Iran. He received his bachelor's degree in Transmission Network Technology Engineering in 2017 from Khuzestan University of Applied Sciences, Faculty of Water and Electricity. He is currently a master's student in power engineering at Institute for Higher Education, ACECR, Khuzestan, Iran. His expertise is in the field of protection of power systems and FACTS devices.

Email: Aabrahim.khanfari@gmail.com

ORCID: [0009-0006-1969-0998](https://orcid.org/0009-0006-1969-0998)

Contribution Statement: Formal analysis, Methodology, Software, Visualization.